DIFFUSION MODELLING TO CONSTRAIN THE DURATION OF METAMORPHISM

Iona R. Stenhouse

A thesis submitted for the degree of

Doctor of Philosophy of The Australian National University

Australian National University

July 2013

Statement of Authorship

I declare, that except where otherwise indicated, the results and conclusions contained within this thesis are the author's own. The work presented was carried out between February 2009 and January 2013 and has not been used for the award of any other degree.

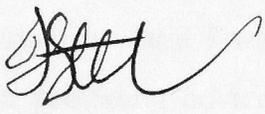

Iona R. Stenhouse

26 July 2013

Acknowledgements

I would first like to express my gratitude towards the members of my supervisory panel, Professor Gordon Lister, Professor Hugh O'Neill, Professor Sumit Chakraborty, Dr Jörg Hermann and Dr Marnie Forster, for providing ongoing assistance and advice throughout my candidature. In particular, I thank Professor Gordon Lister for providing the impetus for this project, as well as continued guidance and support throughout my candidature; Professor Hugh O'Neill, for the supervision of the experimental component and his patience when I was continuing to learn experimental techniques; Dr Jörg Hermann for providing advice on the direction of my project and facilitating the Ivrea-Verbano Zone study that was undertaken as part of my project. Thanks to Dr Marnie Forster for supervision of the argon geochronology component of my project and discussions on the interpretation of results. I would like to thank Professor Sumit Chakraborty and Dr Ralf Dohmen from the Ruhr-Universität, Bochum for hosting my visit to Bochum, Germany to perform experiments and also engaging in valuable discussions concerning my project. I would also like to thank them for performing additional experiments in my absence.

This thesis would not have been possible without the samples provided by Dr Daniel Viete and Dr Tanya Ewing who collected samples during their own PhD candidatures from the Barrovian metamorphic sequence, Scotland and the Ivrea-Verbano Zone, Italy, respectively. Dr Viete also provided beneficial advice on numerous components of my project, including my own field work in Scotland.

I would like to thank the institutes and organisations that have supported my project financially. This includes the Australian National University (ANU) and the Australian Government for providing my PhD scholarship. As well as ANU for providing a Vice-Chancellor's travel grant received for overseas travel and attendance of the European Geosciences Union 2010 conference, Vienna. The Australian Microscopy and Microanalysis Research Facility (AMMRF) for providing funding for the use of the Nanoscale Secondary Ion Mass Spectrometer (NanoSIMS) at the University of Western Australia in Perth and the Australian Institute for Nuclear Science and Engineering (AINSE) for providing funding for use of the Secondary Ion Mass Spectrometer (SIMS) at the University of Western Sydney (UWS).

I would like to express my thanks to the various people who have helped with the technical aspects of my project. Including Dr Robert Rapp for his advice and assistance with analytical techniques on the electron probe microanalyser. Dr Charlotte Allen and Dr Guill Mallmann for their assistance operating the laser ablation ICP-MS. Dr Angela Halfpenny for her constructive suggestions and advice. Dr Matt Kilburn for assistance with analyses on the NanoSIMS. Dr David Nelson for his help with SIMS analyses and Dr Ian Williams for help with preparation of my samples for SIMS analyses. As well as Shane Paxton, David Clarke, Dean Scott and Harri Kokkonen for help with various projects.

Finally, I would like to give special thanks to all of my family and friends for their support, both financial and emotional, throughout my research candidature. A special mention goes to my patient and caring boyfriend, my wonderful parents and my two brothers, without whom this thesis would not have been possible.

Thesis Synopsis

In this study the application of the garnet-ilmenite system to the diffusion modelling technique was investigated. Experiments were undertaken to accurately determine the rates of geochemical processes that are associated with the garnet-ilmenite system. The diffusion parameters of elements within ilmenite have been quantified and it was found that the diffusivity is relatively fast compared to garnet. Therefore in a garnet-ilmenite diffusion model ilmenite diffusivity can be treated as infinite. Additionally, experiments on garnet with an ilmenite thin film as a diffusant source provided further constraints on the rate of diffusion in garnet.

Evidence of diffusion profiles preserved in garnet surrounding ilmenite inclusions in natural samples was obtained. Samples from the Barrovian metamorphic sequence showed possible diffusional features in Mn concentration profiles adjacent to ilmenite inclusions in garnet from sillimanite zone samples. However, it was also observed that analytical artefacts affected Ti concentration profiles up to 30 μm from the boundary.

Further evidence was obtained from samples from the Ivrea-Verbano Zone in Italy. These samples preserved Mn and Mg diffusion profiles adjacent to ilmenite inclusions in garnet. However, in these samples retrograde reactions caused the ilmenite to be enriched in Mn compared to garnet, therefore, partitioning between garnet and ilmenite was incongruent. Nonetheless, this result shows that the garnet-ilmenite system can provide important information on the tectonometamorphic history of a terrane. The garnet-ilmenite system was used to place constraints on the duration of metamorphism. This duration was obtained using a simple forward model of the diffusional processes. From this, the duration of the thermal event associated with the emplacement of magma in the Ivrea-Verbano Zone was determined to be between 100 000 years to 1 Ma.

Additionally, constraints on the duration of Buchan metamorphism in Scotland were obtained from argon diffusion modelling. The results from modelling were compared to apparent age spectra from cordierite grade samples that preserved detrital ages. This comparison allowed a constraint to be placed on the maximum duration these rocks could have endured and still preserve pre-Grampian ages. The results indicate that the peak conditions of the cordierite zone of the Buchan metamorphic sequence could not have endured longer than 100 000 years.

Diffusion modelling to obtain timescales for thermal events provides insight into the tectonometamorphic history of a terrane. The results of this study have added to the mounting evidence that the duration of regional metamorphism is short (e.g. O'Brien and Vrána, 1995; O'Brien, 1997; Dachs and Proyer, 2002; Faryad and Chakraborty, 2005; Viete et al., 2011b; Viete et al., 2011a; Ague and Baxter, 2007; Camacho et al., 2009). However, there are large uncertainties on the diffusion parameters utilised in diffusion models. Therefore for diffusion modelling to provide better constraints on the duration of regional metamorphism accurate rates of diffusion must be determined.

Table of Contents

CHAPTER 1

Introduction

Preface

This chapter discusses the aims and objectives of the research set out in this thesis. These were developed in consultation with my supervisory panel, Professor Gordon Lister, Professor Hugh O'Neill, Dr Jörg Hermann, Dr Marnie Forster and Professor Sumit Chakraborty. The intention of this research was to determine timescales of thermal events using diffusion modelling. Professor Hugh O'Neill, who worked on the calibration of the garnet-ilmenite geothermometer, proposed that this system might be useful in diffusion modelling. Professor David Ellis also provided valuable advice on this project. Otherwise the work presented in this chapter is my own except where due reference is given.

1.1 Thesis Statement

There is mounting evidence that regional metamorphic belts are produced during much shorter heating events than the crustal thickening model of England and Thompson (1984) would allow (e.g. Ague and Baxter, 2007; Camacho et al., 2009; Viete et al., 2011a; Viete et al., 2011b; Wijbrans and McDougall, 1986). The England and Thompson (1984) model is based on instantaneous crustal thickening with heat produced by the decay of radioactive isotopes while the terrane is exhumed by erosion. This process can require up to 50 Ma to produce Barrovian metamorphic assemblages (England and Thompson, 1984), whereas, diffusion modelling studies have determined durations of thermal events on the order of a few million years or less (e.g. Ague and Baxter, 2007; Viete et al., 2011a). These authors have proposed magmatic heating models to account for shorter durations of heating events.

However, the durations determined using the diffusion modelling technique have large uncertainties related to difficulties in defining initial conditions. Particularly, when considering diffusion in garnet it is often hard to differentiate microstructurally between growth zoning and grain-scale diffusion. In addition, there are large uncertainties associated with the diffusion parameters. Published values for garnet diffusion parameters show a large spread (see Viete, 2009). To address these problems, this research set out to calibrate a new mineral system for diffusion modelling involving the exchange and subsequent diffusion of Fe and Mn between ilmenite inclusions and garnet. Potentially this could allow an independent constraint on the duration of thermal events that produced metamorphic belts. Further using the garnet-ilmenite system in conjunction with other techniques such as argon diffusion modelling will provide better constraints on the duration of thermal events. Therefore this thesis presents the results of three different but related themes.

First, before application of the garnet-ilmenite system to diffusion modelling, a well-constrained set of diffusion parameters is required to reduce uncertainty in the diffusion model. Therefore, experiments were carried out to further constrain the diffusion parameters in the garnet-ilmenite system. These included diffusion experiments to determine the diffusion parameters for various elements within ilmenite with respect to temperature, oxygen fugacity and crystallographic orientation (see Chapter 2). Diffusion experiments on garnet-ilmenite couples were also conducted to further investigate the rates of partitioning and diffusion across the interface (see Chapter 3).

Second, in order to evaluate whether this mineral system can be utilised effectively in natural systems and over what temperature and pressure range, it is necessary to observe and measure diffusion profiles surrounding ilmenite inclusions in garnets in metamorphic rocks. For this research samples were selected from two metamorphic belts, that show a continuous progression of increasing metamorphic grade, from the Barrovian metamorphic sequence in Scotland (see Chapter 4) and from the Ivrea-Verbano Zone in Italy (see Chapter 5).

Finally, if the durations obtained from diffusion modelling using a particular mineral system are accurate, the durations obtained via alternative techniques should be comparable. Therefore this study compares durations constrained from Sr in apatite and garnet diffusion modelling from the Barrovian metamorphic series (e.g. Ague and Baxter, 2007; Viete et al., 2001a; Viete et al., 2011b) with durations constrained by forward modelling argon diffusion in white mica from the synchronous Buchan metamorphic sequence. This involved $^{40}Ar/^{39}Ar$ geochronology using a step heating technique applied to samples collected from the northeast coast of Scotland across the Buchan and Barrovian metamorphic sequences (see Chapter 6). Forward modelling of the argon diffusion in white mica was then carried out to constrain the duration of the Buchan thermal event (see Chapter 7).

1.2 The Mathematics of Diffusion

Central to this thesis is the phenomenon of diffusion. Diffusion is random molecular motions of atoms, which increase with temperature. If there is a concentration gradient there will be a net flux of atoms. When there is a net flux the diffusivity of a species can be measured. Fick's First Law describes the flux of a diffusing species mathematically:

$$F = -D\frac{\partial C}{\partial x} \qquad (1.1)$$

Where F is the flux, D is the diffusion coefficient, C is the concentration and x is the spatial coordinate. Fickian diffusion is based on the assumption that the rate of transfer is proportional to the concentration gradient (Crank, 1975). Fick's Law states that the direction of diffusion is controlled by the concentration gradient and the diffusion parameters regulate the efficiency of this exchange.

From Fick's Law the partial differential equation that describes diffusion can be derived. If diffusion is one-dimensional the equation is:

$$\frac{\partial C}{\partial t} = \frac{\partial}{\partial x}\left(D\frac{\partial C}{\partial x}\right) \tag{1.2}$$

Where t is time and all other variables are as defined above. This equation is also known as Fick's Second Law.

Diffusion is a thermally activated chemical process that effectively acts to eliminate concentration gradients within minerals. If diffusion profiles are preserved, the length of the profiles is proportional to the duration of the thermal event. There is a quadratic relation between the length of the diffusion profile produced (L) and timescale (t) over which diffusion occurred with the diffusion coefficient being the constant of proportionality. For Fickian diffusion:

$$L \propto Dt \tag{1.3}$$

The diffusion coefficient or the diffusivity (D) is calculated using the Arrhenius relationship, which describes the temperature and pressure dependence of the diffusivity:

$$D(t) = D_0 e^{-Q/RT(t)} \tag{1.4}$$

Where D_0 is the diffusion coefficient at infinite temperature, R is the universal gas constant, T is the temperature and Q is determined from the activation energy (E), activation volume ($\bar{v}$) and pressure (P) as described in the following equation.

$$Q = E + P\bar{v} \tag{1.5}$$

These equations are the basis for first order numerical analysis of the effects of diffusion in mineralogical systems. To obtain the duration of a thermal event from measured

diffusion profiles the diffusion equation (Eqn. 1.2) needs to be solved with respect to the initial and boundary conditions determined for the system studied. Solving the diffusion equation can be done either explicitly or implicitly. For example using an explicit finite difference method the solution is as follows for a one-dimensional slab:

$$\frac{c_i^{n+1} - c_i^n}{\Delta t} = \frac{D}{2(\Delta x)^2}\left(c_{i+1}^{n+1} - 2c_i^{n+1} + c_{i-1}^{n+1}\right) \tag{1.6}$$

The explicit method is not sensitive to the size of the steps and therefore is fairly stable. Alternatively, the diffusion equation can be solved using the Crank-Nicolson finite difference method (Crank and Nicolson, 1946). This method is both implicit and explicit. For a one-dimensional slab the solution to the diffusion equation using the Crank-Nicolson method is:

$$\frac{c_i^{n+1} - c_i^n}{\Delta t} = \frac{D}{2(\Delta x)^2}\left(\left(c_{i+1}^{n+1} - 2c_i^{n+1} + c_{i-1}^{n+1}\right) + \left(c_{i+1}^{n} - 2c_i^{n} + c_{i-1}^{n}\right)\right) \tag{1.7}$$

This equation gives the rate of change of the concentration at a particular node, i, for the time step, n+1. One of the disadvantages of this method is that it is extremely sensitive to the size of the spatial and time step and as a result the solution can be unstable.

1.3 The Garnet-Ilmenite System

The first four chapters of this thesis concern Fe and Mn partitioning and diffusion in the garnet-ilmenite system. Garnet and ilmenite are found in a variety of igneous and metamorphic rocks with ilmenite commonly occurring as an inclusion within garnet. If this system can be shown to be a suitable candidate for diffusion modelling it will therefore be applicable over a range of terranes and be able to provide information on the tectonometamorphic history of those terranes. The garnet-ilmenite system is characterised by the partitioning behaviour of Fe and Mn. These cations are exchanged at the interface between the two minerals. The efficiency of this exchange is controlled by the partition coefficient and is temperature dependent. This exchange creates a concentration change at the interface that leads to diffusion. Diffusion rates in garnet

are relatively slow; therefore, as the rock is cooled a diffusion profile can be preserved adjacent to the ilmenite inclusion. Modelling these processes could provide a unique way of obtaining durations of thermal events.

Mn is strongly concentrated in the garnet compared to ilmenite and other co-existing phases (Hollister, 1966; Thompson, 1976; Woodsworth, 1977). During thermal events the partitioning acts to redistribute the elements to achieve equilibrium between the two phases as temperature changes. This exchange is described by the following reaction:

$$1/3Fe_3Al_2Si_3O_{12} + MnTiO_3 = 1/3Mn_3Al_2Si_3O_{12} + FeTiO_3 \qquad \textbf{(1.8)}$$

If the minerals are ideal solid solutions the partition coefficient (K_D) for this reaction is described by the following equation:

$$K_D = \frac{X_{Mn}^{gnt}.X_{Fe}^{ilm}}{X_{Fe}^{gnt}.X_{Mn}^{ilm}} \qquad \textbf{(1.9)}$$

Where X is the mole fraction of the element in the phase labelled. Garnet in nature is often a solid solution of almandine, spessartine, grossular and pyrope. In the exchange reaction (Eqn. 1.8) only the phases almandine and spessartine are considered, as the partitioning between these phases has been calibrated in experiments (e.g. Feenstra and Engi, 1998; Kress et al., 1985; Pownceby et al., 1987; Pownceby et al., 1991). Geikilite ($MgTiO_3$) in the ilmenite solid solution is also not considered.

The partitioning of Fe and Mn between garnet and ilmenite has been experimentally calibrated (e.g. Feenstra and Engi, 1998; Ono, 1980; Pownceby et al., 1987; Pownceby et al., 1991; Săbău and Massonne, 2003) and it was determined that the exchange reaction between garnet and ilmenite is highly sensitive to temperature (e.g. Pownceby et al., 1987). This behaviour provided a means to formulate a geothermometer based on the partitioning (e.g. Chatterjee, 1991; Ganguly et al., 1996; Martin et al., 2010; Pownceby et al., 1987; Pownceby et al., 1991).

The garnet-ilmenite geothermometer was first calibrated by Pownceby et al. (1987) in a series of reversal experiments. However, previous experiments studying the partitioning

behaviour of Fe and Mn between garnet and ilmenite had been performed by Ono (1980), Docka (1984), Kress et al. (1985) and Kress (1986). The geothermometry equation was later refined by Pownceby et al. (1991), Chatterjee (1991), Ganguly et al. (1996a) and Martin et al. (2010).

For the geothermometer to be applicable, it is required that the exchange of Fe and Mn between garnet and ilmenite is the only mechanism operating. If other reactions are operating this system will provide incongruent results (Pownceby et al., 1987). This observation was also noted by Spear et al. (1991) when modelling the garnet-biotite system. Selection of ilmenite inclusions for analysis ensures the ilmenite is not in contact with other fast diffusing phases with which it can readily exchange and products of net transfer reactions should be observable (Spear et al., 1991).

If the temperature has been determined independently the geothermometry equation can be rearranged to calculate the partition coefficient at the interface between garnet and ilmenite:

$$K_D = e^{\frac{-\Delta H^0 + W^{ilm}_{FeMn}\left(2X^{ilm}_{Mn}-1\right) - W^{gnt}_{FeMn}\left(2X^{gnt}_{Mn}-1\right) + \Delta S^0}{RT}} \qquad \textbf{(1.10)}$$

Where ΔH^0 is the enthalpy , ΔS^0 is the entropy and W is the absolute magnitudes of interaction parameters for the phase indicated. These thermodynamic parameters were experimentally determined by Pownceby et al. (1987) and are shown in Table 1.1.

Parameter	Value (units)	Error (±)
$\Delta H^0(1,T)$	17108 $Jmol^{-1}$	4217
$\Delta S^0(T)$	6.02 $Jmol^{-1}K^{-1}$	4.1
W^{Ilm}_{FeMn}	1756 $Jmol^{-1}$	180
W^{Gnt}_{FeMn}	322 $Jmol^{-1}$	376

Table 1.1: The thermodynamic parameters determined by Pownceby et al. (1987) associated with the exchange of Fe and Mn between garnet and ilmenite.

During a thermal event as the temperature changes the partitioning behaviour of Fe and Mn between garnet and ilmenite causes a concentration change at the interface,

which then leads to diffusion away from the interface. Ilmenite diffusion is relatively fast, therefore, the diffusivity of garnet is the rate limiting process in this system. This means the garnet preserves the concentration gradient after the ilmenite has re-equilibrated (Fig. 1.1). Measurement of the diffusion profiles that are present adjacent to ilmenite inclusions in garnet provides a means for determining timescales of thermal events, as the length scale of the diffusion profile is related to the timescale over which diffusion was effective.

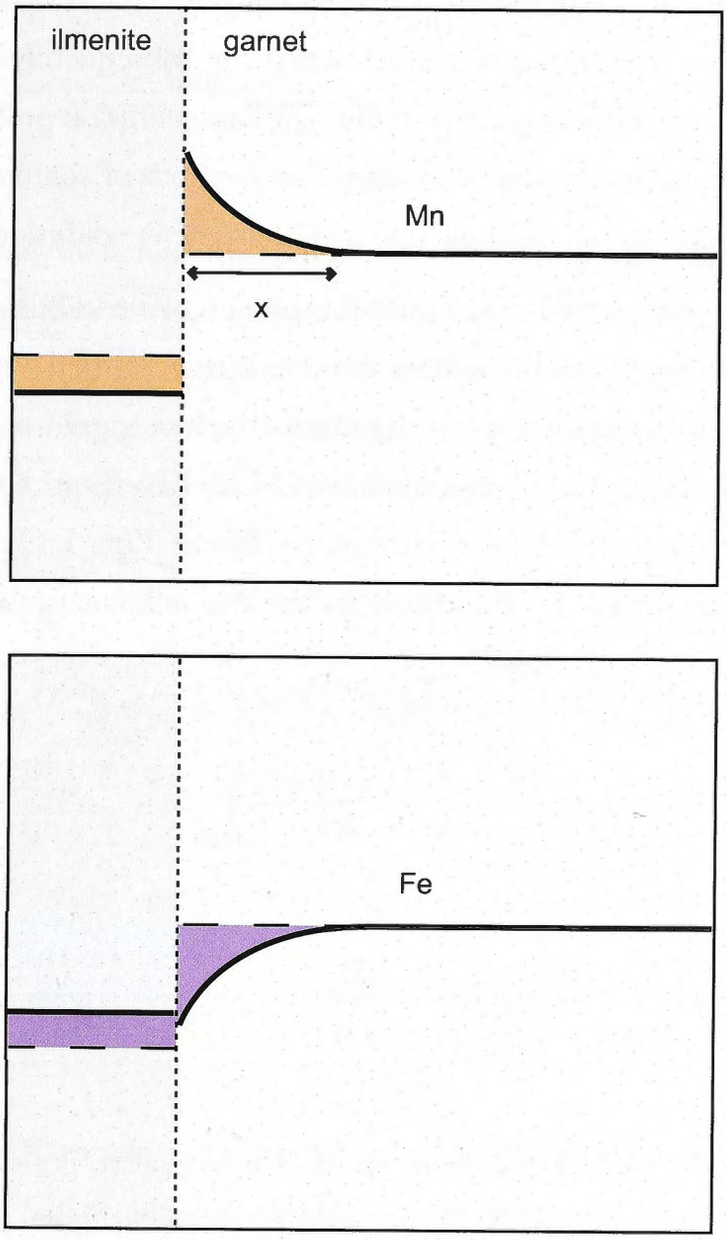

Figure 1.1: Schematic diagram of diffusion profiles of length x. The dotted lines indicate initial concentrations of Fe and Mn in garnet and ilmenite and the solid lines are the final concentrations. The diffusion profiles are the result of a thermal event causing exchange of Mn and Fe between garnet and ilmenite with subsequent diffusion of Mn away from the interface that is preserved in garnet.

In the garnet-ilmenite system the partitioning described by the exchange reaction (Eqn. 1.8) sets up a boundary condition for the diffusion equation. Therefore the concentration at

the garnet-ilmenite boundary is dependent on the partition coefficient and mass balance. The boundary condition is difficult to model in comparison to the typical diffusion models that are based on equilibration of an elements concentration gradient within one phase. Although, it is comparable to the garnet-biotite system that has been addressed by several authors (e.g. Robl et al., 2007; Spear and Parrish, 1996). Methods for solutions in the garnet-biotite system are discussed below. The garnet-biotite system is a similar diffusion problem to the garnet-ilmenite system. These systems are characterised by partitioning of elements initiating concentration gradients that are subsequently erased within the fast diffusing phase and in garnet, a slow diffusing phase, diffusion profiles are preserved. This similarity between the two systems means that methods of solution used for garnet-biotite diffusion modelling can be applied to a garnet-ilmenite diffusion model.

Spear and Parrish (1996) describe a method for solution of the diffusion equation where Fe and Mg are exchanged at the boundary between garnet and biotite. At the boundary Fick's Law (Eqn. 1.1) is used to equate the flux of Fe into garnet with the flux out of biotite. Using a finite difference approximation of Fick's Law (Eqn. 1.11) to calculate the flux and a rearranged equation for the partition coefficient (Eqn. 1.12). This provides two equations that can be solved simultaneously for the two unknowns, the concentration at the boundary for garnet and biotite:

$$D_{Gnt}\left(\frac{X_n - X_{n-1}}{\Delta x}\right)_{Gnt} = -D_{Bt}\left(\frac{X_n - X_{n-1}}{\Delta x}\right)_{Bt} \qquad \textbf{(1.11)}$$

$$K_D = \frac{[(1 - X_n)/X_n]_{Gnt}}{[(1 - X_n)/X_n]_{Bt}} \qquad \textbf{(1.12)}$$

Where D is the diffusion coefficient of Fe for the respective phases, X is the mole fraction of Fe at the points n and n-1 from the boundary, Δx is the spatial step and K_D is the partition coefficient.

Robl et al. (2007) provide another example of a solution for this type of problem, also related to Fe and Mg exchange in the garnet-biotite system. In this study the radial diffusion equation is solved implicitly at the boundary node, which gives the change in concentration at the boundary for a particular time step:

$$\frac{\partial C(r,t)}{\partial t} = \frac{1}{r^2}\frac{\partial}{\partial r}\left(r^2 D(r,t)\frac{\partial C(r,t)}{\partial r}\right) \tag{1.13}$$

Where C is the concentration r is the radius, t is time and D is the diffusion coefficient. Then the surface concentration for the garnet can be determined by rearranging Equation 1.9:

$$X_{Mn}^{GntSurface} = \frac{K_D X_{Mn}^{ilm}}{1 - X_{Mn}^{ilm} + K_D X_{Mn}^{ilm}} \tag{1.14}$$

Where X is the mole fraction of the component in the phase indicated. If the biotite is a finite volume mass balance needs to be taken into account when modelling this system. The model developed by Robl et al. (2007) calculates the change in Mg concentration at the interface assuming that the boundary node is effectively garnet surrounded by the entire volume of biotite. The solution for the rate of change of the concentration is given by:

$$c\frac{\partial X_{n-1}^{Gnt}}{\partial t} = r_{n-3/2}^{Gnt} D_{n-3/2}^{Gnt}\left(X_{n-2}^{Gnt} - X_{n-1}^{Gnt}\right) + \left(c - \frac{1}{2}\right) X_{n-1}^{Gnt}\left(1 - X_{n-1}^{Gnt}\right)\frac{\partial \log K_D}{\partial t} \tag{1.15}$$

Where:

$$c = \frac{1}{2} + \frac{M^{Gnt}\rho^{Bt}V^{Bt}}{M^{Bt}\rho^{Gnt}4\pi R^2 \partial r}\frac{K_D}{\left(X_{n-1}^{Gnt} + K_D\left(1 - X_{n-1}^{Gnt}\right)\right)^2} \tag{1.16}$$

Where c is a calculation of the capacity of the system to exchange Mg and Fe, which is calculated from the molar mass (M) and density (ρ) of the phases, R is the radius of the garnet. This equation provides the means for calculating the change in the boundary concentration, so the garnet concentration profiles can then be modelled by solving the diffusion equation. For garnet and ilmenite pairs, ilmenite inclusions are often orders of magnitude smaller than the garnet. Therefore, the concentration of Mn is a function of the flux of Fe and Mn between garnet and ilmenite and is controlled by the size of the reservoir.

1.4 Thesis Structure and Content

This thesis is focused on the technique of diffusion modelling to constrain the duration of thermal events that produce metamorphic terranes. To address the problems in diffusion models of defining initial conditions and the spread in diffusion parameters, the garnet-ilmenite system was investigated. This study was carried out using experimental techniques and microstructural analysis. A comparative study was undertaken using numerical modelling of argon diffusion in white mica. Written below are the summaries of each chapter contained in this thesis.

1.4.1 Chapter 2: Experimental Determination of Ilmenite Diffusivity

Well-constrained diffusion parameters are necessary to reduce the uncertainty in diffusion models. To aid this a series of experiments was carried out to determine ilmenite diffusion parameters and investigate the influence of temperature, oxygen fugacity and crystallographic orientation on diffusion in ilmenite. The experiments were run with a natural ilmenite crystal immersed in a synthetic ilmenite ($FeTiO_3$) powder, as the diffusant source, doped with trace amounts of Mg, Co, Ni, Zr, Hf, V, Nb, Ta, Al, Cr, Ga and Y. Since, the natural ilmenite crystal contained Mn it was also possible to study diffusion of Mn from the ilmenite crystal. Experiments were performed in a 1 atm furnace over a range of temperatures 800 to 1100 °C, with oxygen fugacity controlled by a flow of a CO-CO_2 gas mixture. The diffusivity for Mn, Co, Ni, Ga, Mg, Y, Al, Cr and Hf was determined to be on the order of 10^{-13} to 10^{-16} m^2s^{-1}, confirming a fast rate of diffusion in ilmenite.

1.4.2 Chapter 3: An Experimental Investigation of Partitioning and Diffusion in the Garnet-Ilmenite System

To further investigate the rates of diffusion in the garnet-ilmenite system experiments were run with a garnet cube coated with an ilmenite thin film as the diffusant source. These experiments were performed in a 1 atm furnace with oxygen fugacity controlled by a flow of a CO-CO_2 gas mixture at temperatures of 800 °C and 850 °C. Analysis was conducted using Secondary Ion Mass Spectrometry (SIMS) depth profiling. These experiments did not produce measurable diffusion profiles although the result allowed limits of the diffusion rate to be constrained.

1.4.3 Chapter 4: Element Concentration Profiles Surrounding Ilmenite Inclusions in Garnet from the Barrovian Metamorphic Sequence in Scotland

To investigate the occurrence of diffusion profiles preserved surrounding ilmenite inclusions in natural garnets analysis of concentration profiles across the interface between ilmenite inclusions and garnet in samples from the Barrovian metamorphic sequence in Scotland was carried out. The samples ranged from staurolite, 590 °C, to sillimanite grade, 640 to 670 °C and were analysed using electron probe microanalysis (EPMA) and nanoscale secondary ion mass spectrometry (NanoSIMS). Changes in the concentration gradients surrounding ilmenite inclusions were observed in EPMA profiles from sillimanite grade samples. However, analytical artefacts and discrepancies between the features meant that further proof of the phenomenon would be required.

1.4.4 Chapter 5: Element Concentration Profiles Surrounding Ilmenite Inclusions in Garnet from the Ivrea-Verbano Zone in Italy

To further investigate diffusion profiles preserved surrounding ilmenite inclusions in natural garnets samples from the Ivrea-Verbano Zone in the Southern Alps, Italy were analysed. The Ivrea-Verbano Zone samples attained higher peak temperatures (650 °C to 1000 °C) than those studied from the Barrovian metamorphic sequence in Scotland. This higher temperature means that growth zoning in garnet is eliminated. Mn diffusion profiles in garnet are measured in this study, however, also observed are the effects of retrograde reactions on the partitioning of elements between garnet and ilmenite. Despite these inconsistencies the duration of the thermal event was broadly constrained.

1.4.5 Chapter 6: $^{40}Ar/^{39}Ar$ Geochronology of the Buchan Sequence on the Northeast Coast of Scotland

This research aimed to make comparisons of durations obtained via different diffusion modelling techniques. To achieve this argon geochronology was carried out on a suite of samples from the northeast coast of Scotland using a furnace step-heating technique to obtain $^{40}Ar/^{39}Ar$ apparent age spectra from white mica. The samples were collected from the biotite to the sillimanite zone of the Buchan metamorphic sequence and the sillimanite and kyanite zone of the Barrovian metamorphic sequence. The results of this study are discussed in relation to the timing of deposition of the Dalradian sediments and the subsequent metamorphism that produced the Buchan and Barrovian metamorphic sequences.

1.4.6 Chapter 7: The Duration of Buchan Metamorphism from Diffusion Modelling of Argon in White Mica

Forward modelling of argon diffusion in white mica was carried out and the results were compared to several $^{40}Ar/^{39}Ar$ apparent age spectra obtained from cordierite zone samples from the Buchan metamorphic sequence, Scotland. Modelling was performed using the MacArgon computer program (Lister and Baldwin, 1996). This modelling provided constraint on the duration of metamorphism and the duration is compared to previous determinations of the duration in the synchronous Barrovian metamorphic series from garnet and Sr in apatite diffusion modelling (Ague and Baxter, 2007; Viete et al., 2011b). The implications these results have on the tectonometamorphic history of the terrane are also discussed.

1.4.7 Chapter 8: Diffusion Modelling to Constrain the Duration of Metamorphism

This chapter summarises the findings and conclusions of this thesis. Outlined are the considerations necessary before the garnet-ilmenite system can be utilised to determine durations of thermal events as well as the implications of the results of this research and other recent studies have for the duration of metamorphism.

CHAPTER 2

Experimental Determination of Ilmenite Diffusivity

Preface

The experiments described in this chapter were undertaken using a method that was adapted from Spandler et al. (2007). Experiments were run under the supervision of Professor Hugh O'Neill and with the technical assistance of Dean Scott and David Clarke. Analysis of the diffusion profiles was carried out on the electron probe microanalyser and laser ablation ICP-MS with the help of Dr Robert Rapp and Dr Charlotte Allen, respectively. I would also like to acknowledge the Centre for Advanced Microscopy an Australian Microscopy and Microanalysis Research Facility (AMMRF) at the Research School of Biology, ANU. At this facility the Zeiss Ultraplus FESEM with EBSD capabilities was used to determine the crystallographic orientation of ilmenite crystals used in experiments. This analysis was carried out with the assistance of Dr Angela Halfpenny, Dr Hua Chen and Dr Frank Brink.

2.0 Synopsis

The set of experiments performed in this study allowed diffusion rates in natural ilmenite to be quantified with respect to temperature, oxygen fugacity and crystallographic orientation. The diffusivities (D) determined confirm that diffusion in ilmenite is fast, with D in the range of 10^{-13} to 10^{-16} m^2s^{-1} at 1000 °C for the elements measured. The order in which the diffusivity of the elements decreases is Mn > Co > Ni > Ga ≥ Mg > Y > Al > Cr > Hf, that is to say that Mn diffuses the fastest and Hf the slowest. The results also show that the crystallographic orientation has no effect on the diffusion rate.

The experiments were performed in a one-atmosphere furnace with oxygen fugacity controlled by a flow of a CO-CO_2 gas mixture with ilmenite crystals immersed in a synthetic powder. Experiments were performed at temperatures ranging from 800 °C to 1000 °C and a percentage of CO_2 in the gas mixture ranging from 50% to 90%. The powder was doped with trace amounts of Mg, Co, Ni, Zr, Hf, V, Nb, Ta, Al, Cr, Ga and Y. Since, the natural ilmenite crystal contained Mn it was also possible to study diffusion of Mn from the ilmenite crystal. The experiments were analysed by electron probe microanalysis and scanning laser ablation inductively coupled plasma mass spectrometry. The diffusion coefficients were obtained by curve fitting the resulting diffusion profiles to a solution of the diffusion equation for a semi-infinite slab using an in-built general curve fit function in the Kaleidagraph program.

The relatively fast diffusivity determined in this study illustrates that if ilmenite is in contact with other phases with which it can readily exchange elements it will not provide information on peak metamorphic conditions.

2.1 Introduction

Ilmenite ($FeTiO_3$) is a common accessory phase in many metamorphic and igneous rocks. It forms a solid solution with pyrophanite ($MnTiO_3$) and geikielite ($MgTiO_3$) with a finite component of Fe_2O_3. Its crystal structure is characterised by alternate layers of Fe and Ti cations as is shown in Figure 2.1.

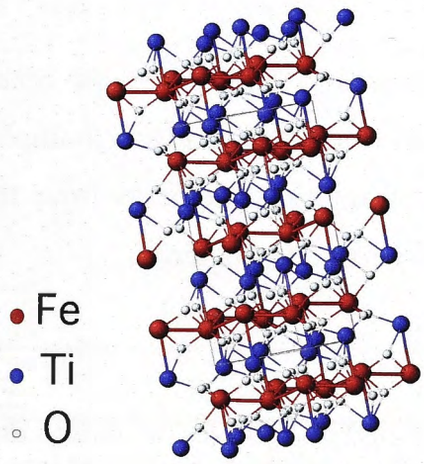

Figure 2.1: The crystal structure of pure ilmenite ($FeTiO_3$) is dominated by alternate layering of Fe and Ti cations. The metal atoms occupy two-thirds of the octahedral sites (Wilson et al., 2005). Wechsler and Prewitt (1984) determined the crystal structural properties used to produce this figure (Modified from Barthelmy, 2010).

Ilmenite is used as a geochemical tool to constrain pressure and temperature in conjunction with other minerals, for example in geothermometers including garnet-ilmenite, olivine-ilmenite and pyroxene-ilmenite. Docka et al. (1986) compared temperatures calculated with the olivine-ilmenite, orthopyroxene-ilmenite and olivine-orthopyroxene geothermometers. This study concluded that knowing diffusion rates of ilmenite would aid in reducing the discrepancies between the resulting temperatures obtained from these systems.

Diffusion acts to redistribute elements within a mineral during thermal events. In fast diffusing phases geochemical information on the peak conditions is lost unless it is an inclusion within a slow diffusing phase, thus making it a closed system. The diffusion rate of ilmenite has been inferred to be relatively fast from observations of resetting of Fe and Mn between garnet and ilmenite in natural samples (e.g. Pownceby et al., 1987), although, experiments to quantify ilmenite diffusivity have not been conducted previously. This set of experiments was designed to quantify the diffusion rates of selected elements within ilmenite and investigate the influence of temperature and oxygen fugacity.

The crystallographic orientation of the experiments was also determined to investigate if there were systematic differences in diffusion rates measured parallel and perpendicular to the c-axis. Factors not explored in this study that would have an effect on the diffusion rate include the major-element composition of the ilmenite and pressure.

2.2 Experimental Technique

The method used in these experiments was based on Spandler et al. (2007). This method involves the diffusant source being doped with multiple trace elements, enabling measurement of diffusion rates of multiple elements from the one experiment. Thus reducing the overall amount of experiments required.

2.2.1 Sample Preparation

Diffusion experiments were performed on samples of natural ilmenite from the Vishnevye Mountains, Urals, Russia. The ilmenite crystal had approximate dimensions of 25 by 15 mm. It was analysed prior to experiments using the Cameca SX100 electron probe microanalysis (EPMA) to determine an average starting composition, results are shown in Table 2.1. The chemical composition of the ilmenite crystal was determined from normalisation of the EPMA data and the amount of Fe^{3+} in the ilmenite was calculated based on stoichiometry. From this, a formula for the ilmenite was obtained:

$$\mathbf{Fe^{2+}_{0.84}Fe^{3+}_{0.16}Mn_{0.07}Mg_{0.01}Ti_{0.92}O_3}$$

The ilmenite crystal was set in epoxy and sectioned with a 10-inch blade saw. This process largely constrained the amount of experiments that could be run and the crystallographic orientation. Samples used in the experiments had approximate dimensions of 3 by 3 mm. The individual crystals were then polished with 1 μm diamond paste and removed from the epoxy after heating in a 100 °C oven to soften it.

2.2.2 Synthetic Powder

The diffusant source was a synthetic ilmenite powder doped with thirteen trace elements. The trace elements used in the synthesis of the powder were Mg, Co, Ni, Zr, Hf, V, Nb, Ta, Al, Cr, Ga and Y. The trace elements were added in concentrations between 0.1 and 1.0 wt%, in the proportions as shown in Table 2.2.

Oxide		Cations to 3 oxygens p.f.u	
SiO_2	0.03	Si	0.00
TiO_2	48.73	Ti	0.92
Al_2O_3	0.03	Al	0.00
Fe_2O_3	8.26	Fe^{3+}	0.16
FeO	37.70	Fe^{2+}	0.84
MnO	3.38	Mn	0.07
MgO	0.27	Mg	0.01
CaO	0.00	Ca	0.00
Na_2O	0.01	Na	0.00
Total	**98.42**		**2.00**

Table 2.1: EPMA normalised analysis of major oxides in a natural ilmenite crystal from the Vishnevye Mountains in Russia. The amount of Fe_2O_3 and the Fe^{3+} value was calculated based on stoichiometry.

2.2.3 Diffusion Experiments

A platinum capsule was welded closed on one end, then packed with the synthetic powder and an ilmenite crystal with one highly polished surface was fully immersed in the powder. The powder was compressed to ensure contact between the powder and the polished surface of the crystal. The capsule was hung by a platinum wire and placed in a one atmosphere furnace with oxygen fugacity controlled by flow of a CO-CO_2 gas mixture.

The experiments were designed to investigate the dependence of diffusivity in ilmenite on temperature and oxygen fugacity. A summary of experimental conditions is shown in Table 2.3. The temperature range of experiments was between 800 and 1100 °C. The experiments intended to investigate the dependence of diffusivity on oxygen fugacity were centered on the Wüstite-Magnetite (WM) buffer, with two experiments run at a higher oxygen fugacity and two lower as well as one at WM buffer oxygen fugacity at 1000 °C, this is illustrated in Figure 2.2. All values for oxygen fugacity in this chapter are represented as CO_2% in the CO-CO_2 gas mixture; the equivalent oxygen fugacity is shown in Table 2.3.

Compound	Weight (g)	Weight %
Fe_2O_3	2.4745	47.933
MgO	0.0509	0.986
Co_3O_4	0.0532	1.031
NiO	0.0516	1.000
TiO_2	2.4853	48.142
ZrO_2	0.0053	0.130
HfO_2	0.0062	0.120
V_2O_5	0.0061	0.118
Nb_2O_5	0.0054	0.105
Ta_2O_5	0.0049	0.095
Al_2O_3	0.0045	0.087
Cr_2O_3	0.0046	0.089
Ga_2O_3	0.0048	0.093
Y_2O_3	0.0051	0.099
Total	**5.1624**	**100**

Table 2.2: Proportions of powdered compounds that were combined to produce the synthetic ilmenite powder prepared as a diffusant source for experiments.

Experiments were optically examined after annealing to ensure that there were no surface alterations that would affect diffusion rates. Experiments that showed evidence of surface reactions were not used for the determination of diffusion parameters.

2.3 Analytical Methods

Analysis of the experiments was carried out using EPMA and laser ablation inductively coupled plasma mass spectrometry (LA-ICP-MS) for trace elements. The crystallographic orientations were determined using electron backscattered diffraction (EBSD).

Variable	Temperature (°C)	CO_2%	-log fO_2	Time (hrs)	Crystallographic Orientation to c-axis	Run
T	1100	75	11.5	82	-	1_09
	1000	90	12.2	4	Perpendicular	4_09
	1000	90	12.2	24	Perpendicular	5_09
	900	90	14.2	20	Perpendicular	6_09
	900	90	14.2	120	Parallel	9_09
	800	90	16.5	100	Parallel	10_09
fO_2	1000	80	12.9	4	40°	7_09
	1000	75	13.2	4	Parallel	2_09
	1000	60	13.8	4	Parallel	8_09
	1000	50	14.1	4	Parallel	3_09

Table 2.3: A summary of the range of temperature, oxygen fugacity, duration and crystallographic orientation of experiments performed in this study. The values for oxygen fugacity were calculated using a spreadsheet designed by R.Farla (Pers. Comm. 2010).

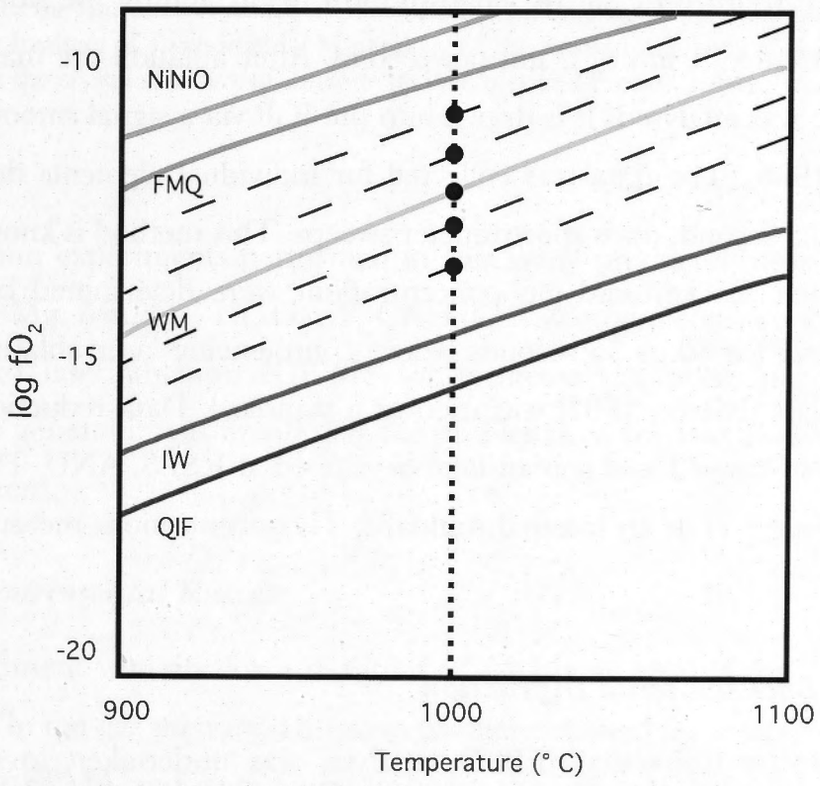

Figure 2.2: Conditions of experiments run to determine the dependence of diffusion rate on oxygen fugacity, points represent each experiment. The lines represent the common buffer assemblages nickel-nickel oxide (NiNiO), fayalite-magnetite-quartz (FMQ), wüstite-magnetite (WM), iron-wüstite (IW) and quartz-iron-fayalite (QIF) at 1 bar pressure (Buffer assemblages from Frost, 1991).

2.3.1 Electron Probe Microanalysis

Analysis of major and minor elements was conducted using the Cameca SX100 EPMA with wavelength-dispersive spectrometers (WDS) at the Research School of Earth Sciences, ANU. The TiO_2, Roberts Victor Mine (RVM) garnet and chromite standards were used for calibration. Average composition of the starting ilmenite was determined by point analyses of an unannealed crystal with a 15 keV accelerating voltage and a 20 nA beam current. Transects to analyse experiments after completion were carried out at 15 keV accelerating voltage and a 100 nA beam current with a dwell time of approximately 290 seconds. These conditions were chosen to give higher count rates on trace elements allowing a comparison with LA-ICP-MS profiles.

2.3.2 Laser Ablation ICP-MS

The scanning laser ablation ICP-MS was used to measure concentration profiles of trace elements. Analyses were carried out using an Agilent 7500 series quadrapole (ICP-MS) with a Resonetics 193 nm excimer laser and a custom-built sample chamber, filled with helium-argon gas (Eggins et al., 1998). The pulse rate of the laser was 5 Hz. The laser passed through a 6 μm wide slit of length 60 μm before hitting the sample. The scan speed was set at either 1 μm or 2 μm per second. After ablation the material removed from the sample was analysed. It is drawn into the ICP via a signal smoothing manifold (Eggins et al., 1998). The data was collected for individual elements during periodic, approximately 0.5 second, mass spectrometer sweeps. This method is known as the peak hopping approach. Background gas concentrations were determined by running the mass spectrometer for 30 to 35 seconds before commencing laser ablation. The NIST 610 synthetic glass (Pearce, 1997) was used as a standard. Data reduction was carried out using a macro-based Excel spreadsheet developed at RSES, ANU. The results were quantified by using ^{47}Ti as an internal standard; Ti concentrations measured by EPMA were used.

2.3.3 Electron Backscattered Diffraction

Electron backscatter diffraction (EBSD) analysis was undertaken to determine the crystallographic orientation of the experiments. Crystallographic orientation is acquired by analysis of the Kikuchi patterns, which are formed by electrons backscattered from

the sample onto a phosphor screen. The patterns were collected with an Oxford HKL attachment on a Zeiss Ultraplus field emission scanning electron microscope (FESEM) operating at 25 keV. The patterns are then matched to a crystallographic orientation using information known about the structure of the crystal that is being analysed, in this case ilmenite. This information is entered into the EBSD software prior to analysis. The data that was used to match the Kikuchi patterns for ilmenite is listed in Table 2.4. Prior to analysis samples were polished using colloidal silica and lightly coated with carbon.

Parameter	Value
Space Group	R(-)3
Unit Cell Parameters	a=5.0820, c=14.0260
Location of atoms	Fe: x=0, y=0, z=0.3580
	Ti: x=0, y=0, z=0.250
	O: x=0.305, y=0.015, z=0.250
Occupancy	Fe:1, Ti:1, O:1
Minimum Spacing	0.5 Å

Table 2.4: Data for the Ilmenite crystal file used in EBSD. This data was obtained from the XRAYPOL data files from the Institute of Experimental Mineralogy of the Russian Academy of Sciences and an extensive study on the crystal structure of ilmenite by Wechsler and Prewitt (1984).

2.4 Results

Ilmenite diffusion experiments performed in this study produced measurable diffusion profiles for Al, Mg, Mn, Co, Ni, Ga, Y, Cr and Hf. Comparisons were made between the EPMA and laser ablation ICP-MS for elements that were measured on both instruments. In general it was found that the profiles from the two analytical techniques were in agreement.

2.4.1 First Experimental Result

The first experiment was run for a duration of 82 hrs at 1100 °C in a 1 atm furnace with 75% CO_2 in the gas mixture. Diffusion profiles obtained from this experiment were measured using EPMA and were found to be on the order of 1000 μm (Fig. 2.3). This result attests to extremely fast diffusion. However, lamellae were observed in the crystal in backscattered electron images (Fig. 2.4). At the temperature and oxygen fugacity

conditions for this run the composition of the ilmenite crystal is outside of the single phase field of ilmenite, as indicated by phase relations in the system Fe-Ti-O (e.g. Ghiorso, 1997; McEnroe et al., 2002 and Hollister et al., 2004). The lamellae were too small to be analysed by EPMA, although, the lamellae are assumed to be due to exsolution of titanomagnetite. Careful examination of backscattered electron images of subsequent experiments showed no sign of exsolution lamellae or other defect structures. The results of this first experimental run are not included in subsequent data analysis as the lamellae may provide fast diffusion pathways to enhance the diffusion rate.

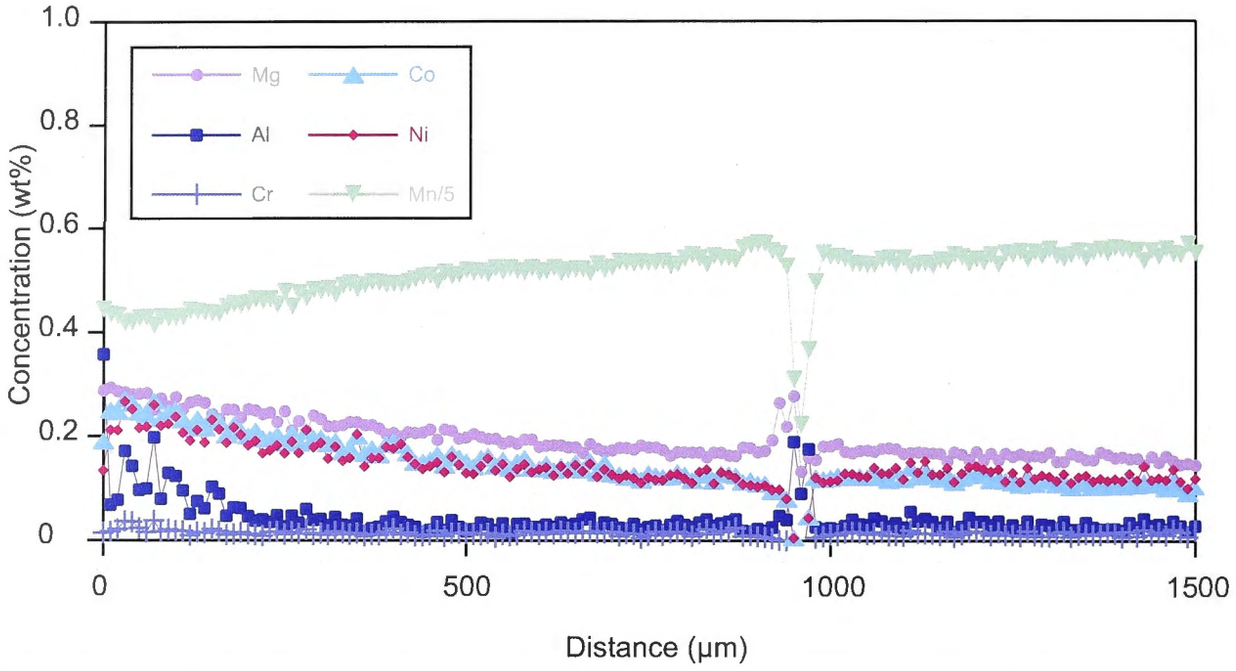

Figure 2.3: EPMA transect of major and minor element from an experiment run for 82 hrs at 1100 °C with 75% CO_2 in the gas mixture.

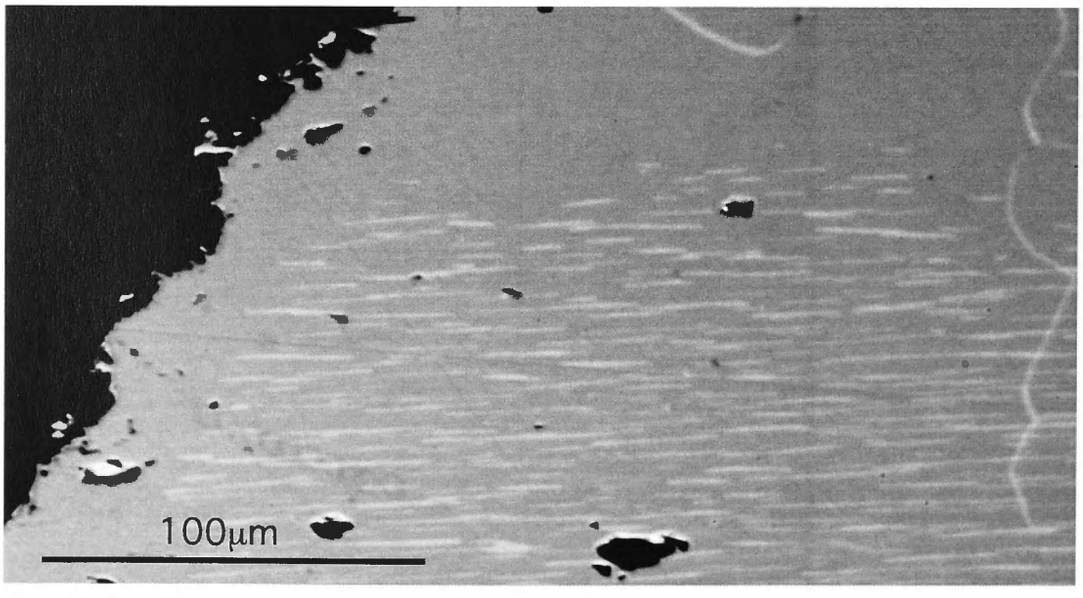

Figure 2.4: Back-scattered electron image of lamellae seen in ilmenite crystal from experiment run for 82 hrs at 1100 °C with 75% CO_2 in the gas mixture.

2.4.2 Diffusion Profiles

Diffusion profiles were measured for Al, Mg, Mn, Co, Ni, Ga, Cr, Hf and Y. Since Mn was not added to the synthetic powder and the natural ilmenite crystal contained Mn it was possible to measure diffusion of Mn out of the ilmenite crystal. Figure 2.5 shows the depletion in Mn towards the edge of the crystal. Zr, V, Nb and Ta did not produce measurable diffusion profiles as diffusion of these elements within ilmenite is too slow for the times and temperatures studied. Diffusion profiles for Co, Ni, Ga and Y were clean and showed limited scatter in the data. However, diffusion profiles of Al, Mg, Mn, Cr and Hf had short profiles or displayed significant scatter in the data and as a result diffusion parameters determined from these elements have a greater uncertainty. Diffusion profiles produced in experimental run 4_09 are displayed in Figure 2.6.

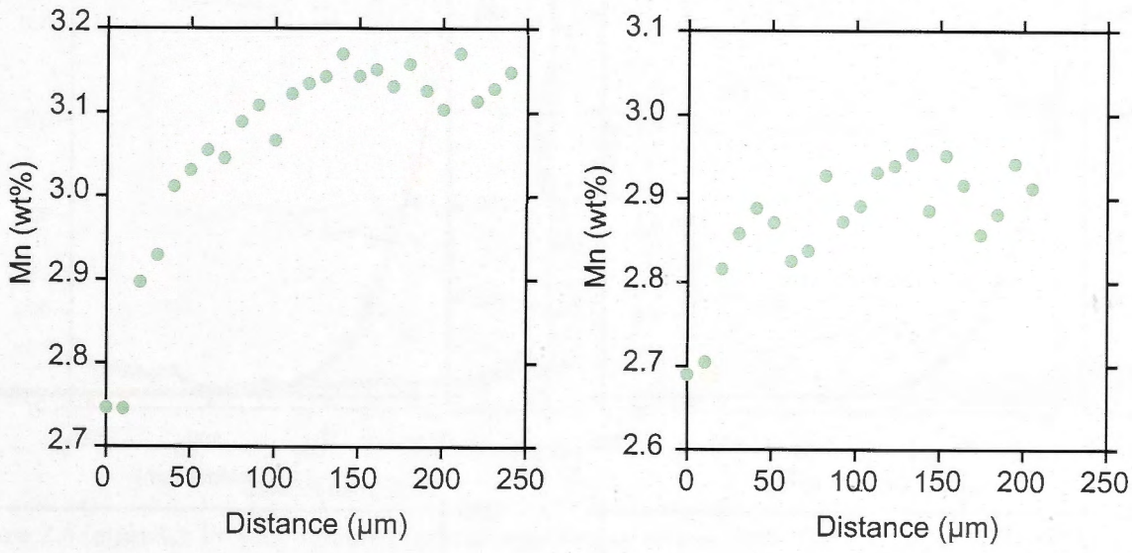

Figure 2.5: Mn diffusion profiles from experiments run at 1000 °C for 4 hrs and 800 °C for 100 hrs, respectively. Both experiments were annealed at a 90% CO_2 gas mixture.

The effect of micro-inclusions within ilmenite must be taken into account. Micro-inclusions within the ilmenite crystals can add extra complexity to the diffusion profiles obtained. This phenomenon was most commonly seen in the Zr and Hf profiles, which tend to mimic each other as seen in Figure 2.7. If these inclusions are close to the polished surface of the ilmenite they can affect the curve fitting of diffusion profiles and in these cases the profiles could not be used to obtain diffusion parameters.

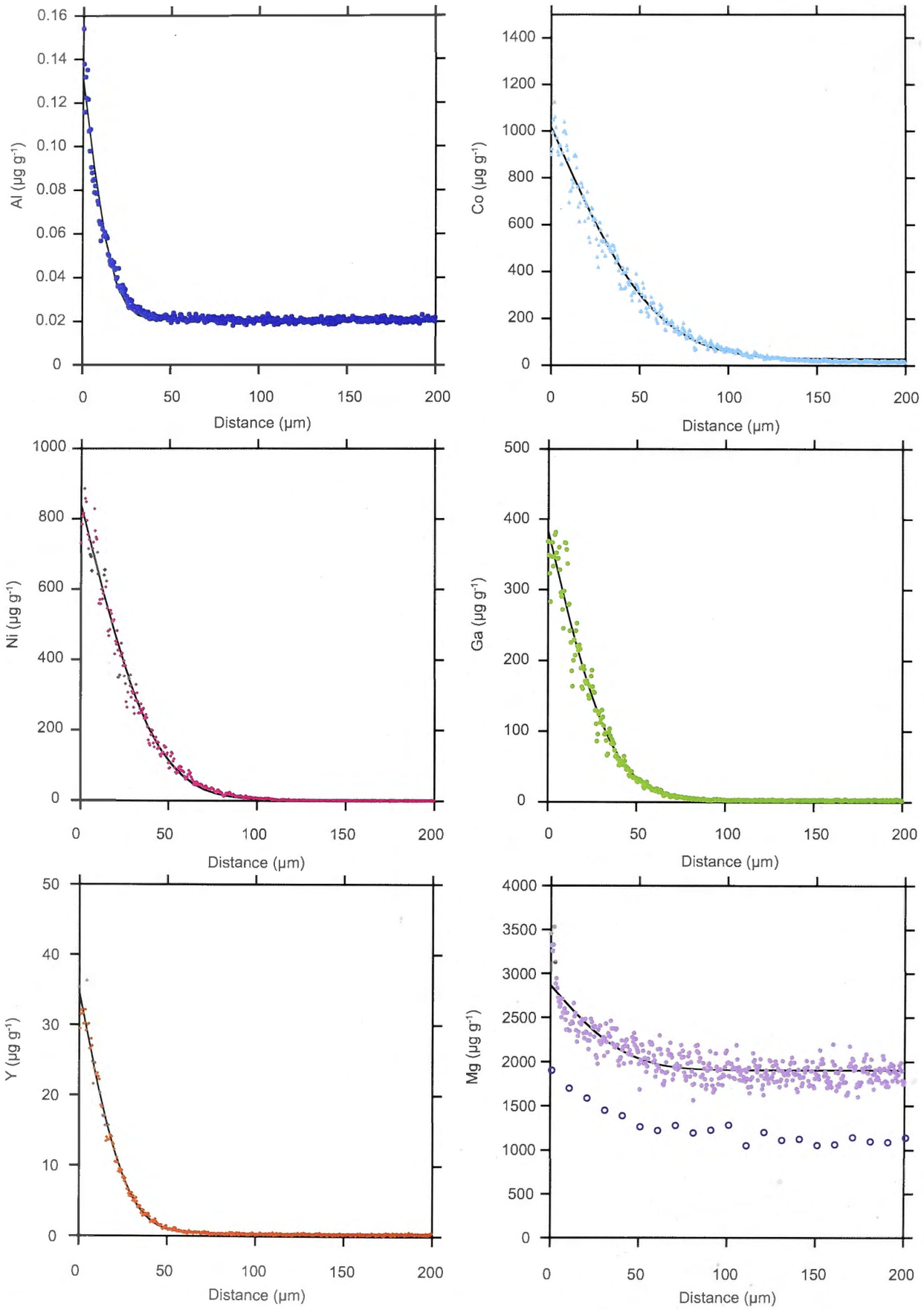

Figure 2.6: Profiles obtained from an experiment run at 1000 °C for 4 hours at 90% CO_2 in the gas mixture.

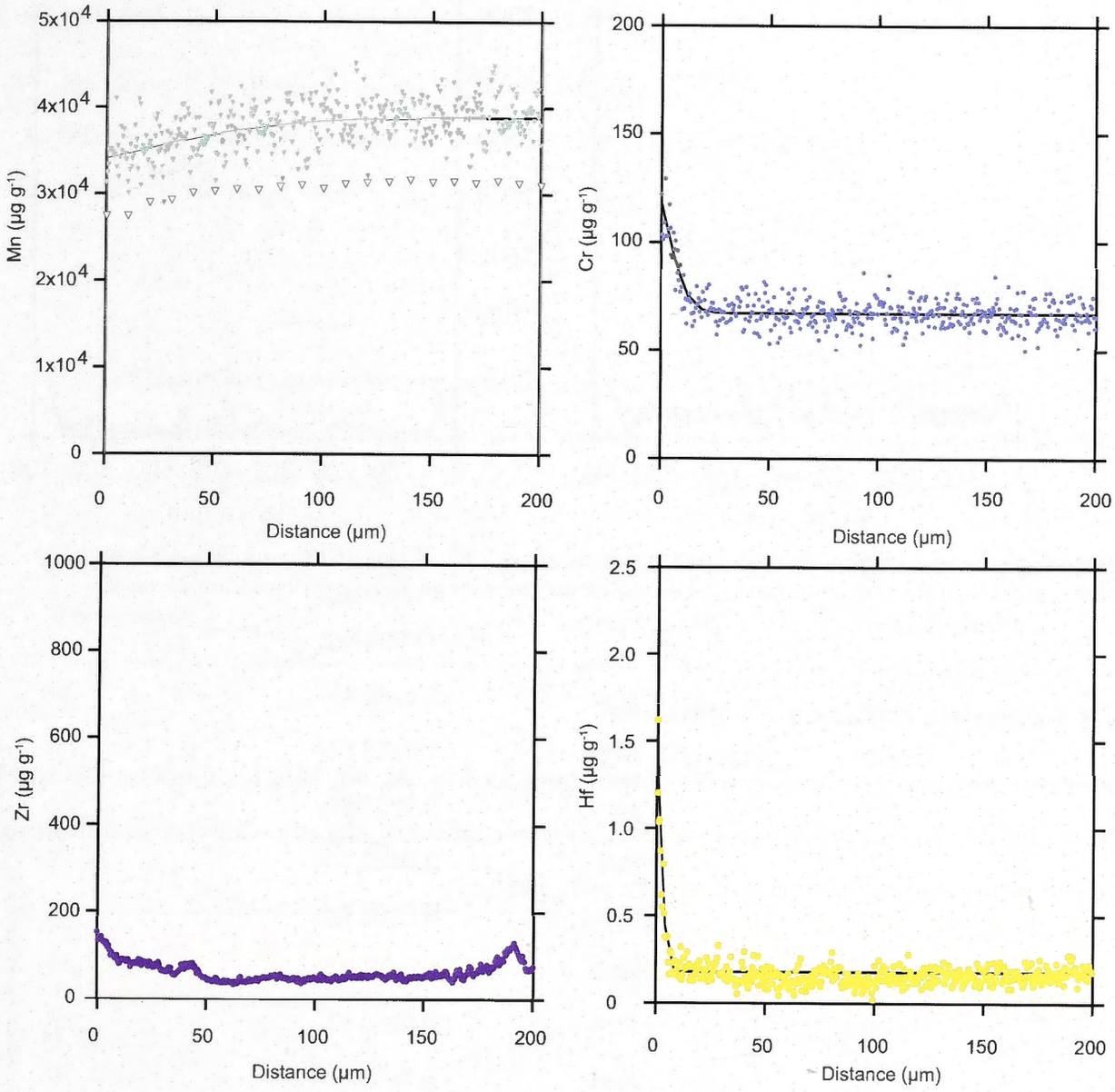

Figure 2.6 (contd.): Profiles obtained from an experiment run at 1000 °C for 4 hours at 90% CO_2 in the gas mixture. At these conditions diffusion in Hf and Cr is only just visible. EPMA transects shown in the Mn and Mg plots (open symbols) were taken with a 10 µm step size and show concentrations measured with LA- ICP-MS are higher than EPMA results. This may be related to the values used for the NIST610 glass standard.

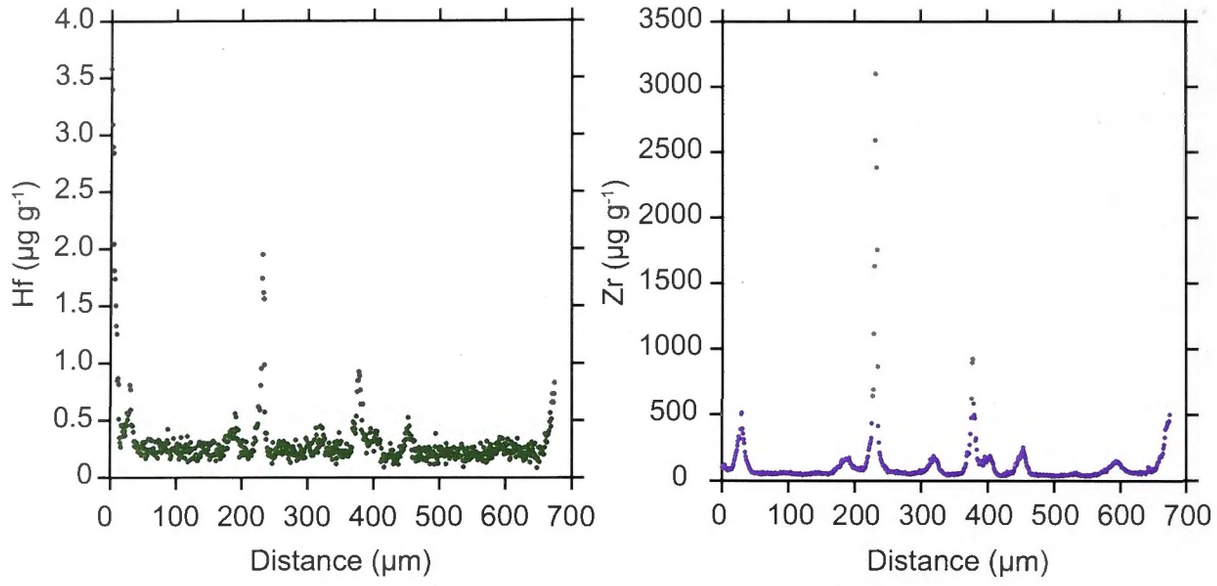

Figure 2.7: Zr and Hf profiles from an experiment run at 1000 °C for 24 hrs with 90% CO_2 in the gas mixture. Peaks in the concentrations of Hf and Zr are possible micro-inclusions within ilmenite.

2.4.3 Ilmenite Diffusion Parameters

Ilmenite diffusion coefficients were determined for Mg, Al, Ni, Mn, Cr, Co, Ga, Hf and Y by fitting the measured diffusion profiles to the solution of the one-dimensional diffusion equation for a semi-infinite slab (e.g. Crank, 1975):

$$\frac{c_i - c(x)}{c_i - c_0} = erf\left(\frac{x}{2\sqrt{Dt}}\right) \qquad (2.1)$$

Where c_i is the concentration at the interface x=0, c(x) is the concentration at distance x, c_0 the initial concentration, D is the chemical diffusion coefficient and t is the duration of the experiment. Least-squares curve fitting was carried out using the Levenberg-Marquardt algorithm implemented in Kaleidagraph software. To determine the value of M_1 where:

$$M_1 = 2\sqrt{Dt} \qquad (2.2)$$

The diffusion coefficients for ilmenite for the elements that were measured in this study at 1000 °C and 90% CO_2 in the gas mixture are shown in Table 2.5. The frequency factor (D_0) and the activation energy (E) were determined by plotting log D against inverse temperature (Fig. 2.8 and 2.9). The linear fit shown in Figure 2.8 and 2.9 represents

Equation 2.3, where D is the diffusion coefficient, D_0 is the frequency factor or D at infinite temperature, E is the activation energy, R is the universal gas constant and T is the temperature:

$$D = D_0 e^{-Q/RT} \tag{2.3}$$

The diffusion parameters determined for Co, Ni, Ga and Y are well defined, whereas, the diffusion parameters for Al, Mg, Mn, Hf and Cr are not as well constrained from profiles, although still give an indication as to the rate of diffusion for these elements.

Component	log D (m^2s^{-1}) T=1000°C	log D_0 (m^2s^{-1})	E($KJ^2K^{-1}mol^{-1}$)
Ni	-13.55±0.2	-2.37	273
Co	-13.27±0.2	-4.61	212
Ga	-13.72±0.2	-4.55	224
Y	-13.95±0.2	-5.41	208
Al	-14.59±0.5	-10.16	116
Mg	-13.74±0.5	-8.57	137
Mn	-13.06±0.5	-5.71	179
Hf	-15.57±0.5	-9.37	155
Cr	-15.03±0.5	-13.09	55

Table 2.5: Diffusion parameters determined at 1000 °C and 90% CO_2 in the gas mixture.

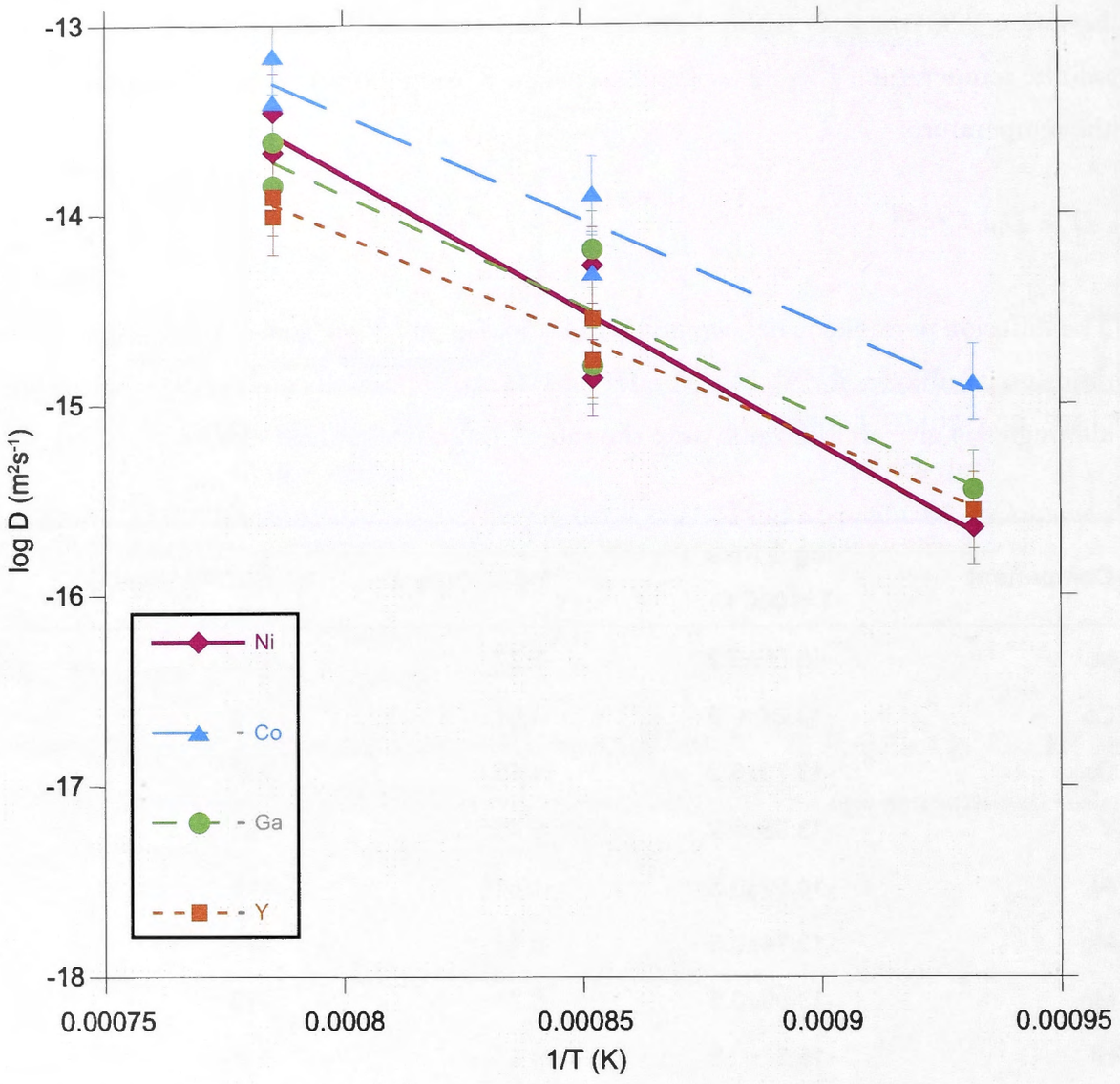

Figure 2.8: Arrhenius plot of diffusion coefficients at 1 atm for Ni, Co, Ga and Y. The linear fit plotted represents Equation 2.3 and allows for determination of activation energy and frequency factor.

The error that is calculated in the Kaleidagraph software for the value of M_1 is incredibly low. For example for the Ni diffusion profile from experimental run 4_09 (Fig. 2.6) the value of M_1 was 47.1 ± 0.2. The calculation of the error was investigated using Excel with the Solver application. The same process of fitting the data to the solution of the one-dimensional diffusion equation for a semi-infinite slab (Eqn. 2.1) was used to calculate the parameters c_i, c_0 and M_1 by minimising the sum of the squares of the difference between the measured and calculated value. This process gives the same parameters as the curve fit algorithm in Kaleidagraph. For the Ni diffusion profile from experimental run 4_09 the values were; $c_i = 0.08$, $c_0 = 0.0003$ and $M_1 = 47.1 \pm 0.2$

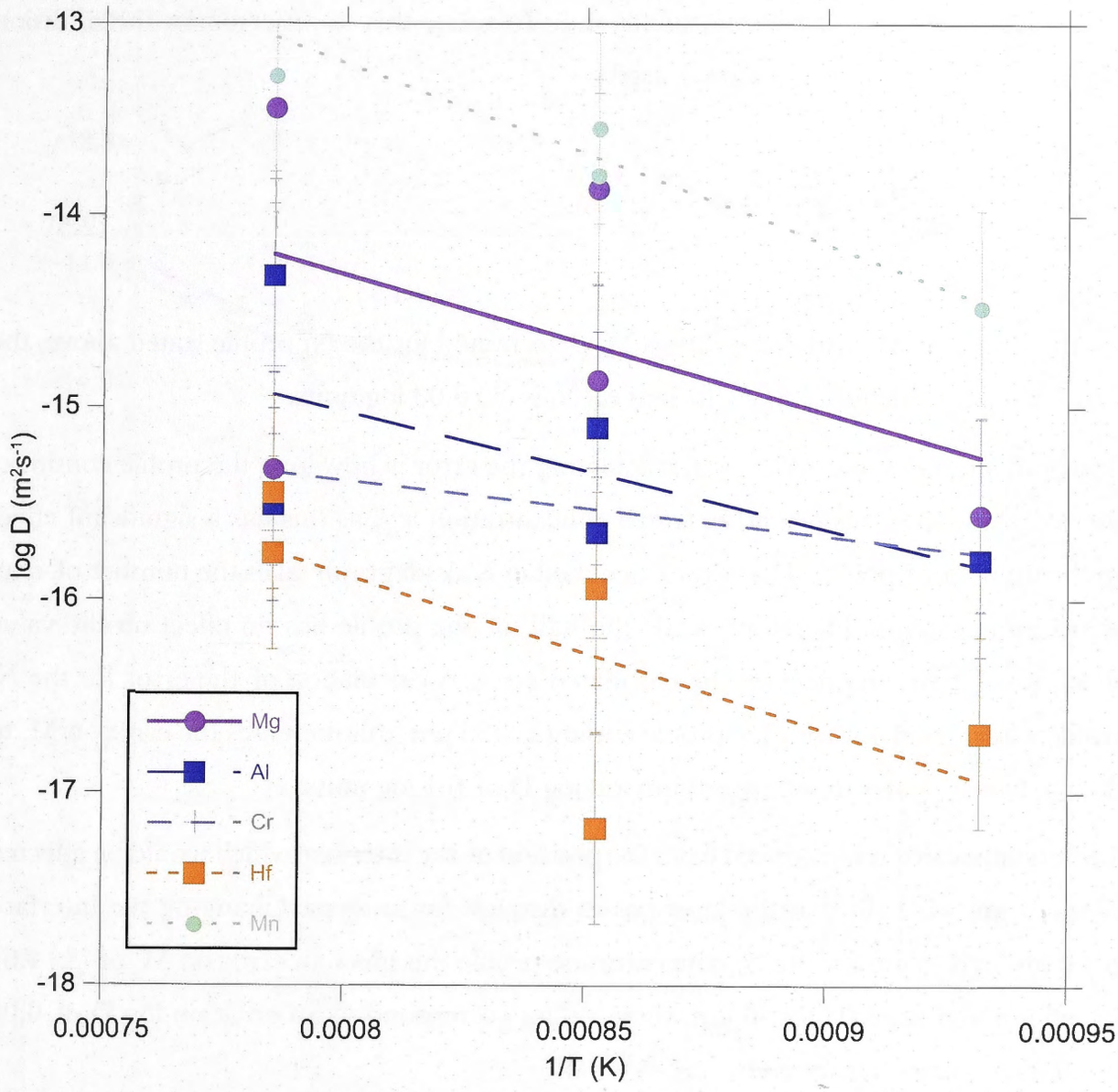

Figure 2.9: Arrhenius plot of diffusion coefficients at 1 atm for Mg, Mn, Al, Cr and Hf. The linear fit plotted represents Equation 2.3 and allows for determination of activation energy and frequency factor.

The reason for the reported error being low is due to the least squares regressions not taking into account the variance and effectively making it equal to one. The actual error on M_1 can be calculated by:

$$\sigma(M_1) = \frac{\sigma(M_1)_{kaleidagraph}}{\sqrt{\chi^2}} \tag{2.4}$$

For Ni this gives an error on M_1 of (±) 4.6. To relate this to an error on the diffusion coefficient the following equation is used:

$$\sigma(logD) = \frac{2}{2.303}\frac{\sigma(M_1)}{M_1} \qquad (2.5)$$

For the values of M_1 and the error on M_1 determined for the Ni profile stated above, the actual error for the diffusion coefficient of Ni is (±) 0.08 log units.

However, another consideration in calculating the error is how long the profile continues after reaching the background or initial concentration (c_0), as this has a significant effect on the number of points. The error calculated in Kaleidagraph takes the number of data points into account. Therefore, while the 'tail' of the profile has no effect on the value of M_1 it will have an effect on the calculated error. A calculation of the error for the Ni profile was carried out with the profile ending at 135 μm, this increases the error on M_1 to (±) 5.5, which relates to an uncertainty on log D of 0.1 log units.

Additionally, error is introduced from the position of the interface which would be effected by the 6 μm wide slit that the laser passes through for analysis. Changing the interface to +6 μm and -6 μm for the Ni concentration profile this gives an error on M_1 of (±) 4.64 for +6 μm and (±) 3.02 for -6 μm, these values correspond to an error on log D of 0.08 and 0.05 log units, respectively.

Taking into consideration the error caused by the placement of the interface and the curve fit error it is estimated that the uncertainty on the determined diffusion coefficient for the well-constrained data of Ni, Co, Ga and Y is approximately 20%, which corresponds to approximately (±) 0.2 log units. For the elements that could only provide indicative diffusion coefficients Al, Mg, Mn, Hf and Cr the uncertainty is significantly higher on the order of 50%.

The diffusion coefficients determined are plotted against the CO_2/CO in Figures 2.10 and 2.11. A parabolic line of best fit is shown for the majority of elements, this was found to best approximate the trend of the results. Figures 2.10 and 2.11 shows a minimum in diffusivity at a 75% CO_2 gas mixture, which corresponds to a $\log fO_2$ of -11.5 in value.

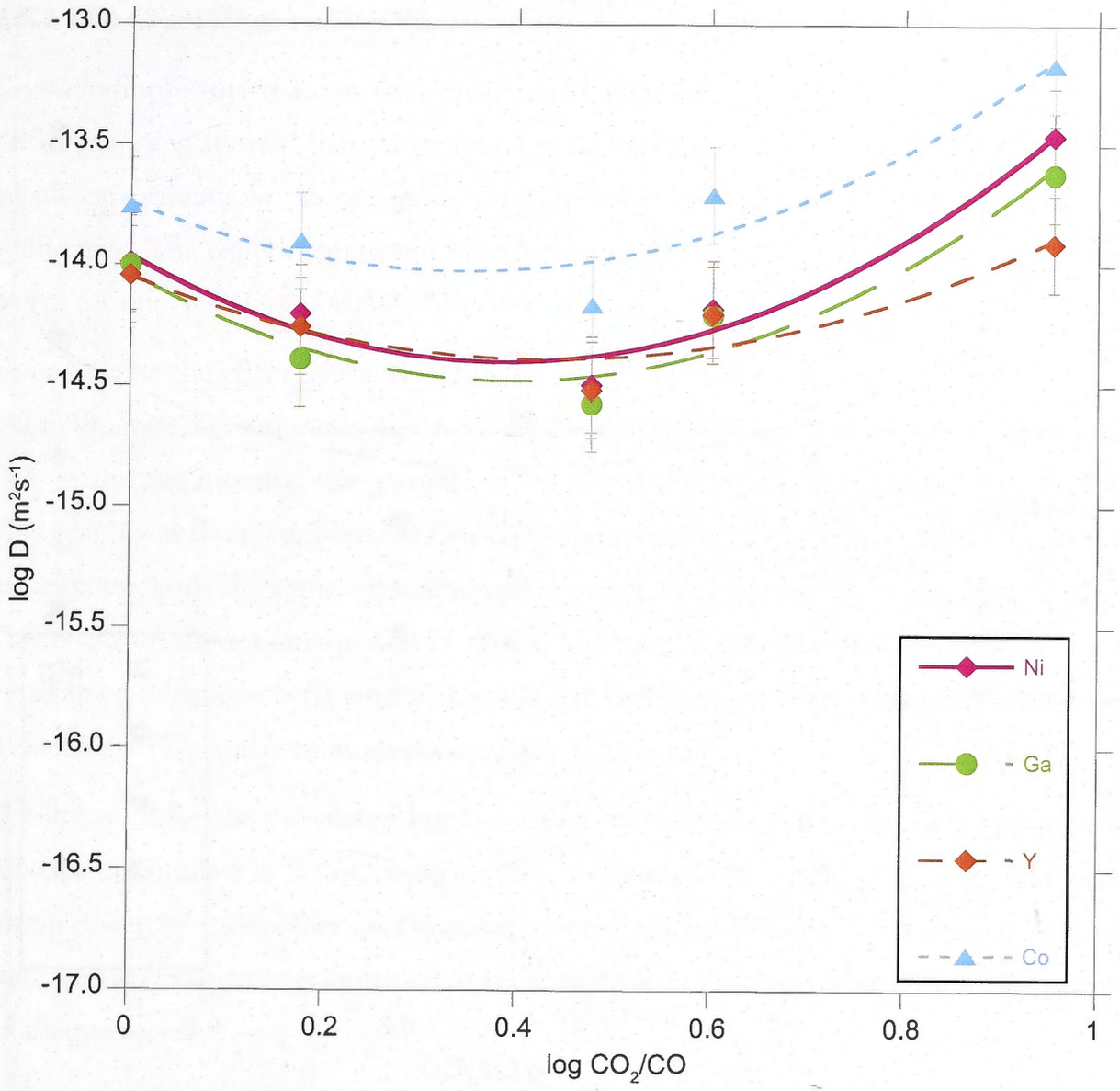

Figure 2.10: Logarithmic plot of the diffusion coefficient for Ni, Co, Ga and Y against CO_2/CO, which controls the oxygen fugacity. This plot shows a near to parabolic relationship between diffusion rates and oxygen fugacity.

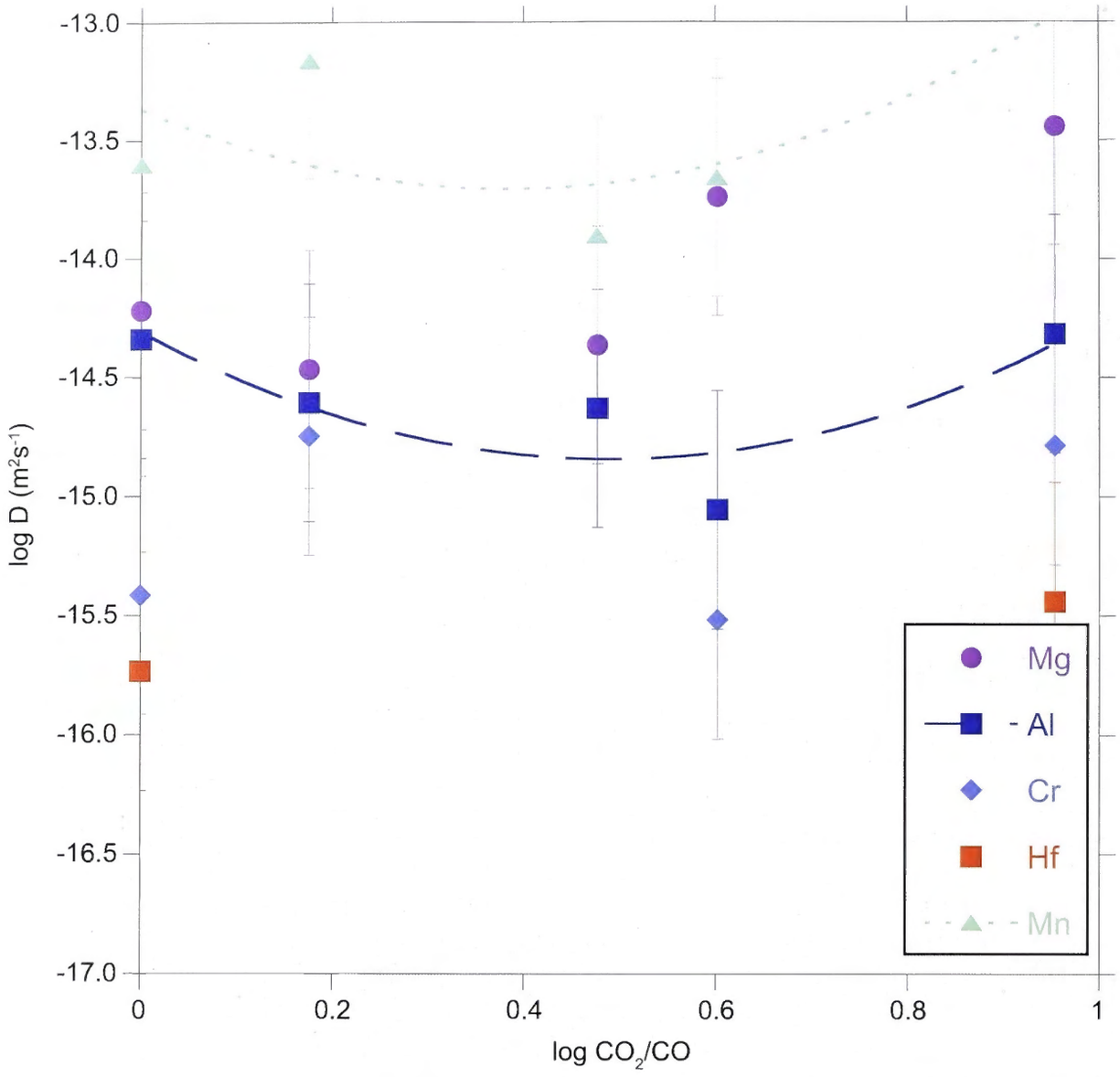

Figure 2.11: Logarithmic plot of the diffusion coefficient for Mg, Mn, Al, Cr and Hf against CO_2/CO which controls the oxygen fugacity. This plot shows a near to parabolic relationship between diffusion rates and oxygen fugacity.

2.5 Discussion

Ilmenite is a common phase in metamorphic and igneous rocks and as such is used in many geochemical tools. Therefore it is necessary to have a set of well-constrained diffusion parameters. The effect of temperature, oxygen fugacity and the crystallographic orientation on the diffusion rate of several elements within ilmenite was investigated in this study. The results are discussed below.

2.5.1 The Crystallographic Orientation

Crystallographic orientations were determined using EBSD after annealing. Results from EBSD mapping showed that the orientation of the crystals was internally homogeneous for all experiments i.e. no evidence for significant misorientation across any subgrain boundaries. The experiments are orientated either parallel or perpendicular to the c-axis except for one, which is at 40° to the c-axis.

To investigate the effect of the crystallographic orientation on diffusion rate of elements within ilmenite a comparison was made for the two experiments run at 900 °C with 90% CO_2 in the gas mixture, one parallel to the c-axis and one perpendicular (Fig. 2.12b). This graph was then compared to two experiments run at 1000 °C with 90% CO_2 in the gas mixture, with the same crystallographic orientation, parallel the c-axis (Fig. 2.12a). The result of these comparisons is shown in Figure 2.12. The linear fit for the well constrained diffusion coefficients of Co, Ga, Ni and Y indicates that diffusion in ilmenite at these experimental conditions is essentially isotropic.

The linear fit for the calculated log D for two experiments run at the same conditions but different times (Fig. 2.12a) confirms these profiles are the result of diffusion and were not produced by some other geochemical process. As the diffusion coefficients calculated from the two experiments annealed at the same conditions for different durations are in good agreement.

2.5.2 The Relation Between Diffusivity and Oxygen Fugacity

Diffusion coefficients at 1000 °C are plotted against oxygen fugacity in Figures 2.10 and 2.11. This graph shows an almost parabolic relationship with a minimum at 75% CO_2 in the gas mixture ($\log fO_2$ = -13.2, Δ Quartz-Fayalite-Magnetite = -2.1) from which diffusion rates increase towards higher and lower oxygen fugacity. This result suggests that the vacancies and interstitials associated with the conversion of Fe cations are an important control on diffusion in ilmenite.

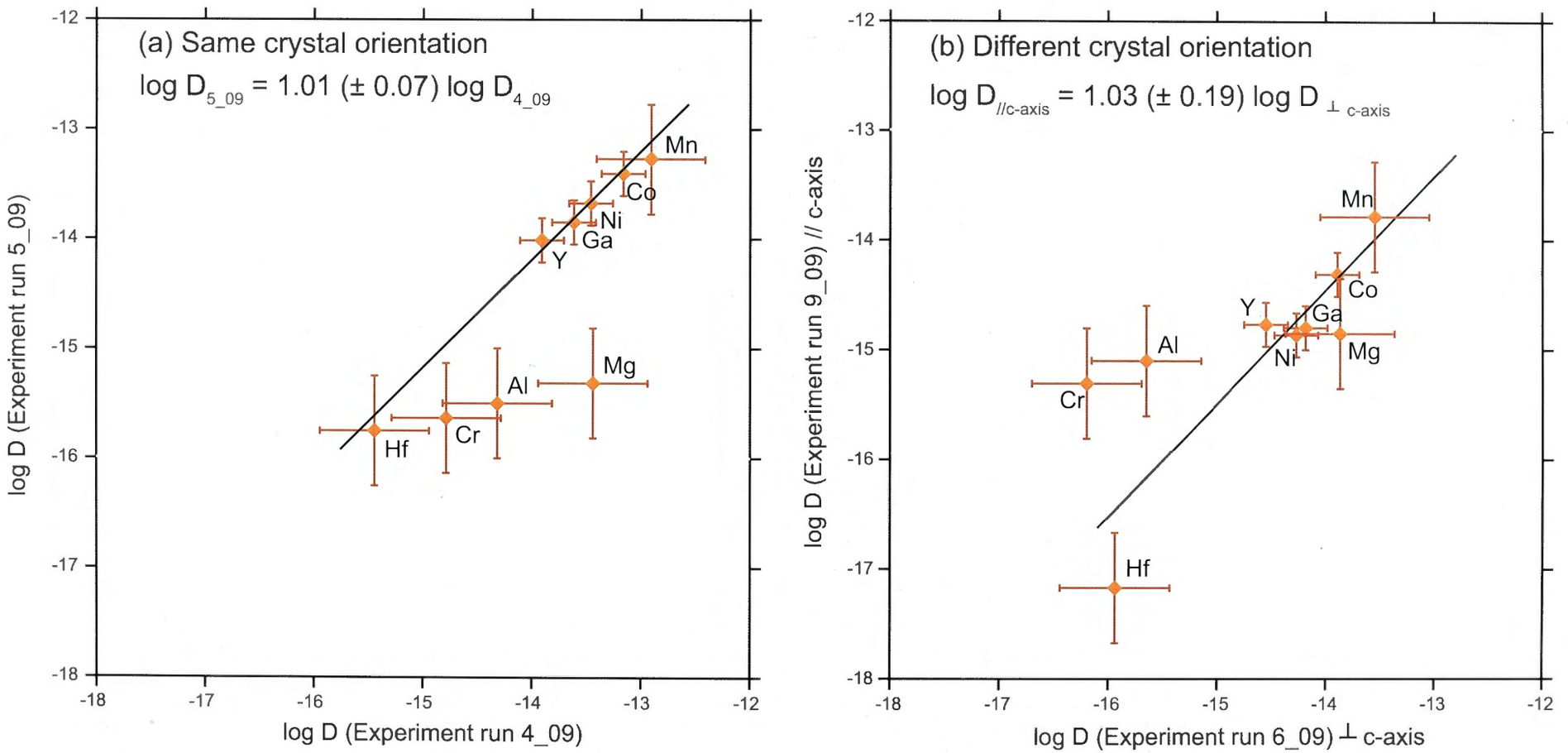

Figure 2.12: A comparison of diffusion coefficients calculated from different experimental runs with a linear fit of the well constrained elements Co, Ni, Ga and Y. (a) Log D calculated from experiment 4_09 against log D calculated from experiment 5_09 with diffusion parallel to the c-axis for both experiments. (b) Log D calculated from experiment 6_09 against 9_09, with diffusion perpendicular to the c-axis and parallel to the c-axis, respectively.

A similar relationship between diffusivity and oxygen fugacity has been observed in diffusion experiments performed on magnetite (Fe_3O_4) by Dieckmann and Schmalzreid (1977a). Their results can be seen in the bottom graph in Figure 2.13. In their study it was concluded that the minimum in the diffusion rate is due to a Frenkel disorder in the crystal lattice. That is, within magnetite, at relatively high oxygen fugacity the amount of cation vacancies increases, and at low oxygen fugacity magnetite has an excess of cations, and as a consequence interstitial cations (Dieckmann and Schmalzried, 1977b). However, the minimum in diffusivity does not occur exactly at the point corresponding to the lowest concentration of defects in the crystal lattice because the excess of cations that dominates at the lower oxygen fugacity has a stronger control on diffusion rate than the cation vacancies that dominate at higher oxygen fugacity, this is a result of interstitial cations having a higher mobility. This phenomenon may explain the minimum of diffusion rate at a particular oxygen fugacity in the ilmenite results (Fig 2.10), as defects within the crystal lattice whether they are interstitial cations or cation vacancies allow for faster diffusion compared to a defect free crystal lattice.

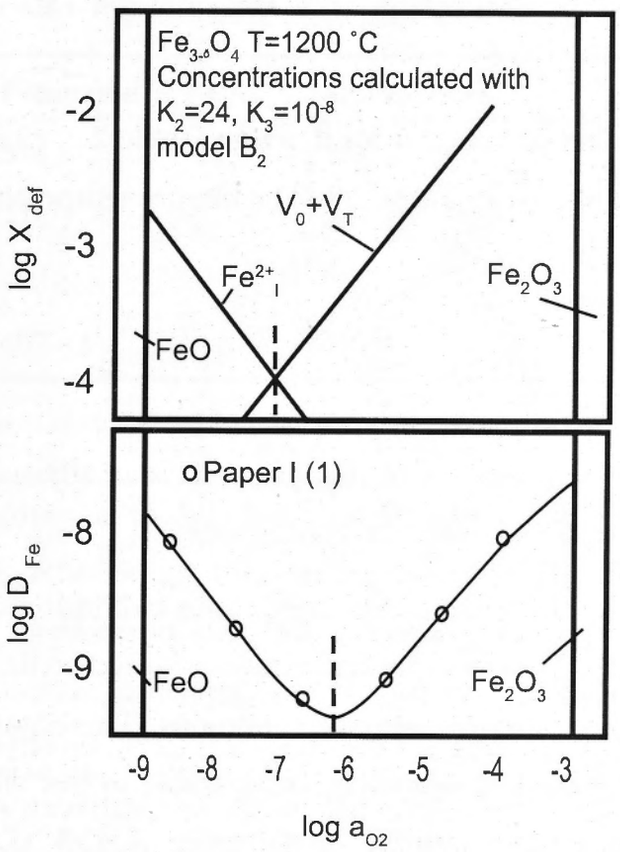

Figure 2.13: Calculated defect concentrations as a function of oxygen activity compared to Fe tracer diffusion coefficients in magnetite. Figure modified from Dieckmann and Schmalzried (1977b) where the defect concentrations were determined using a model (B_2) that assumes the point defects form an ideal solid solution with the crystal. K_n is the equilibrium constant for equations outlined in Dieckmann and Schmalzried (1977b), V_0 is the vacancies at octahedral sites, V_T is the vacancies at tetrahedral sites, and Fe^{2+}_I is the interstitial cations of Fe^{2+}.

2.5.3 The Rate of Diffusion in Ilmenite

It had been assumed that diffusion within ilmenite would be relatively fast from observations of Fe and Mn in garnet and ilmenite resetting in natural samples (Pownceby et al., 1987). Therefore, this has been taken into account by previous authors when using geothermometry systems that contain ilmenite. Docka et al. (1986) compared temperatures obtained from several geothermometers, from the mafic and ultramafic rocks of the Kiglapait Aureole, this included clinopyroxene-ilmenite, orthopyroxene-ilmenite and olivine-ilmenite. In their study the clinopyroxene-ilmenite geothermometer gave temperatures that were systematically too high and the orthopyroxene-ilmenite and olivine-ilmenite gave erratic temperatures. As with other studies there was an assumption made that cations within ilmenite would diffuse faster than clinopyroxene, orthopyroxene and olivine. Quantifying rates of cation diffusion in ilmenite has validated this assumption.

Further, a comparison of diffusion rates of elements within ilmenite determined in this study to other known rates of diffusion in common metamorphic and igneous minerals (Brady, 1995) confirms the assumption of a fast diffusion rate in ilmenite; shown in Table 2.6.

From the derived diffusion parameters for ilmenite (Table 2.5) closure temperatures can be calculated; these are shown in Table 2.7. The closure temperatures were obtained by Dodson's equation (Dodson, 1973):

$$\frac{E}{RT_c} = \ln \alpha \frac{D_0}{l_B^2} \frac{RT_c^2}{Es} \qquad (2.6)$$

Where T_C is the closure temperature of the system, α is an adjustable parameter, l is the diffusion radius of the system and s is the cooling rate.

The closure temperatures have been calculated using a diffusion radius of 2 mm and a cooling rate of 5 °C/Ma. These closure temperatures would be different for crystals with different sizes, cooling rates and boundary conditions. These parameters were chosen so that the closure temperatures would be comparable to the diffusion data compiled by Brady (1995). Closure temperatures, on the order of 450 °C, indicate that even at low-metamorphic conditions ilmenite is open to exchange cations with other phases. This is assuming that ilmenite is in contact with another mineral with which it is able to exchange cations.

Mineral	Composition	Orientation	Diffusing Component	log D (m^2s-1) T=800°C	T_C(°C)	Reference
Olivine	$Fo_{93.7}Fa_{6.3}$	//c-axis	Ni	-18.4	404	Clark and Long, 1971
Garnet (couple)	$Alm_{80}Pyr_{20}$-$Spess_{94}Alm_6$	Isotropic	Mg	-20.8	604	Chakraborty and Ganguly, 1992
Garnet (couple)	$Alm_{80}Pyr_{20}$-$Spess_{94}Alm_6$	Isotropic	Mn	-19.6	526	Chakraborty and Ganguly, 1992
Akermanite (syn)	$Ca_2MgSi_2O_7$	//c-axis	Co	-19.0	474	Morioka and Nagasawa, 1991
Ilmenite	Fe (Mg,Mn, Fe^{3+}) TiO_3	Isotropic	Ni	-15.68	514	This Study

Table 2.6: A comparison of diffusion rates of selected elements for common metamorphic and igneous minerals, data from Brady (1995). For experimental conditions see reference.

Component	Estimated T_C (°C)	Component	Estimated T_C (°C)
Ni	514	**Mg**	332
Co	418	**Al**	317
Ga	469	**Mn**	366
Y	452	**Hf**	450

Table 2.7: Closure temperatures calculated from the diffusion parameters determined in this study.

The applicability of a mineral to diffusion modelling to obtain the duration of thermal events depends on the diffusivity and size of the mineral. The rate of diffusion within ilmenite for the range elements in this study prevents it from being useful as a way of measuring timescales that are associated with metamorphic thermal events. The ilmenite diffusion parameters determined in this study are too fast to be of use for measurement of kinetic processes in metamorphic rocks. However, the results of this study may be useful for geochemical modelling of systems containing ilmenite or kinetic processes of a shorter duration i.e. days.

2.6 Conclusions

This study examined the effect of temperature, oxygen fugacity and crystallographic orientation on the rates of diffusion of multiple elements within ilmenite. Diffusion parameters were well constrained for Co, Ni, Ga and Y and an indication of the rate of diffusion of Mn, Mg, Al, Cr and Hf was also determined. It was found that the diffusivity of ilmenite has a strong dependence on temperature and oxygen fugacity, with the diffusion coefficients showing a minimum in diffusivity at an oxygen fugacity corresponding to 75% CO_2 in the gas mixture in experiments run at 1000 °C. Additionally, the results indicate the diffusivity is independent of crystallographic orientation. The diffusion rates measured were on the order of 10^{-13} to 10^{-16} m^2s^{-1} at 1000 °C for the range of elements measured. Diffusion rates for Zr, V, Nb and Ta were unable to be quantified for the experimental conditions covered in this study.

Further experiments would need to be carried out to better constrain the diffusion parameters as well as determining the influence of other factors, such as pressure and composition. As ilmenite is utilised by several geothermometers accurate knowledge of the diffusion parameters may resolve discrepancies between geothermometers.

In relation to a garnet-ilmenite diffusion model, the rate of diffusion in ilmenite has been shown to be fast when compared to garnet, thus garnet diffusivity is the rate-determining factor in the garnet-ilmenite system. However, the rapidity of ilmenite diffusivity should be taken into account when selecting garnet-ilmenite pairs within natural samples for analysis. If ilmenite is in contact with another fast diffusing phase with which it can readily exchange it will no longer retain accurate information. This contact can either be direct or via cracks that provide diffusion pathways. Therefore to obtain accurate information for modelling purposes, as well as geothermometry, ilmenite inclusions that are isolated from other minerals in three dimensions should always be selected. This ensures that the partitioning of Fe and Mn between garnet and ilmenite is represented by the exchange reaction as described in Chapter 1 (Eqn. 1.8).

CHAPTER 3

An Experimental Investigation of Partitioning and Diffusion in the Garnet-Ilmenite System

Preface

The experiments undertaken for this study were carried out at Ruhr Universität, Bochum (RUB) in Germany in collaboration with Professor Sumit Chakraborty and Dr Ralf Dohmen. The analytical work was carried out in collaboration with Dr David Nelson of UWS at the Secondary Ion Mass Spectrometer (SIMS) facility at the University of Western Sydney (UWS). The Australian Institute of Nuclear Science and Engineering (AINSE) research awards, ALNGRA11041 and ALNGRA12013, provided funding for analysis. Dr Ian Williams of RSES provided valuable advice on SIMS analytical procedures. The electron probe microanalysis was carried out at RSES, ANU with the assistance of Dr Robert Rapp.

3.0 Synopsis

A new experimental technique for constraining the rate of diffusional processes was investigated in this study. Experiments were carried out using an ilmenite thin film as the diffusant source on a garnet substrate. Cubes of almandine-pyrope garnet were coated with a 50 to 150 nm thin film of ilmenite by pulsed laser deposition. The starting materials of the experiments were characterised by electron probe microanalysis. Experiments were performed in a one atmosphere furnace with oxygen fugacity (fO_2) controlled by a gas mixture of CO_2 and CO at a $\log fO_2$ of -16 and -17.5 at temperatures of 850 °C and 800 °C, respectively. Post-annealing concentration profiles were measured by depth profiling through the ilmenite thin film into the garnet substrate using secondary ion mass spectrometry. In this study the analytical technique for measuring across a boundary of this type was refined.

The experiments carried out in this study failed to produce measurable diffusion profiles. Possible impediments on the exchange and diffusion of Fe and Mn in these experiments are discussed, although none of these potential obstacles satisfactorily explain the complete absence of measurable diffusion profiles. Analytical and methodological concerns are also discussed, and these cannot be completely dismissed, in particular the implications of Si and Al concentrations measured in the ilmenite thin films. Nonetheless the null result does allow a limit on the maximum rate of diffusion in this system to be constrained and requires diffusion to be at least one order of magnitude slower than previously inferred rates of diffusion in garnet at these temperatures.

3.1 Introduction

Diffusion modelling allows timescales of metamorphism to be constrained by relating the length of diffusion profiles preserved within minerals to the duration of the thermal event. This technique is now widely used for placing time constraints on the formation of metamorphic terranes. Monocrystalline diffusion modelling, particularly in garnet, has been the focus of many studies (e.g. Camacho et al., 2009; Dachs and Proyer, 2002; O'Brien and Vrána, 1995; Olker et al., 2003; Philippot et al., 2001; Sautter et al., 2001; Trepmann et al., 2004; Weyer et al., 1999). In general, garnet diffusion modelling is based on diffusion of major elements and a duration is constrained by forward modelling the effect of thermal events on initial garnet zoning profiles. There are two major difficulties with this method, one being differentiating between the growth zoning of garnet and later diffusional modification, and secondly the spread in the experimentally determined diffusion parameters for garnet.

The garnet-ilmenite system provides a solution to the problem of how to differentiate between growth zoning and diffusional modification. Diffusion profiles can be preserved in garnet surrounding ilmenite inclusions (Fig. 1.1, Chapter 1) and these can be correlated with grain scale diffusion. This provides a method for independently establishing the timescales over which diffusional processes are effective within garnet. However, garnet diffusion parameters are inadequately constrained. This inadequacy has been discussed by several previous studies (Ayres and Vance, 1997; Chakraborty, 2008; Viete et al., 2011b) and is related, in part, to the difficult and time consuming nature of garnet diffusion experiments.

Therefore experiments were conducted to better constrain the rate of diffusion in garnet with an ilmenite thin film as a diffusant source. These experiments were designed to investigate if using thin films is a valid method for studying these types of diffusion problems, which are characterised by diffusion being induced by the partitioning of elements between two phases. Not investigated in this study was the effect of composition and pressure on the diffusivity.

For these experiments almandine-pyrope cubes were coated with an ilmenite thin film produced by pulsed laser deposition (PLD). Using this innovative methodology in conjunction with secondary ion mass spectrometry (SIMS) depth profiling allows analysis of small-scale diffusion profiles, on the order of 1 μm without difficulty. With this

capability it should be possible to run experiments at temperatures closer to those actually achieved in the Earth, and/or over shorter durations than previously required when using conventional analytical techniques, e.g. electron probe microanalysis. The temperature (800 and 850 °C) and oxygen fugacity ($\log fO_2$ of -17.5 and -16) of experimental runs were chosen to be within the stability field of garnet at 1 atm. At these temperatures, extrapolation of existing diffusion parameters (e.g. Loomis et al., 1985; Chakraborty and Ganguly, 1992) indicates that profiles would be on the order of 1 μm, hence diffusion profiles should be measurable with the SIMS depth profiling technique. If the diffusivity can be determined from experiments in this relatively low temperature range the results would significantly improve the constraint on the diffusion parameters by broadening the data set and constraining the diffusivity at considerably lower temperatures than previous experiments were able to (e.g. Loomis et al. 1985; Chakraborty and Ganguly, 1992).

3.2 The Garnet-Ilmenite System

Diffusion in the garnet-ilmenite system is controlled by the partitioning behaviour between the two phases. The partitioning of Fe and Mn causes movement of these elements across the interface between garnet and ilmenite. Diffusion then acts to redistribute the resulting concentration change away from the interface. Diffusion within ilmenite is relatively fast compared to garnet. Therefore, the slower diffusion kinetics of garnet allows for diffusion profiles to be preserved in natural samples under certain conditions (Fig. 1.1; Chapter 1).

The partition coefficient for the exchange reaction of Fe and Mn between garnet and ilmenite has been calibrated experimentally by Ono (1980), Docka (1984) and Kress et al. (1985) and was found to be highly sensitive to temperature. Due to this sensitivity the garnet-ilmenite system has been applied to geothermometry by Pownceby et al. (1987; 1991) and Feenstra and Engi (1998). The results of these partitioning experiments are displayed in Figure 3.1.

The subsequent diffusion of Mn and Fe in garnet is controlled by the diffusion parameters, which have been constrained by previous studies (e.g. Carlson, 2006; Chakraborty and Ganguly, 1992; Loomis et al., 1985). There is a large spread in the diffusion parameters obtained by these different studies as is seen in Table 3.1. However, it is worth noting that these data sets are not independent. Chakraborty and Ganguly (1992) added their data to the experimental data set of Loomis et al. (1985) to determine the diffusion rates in garnet

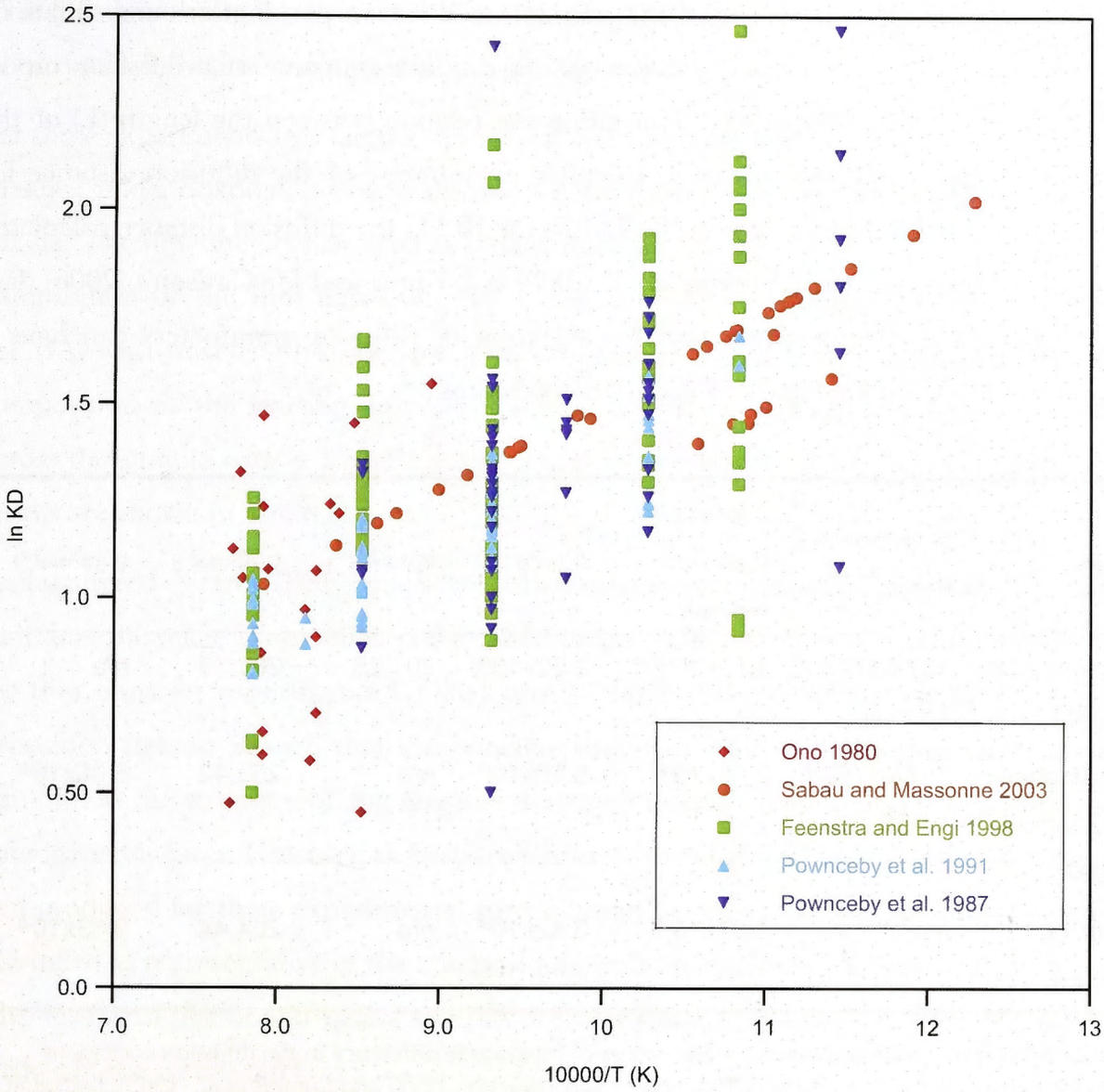

Figure 3.1: Results from partitioning experiments investigating the exchange of Fe and Mn between garnet and ilmenite by previous studies over varied experimental conditions. The experimental data was obtained by Ono (1980), Docka (1984), Kress et al. (1985), Pownceby et al. (1987; 1991) and Feenstra and Engi (1998). This illustrates the strong dependence of the partition coefficient on temperature.

as reported on in the paper and Carlson (2006) places lower temperature constraints on the experimental data, of Loomis et al. (1985) and Chakraborty and Ganguly (1992), using natural samples. In general, it has been determined by these studies that garnet diffusion parameters have a strong dependency on composition and oxygen fugacity, which could account for some of this spread. This dependence results in the selection of a set of parameters making a significant difference in the final outcome of a diffusion model. To minimize the uncertainty this introduces into diffusion models it is preferable that the selected diffusion parameters were determined from garnets of similar compositions to the garnets being modelled.

To demonstrate the importance of the selection of diffusion parameters, an estimate of the influence of the diffusion coefficient (D) on the final outcome of a diffusion model can be determined. This can be done using the relation between the length (L) of the diffusion profile and timescale (t) to calculate an estimate of the diffusion distance for one-dimensional diffusion. At 660 °C (933 K) for 10 Ma the diffusion distance calculated from the diffusion data of Loomis et al. (1985) is 2.7 mm and for Carlson's (2006) data is 0.1 mm. This demonstrates that the selection of diffusion parameters can have a significant effect on the results of diffusion modelling.

Study	Experimental Range	D (m^2s^{-1}) (T=933K, P=6kbar)	D_0(m^2s^{-1})	E($KJmol^{-1}$)	Q($KJmol^{-1}$)	$\bar{v}$ (m^3mol^{-1})
Loomis et al. (1985)	1573-1773 K, 40 kbar	$1.19x10^{-20}$	$2.20x10^{-14}$	201.25	201.39	n/a
Chakraborty & Ganguly (1992)	1573-1752 K, 14-35 kbar	$2.09x10^{-22}$	$5.10x10^{-8}$	n/a	253.42	$6.00x10^{-6}$
Carlson (2006)	n/a	$1.67x10^{-23}$	$3.42x10^{-8}$	n/a	264.44	$9.63x10^{-6}$

Table 3.1: Garnet diffusion data showing orders of magnitude difference in the diffusion coefficient (D) determined by Carlson (2006), Chakraborty and Ganguly (1992) and Loomis et al. (1985). Diffusion parameters presented are D_0 which is D at infinite temperature, the activation energy (E) and activation volume ($\bar{v}$) which are related by $Q=E+P\bar{v}$, where P is pressure.

3.3 Experimental Method

Experiments were performed on almandine-pyrope cubes that were coated with a thin film of ilmenite (50 to 150 nm) using pulsed laser deposition (PLD). The method for the production of thin films from PLD is based on Dohmen et al. (2002).

3.3.1 Starting Material

The pulsed laser ablating a starting material, called a target, produces the thin film. The target is spinning as the laser ablates it. This process converts the target material into plasma before being deposited onto the garnet sample as an amorphous thin film.

The film has the bulk chemistry of the target that has been ablated. It then forms a polycrystalline matrix during annealing (Dohmen et al., 2002).

For these experiments two targets were made from natural ilmenite crystals, one from the Blaafjell mine, Sokndal, Norway and the second from the Vishnevye Mountains, Urals, Russia. The ilmenite crystals used as targets were analysed to determine average starting composition of the thin film using the Cameca SX100 electron probe microanalyser (EPMA) with wavelength-dispersive spectrometers (WDS) at RSES, ANU. The average composition of the starting ilmenite was determined by random point analyses from across the sample with a 15 keV accelerating voltage and a 20 nA beam current. The results are shown in Table 3.2.

Backscattered electron (BSE) images of both targets were inspected. The Blaafjell ilmenite contained lamellae observable in the BSE images. This target was used for producing the thin films for experiments G5Ilm1 and G5Ilm2 and control sample G5Ilm3. The deposition process is such that the lamellae should not affect the homogeneity of the thin film as the structure of the target is destroyed during ablation and is deposited as a homogeneous layer. However, to best approximate the chemical composition of the thin film produced for these experimental runs a broad beam analysis of the target ilmenite was taken as representative of the composition, with an approximate beam size of 50 μm. The results of the broad beam analysis are contained in Table 3.2. This is discussed further in the results Section 3.5.1.

The second ilmenite target was analysed using the same EPMA operating conditions. The ilmenite was from the Vishnevye Mountains and was used to produce the thin film for experiments G5Ilm4 and G5Ilm5 and control sample G5Ilm6. Due to the homogenous nature of the ilmenite, a broad beam analysis was not necessary for determination of a representative analysis and a beam size of 1 μm was used (Table 3.2).

The composition of the almandine-pyrope cubes used in the experiments was determined using EPMA at Ruhr Universität, Bochum (RUB) and the results are shown in Table 3.2.

Garnet	Wt%	Ilmenite Target Blaafjell	Wt%	Ilmenite Target Vishnevye	Wt%
SiO_2	40.93				
TiO_2	0.02	TiO_2	47.83	TiO_2	48.73
Al_2O_3	23.44	Al_2O_3	0.06	Al_2O_3	0.03
Cr_2O_3	0.01	Cr_2O_3	0.26	Cr_2O_3	0.00
Fe_2O_3	0.56	Fe_2O_3	17.71	Fe_2O_3	8.26
FeO	17.73	FeO	30.89	FeO	37.70
MnO	0.23	MnO	0.25	MnO	3.38
MgO	16.97	MgO	5.63	MgO	0.27
CaO	1.23	CaO	0.00	CaO	0.00
		K_2O	0.01	K_2O	0.00
Total	101.13		102.63		98.42

Table 3.2: Major and minor elemental concentrations for the experimental starting materials. The results show normalised concentrations with Fe^{3+} component calculated from the stoichiometry.

3.3.2 Pulsed Laser Deposition

The thin film was deposited using the PLD set up at Ruhr Universität, Bochum (RUB), which is shown in Figure 3.2. An Ar-F Laser 193 nm was used for ablation of the target material. To determine the deposition rate, the ilmenite target was ablated with a SiO_2 wafer in the sample holder. The thickness of the ilmenite film on the SiO_2 wafer was determined using the birefringence patterns that resulted. A deposition time for producing a thin film, approximately 100 nm thick, on the garnet cubes was then estimated. Before deposition the garnet cubes were cleaned in an ultrasonic bath. Then the garnet was placed in the vacuum chamber of the PLD set up and heated to 400 °C for 15 minutes to allow any residual moisture on the surface to evaporate. The cubes were then allowed to cool before coating in the thin film.

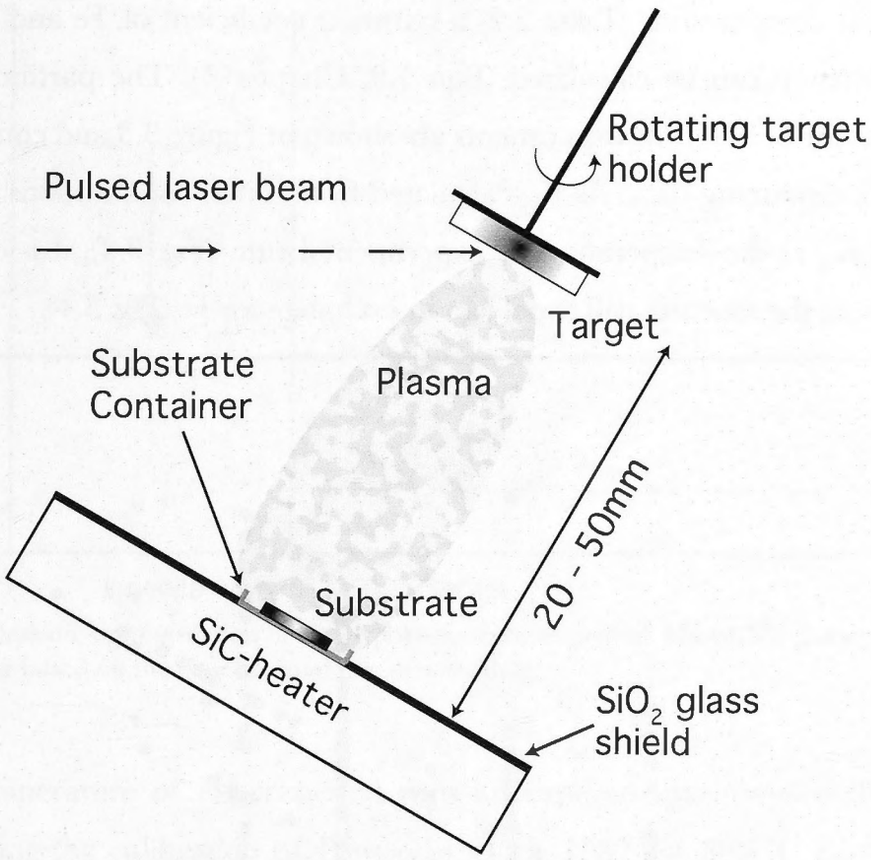

Figure 3.2: Illustration of the pulsed laser deposition set up at the Institut für Geologie, Mineralogie und Geophysik (RUB). Figure was modified from (Dohmen et al., 2002).

3.3.3 Diffusion Experiments

Experiments were performed in a one atmosphere furnace with the oxygen fugacity (fO_2) controlled by a gas mixture of CO_2 and CO. Experiments were run at a $\log fO_2$ of -16 and -17.5 (Wüstite-Magnetite buffer) with temperatures of 850 °C and 800 °C, respectively. Experimental conditions are detailed in Table 3.3.

Run	Ilmenite target	Thin film (nm)	Temperature (°C)	log fO_2	time (hrs)
G5Ilm1	Blaafjell	50	846	-16	21.67
G5Ilm2	Blaafjell	50	800	-17.5	46.83
G5Ilm3	Blaafjell	50	-	-	-
G5Ilm4	Vishnevye	150	800	-17.5	189.83
G5Ilm5	Vishnevye	150	850	-16	72.17
G5Ilm6	Vishnevye	150	-	-	-

Table 3.3: Experimental conditions for garnet-ilmenite thin film samples. For each ilmenite target a reference sample was coated that would not be annealed to provide a comparison for analysis.

From the initial compositions (Table 3.2) a partition coefficient of Fe and Mn between garnet and ilmenite can be calculated (Eqn 1.9, Chapter 1). The partition coefficient (K_D) calculated for both sets of experiments are shown in Figure 3.3 and compared to the experimental partitioning data. As K_D calculated from initial compositions is lower than the projected K_D at the temperature of experimental runs (Fig. 3.3), it is expected that during annealing the ilmenite will expel Mn in exchange for Fe (Fig. 3.4).

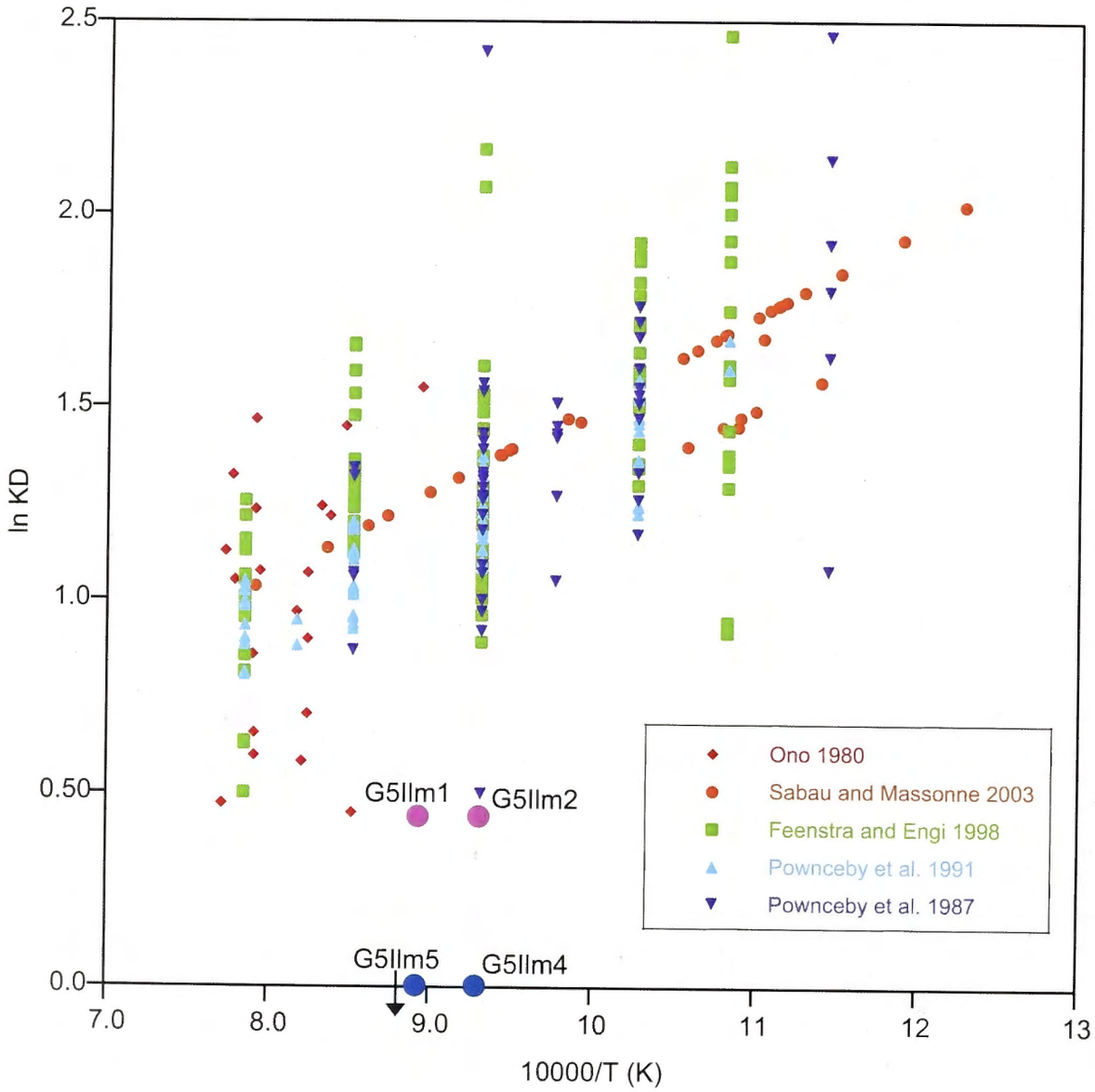

Figure 3.3: The partition coefficients calculated from the initial compositions of the garnet and ilmenite targets compared to the experimental partitioning data of Ono (1980), Docka (1984), Kress et al. (1985), Pownceby et al. (1987; 1991) and Feenstra and Engi (1998).

The amount of Mn that was available for exchange in the ilmenite thin film was also calculated. For these calculations concentration is in terms of mol/volume that is calculated by dividing the total number of cations per formula unit by the molar volume (Dohmen, 2008).

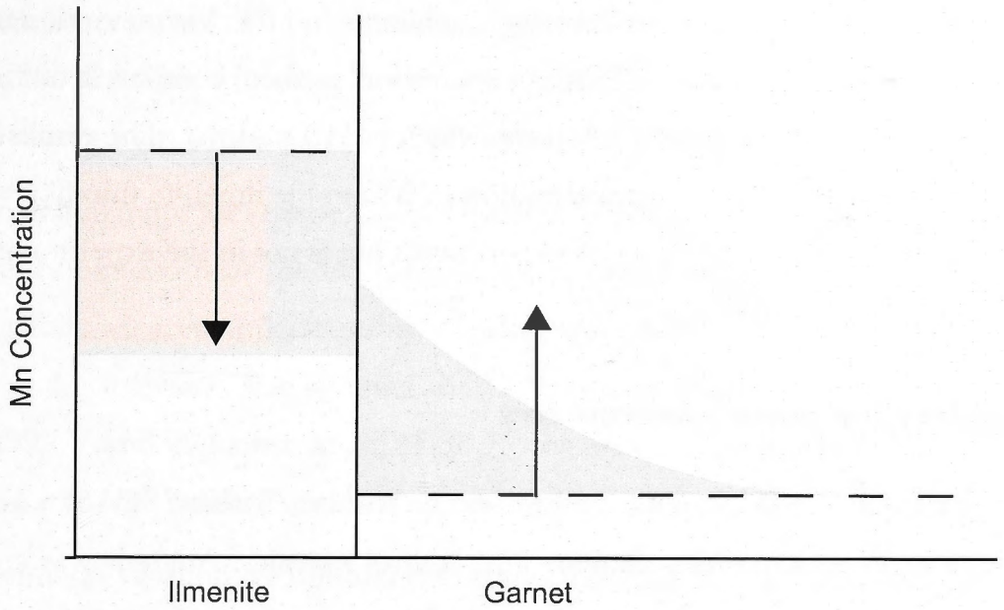

Figure 3.4: Schematic representation of the hypothetical movement of Mn within garnet and ilmenite during annealing based on the experimental partitioning data.

From the temperature of experimental runs an expected partition coefficient can be calculated using the calibration of Pownceby et al. (1987), at 800 °C K_D= 3.68 and at 850 °C K_D= 3.31. Rearranging the K_D equation (Eqn 1.2, Chapter 1) provides a means for calculating the expected ratio of Fe and Mn in the ilmenite:

$$K_D \frac{X_{Fe}^{gnt}}{X_{Mn}^{gnt}} = \frac{X_{Fe}^{ilm}}{X_{Mn}^{ilm}} \qquad (3.1)$$

Where X is the mole fraction of the element in the phase labelled. At 800 °C the expected ratio is of Fe to Mn is 267.6 and at 850 °C the expected ratio is of Fe to Mn is 239.7.

The amount of Fe and Mn exchanged is constrained by the assumption that only these two elements participate in the exchange reaction. Therefore, the sum of the concentrations remains constant. From this the expected Mn concentration at equilibrium in the thin film can be calculated. For the Blaafjell Ilmenite used for coating G5Ilm1, G5Ilm2 and G5Ilm3 the estimated Mn concentration at equilibrium is 80 mol m^{-3} and for Vishnevye Ilmenite used for coating G5Ilm4, G5Ilm5 and G5Ilm6 is 116 mol m^{-3}. The amount of Mn that is available for exchange can then be calculated from the initial compositions. The initial concentration in the ilmenite thin films was 155 mol m^{-3} and 2267 mol m^{-3} for the Blaafjell Ilmenite and Vishnevye ilmenite, respectively. Thus the Blaafjell ilmenite

thin film has 75 mol m^{-3} of Mn available for exchange and the Vishnevye ilmenite thin film has 2150 mol m^{-3} available. This concentration is then compared to the initial concentration of Mn in the garnet substrate, which is 118 mol m^{-3}. The results of these calculations indicate that the low concentration of Mn in the ilmenite thin film may be a constraint on diffusion in the first set of experiments but is not in the experiments coated with the Vishnevye ilmenite target.

3.4 Secondary Ion Mass Spectrometry

The Cameca IMS 5f SIMS at the University of Western Sydney (UWS) was used to obtain depth profiles of the experiments and control samples. Analysis was conducted over three sessions and various operating conditions were tested to achieve the best results and minimize analytical artefacts in the profiles. Photomicrographs of all samples analysed are shown in Figure 3.5.

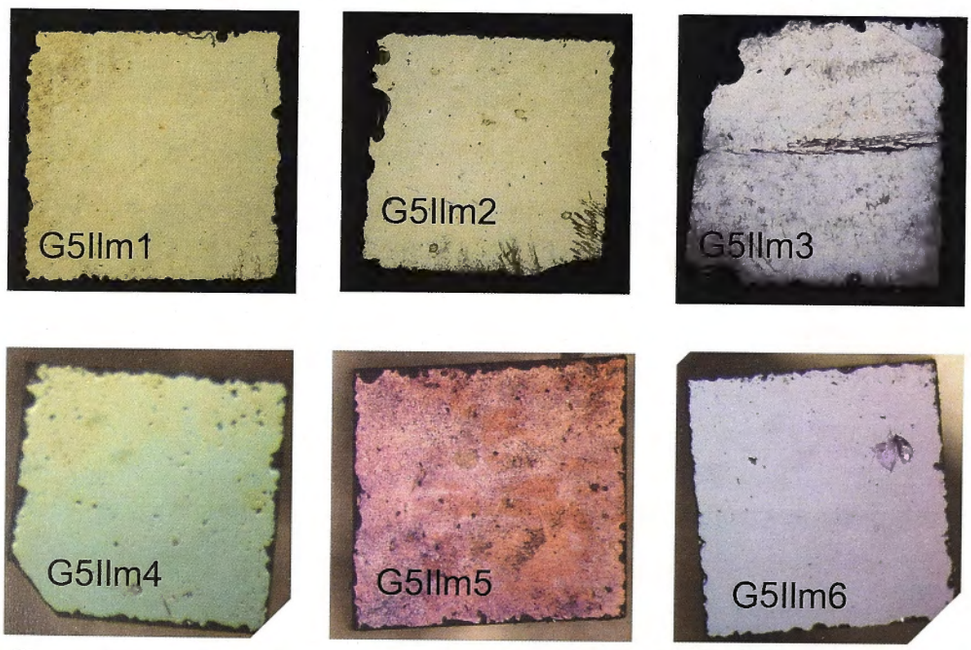

Figure 3.5: Photomicrographs of the surface of each experiment and control samples. Top: Experiments G5Ilm1 and G5Ilm2 and the control sample, G5Ilm3. Bottom: Experiments G5Ilm4 and G5Ilm5 and the control sample, G5Ilm6. The colour difference between samples on the top and bottom of this figure is due to different microscopes being used for the photography. The reason for the notable colour contrast between G5Ilm4 and G5Ilm5 is unknown.

For experiments G5Ilm1, G5Ilm2 and G5Ilm3 analysis was performed using a Cs^+ primary ion beam with an impact energy of 5000 V and a 47.1° incidence angle. Elements measured in analysis included ^{27}Al, ^{28}Si, ^{55}Mn, ^{56}Fe, ^{24}Mg, ^{25}Mg, ^{48}Ti, ^{47}Ti, ^{52}Cr, ^{40}Ca and ^{16}O. The electron gun was used to balance the charge as it crossed the interface

from ilmenite to garnet. The e-gun was set with an emission of 1.03 mA. The analysed area was 100 μm with a primary beam current of 5.4 nA. The e-gate was set at 50% to reduce the area from which the secondary ions were collected.

SIMS elemental maps for sample G5Ilm1 were produced for the analysis pits from profiles that were terminated near the interface between garnet and ilmenite. This analysis was done to gain a clearer understanding of what was causing some of the concentration changes at the interface. For imaging the O^{2+} primary beam was used with an impact energy 9999 V and incidence angle of 38.7°, the area analysed was 225 μm. The e-gun was used for charge balance and had an emission of 0.49 mA.

For experiments G5Ilm4, G5Ilm5 and G5Ilm6 the analytical method was based on the previous setup with slight variations to optimize results. Elements measured were ^{16}O, ^{25}Mg, ^{27}Al, ^{28}Si, ^{47}Ti, ^{55}Mn, ^{56}Fe, ^{133}Cs and $^{133}Cs + {}^{197}Au$. The ^{133}Cs ions were measured to track the fluctuations in the primary beam and the $^{133}Cs + {}^{197}Au$ indicates when the Au coat is removed from the analysed area. The analysed area was 150 μm with a raster size 250 μm and a primary beam current of 7.0 nA. The charge was balanced with an e-gun emission of 2.8 mA.

The G5Ilm4, G5Ilm5 and G5Ilm6 experiments were also analysed using an O^{2-} primary ion beam. This ion beam was used to eliminate the charging behaviour. Elements measured were ^{16}O, ^{25}Mg, ^{27}Al, ^{28}Si, ^{47}Ti, ^{55}Mn, ^{56}Fe and ^{197}Au. The analysed area was 150 μm with a raster size 250 μm and a primary beam current of 9.5 nA. The measurement of the secondary ions switched between the electron multiplier and Faraday cup in these analyses, hence the counts have been corrected by subtracting the offset between the two collectors.

Profiles across analysis pits were obtained using the profilometer at the SIMS facility (UWS). The depths of all profiles were measured using this instrument. It also provided information as to the topographical features of the samples, which can affect depth resolution across interfaces.

3.5 Results

Results from four experiments are compared to control samples. The experiments and control samples were coated in the PLD chamber at the same time.

3.5.1 Characterising the Thin Film

The targets used to produce the thin films were both natural ilmenite crystals. The EPMA analysis of the ilmenite used for producing the thin film is detailed in Table 3.2. The Blaafjell ilmenite target was found to have lamellae when examined with backscattered electron microscopy (Fig. 3.6). Table 3.4 shows the results of analysis of the Blaafjell target with separate results for the lamellae, however, due to the size of lamellae the analyses are probably mixed. Taking this into consideration the lamellae are probably Fe_2O_3 with some impurities e.g. Cr and Al.

When producing the thin film a phenomenon that is often observed is droplets of the target material forming on the surface, this is referred to as 'splashing'. It is particularly problematic when analysing using the SIMS as the ion beam accentuates original surface topographic features and this reduces spatial resolution. If it has occurred 'splashing' can be seen by reflected light microscopy (Dohmen et al., 2002). For all experiments and control samples in this study no evidence of splashing was seen.

To check for surface reactions during annealing photomicrographs were taken of experiments before and after the runs and only minor surface inconsistencies were noted. The inconsistencies were mainly due to later removal of the ilmenite thin film possibly during the process of mounting the experiments in epoxy. The photomicrographs of the control samples and experiments after annealing are shown in Figure 3.6. Experiments were also imaged on the EPMA to produce Backscattered electron images after the diffusion anneals to characterize surface features (Fig. 3.7).

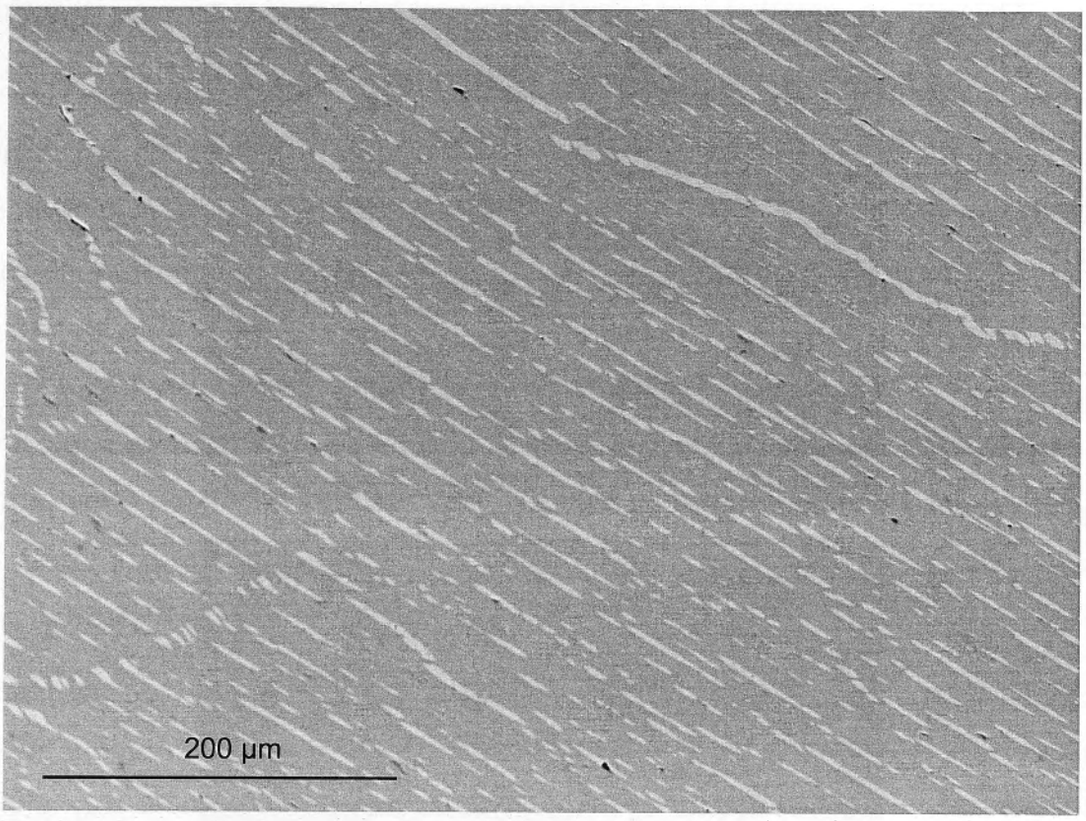

Figure 3.6: Backscattered electron image of the Blaafjell ilmenite that was used as a target material in the production of the thin films for G5Ilm1, G5Ilm2 and G5Ilm3 showing lamellae.

Oxide wt%	TiO_2	Al_2O_3	Cr_2O_3	Fe_2O_3	FeO	MnO	MgO	Total
Ilmenite	44.02	0.05	0.24	16.30	28.43	0.23	5.19	94.46
Lamellae	9.55	0.21	1.03	79.24	7.65	0.00	0.26	97.94

Table 3.4: Results from EPMA for ilmenite used as a target in PLD for sample G5Ilm1, G5Ilm2 and G5Ilm3 in oxide weight percent. Showing normalized analysis of ilmenite with calculated Fe^{3+} component.

The profilometer at UWS provided a method for measuring the thickness of the thin film. Using the SIMS the samples were depth profiled to the boundary between ilmenite and garnet. The drop in the count rate of ^{47}Ti indicated the boundary. The depth of the produced pit was then measured using the profilometer. Using this method the ilmenite thin film was determined to be approximately 50 nm thick for G5Ilm1, G5Ilm2 and G5Ilm3 and approximately 150 nm thick for G5Ilm4, G5Ilm5 and G5Ilm6.

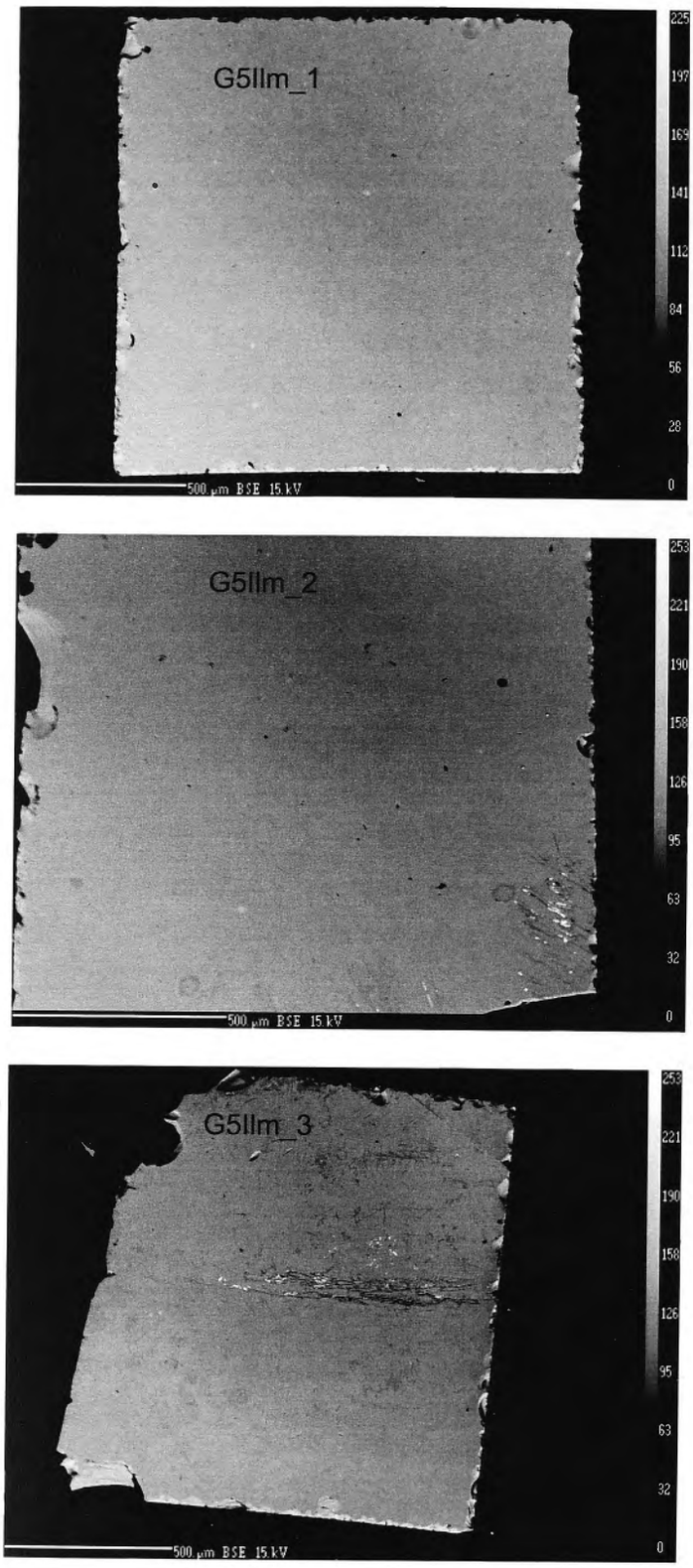

Figure 3.7: Backscattered electron images were taken for checking the surface was free from topographic features. Shown are experiments G5Ilm1 and G5Ilm2 and the control sample, G5Ilm3.

3.5.2 Depth Profiles

The concentrations of elements were measured in counts per second these were then normalized to the counts for ^{28}Si, which have been assumed to be relative to a constant concentration in garnet. Concentration profiles of all annealed samples G5Ilm1 and G5Ilm2 showed no marked difference in Mn or Fe concentration within garnet when compared to the control samples G5Ilm3, thus no measurable diffusion occurred (Fig. 3.8). However, for experiments G5Ilm4 and G5Ilm5 (Figs. 3.9 and 3.10) a concentration gradient was observed in the $^{55}Mn/^{28}Si$ profiles. This gradient is evident until approximately 50 nm into the garnet, this may be the result of diffusion although the profile is not long enough to accurately determine diffusion parameters. The constraint this would place on the rate of diffusion is discussed in Section 3.6.3.

The analysis carried out on G5Ilm4, G5Ilm5 and G5Ilm6 using the O^{2-} ion beam (Fig. 3.10) provided much clearer profiles due to the elimination of the charging behaviour at the interface between ilmenite and garnet.

The pits produced by all analyses were measured with a profilometer; the bottoms of the pits were relatively flat, with topographical variations generally on the order of 20 nm (Fig 3.11).

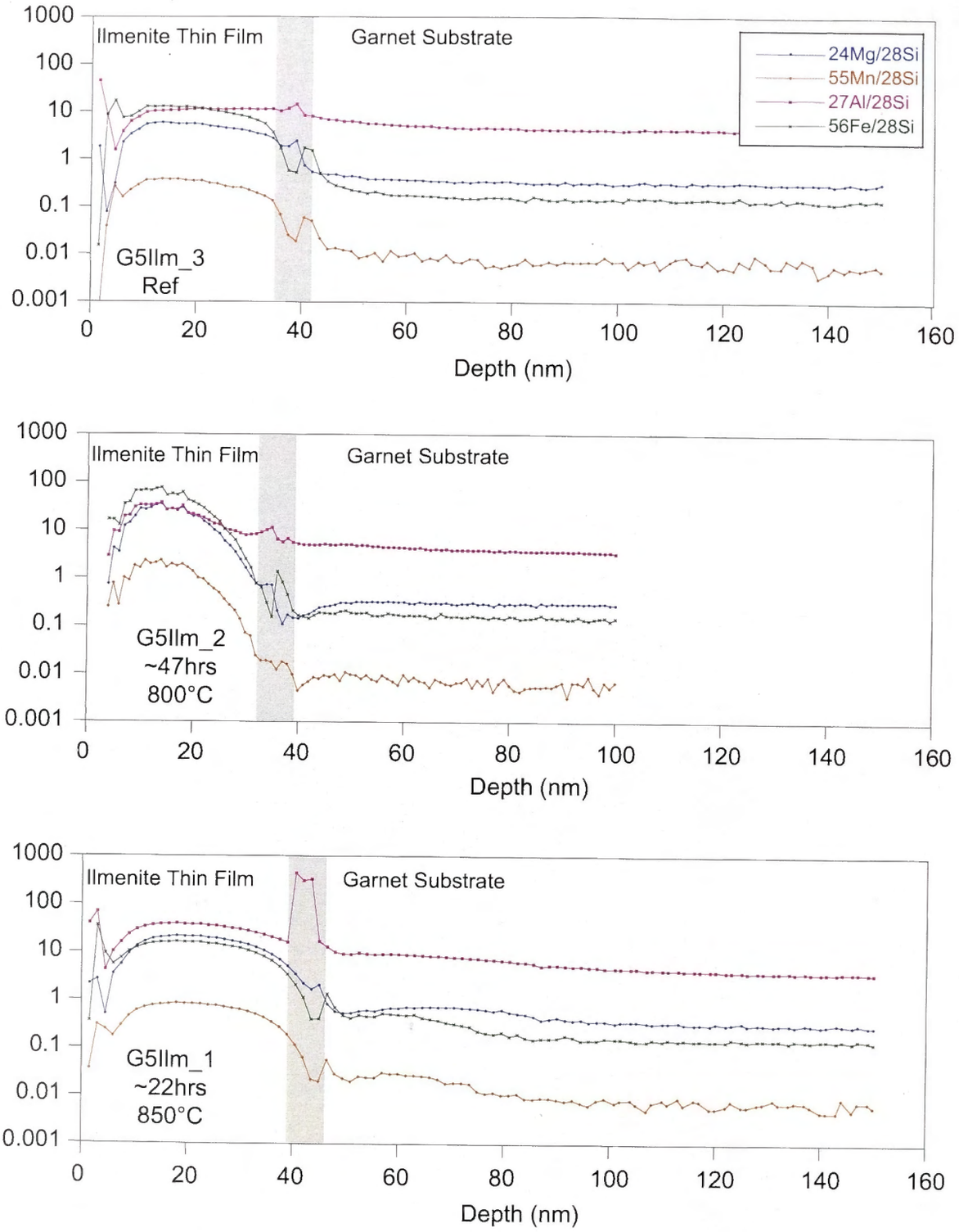

Figure 3.8: SIMS depth profiles performed using a Cs^+ ion beam for G5Ilm3, G5Ilm2 and G5Ilm1. The shaded area represents the estimated depth of the boundary between the ilmenite thin film and garnet substrate.

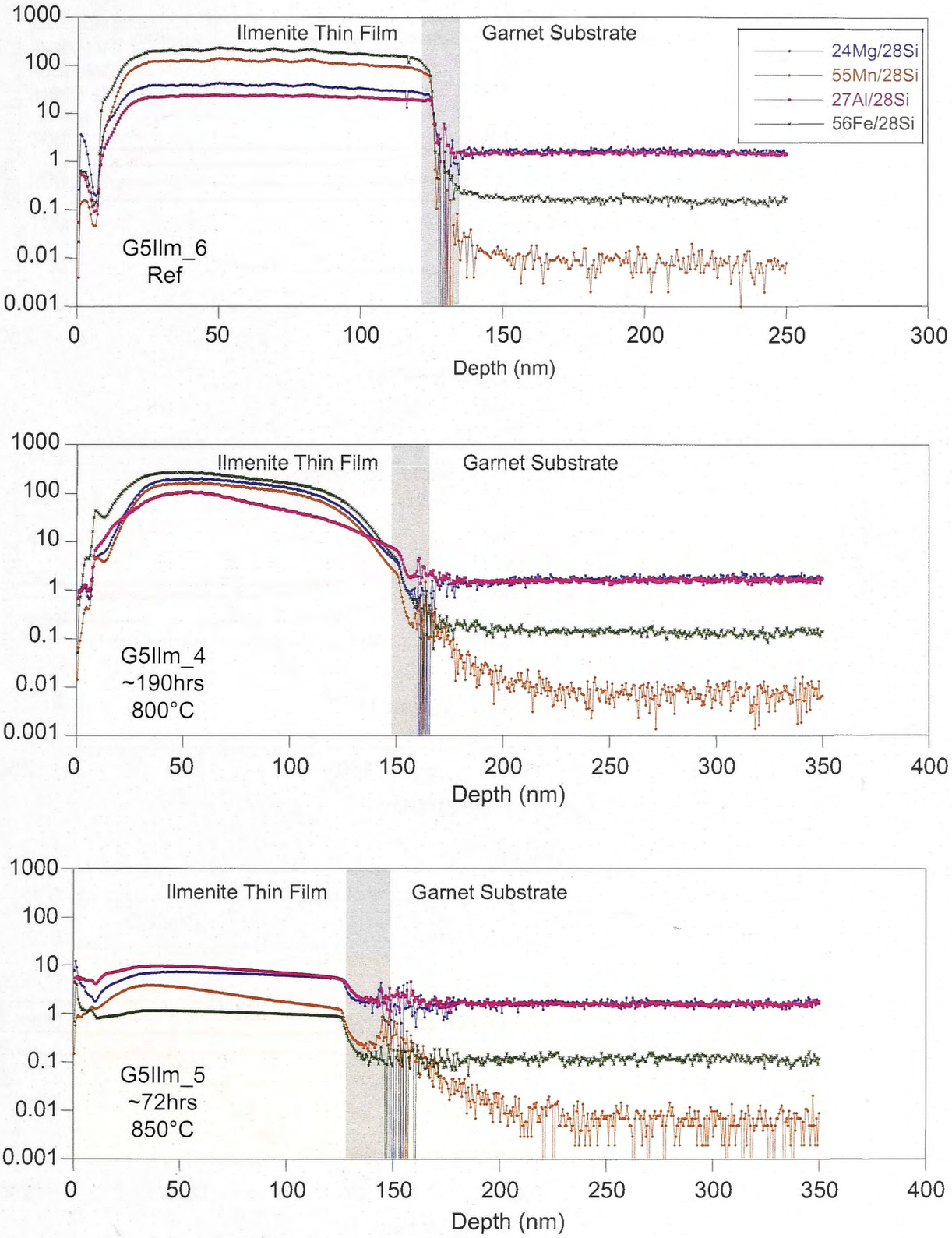

Figure 3.9: SIMS depth profiles performed using a Cs^+ ion beam for G5Ilm4, G5Ilm5 and G5Ilm6. The shaded area represents the estimated depth of the boundary between the ilmenite thin film and garnet substrate.

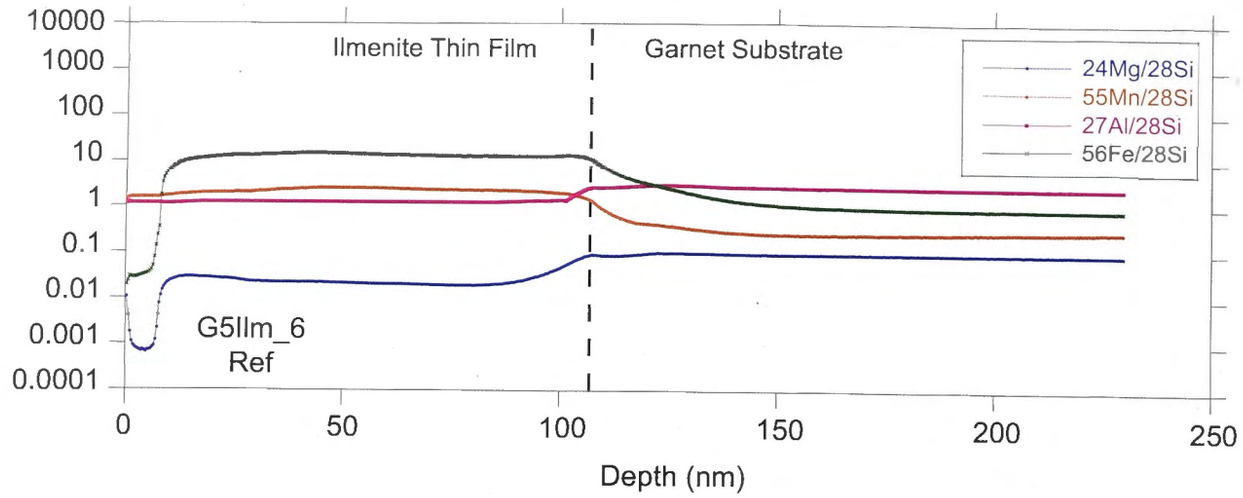

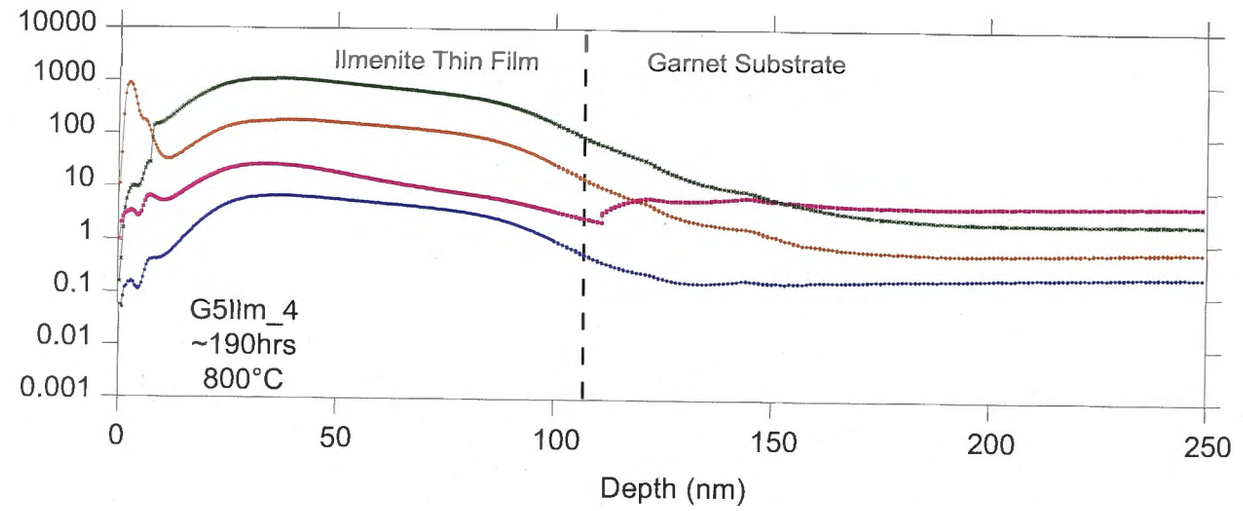

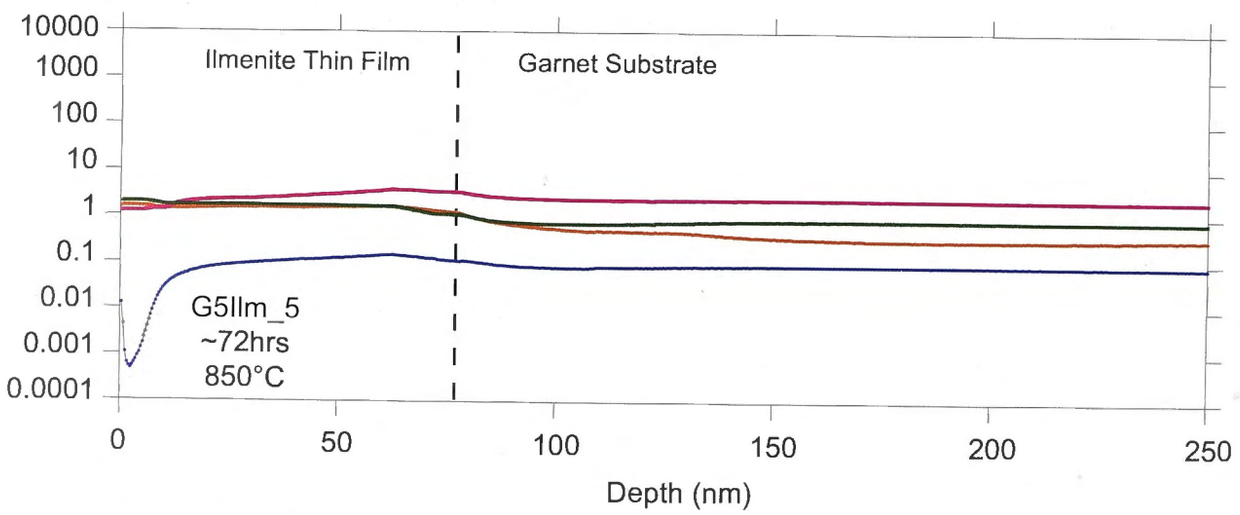

Figure 3.10: SIMS depth profiles performed using O^{2-} primary ion beam for G5Ilm4, G5Ilm5 and G5Ilm6. The dotted line represents the estimated depth of the boundary between the ilmenite thin film and garnet substrate. Note that there is no sharp drop in counts as the charging behaviour is eliminated.

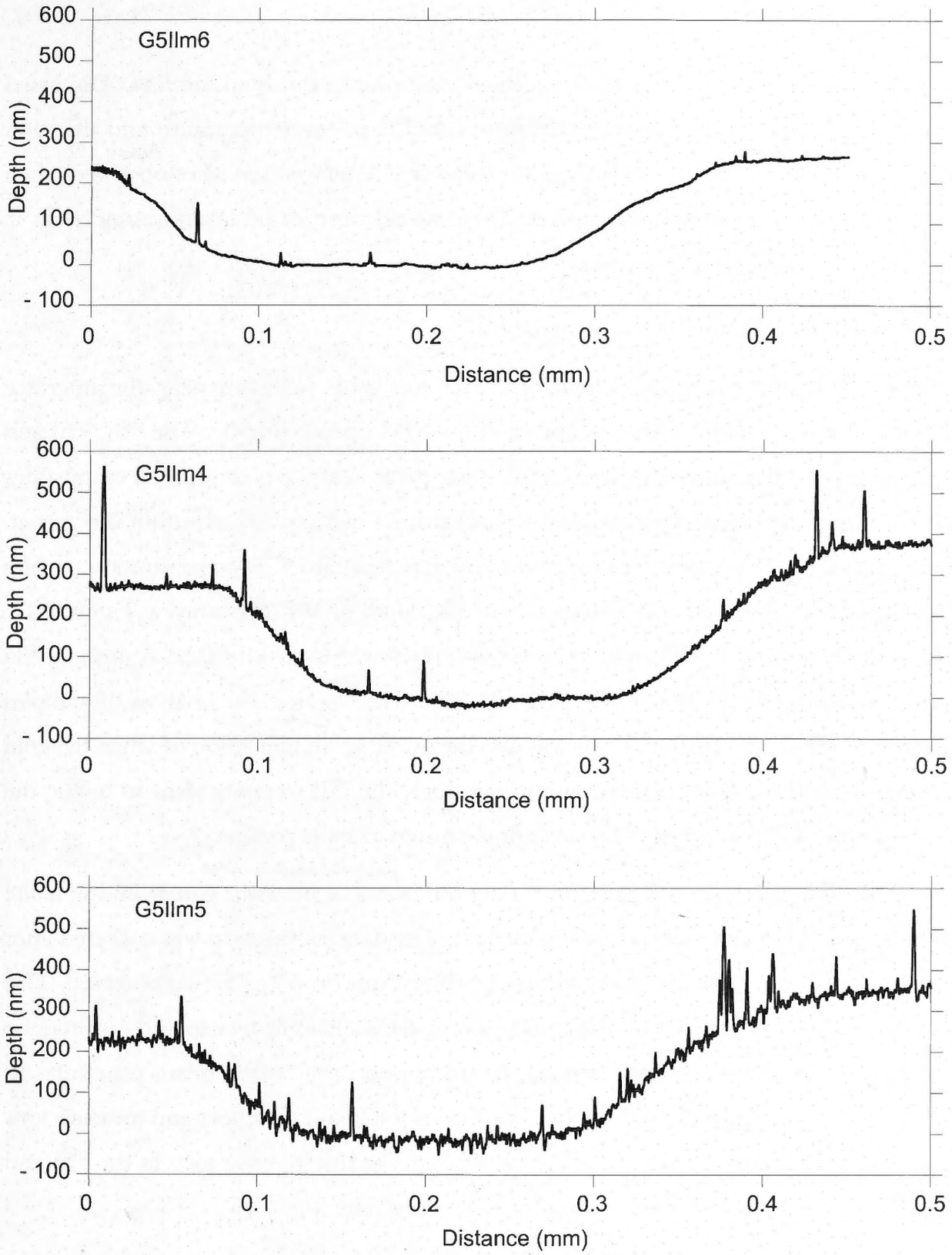

Figure 3.11: Measured analysis pits obtained from the profilometer for samples G5Ilm4, G5Ilm5 and G5Ilm6.

3.6 Discussion

This set of experiments failed to produce measurable diffusion profiles. Discussed below are possible impediments to diffusion other than the temperature and duration of the experiments. Also discussed are the analytical artefacts that were observed when traversing the ilmenite-garnet interface. These would need to be taken into account if further experiments were to be run.

3.6.1 Depth Resolution at the Interface

Features that are attributed to analytical artefacts were observed near the interface between the ilmenite thin film and garnet in the SIMS depth profiles. The ^{28}Si, ^{27}Al and ^{40}Ca counts increase towards the interface then there is a sharp drop in all count rates followed by a rise before flattening out to background concentrations within the garnet. To highlight the effects that are observed in the ilmenite thin film, concentration profiles showing only the ilmenite thin film section of the depth profile are shown in Figure 3.12. The count rates for ^{28}Si, ^{27}Al and ^{40}Ca rise steadily towards the interface. A drop in ^{48}Ti counts is also apparent as the ^{28}Si, ^{27}Al and ^{40}Ca starts to rise. For analysis of samples G5Ilm4, G5Ilm5 and G5Ilm6 ^{197}Au was also measured as an indication of when the gold coating on the sample is removed and interestingly the ^{197}Au counts seem to mimic the profile forms of ^{28}Si and ^{27}Al (^{40}Ca was not measured in these profiles).

The elemental concentration map for ^{48}Ti at the interface between garnet and ilmenite for experiment G5Ilm1 is shown in Figure 3.13. The data for the map was collected after using the ion beam to drill to the interface, where a sharp drop in ^{48}Ti was observed. This concentration map indicates that although part of the pit has garnet exposed the ilmenite layer has not been completely removed. It also appears that as the beam penetrates to the garnet substrate the charging behaviour causes the beam to deflect and measure ions from the surface surrounding the pit. This effect may cause the rise seen in the ^{28}Si and ^{27}Al as it accounts for the mimicry by the ^{197}Au count rate.

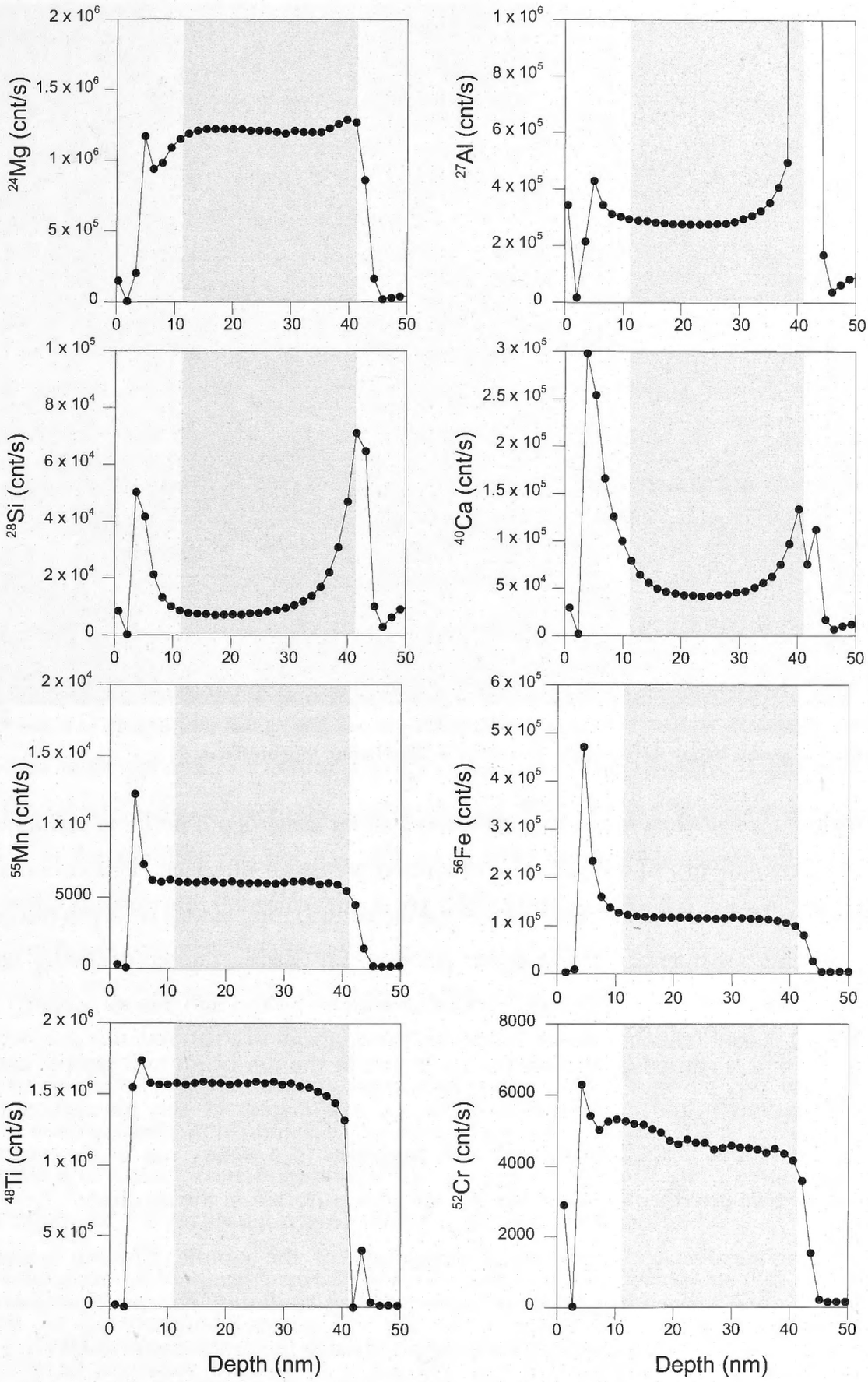

Figure 3.12: Concentration profiles for ^{27}Al, ^{28}Si, ^{52}Cr, ^{40}Ca, ^{55}Mn, ^{56}Fe, ^{24}Mg, ^{48}Ti within the ilmenite thin film (shaded area) of experiment G5Ilm1. The elements ^{40}Ca, ^{28}Si and ^{27}Al have high concentration in garnet and ^{52}Cr, ^{48}Ti and ^{55}Mn have relatively high concentrations in the ilmenite.

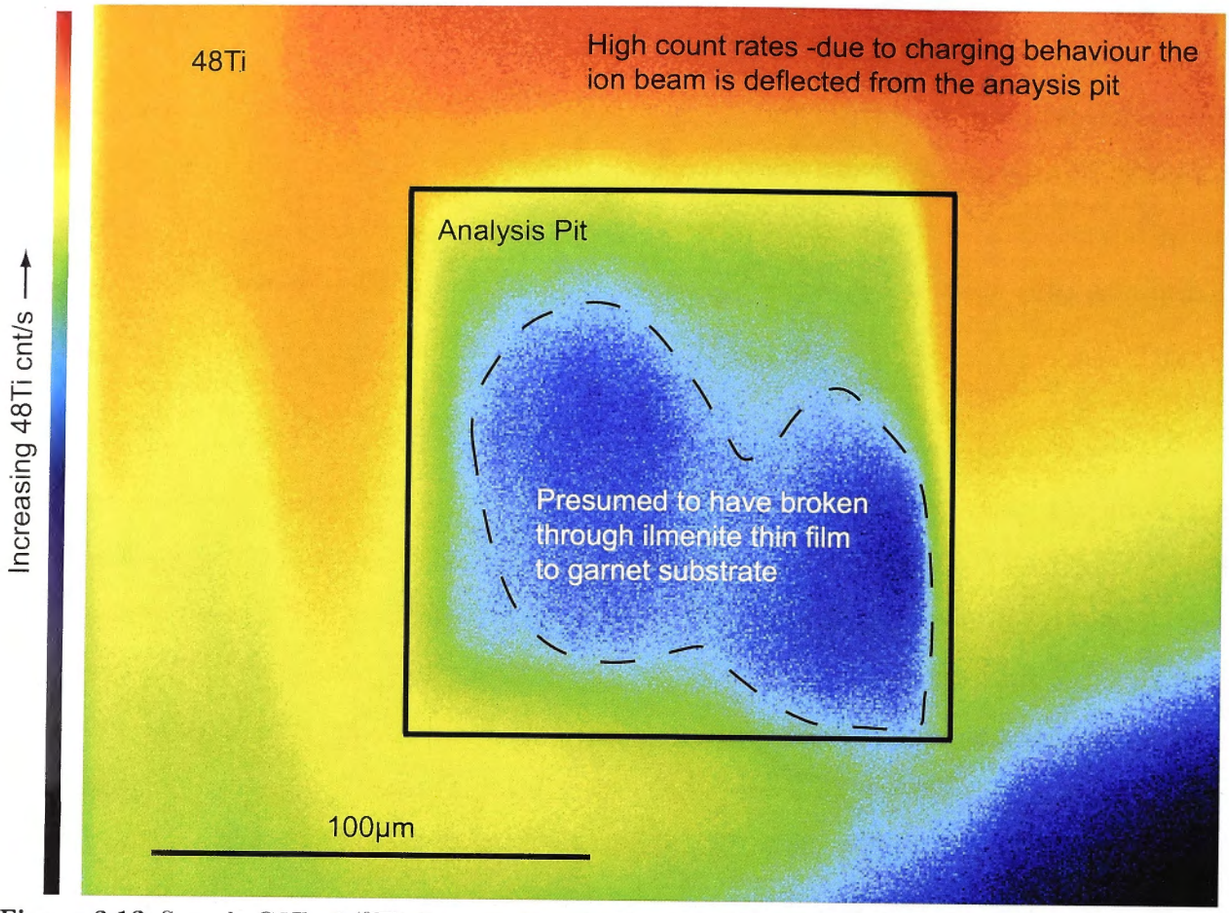

Figure 3.13: Sample G5Ilm1 ^{48}Ti element map of a depth profiling pit that was terminated as the ^{28}Si, ^{27}Al and ^{40}Ca counts began to rise in the ilmenite thin film before the interface.

The main concern when measuring diffusion profiles using depth profiling techniques is the depth resolution, in particular the resolution across an interface. This concern was addressed by Hofmann (2004) who quantified the contributing factors of depth resolution when crossing an interface using depth profiling on SIMS. The contributing factors outlined in the study are atomic mixing, surface roughness and information depth.

Atomic mixing is caused by the interaction between the ion beam and sample causing recoil implantation and cascade mixing. For an explanation of this phenomenon see Magee and Honig (1982). This interaction manifests in a steady rise in concentration towards the true interface for elements of high concentration in the substrate.

Surface roughness relates to the initial topography of the sample. The ion beam will accentuate initial surface roughness as depth profiling continues. For the experiments in this study profiles across analysis pits were obtained using the profilometer at UWS. These are shown in Figure 3.11 for samples G5Ilm4, G5Ilm5 and G5Ilm6. The profilometer results give an indication that the experiments conducted at higher temperatures have a slight increase in topographic variation.

Information depth is the mean depth from which the ions are escaping from the sample and thus being analysed. The information depth for SIMS is low (Hofmann, 2004) making atomic mixing the dominant variable when determining depth resolution. For further discussion on the depth resolution across an interface using SIMS depth profiling see Hofmann (2004).

The elements that are seen to increase towards the interface ^{28}Si, ^{27}Al and ^{40}Ca (Fig. 3.12) in these samples are also the elements that have orders of magnitude higher concentrations in the garnet. Similar peaks approaching an interface have also been observed in previous SIMS analysis, for example the study of Hofmann and Schubert (1998). In their study the steady rise towards the true interface is largely attributed to atomic mixing. However, if the peak observed in this study was purely due to atomic mixing ^{48}Ti counts should decrease at roughly the same rate as the rise in ^{28}Si, ^{27}Al and ^{40}Ca counts.

An equivalent concentration profile to an atomic mixing profile would be obtained if the beam approaching the interface analyses the garnet before the ilmenite thin film has been completely sputtered away. Topographical variations of the analysis pit will accentuate this feature. For samples analysed in this study the topographical variations have been shown to be on the order of 20 nm (Fig. 3.11). Elemental mapping of a depth profile pit that was terminated just before the interface as the ^{28}Si, ^{27}Al and ^{40}Ca were rising shows a slope in the profiling pit that has half broken through to the garnet and the other half is still the ilmenite thin film (Fig. 3.13). This scenario still does not account for the ^{48}Ti counts not dropping significantly. However, it is possible that the difference in the decrease in ^{28}Si, ^{27}Al and ^{40}Ca and compared to only a slight increase in ^{48}Ti could be attributed to the difference in ionization efficiency of these elements. That is the ratio of the ions produced to the number of bombarding ions used. There are also several other factors that may have contributed to the artefacts at the interface. These include but are not limited to surface contamination of the sample, charging of the analysed area and the hardness of the garnet substrate relative to the ilmenite thin film.

Contamination of the garnet surface is unlikely due to the precautions that were taken during the experimental process. The garnets were polished with colloidal silica and placed in an ultrasonic bath for cleaning. The garnet cubes are then heated to 400 °C for 15 minutes to remove any moisture from the surface before deposition. Although, if the polishing process was the source of contamination a strong peak of ^{28}Si would be expected but the mimicry of the ^{40}Ca and ^{27}Al concentration profiles would not be.

The sharp drop in counts after the interface (Fig. 3.9) is related to the sample charging briefly before the e-gun is able to balance the charge. As charging was solely a problem within the garnet substrate due to the low conductivity of garnet this is a difficult situation to prevent when using a positive ion beam. After this drop a steady state within the garnet is recovered after approximately 50 nm, which is the slow rise after the interface seen in the profiles. This affects all of the elements count rates but given the recovery, after 50 nm, measurement of diffusion profiles is still possible, especially as the intention was to produce profiles on the order of 1 μm. This issue was resolved by using O^{2-} primary ion beam for analysis and this feature is not observed in profiles obtained using an O^{2-} primary ion beam (Fig. 3.10).

Another consideration is the difference in beam-sample interactions between the two phases due to the respective atomic structures of garnet and ilmenite. This is observed in the difference in sputtering rate between the ilmenite and garnet. The sputtering rate in the garnet is slower therefore ions do not penetrate the garnet as easily. This may relate to the relative hardness of garnet compared to ilmenite. At the interface this difference in hardness between the thin film and garnet can cause the primary ions to bounce off the surface instead of penetrating the garnet causing more damage in the ilmenite layer and increasing the count rate. This could explain why the ^{48}Ti and other cations with high concentrations in the ilmenite do not drop off markedly because this artefact is counteracting the drop in counts that would be expected from atomic mixing.

3.6.2 Thin Film Analysis

The thin film is deposited as an amorphous layer with a composition matching the target material by the process described in Section 3.3.1. However, during the annealing process the thin film develops a polycrystalline nature. In a study by Dohmen et al. (2008) the evolution of this texture in an olivine thin film was documented by scanning electron microscopy (SEM) analysis. At 900 °C they found that after 15 minutes the film re-crystallized with 10 to 100 nm grain size and with further annealing grain growth continues until an equilibrium texture is reached. This change from amorphous to a polycrystalline nature of the thin film changes the way the ion beam interacts with the sample and could be a possible explanation for the apparent change in concentrations of some of the elements between the annealed and unannealed samples as well as change

in the position of the interface. Rather than being actual concentration changes they are a reflection of the susceptibility of the sample to sputtering. Despite this change in the ilmenite thin film between the control and experiments, the control sample still provides an adequate standard as the sputtering conditions of garnet between the unannealed and annealed samples remains the same.

^{28}Si and ^{27}Al concentrations are observed in the ilmenite thin film for the control samples as well as the experiments. The EPMA analysis of both the ilmenite targets shows no Si and only trace amounts of Al. However, preferential sputtering of ^{28}Si and ^{27}Al in SIMS analysis may cause the concentrations of these elements to be exaggerated and actual concentrations may not be that high. Still, the measured concentrations mean that the thin film is contaminated during deposition of the film. This may be from small inclusions within the ilmenite target or contamination from residue within the vacuum chamber of the PLD set-up.

Before progressing further with these experiments the Si and Al contamination in the thin film needs to be addressed. Further investigation of this phenomenon was not carried out in this study due to time constraints. However, it would be useful to analyse the targets using a different analytical technique, such as XRF, to see if they show Si and Al concentrations. This would give an indication as to whether micro-inclusions in the target material are causing the contamination or if it is from another source. A way around the contamination of thin film from the natural targets would be to synthetically produce a pure ilmenite target from component powders.

3.6.3 Constraints on the Rates of Diffusional Processes

Taking into account the spatial resolution of the SIMS across the boundary between garnet and ilmenite it is possible that diffusion did occur in these experiments but on a smaller scale than we can measure accurately. For example experiments G5Ilm4 and G5ilm5 show possible diffusion profiles that are shorter than 100 nm. A possibility for the lack of measurable diffusion profiles is that the interface between the ilmenite thin-film and garnet hindered diffusion. This could have occurred due to the formation of an intermediate phase at the boundary. Although, the surface roughness indicated by the profilometer measurements does not give evidence for a surface reaction occurring during the experiments. There is also no evidence in the SIMS analytical results of the

formation of a different phase at the interface that would cause a barrier for diffusion. The change of state of the ilmenite thin film, from amorphous to polycrystalline, may have also impeded the exchange reaction.

Despite the null result of these experiments a constraint can be placed on the effect the partitioning has on the rate of diffusion in this system. Taking into account the depth resolution across the interface, if diffusion was faster, profiles longer than 100 nm would have been observed. Therefore a maximum constraint can be placed on the effect the partitioning has on the rate of diffusion by calculating the diffusion coefficient for a 100 nm diffusion profile had one been produced from experiments. For one-dimensional diffusion this length scale is approximately equal to $2\sqrt{Dt}$ from this D can be determined. In Figure 3.14 this maximum constraint is compared to the experimental data of Chakraborty and Ganguly (1992). It shows that the diffusivity is at least an order of magnitude slower than previously determined diffusion coefficients.

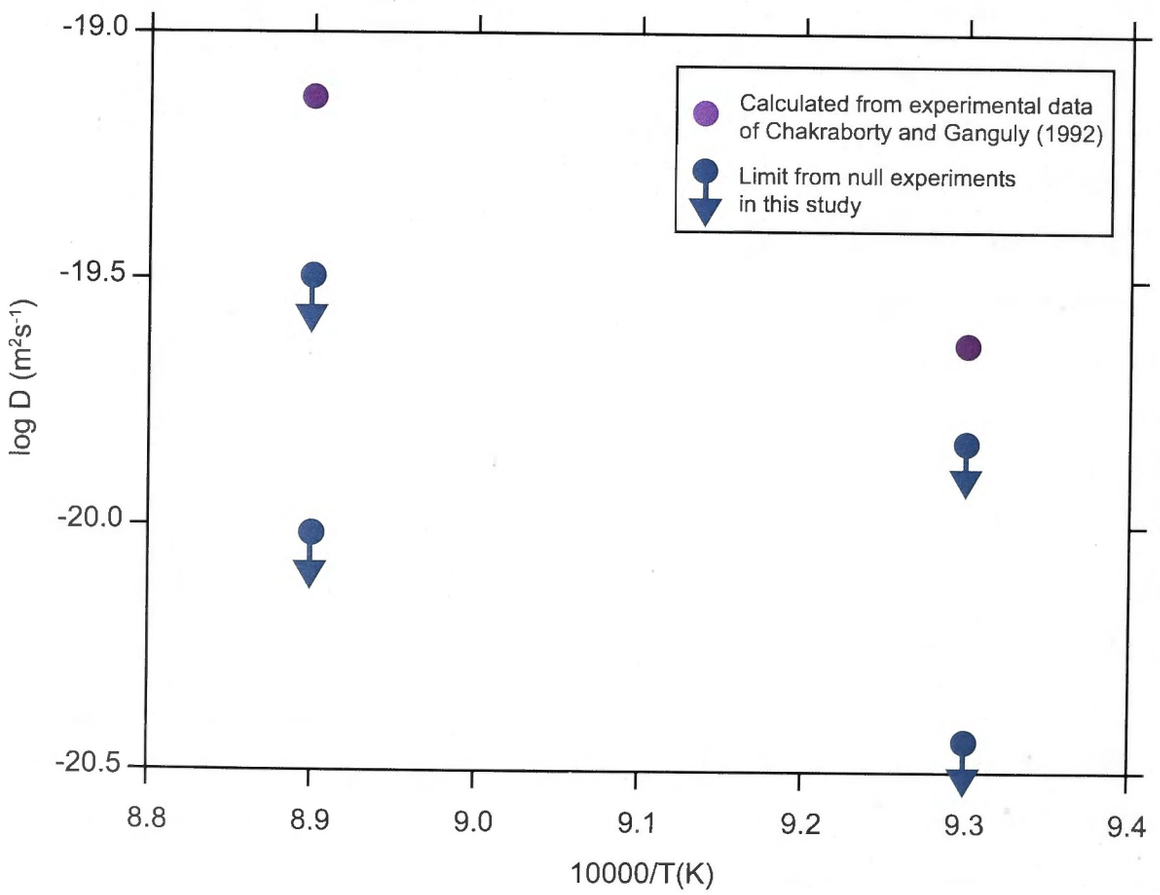

Figure 3.14: Maximum constraint on the rate of diffusion in the garnet-ilmenite system compared to the experimental data of garnet diffusivity from Chakraborty and Ganguly (1992).

Further, since possible diffusion profiles were observed in experiments G5Ilm4 and G5ilm5 that were approximately 50 nm in length it is possible to place minimum limit on the diffusivity as well as a maximum. A diffusion profile of 50 nm would indicate that the inferred diffusivity of garnet is no more than two orders of magnitude slower when compared to the extrapolated diffusivity from the experimental data of Chakraborty and Ganguly (1992). As described by the following:

$$-2 < \log_{10}(D/D') < -1$$

Where D is the estimated diffusivity from these experiments and D′ is the diffusivity extrapolated from the diffusion parameters of Chakraborty and Ganguly (1992).

3.7 Conclusions

Quantifying the rates of diffusional processes in the garnet-ilmenite system at temperatures of 800 and 850 °C would better constrain the diffusion parameters of garnet and aid in the development of a garnet-ilmenite diffusion model. This study developed the experimental procedure for producing diffusion profiles within garnet from an ilmenite diffusant source that allows experiments to be run at lower temperatures and/or for shorter durations. It has been shown that this method could be viable for determining rates of diffusion in the garnet-ilmenite system. However, in order to produce diffusion profiles of a measurable length and accurately quantify the rate slight modifications to the method used in this study would be required. Most importantly experiments would require longer annealing times and a synthetic ilmenite target should be used for producing the thin films to avoid contamination. Nevertheless the null result of these experiments allows a maximum and minimum constraint to be placed on the rate of diffusion at these temperatures. The experiments show that the diffusivity is at least one order of magnitude slower compared to the diffusivity extrapolated to these temperatures from previously determined garnet diffusion parameters (Chakraborty and Ganguly, 1992), but is no more than two orders of magnitude slower. However this minimum constraint relies on the profiles observed in G5Ilm4 and G5ilm5 being the result of diffusional processes and not analytical artefacts or error in the measurement process.

CHAPTER 4

Element Concentration Profiles Surrounding Ilmenite Inclusions in Garnet from the Barrovian Metamorphic Sequence in Scotland

Preface

The samples analysed in this study were collected by Dr Daniel Viete. The samples were analysed by electron probe microanalysis at RSES, ANU with the assistance of Dr Robert Rapp. NanoSIMS analysis was undertaken at the Centre for Microscopy, Characterization and Analysis (CMCA) at the University of Western Australia (UWA) with assistance from Associate Professor Matt Kilburn for analysis and preparation of samples. The NanoSIMS analytical work for this research was funded through the Travel and Access Program of the Australian Microscopy and Microanalysis Research Facility (AMMRF). All other funding for this study was provided by RSES, ANU and ARC Discovery Grant DP0877274 "Tectonic mode switches and the nature of orogenesis".

4.0 Synopsis

Samples from the Barrovian metamorphic sequence in Scotland provide possible evidence for diffusional features, namely Mn concentration profiles surrounding ilmenite inclusions within sillimanite grade garnets. If the concentration gradients can be attributed to diffusional processes then the quadratic relation between the length of diffusion profiles and the duration over which the profiles were produced can be utilised. This system provides an independent method for determining the duration over which diffusional processes are effective in garnet and can be correlated with grain-scale diffusion. This would provide a solution to the obstacle of differentiating between growth zoning profiles and subsequent grain-scale diffusion in garnet. However, current spatial resolution for common analytical techniques makes separating diffusional features from analytical artefacts difficult. In particular, the results from electron probe microanalysis show concentration profiles of Ti in garnet that are longer than the observed features in the Mn concentration profiles. These Ti concentration profiles have been determined to be a result of secondary fluorescence. Additionally, garnet-ilmenite geothermometry carried out in this study to determine the peak temperatures of these samples recorded temperatures consistent with previous estimates for low grade samples but gave unrealistic temperatures for the samples above staurolite grade. This result may be partly attributed to the low Mn concentrations in garnet and ilmenite in these samples but there is also evidence of retrograde reactions occurring, which would effect the partitioning between garnet and ilmenite and thus affects the applicability of the garnet-ilmenite geothermometer. Further proof of this phenomenon occurring in natural samples is required before applying the garnet-ilmenite system to diffusion modelling.

4.1 Introduction

The technique of garnet diffusion modelling can be used to determine timescales associated with metamorphism. This technique is based on forward modelling of the diffusion of major elements within garnet during thermal events with respect to initial concentration profiles. Concentration profiles in garnet are initially zoned as a result of the changing availability of elements as the garnet is growing. This process can be described by Rayleigh fractionation and produces bell-shaped concentration profiles of Mn, Fe, Mg and Ca in garnet. It has been shown by several studies (Anderson, 1977; Woodsworth, 1977; Yardley, 1977) that with increasing metamorphic grade these bell-shaped concentration profiles are lost. This has been attributed to diffusive modification to the original growth zoning profiles. To quantitatively forward model the effect of this process an initial concentration profile must be input. However, it is often difficult to differentiate between growth zoning profiles and the effect of subsequent grain-scale diffusion.

To advance, a technique that provides independent constraints on the duration over which diffusional processes are effective within garnet is required. The garnet-ilmenite system offers such a method. In the garnet-ilmenite system, as temperature changes during a thermal event, Fe and Mn are exchanged at the interface between garnet and ilmenite. This partitioning has been well-constrained and is highly sensitive to temperature (Pownceby et al., 1987). The partitioning behaviour causes a change in concentration of Fe and Mn at the interface between garnet and ilmenite and diffusion within the phases acts to re-distribute the concentration gradient that has been produced. Ilmenite diffusion is relatively fast and any concentration changes are quickly eliminated. However, as garnet diffusion is relatively slow, this process can leave stranded diffusion profiles in garnet surrounding ilmenite inclusions. If evidence for these diffusion profiles can be found in natural samples forward modelling of the partitioning and diffusion in this system can be used to constrain the duration of the thermal event associated with metamorphism. Durations determined from a garnet-ilmenite diffusion model can be correlated with results from a grain-scale garnet diffusion model to further constrain the duration of thermal events. Observation and measurement of these diffusion profiles in natural samples is an important step in evaluating whether this method can be applied and over what temperature and pressure range it may be useful.

Samples from the Barrovian metamorphic sequence in Scotland were chosen to investigate this system in natural samples. It is the type locality of Barrovian Metamorphism and there has been extensive work already undertaken in the area to determine peak metamorphic conditions (e.g. Harte and Hudson, 1979; Beddoe-Stephens, 1990; Viete, 2009). Therefore, the pressure and temperature of metamorphism are well constrained. Also, the samples from the Barrovian metamorphic sequence in Scotland have been previously examined for diffusional modification to growth zoning profiles of major elements in garnet across metamorphic grades (Viete et al., 2011b) and diffusion modelling has been carried out on Sr diffusion in apatite (Ague and Baxter, 2007). However, the durations determined in these studies are an order of magnitude apart. If diffusion modelling of the garnet-ilmenite system could be utilised for these samples it would provide further insights into the durations of thermal activity that can be associated with the formation of the Barrovian metamorphic sequence.

In this study electron probe microanalysis (EPMA) was used to measure concentration profiles across ilmenite inclusions and into the surrounding garnet. There was also an attempt made to image the distribution of elements surrounding ilmenite inclusions within garnet using the Cameca NanoSIMS 50 (nanoscale secondary ion mass spectrometer) to determine if diffusional features are evident on a smaller scale.

4.2 The Grampian Orogenic Event and Barrovian Metamorphism

During the Grampian orogenic event the Dalradian sediments were metamorphosed, which produced the Barrovian metamorphic sequence and the Buchan metamorphic sequence in the northeast of Scotland (Figure 4.1a). Detailed structural mapping (Fettes, 1986) and previous geochronology (Oliver et al., 2008) indicates that the Buchan and Barrovian metamorphism occurred during a single event, with peak metamorphism at *c.* 470 Ma (e.g. Oliver et al., 2000). Although, complicated patterns in the metamorphic isograds have been produced from syn-metamorphic and post-metamorphic folding (Chinner, 1966).

The Barrovian metamorphic sequence at Glen Clova in the east of Scotland was first described by Barrow (1893). The metamorphic zones in the Barrovian sequence are characterised by presence of indicator minerals biotite, garnet, staurolite, kyanite and

sillimanite. The approximate peak temperatures and pressures for the metamorphic zones of the Barrovian sequence determined from THERMOCALC by Viete (2009) are listed in Table 4.1.

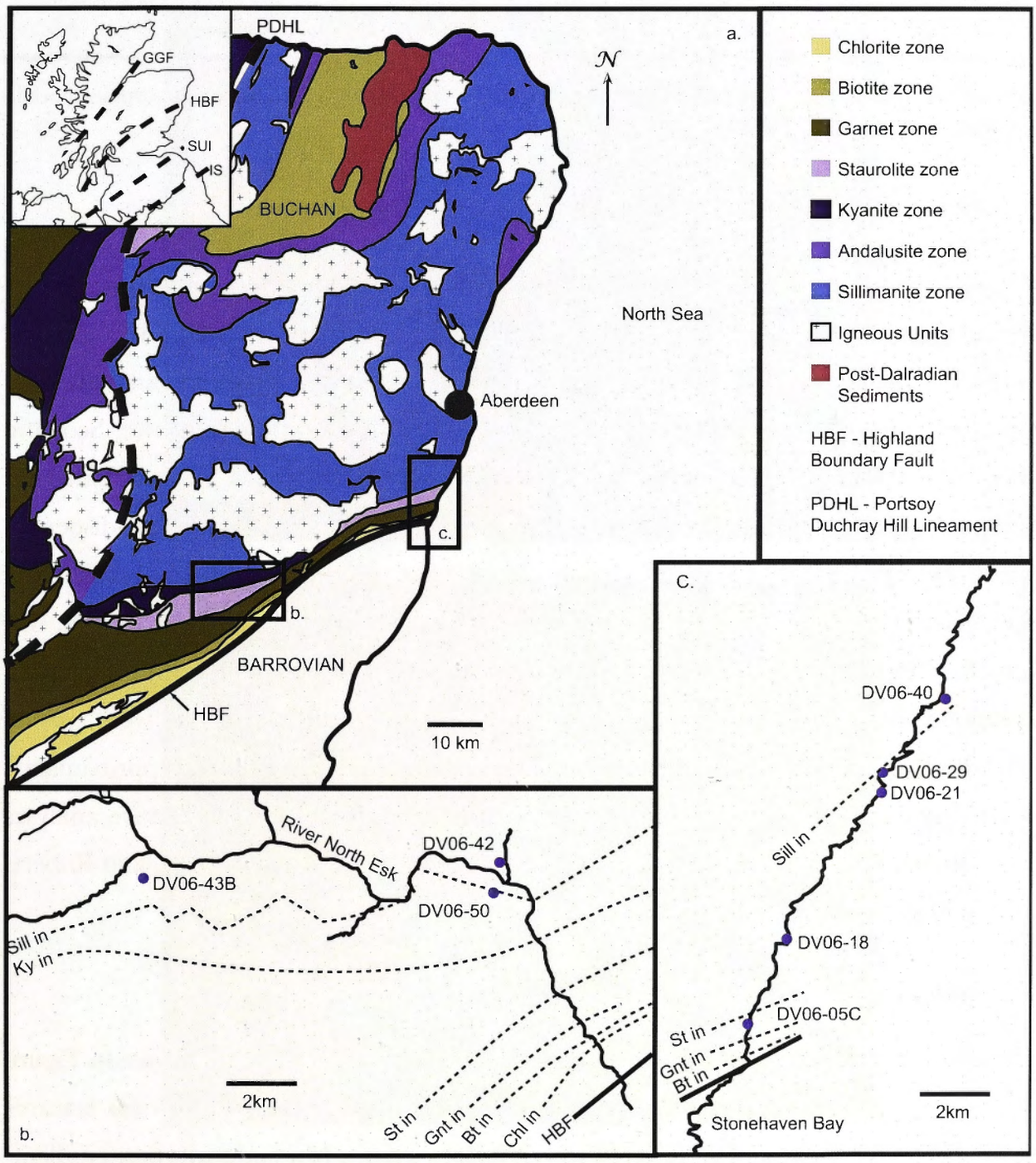

Figure 4.1: (a) Map of metamorphic zones in Scotland, showing the Barrovian and Buchan metamorphic sequence and major faults that bound the Grampian Terrane, HBF: Highland Boundary Fault, GGF: Great Glen Fault, PDHL: Portsoy Duchray Hill lineament (Fettes, 1986) SUF: Southern Uplands Fault IS: Iapetus Suture. (b) Glen Esk transect and (c) Stonehaven transect, with sample localities labelled. (Figure modified from Viete, 2009).

Metamorphic zone	T (°C)	P (kbar)
Biotite	400	2.0
Garnet	500	3.3
Staurolite	580	5.5
Sillimanite	640	5.8

Table 4.1: Approximate peak temperatures and pressures that correspond to the metamorphic zones in the Barrovian sequence, Scotland (Viete, 2008).

4.3 Electron Probe Microanalysis

Profiles across the garnet-ilmenite interface and major element composition maps of ilmenite inclusions within garnet were carried out using the Cameca SX100 electron probe microanalyser (EPMA) at RSES, ANU. Garnets were selected for analysis from thin sections of samples collected from the Barrovian metamorphic sequence, Scotland (Fig. 4.1). Ilmenite inclusions within the garnet were selected for analysis based on size and absence of fractures. Analyses were performed using wavelength-dispersive spectrometers (WDS). Qualitative count maps were produced with an accelerating voltage of 15 keV and a 40 nA beam current. Counts were collected for Ca, Ti, Mn and Fe. Maps were quantified by point analyses performed with the same operating conditions and compared to natural standards. Traverses across ilmenite were carried out with the same conditions as the maps. The point analyses were spaced approximately 1 μm apart and with a dwell time of 210 seconds on each point. Quantitative analyses were obtained for Na, Mg, Al, Si, K, Mn, Fe, Ca and Ti. Standards of TiO_2 and Roberts Victor Mine (RVM) garnet were used.

4.3.1 Results

Quantitative EPMA Mn maps for samples DV06-18 and DV06-50 are shown in Figure 4.2. Sample DV06-18 from the staurolite zone shows no sign of diffusional features surrounding the ilmenite inclusion, however, it does show a Mn concentration gradient. This gradient is likely to be related to grain-scale zoning of the garnet. Sample DV06-50 from the sillimanite zone also shows grain-scale zoning as well as unusual asymmetric zoning surrounding the ilmenite inclusion. It has been inferred that the asymmetry of this feature is an analytical artefact, possibly due to the orientation of the ilmenite grain

boundary with respect to the garnet. If the grain boundary is at a shallow angle, when analysed, the garnet beneath is included in the excitation volume of the sample and the concentration map appears to show the Mn concentration increase in the ilmenite rather than in the garnet.

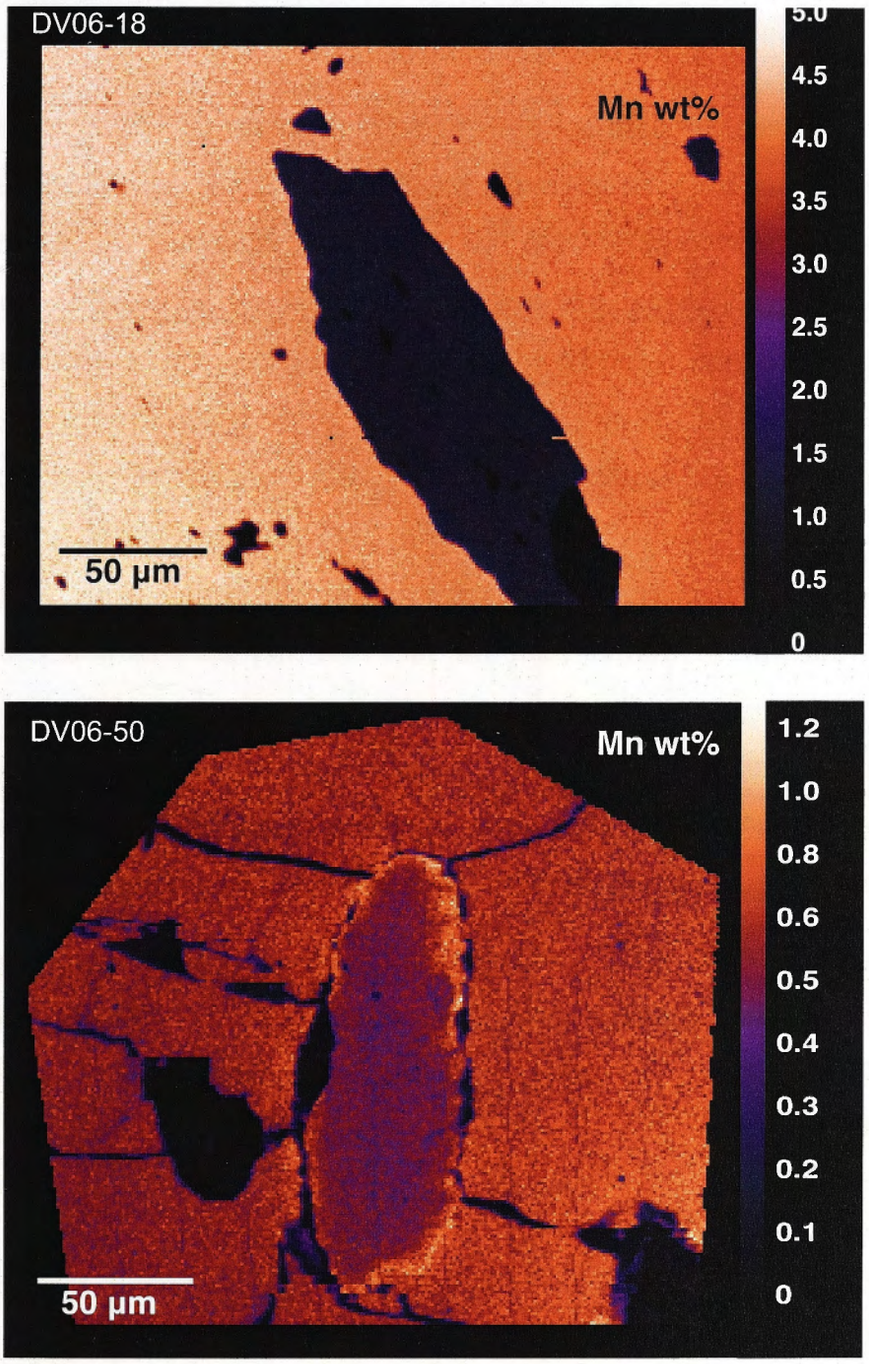

Figure 4.2: Mn element concentration maps of ilmenite inclusions in garnet from samples DV06-18 and DV06-50 from the staurolite and sillimanite zones, respectively.

The transects across ilmenite inclusions are shown for samples DV06-18 from the staurolite zone and DV06-50, DV06-42, DV06-40 and DV06-43b from the sillimanite zone with quantitative analyses of Al, Ca, Fe, Mg, Mn and Ti (Figs. 4.3 to 4.7). The ilmenite inclusions analysed from samples DV06-50 and DV06-43b were towards the edge of the garnet whereas the inclusion in DV06-40 was towards the centre of the garnet crystal.

Sample DV06-42 from the sillimanite zone shows depletion in Mn towards the ilmenite inclusion (Fig. 4.6). The concentration profiles for sample DV06-50, also from the sillimanite zone, are complicated due to cracks that surround the ilmenite inclusion (Fig. 4.4). However, diffusional features in this sample are indicated by a peak in the Mn concentration profiles adjacent to the ilmenite inclusion that decreases away from the inclusion (Fig. 4.4, Mn profile). The opposite trend is observed in the Fe and Mg concentration profiles. In sample DV06-40 (Fig. 4.5) from the sillimanite zone the Mn concentration peaks adjacent to the ilmenite inclusion before decreasing and then increasing again to the background concentration of Mn in the garnet. As these samples are all from within the sillimanite zone the fact that they have exhibited different form in the Mn concentration profiles makes it unlikely that they are diffusion related. The differences may be related to the initial conditions of the sample or may be analytical. The spatial resolution of the EPMA across a grain boundary is diminished and therefore measuring small-scale diffusional features is problematic.

In all of the samples analysed Ti concentration profiles are seen up to 30 μm from the ilmenite grain boundary into the garnet. An example of this Ti concentration profile is shown in Figure 4.8. This is probably due to analytical edge effects and is discussed further in Section 4.6.1.

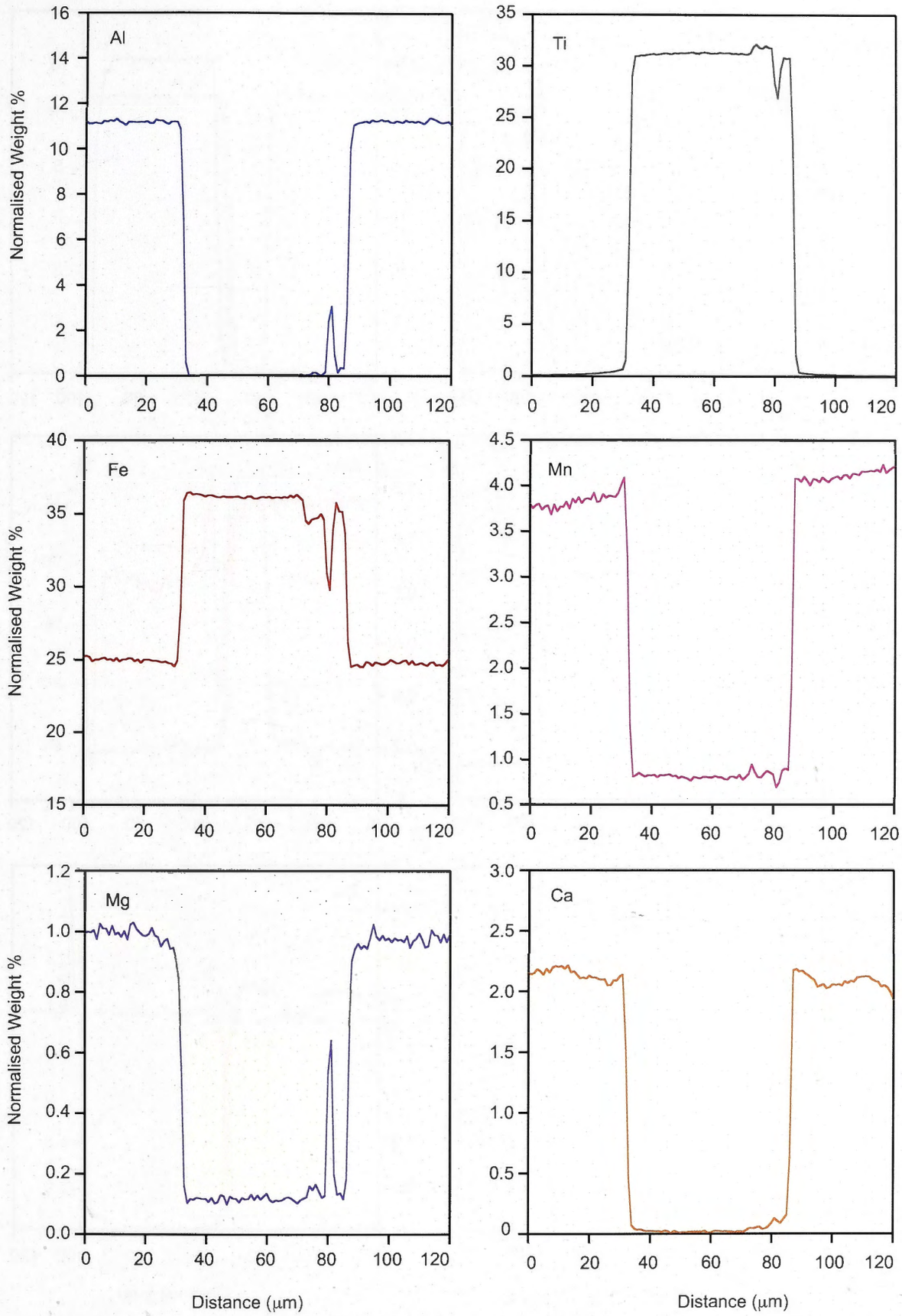

Figure 4.3: EPMA transect for Al, Ca, Fe, Mg, Mn and Ti concentrations across an ilmenite inclusion in garnet from sample DV06-18 from the staurolite zone. The ilmenite inclusion spans from *c.* 35 to 90 μm as shown by high Ti concentrations. Possible garnet growth zoning is evident in the Mn profile.

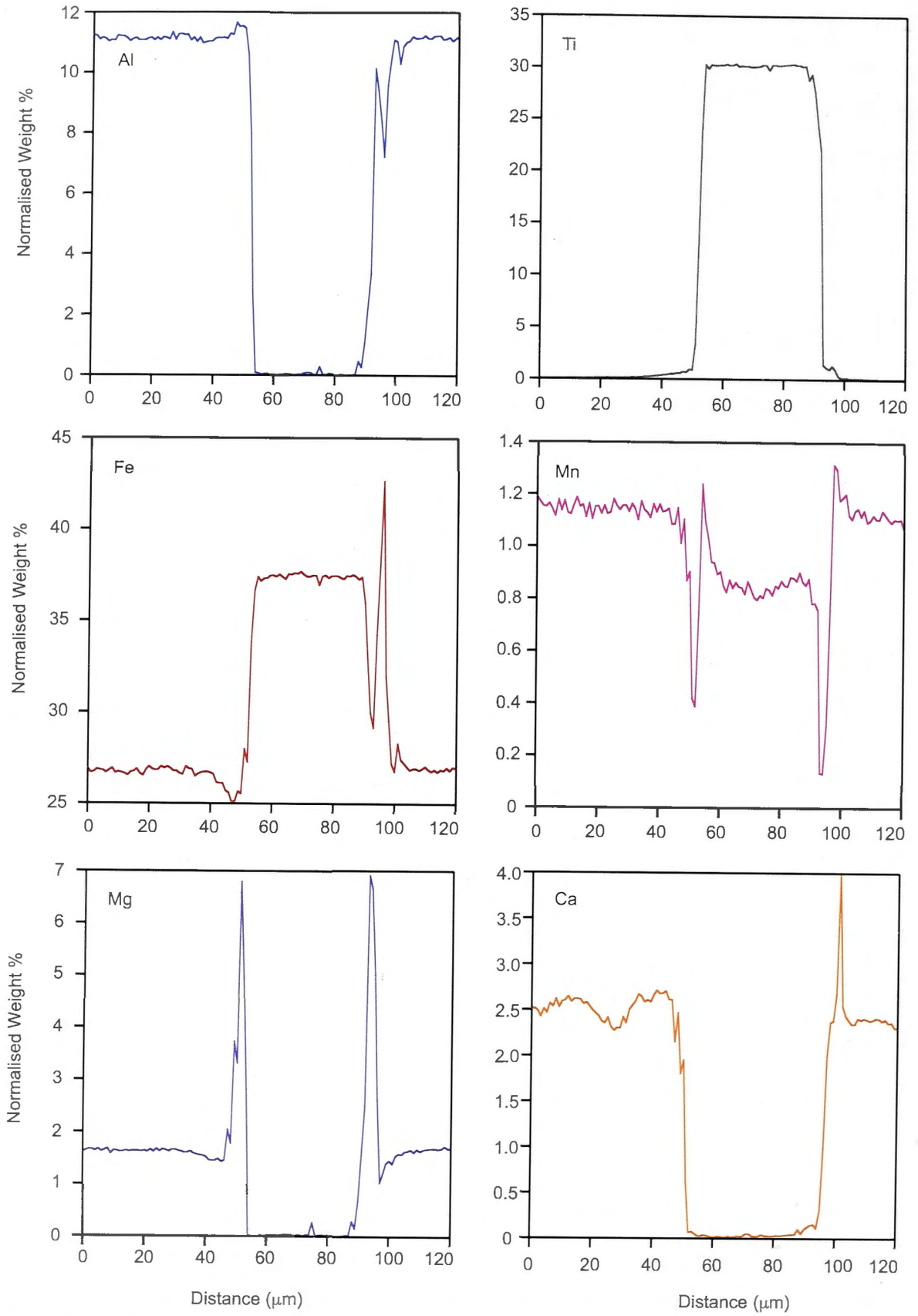

Figure 4.4: EPMA transect showing Al, Ca, Fe, Mg, Mn and Ti concentrations across an ilmenite inclusion in garnet from sample DV06-50 from the sillimanite zone. Ilmenite inclusion spans from *c.* 50 to 90 μm as shown by high Ti concentrations. Sharp peaks and troughs at boundaries may be due to edge effects rather than reflecting actual concentrations.

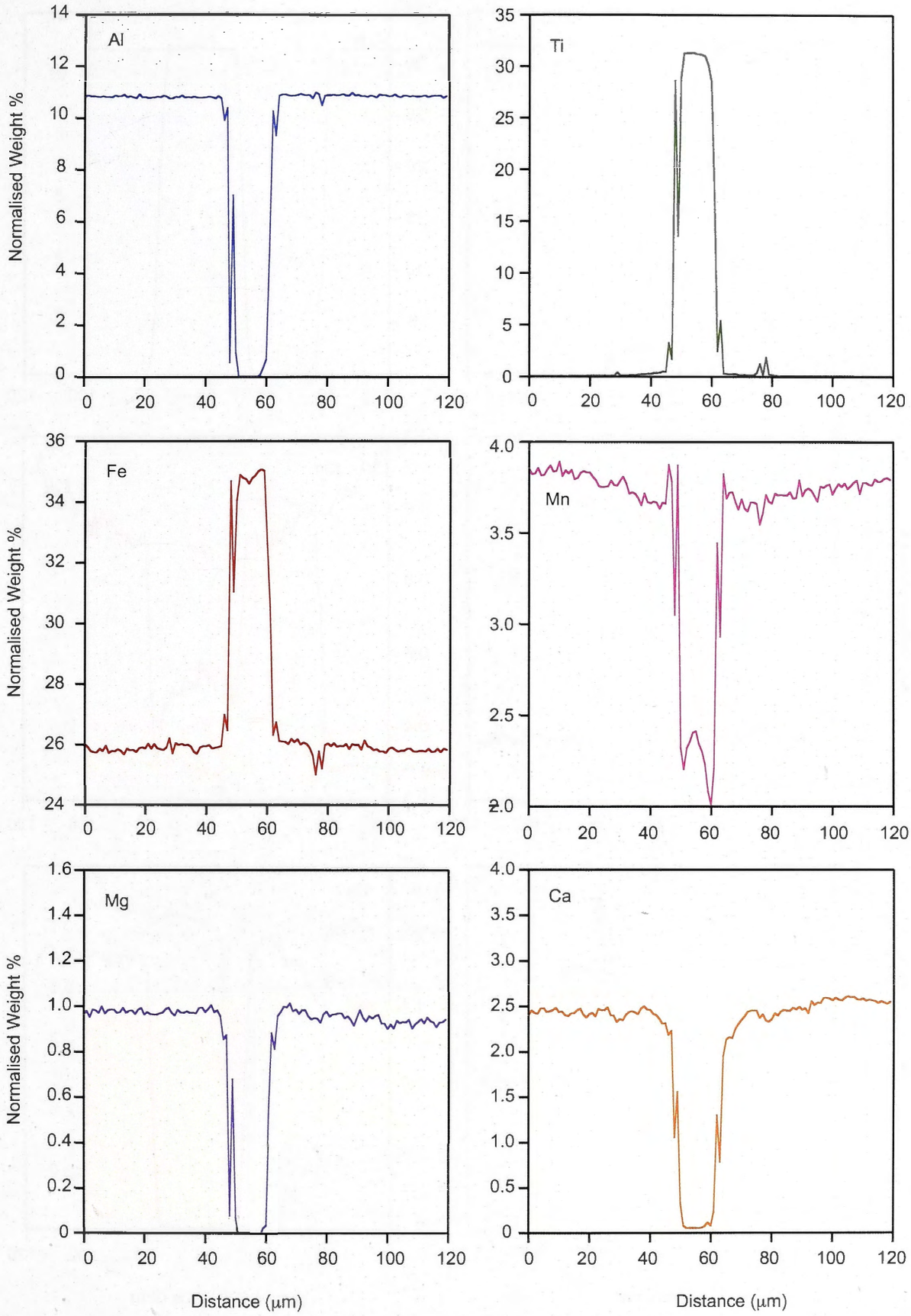

Figure 4.5: EPMA transect of Al, Ca, Fe, Mg, Mn and Ti concentrations across an ilmenite inclusion in garnet from sample DV06-40 from the sillimanite zone. The ilmenite inclusion spans from *c.* 50 to 60 μm as shown by high Ti concentrations. Concentration profiles for Mn show a peak adjacent to the ilmenite inclusion followed by a trough before returning to a steady concentration.

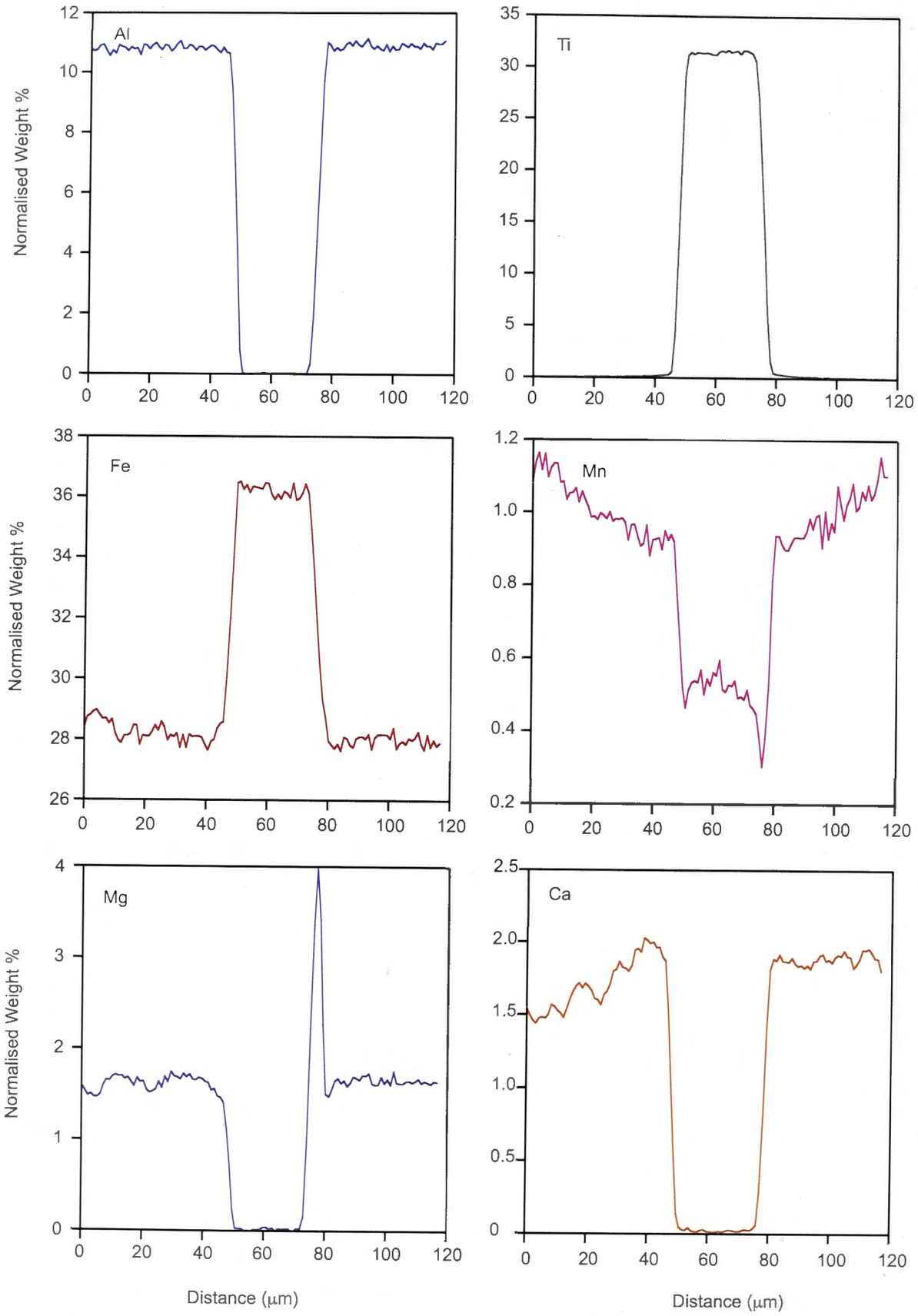

Figure 4.6: EPMA transect of Al, Ca, Fe, Mg, Mn and Ti concentrations across an ilmenite inclusion in garnet from sample DV06-42 from the sillimanite zone. The ilmenite inclusion spans from *c.* 50 to 80 μm as shown by high Ti concentrations. The Mn profile displays decreasing concentration towards the ilmenite inclusion.

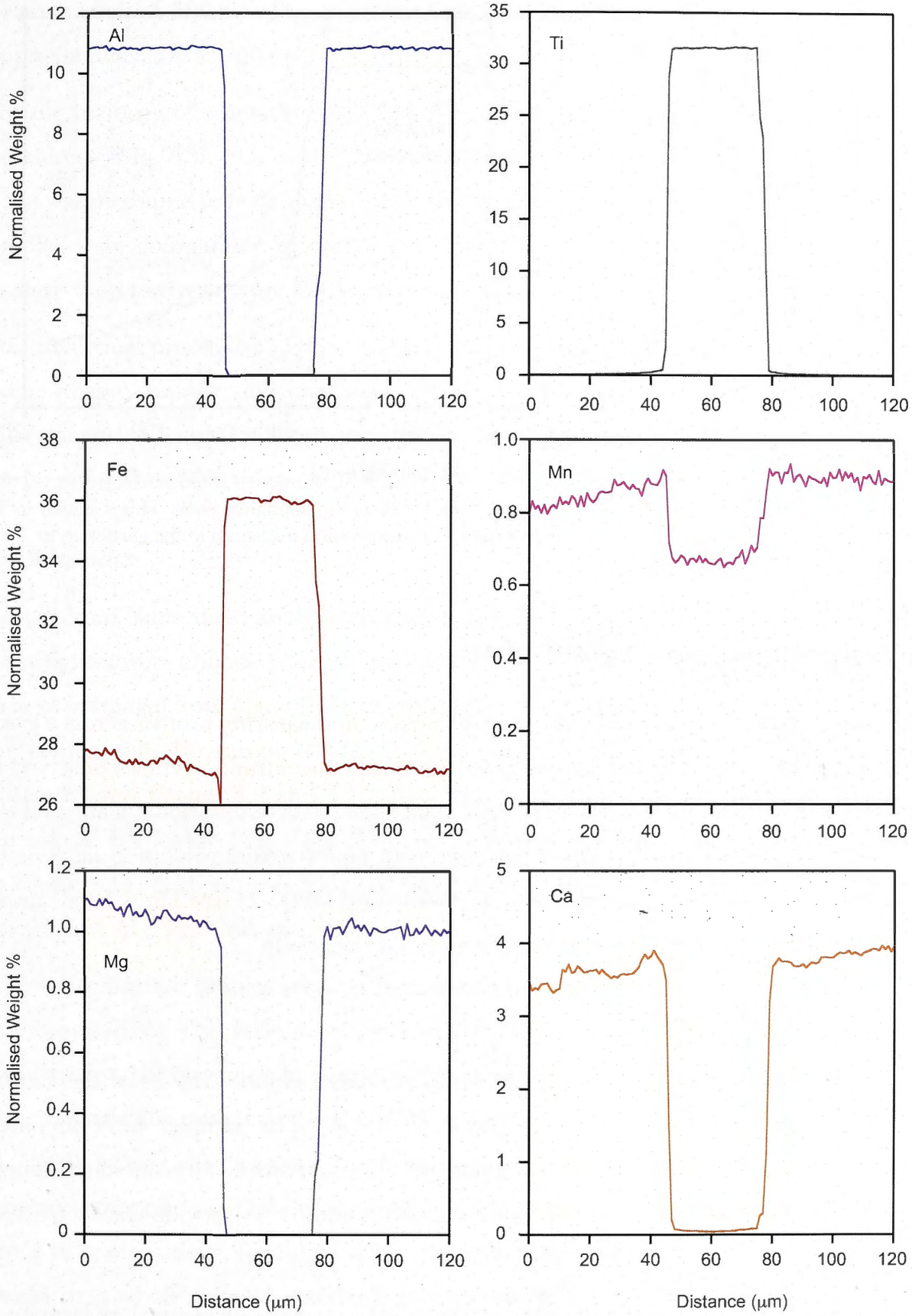

Figure 4.7: EPMA transect of Al, Ca, Fe, Mg, Mn and Ti across an ilmenite inclusion in garnet from sample DV06-43b from the sillimanite zone. The ilmenite inclusion spans from *c.* 50 to 80 μm as shown by high Ti concentrations. Growth zoning in garnet is evident in these profiles.

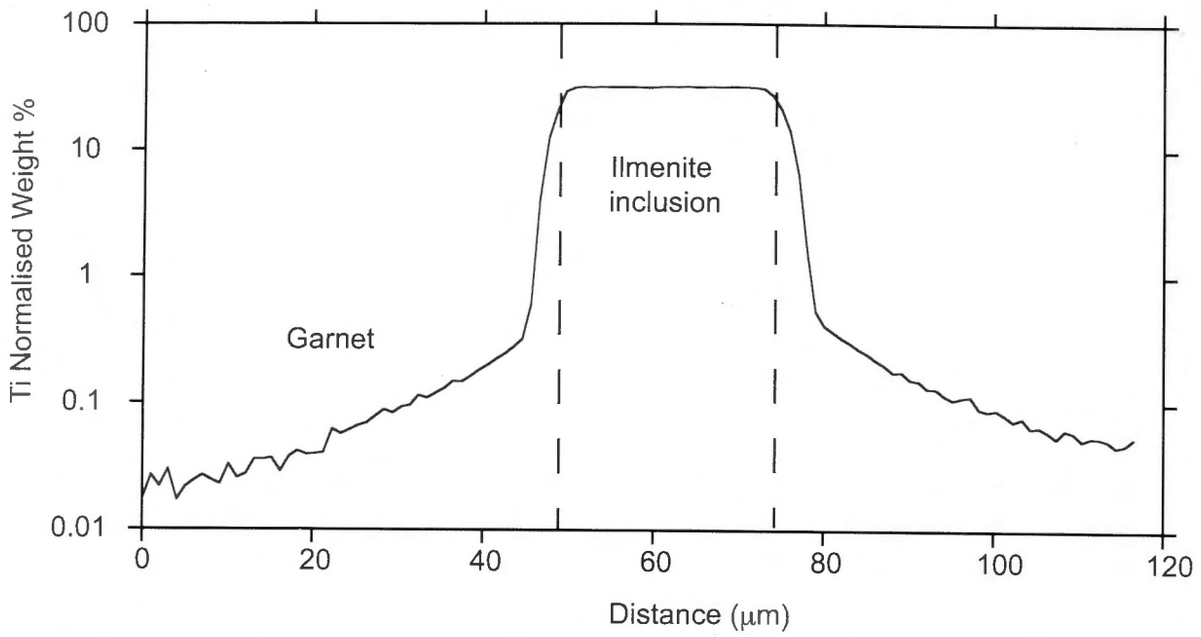

Figure 4.8: Ti concentration profile from sample DV06-42 from the sillimanite zone. This is similar to Ti concentration profiles observed in all transects with a Ti concentration measured in the garnet up to 30 μm away from the ilmenite inclusion.

4.4 Observations from NanoSIMS

The spatial resolution of the EPMA was problematic in measuring profiles across a grain boundary. This was evidenced by the presence of Ti concentration profiles observed in garnet for all samples that were longer than any of the possible diffusional features (Figs. 4.3 to 4.7). In an attempt to obtain traverses with better spatial resolution analysis by NanoSIMS was carried out on samples DV06-43b and DV06-21 (see Fig. 4.1 for sample localities) from the sillimanite and staurolite zones, respectively.

4.4.1 Analytical Technique

Analysis of the samples was carried out on the Cameca NanoSIMS 50 at the Centre for Microscopy, Characterization and Analysis, UWA. The samples were prepared by polishing with colloidal silica and cutting the thin sections to fit a one-inch sample holder. For analysis it was necessary to gold coat the sample to provide conductivity at high voltage.

Bombardment of the samples was carried out with an O^- primary ion beam (duoplasmatron source). The net impact energy was 16 keV. Each analysis area was presputtered prior to analysis by rastering the primary ion beam across the surface to remove contaminants and implant O^- ions into the sample matrix. Presputtering was conducted with a primary

beam current of 300 pA. The spatial resolution of the NanoSIMS at these conditions is approximately 200 to 400 nm.

For the majority of transects ^{27}Al, ^{24}Mg, ^{55}Mn and ^{48}Ti were analysed and one transect measured ^{24}Mg, ^{28}Si, ^{40}Ca and ^{56}Fe. Only four elements could be measured at a time, ^{24}Mg was measured in both analyses for comparison of count rates to ensure the obtained profiles were comparable to each other. Standards were not used in the NanoSIMS analysis therefore results are in counts per second.

Post analytical processing of the images obtained from the NanoSIMS was conducted using image analysis software ImageJ with the Open Multi-isotope Imaging Mass Spectrometry (OpenMIMS) plug-in. The plug-in was developed at the National Resource for Imaging Mass Spectrometry (NRIMS).

4.4.2 Results

Results from NanoSIMS analysis are shown in Figures 4.9 to 4.12. The profiles shown in these figures were obtained directly using the NanoSIMS and also using the OpenMIMS plug-in in ImageJ from NanoSIMS element maps, the profiles from both of these methods are comparable. For sample DV06-21 ^{28}Si, ^{27}Al, ^{48}Ti, ^{56}Fe, ^{55}Mn, ^{24}Mg and ^{40}Ca were measured and Figures 4.9 and 4.10 show the results from a profile taken from ImageJ. For sample DV06-43b ^{27}Al, ^{48}Ti, ^{55}Mn and ^{24}Mg were measured and the profile is shown in Figure 4.11. Both samples analysed showed features adjacent to ilmenite inclusions in garnet for ^{27}Al, ^{56}Fe, ^{55}Mn and ^{24}Mg.

The concentration profiles are shown in counts per second, as standards were not used in these analyses. This is because standards for SIMS are notoriously difficult due to the requirement that they are matrix matched to the samples being analysed. This difficulty is due to matrix effects that are seen in SIMS analysis (e.g. Riciputi et al., 1998; Vielzeuf et al., 2005). Matrix effects are when instrumental mass fractionation occurs due to mineral type and composition. This becomes particularly difficult for garnet as it has such a wide range of compositions. For minerals that form complex solid solutions either a predictive model or a whole suite of standards is required (Riciputi et al., 1998). For this study qualitative determination of the diffusional features in the vicinity of ilmenite inclusions in garnet would be sufficient for proving the phenomenon exists and, once observed, then appropriate standards could be found and quantitative measurements could be acquired.

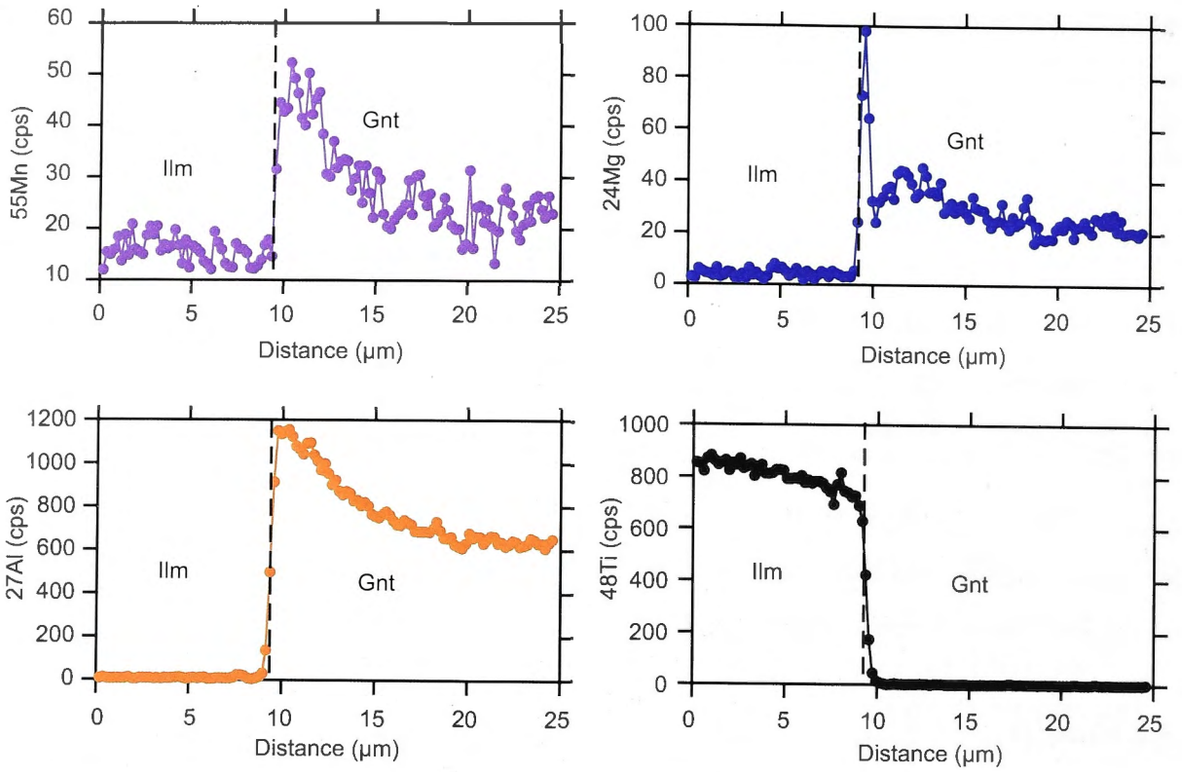

Figure 4.9: Elemental concentration profiles from the transcect across the ilmenite garnet grain boundary for ^{55}Mn, ^{24}Mg, ^{27}Al and ^{48}Ti in sample DV06-21 from the staurolite zone. The grain boundary is marked with a dotted line.

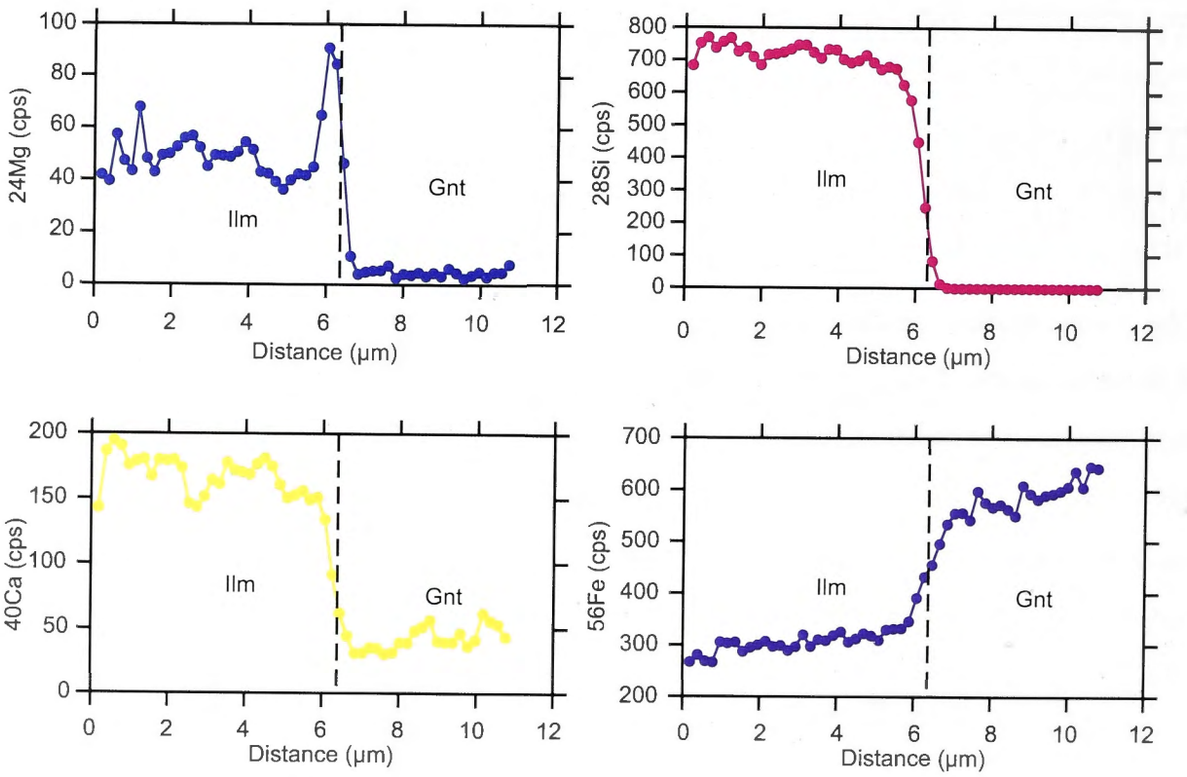

Figure 4.10: Elemental concentration profiles from the transect across the ilmenite garnet grain boundary for ^{24}Mg, ^{28}Si, ^{40}Ca and ^{56}Fe in sample DV06-21 from the staurolite zone. The grain boundary is marked with a dotted line.

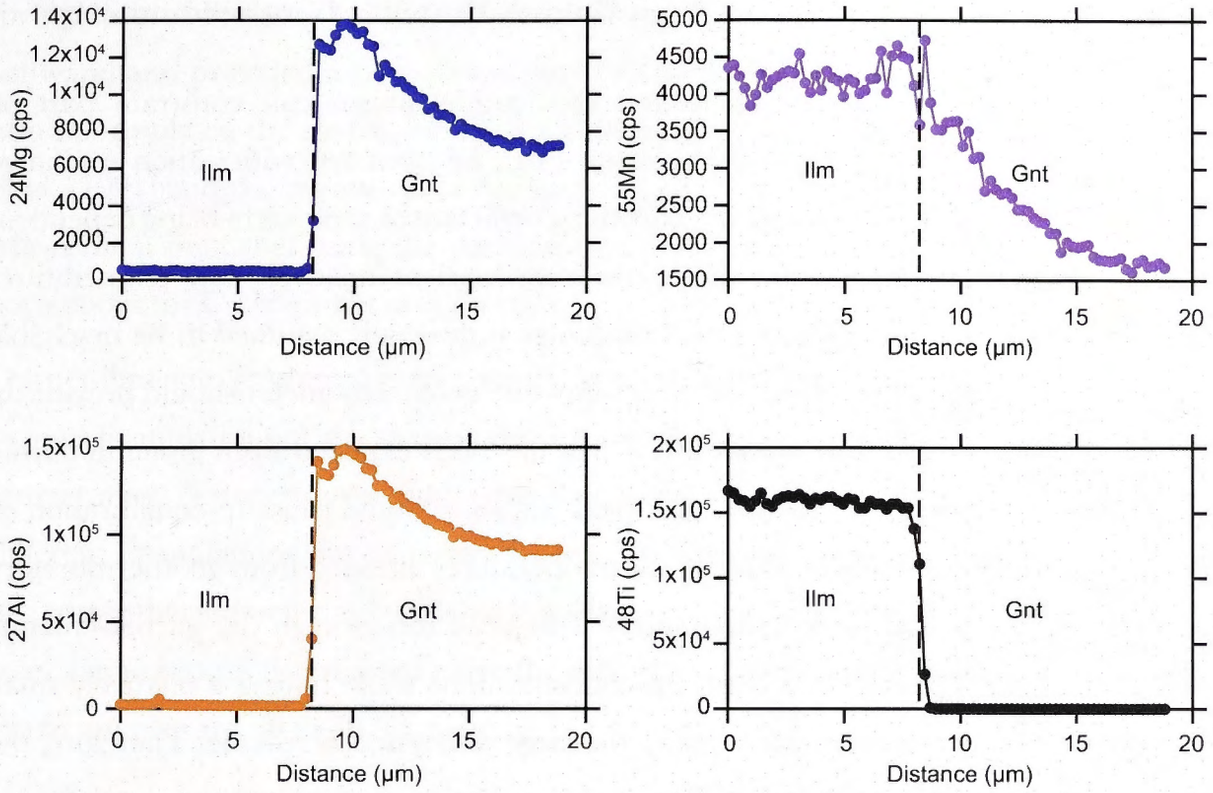

Figure 4.11: Elemental concentration profiles from the transcect across the ilmenite garnet grain boundary for ^{55}Mn, ^{24}Mg, ^{27}Al and ^{48}Ti in sample DV06-43b from the sillimanite zone. The grain boundary is marked with a dotted line.

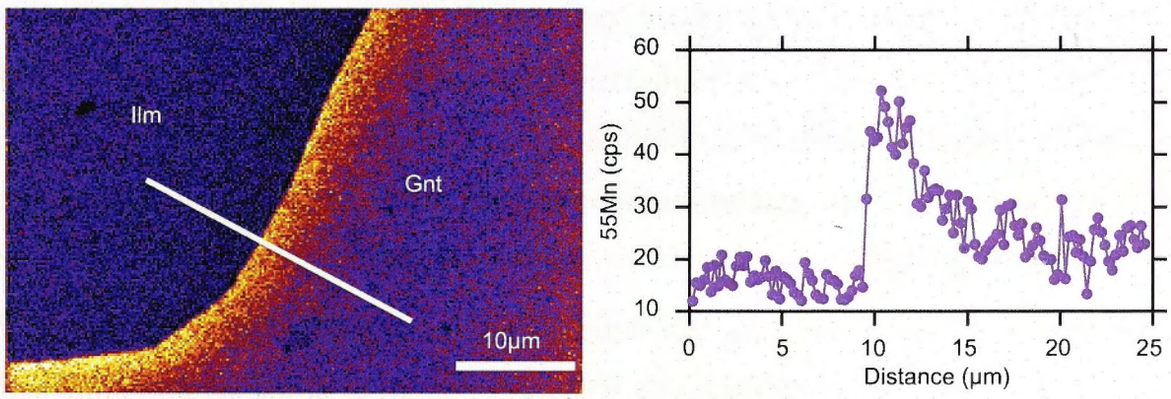

Figure 4.12: Elemental map and Mn concentration profile produced on the Cameca NanoSIMS 50 of a grain boundary between an ilmenite inclusion and the surrounding garnet from sample DV06-21 from the staurolite zone of the Barrovian metamorphic sequence, Scotland.

4.5 Incongruous Temperatures from Garnet-Ilmenite Geothermometry

The determination of peak temperatures of metamorphism can constrain part of the T-t history of a rock. These temperatures can be obtained with cation exchange geothermometry, which is based on the partition coefficient of the system being dependent on temperature. The samples in this study have been at relatively low temperatures and therefore the amount of retrograde exchange is generally assumed to be negligible (Pattison et al., 2003). In this case the garnet-ilmenite geothermometer should provide an estimate of peak temperature. However, if Mn has been expelled from ilmenite during cooling due to an exchange reaction, post-peak diffusion would cause re-equilibration of the garnet and ilmenite would result in the temperatures attained from geothermometry not reflecting the actual peak temperatures. Post-peak diffusion in the garnet-ilmenite system would significantly effect ilmenite concentrations while having a relatively small effect on the garnet concentrations due to the large difference in volume. Therefore, the garnet-ilmenite geothermometer would provide a minimum temperature constraint on the peak temperature.

Experiments studying the partitioning behaviour of Fe and Mn between garnet and ilmenite had been performed by Ono (1980), Docka (1984), Kress et al. (1985) and Kress (1986). The results of these studies are summarised in Chapter 3 (Fig. 3.1). The garnet-ilmenite geothermometer was first calibrated by Pownceby et al. (1987) in a series of reversal experiments. The geothermometry equation was later refined by Pownceby et al. (1991), Chatterjee (1991), Ganguly et al. (1996a) and Martin et al. (2010).

The peak temperature a rock unit has reached can be calculated using Equation 4.1 (Pownceby et al., 1987), in conjunction with elemental analysis of garnet and ilmenite:

$$T = \left(\frac{-4089+420(2X_{Mn}^{ilm}-1)-77(2X_{Mn}^{gnt}-1)}{-R\ln K_D - 1.44} \right) - 273.15 \qquad \textbf{(4.1)}$$

Where T is the temperature in degrees Celsius, X is the mole fraction, R is the Universal Gas Constant in cal $K^{-1}mol^{-1}$ and K_D is the partition coefficient.

Pownceby et al. (1991) later provided a correction for the effect of the Ca concentration of garnet. This correction is only required if $X_{Ca} \geq 0.35$, otherwise the previously stated geothermometry equation (Eqn. 4.1) is adequate. Ganguly et al. (1996a) noted that the

formulation of Pownceby et al. (1991) was incorrect, due to erroneous input into regression software, and provided a new formulation of the geothermometer. Martin et al. (2010) also reformulated the thermometric equation using the experimental data of Pownceby et al. (1991) and the regression of Ganguly et al. (1996a), as well as a correction for the Mg content in garnet using the solution model of Ganguly et al. (1996b) and omitting corrections for Ca in garnet and pressure.

Garnet-ilmenite geothermometry results from this study are shown in Table 4.2. The various formulations of the thermometer result in only minor variations in the calculated temperature. Temperatures that were calculated for samples in this study using the different formulations are generally within 30 °C of each other, which is within error of the geothermometer as formulated by Pownceby et al. (1987) of ± 30 °C. However, some temperatures determined using the different formulations particularly in the higher grade samples are up to 80 °C apart.

Comparison of the results to previous temperature determinations for the Barrovian samples (e.g. Beddoe-Stephens, 1990; Viete, 2009) indicates that the garnet-ilmenite geothermometer produces reasonable temperature estimates for the staurolite and garnet grade samples, DV06-18 and DV06-05c. However, for sample DV06-29 the temperature calculated is lower than peak temperature by approximately 100 °C and samples DV06-50, DV06-40 and DV06-43b have temperature estimates that are exceptionally high.

The temperatures from this study are likely to be incongruous for several reasons. The first being very low Mn concentrations in both the ilmenite and garnet compared to the experimental compositions. This means that small errors in the microprobe analysis would result in a large error in temperature (see figure 1 in Pownceby et al., 1987). This difficulty was noted in a study by Hamblock (2007), who used the garnet-ilmenite geothermometer to estimate temperatures in granulites on garnet and ilmenite with low Mn concentrations. The temperatures they determined were erratic compared to temperatures determined using the plagioclase and K-feldspar geothermometer of Fuhrman and Lindsley (1988).

The diffusive modification to the grain-scale major element concentration profiles in garnet must be taken into account; the effect of this modification would vary from core to rim of a garnet. Săbău and Massonne (2003) used ilmenite inclusions within garnet to determine temperatures in the Lotru Metamorphic suite, Carpathians, Romania. They employed the refinements, based on the non-ideality of the system, of Chatterjee (1991)

Sample	Metamorphic zone	XMnGnt	XFeGnt	XMnIlm	XFeIlm	lnKD	T (°C)	Temperature estimates using gnt-ilm (°C)			
								Pownceby et al. 1987	Pownceby et al. 1991	Ganguly et al. 1996	Martin et al. 2010
DV06-18	Staurolite	0.124	0.724	0.023	0.966	1.973	590	554.1	523.8	523.5	543.3
	Staurolite	0.113	0.733	0.023	0.969	1.872	590	586.2	556.7	557.0	561.9
DV06-50	Sillimanite	0.035	0.753	0.025	0.965	0.564	640	1452.4	1542.4	1565.1	1542.2
DV06-40	Sillimanite	0.116	0.716	0.065	0.933	0.844	660	1137.9	1162.7	1173.9	1179.5
	Sillimanite	0.115	0.718	0.064	0.935	0.852	660	1130.5	1154.4	1165.0	1171.2
DV06-43B	Sillimanite	0.027	0.745	0.019	0.979	0.652	670	1343.5	1403.7	1428.0	1421.5

Table 4.2: Temperatures obtained from average concentrations measured by EPMA for various calibrations of the garnet-ilmenite geothermometer. Measured ilmenite inclusions from samples DV06-50 and DV06-43b were towards the edge of the garnet where as DV06-40 was towards the centre. Temperatures for comparison from Viete (2008) were derived from THERMOCALC.

of the formula by Pownceby et al. (1987). In this study the inconsistency of the results of the geothermometer were attributed post-peak modifications to garnet grain-scale zoning. Post-peak diffusion would also account for the inconsistent temperatures only being obtained for the higher grade samples where evidence of possible diffusion has been obtained. However, the EPMA transects show that the amount of post-peak diffusion was not significant even in the higher grade samples. Therefore, post-peak diffusion is unlikely to have had large effect.

One other explanation is retrogression of the samples. Pownceby et al. (1987) noted in their study that if samples are highly retrogressed this would result in incongruent temperatures. This is because the occurrence of net-transfer reactions makes the partitioning inconsistent. Evidence is seen in the Barrovian samples of the garnet reacting in these samples where the rims of the higher grade garnets are ragged and retrograde Mn zoning profiles are observed (see figures 2 and 3 in Viete et al., 2011b). If this is the cause for the irregular temperatures that were attained the system cannot be modelled, as a diffusion model of the garnet-ilmenite system would rely on the partitioning of Fe and Mn as calibrated by the experimental data.

4.6 Discussion

Features in Fe, Mg and Mn concentration profiles adjacent to ilmenite inclusions in garnet were observed (Figs. 4.3 to 4.7) in several samples from the sillimanite zone of the Barrovian metamorphic sequence in Scotland. However, these features were not consistent across samples and analytical artefacts are also observed in concentration profiles adjacent to ilmenite inclusions in garnet. Therefore, these features are unlikely to be diffusion related.

4.6.1 Spatial Resolution of Analytical Techniques

The issue with observing small-scale diffusional features is the spatial resolution of readily available analytical techniques. EPMA can produce concentration profiles with a step size of approximately 1 μm. However, the excitation volume of the sample would be larger. The excitation volume is the volume of the sample that is penetrated by the electron beam. The penetration depth is dependent on the accelerating voltage. For example the accelerating voltage used in this study was 15 keV at this voltage, the electrons should not penetrate further than 2 μm into the sample (Goldstein, 2003). The excitation volume

can be modelled for specific phases using the CASINO computer program developed by Drouin et al. (2007). This program is a Monte Carlo simulation of the electron trajectories within the sample. The excitation volume for the operating conditions used in this study (accelerating voltage of 15 keV and a beam current of 40 nA) was modelled and the result can be seen in Figure 4.13.

To investigate the effect of excitation volume on transects across a boundary between ilmenite and garnet, CASINO was used to simulate the electron beam-sample interactions for a line scan. The sample was set as almandine with a 20 μm wide ilmenite inclusion in the centre and vertical boundaries between the two phases. The beam was set to an accelerating voltage of 15 keV with a spot size of 1 μm, which are the conditions used in EPMA analysis for this study. Standard physics models as outlined in Drouin et al. (2007) were used for the simulation. A simulation was run for a line scan 20 μm long from the centre of the ilmenite inclusion into the almandine. Images of electron trajectories for each point were simulated as well as profiles across the garnet-ilmenite boundary; these results are shown in Figures 4.14 and 4.15.

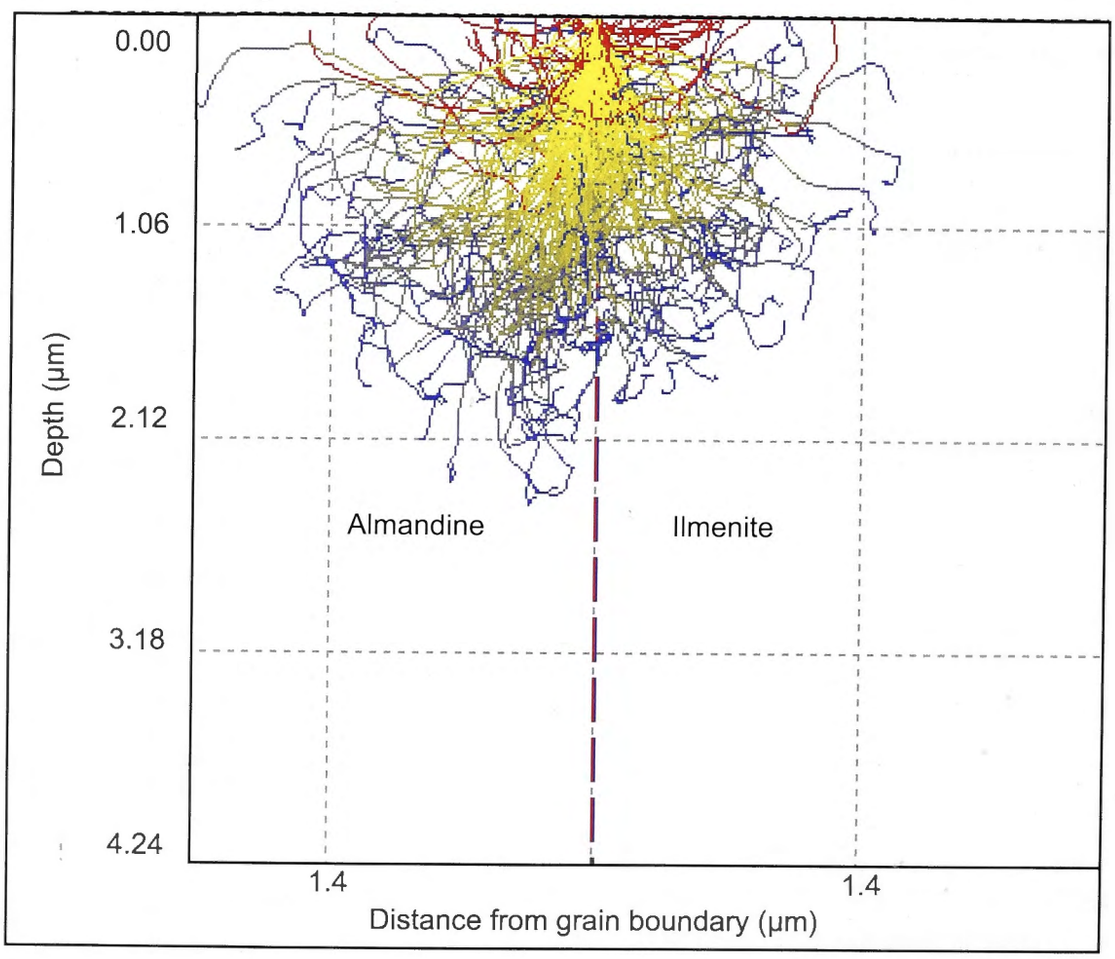

Figure 4.13: A Monte Carlo simulation produced by CASINO 2.42 (Drouin et al., 2007) of electron trajectories at the boundary between almandine and ilmenite with an accelerating voltage of 15 keV.

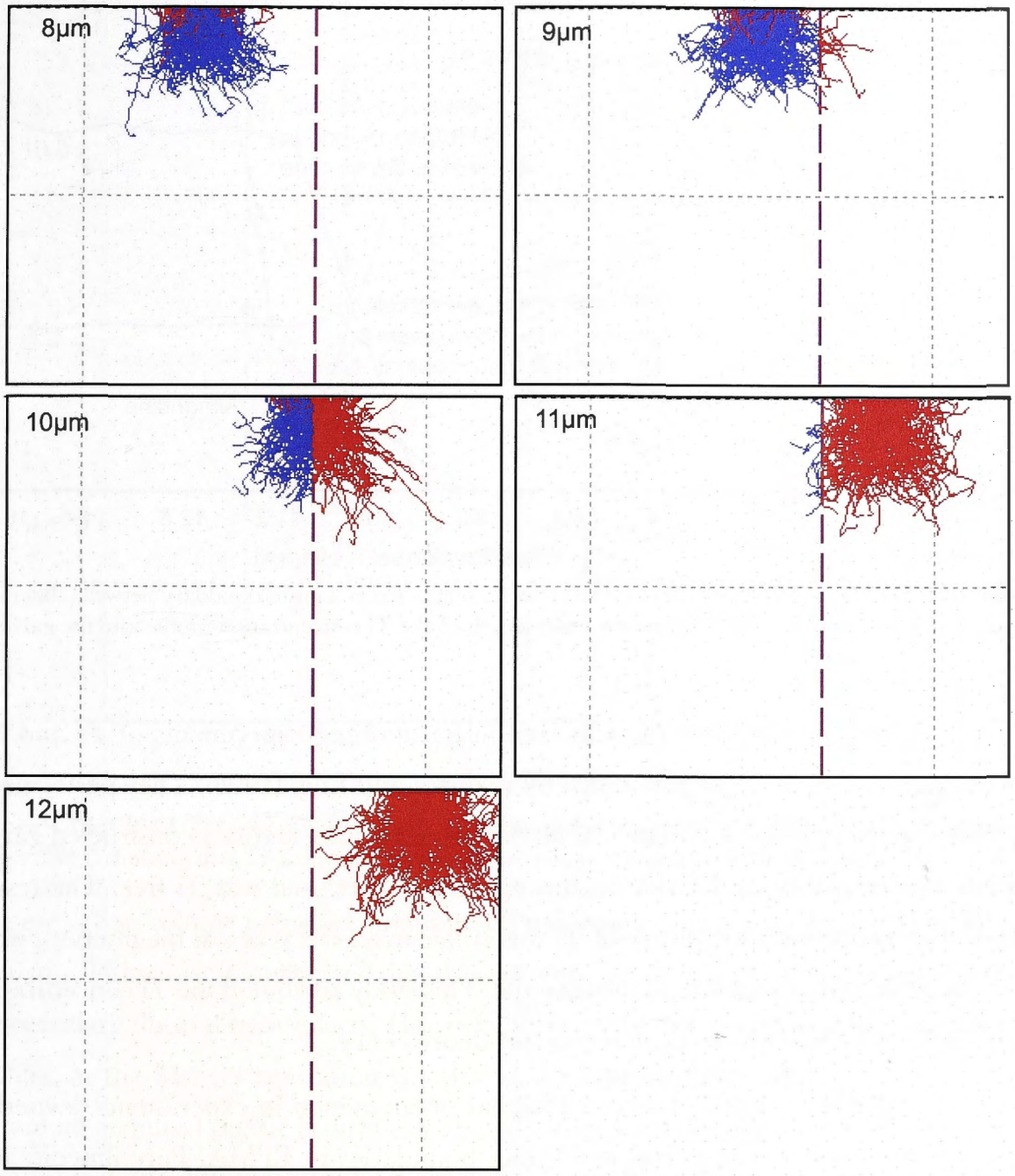

Figure 4.14: Simulated electron trajectories for a beam with a 1 µm diameter and an accelerating voltage of 15 keV at points approaching the grain boundary between the ilmenite and garnet, which is set at 10 µm. The distances displayed are measured from the centre of the ilmenite.

The results from the CASINO simulation show that the Ti concentration profiles that were observed in garnet are not produced from the excitation volume of the beam alone as that stops affecting the profiles approximately 2 µm from the ilmenite-garnet boundary. Results from EPMA transect in garnet adjacent to ilmenite inclusions show Ti concentration profiles approximately 20 to 30 µm (Figs. 4.3 to 4.7) into the garnet. These profiles are observed in all EPMA transects and are not observed in the NanoSIMS results (Figs. 4.9 and 4.11).

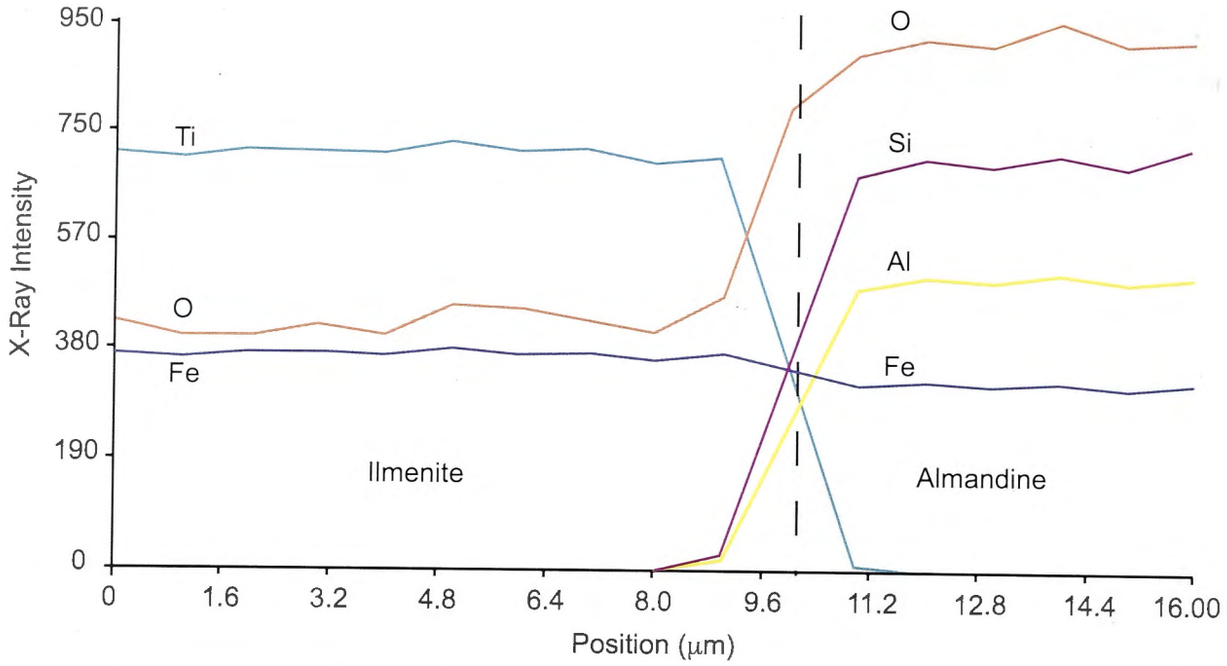

Figure 4.15: Simulated profiles of an electron beam scanning across a grain boundary between ilmenite and garnet for Fe, Al, Si, O and Ti. Note the short length of the Ti concentration profile into the garnet.

A similar Ti concentration profile was seen in partitioning experiments of Fe and Mn between garnet and ilmenite performed by Feenstra and Engi (1998). They performed a test to determine if it was an analytical artefact by traversing across a constructed garnet and ilmenite couple using EPMA. In this test, the garnet used was Ti free. The results showed that a concentration profile of Ti was visible in transects across the interface up to 50 μm into the garnet adjacent to the ilmenite. This study attributed the Ti concentration profile, seen in EPMA transects, to secondary fluorescence.

Maaskant and Kaper (1991) observed a similar phenomenon in experiments devised to investigate the fluorescence effects near grain boundaries in EPMA. Pure ilmenite and pure haematite were mounted adjacent to each other separated by 2 μm thick glass. In this study Ti was measured in the haematite up to 100 μm from the ilmenite boundary. From examination of the Ti concentration profiles (Fig. 4.16) they concluded that as the primary excitation volume of the beam moved and was no longer entirely within the ilmenite the profiles would start to curve downwards. The inflection point of the curve marks the point at which the primary excitation volume is no longer within the ilmenite and at this stage the concentrations must be due to secondary fluorescence. In particular the Fe-Kα radiation from the haematite exciting the Ti-Kα in the ilmenite.

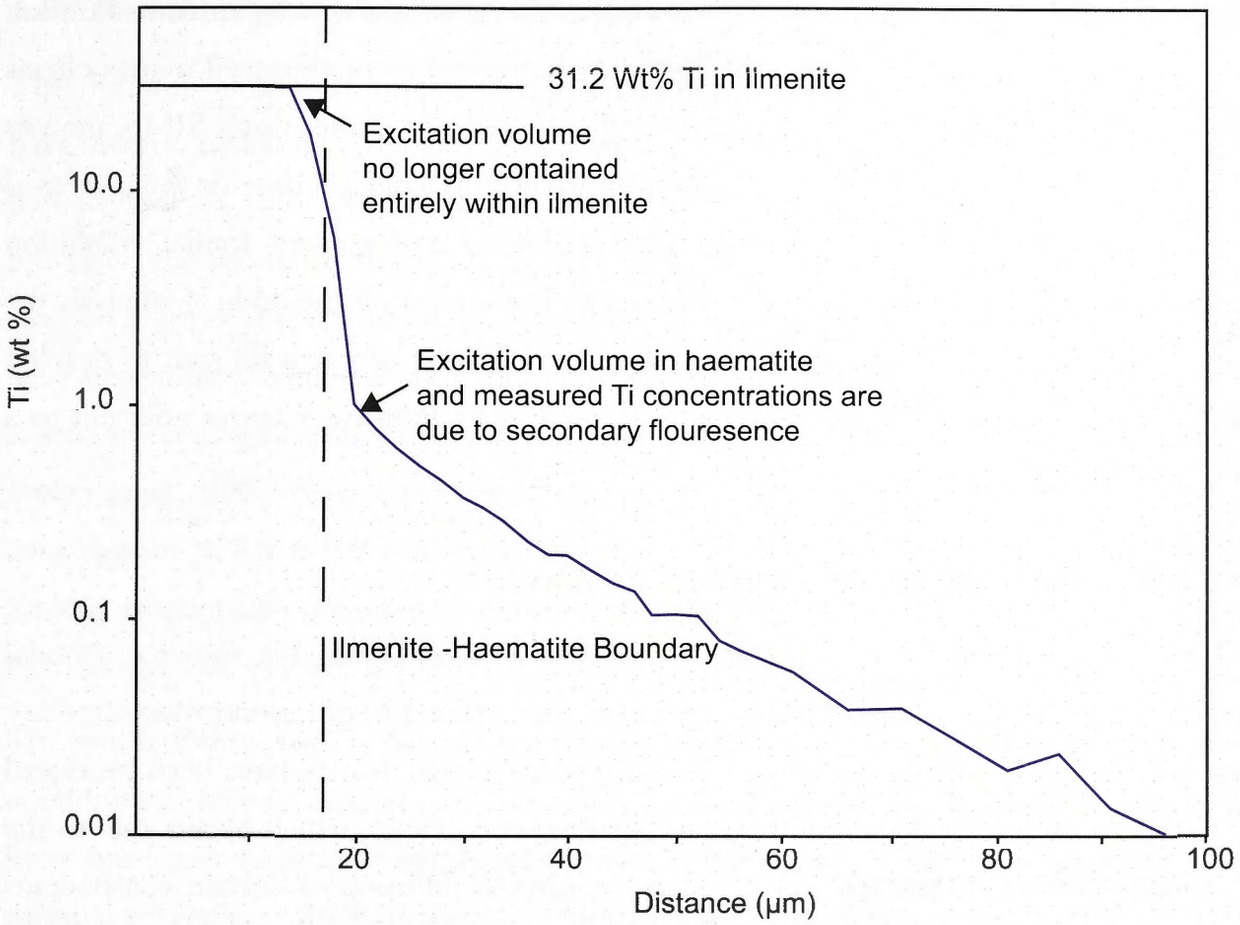

Figure 4.16: EPMA Ti concentration profile across an ilmenite-haematite boundary after Maaskant and Kaper (1991) showing that Ti-Kα radiation is measured up to 100 μm from the boundary.

The excitation volume being approximately 3 μm would not account for the Ti profiles up to 30 μm. Therefore, it is expected that these profiles are analytical artefacts caused by edge or secondary fluorescence effects. However, this should not affect the Mn concentration profiles, as the Mn concentration is lower in the ilmenite than garnet. Although, to be certain an acquired profile is diffusion related rather than analytical artefacts it would be favourable if the diffusion profiles exceeded the length of the known analytical artefact. For the samples in this study this is not the case.

The attempt to attain better spatial resolution by using NanoSIMS did not resolve this issue. Despite the NanoSIMS profiles not showing Ti concentration profiles in garnet other analytical artefacts were observed adjacent to the grain boundary of the ilmenite inclusions measured. Peaks of ^{55}Mn, ^{24}Mg, ^{27}Al and ^{56}Fe in garnet adjacent to the ilmenite inclusion were observed; this is highlighted for ^{55}Mn in Figure 4.12 for sample DV06-21. However, these features are not likely to be attributed to diffusional processes and are likely to be analytical artefacts, as the stoichiometry of garnet would not allow for the

observed concentration changes. For example, ^{27}Al shows a doubling in concentration towards the ilmenite grain boundary. This may be related to pronounced matrix effects at the interface as has been documented in depth profiling studies using SIMS analysis (Hofmann and Schubert, 1998). As a result the NanoSIMS did not provide the increased spatial resolution that was expected. This is due to a decreased spatial resolution when traversing an interface between phases and in almost all methods of analysis the spatial resolution is diminished across an interface. This is why it is difficult to develop a method that requires the measurement of small scale diffusive features adjacent to a grain boundary.

4.6.2 Bimodality of Mn Concentration Profiles

Mn concentration profiles in sample DV06-40, as seen in Figure 4.5, shows a bimodal profile adjacent to the ilmenite. If these features are related to diffusion processes, there are two hypotheses for the formation of this type of profile. It may have been produced by a phenomenon called uphill diffusion (Chakraborty, 1995), which occurs due to the exchange kinetics of multiple components resulting in diffusion of certain components against their own concentration gradient. For instance Mg may be another component that is involved in the garnet-ilmenite system.

Equally, the bimodal profile can be described by the exchange of Fe and Mn between garnet and ilmenite, due to a change in the partitioning behaviour. At temperatures higher than the growth temperature, ilmenite will act as a diffusional sink for Mn, on the cooling path, however, the ilmenite inclusion will expel Mn into the garnet host. This exchange has the potential to produce a "rim and moat" in the Mn concentration surrounding an ilmenite inclusion in the garnet host as is seen in the DV06-40 profile (Fig. 4.5). Proof of this phenomenon of preserving prograde information would be valuable in garnet diffusion modelling techniques already used for determining timescales of thermal events. Numerical modelling of the garnet-ilmenite system would be useful to fully understand the exchange kinetics.

4.6.3 Durations of Barrovian Metamorphism

The duration of the Grampian Orogeny has been constrained by previous studies to have lasted *c.* 15 Ma by U-Pb geochronology of Scotland (Oliver et al., 2000) and Ireland (Friedrich et al., 1999). The duration of the thermal event that produced the Barrovian metamorphic sequence has been a topic of debate, therefore, if the garnet-ilmenite method is applicable it could help constrain durations. Previous studies in the Barrovian have determined relatively short durations of metamorphism compared to the classic crustal thickening model of metamorphism proposed by England and Thompson (1984). Baxter et al. (2002) conducted Sm-Nd dating of garnets from the sillimanite zone that gave ages of 472.9 ± 2.9 Ma and 464.8 ± 2.7 Ma. These ages were compared to the Sm-Nd average ages obtained by Oliver et al. (2000) for garnet growth in the garnet and kyanite zones of 467.6 ± 2.5 Ma and 472 ± 2 Ma, respectively.

The results of these two studies indicate that the different metamorphic zones reached peak conditions almost simultaneously. Baxter et al. (2000) noted that, due to this conclusion, there must have been a secondary heat source operating in the area in conjunction with thermal relaxation, which they stated was supplied by magmas and associated fluid flow, with a short duration of heating. This was followed by the study of Ague & Baxter (2007) that concluded the Barrovian sequence in Scotland underwent brief thermal pulses that reached the peak metamorphic conditions spanning a duration of 200 to 300 ka. This was inferred from modelling Sr diffusion in apatite and corroborated by garnet major element diffusion models. More recently, Viete et al. (2011b) conducted a study on major and trace element concentration profiles across garnet. Viete et al. (2011b) observed diffusion profiles on two scales *c.* 100 μm and *c.* 1000 μm. The quadratic relation between the length and timescale of diffusion was utilised to deduce that the Barrovian metamorphic sequence resulted from shorter timescale (*c.* 10 ka) thermal pulses in conjunction with the background regional thermal event, which lasted a few million years. This result is in contrast to the previous determination by Ague and Baxter (2007). These studies propose different tectonic environment for the metamorphism to explain these short timescales but both call upon magmatic intrusions for added heat, as was suggested originally by Barrow (1893). These models will be discussed further in Chapter 7.

4.7 Conclusions

Possible diffusional features adjacent to ilmenite inclusions in garnet have been observed for Mn, Mg and Fe concentration profiles in samples from the Barrovian metamorphic sequence in Scotland. These diffusional features are only seen in garnets from the sillimanite zone. However, Ti concentration profiles were also observed approximately 30 μm into the garnet adjacent to ilmenite inclusions that are inferred to be analytical artefacts. This study demonstrates the difficulty in measuring small scale diffusional features adjacent to a grain boundary, particularly with respect to the current spatial resolution of analytical techniques. It also introduces significant doubt as to whether the features of a shorter length observed in other concentration profiles are real and whether the features are produced by diffusional processes. Additionally, the garnet-ilmenite geothermometry results indicated that the partitioning between garnet and ilmenite in the higher grade samples was not consistent with experimental constraints and this is likely to be due to retrograde reactions occurring in the samples.

To progress, analysis of samples that should produce longer Mn diffusion profiles (i.e. samples with a higher peak temperature) is needed as these will reduce the uncertainty with respect to analytical artefacts apparent across the interface between garnet and ilmenite. Then a numerical model would allow constraints to be placed on the duration of metamorphism by forward modelling the production of diffusion profiles surrounding ilmenite inclusions within garnet, as was outlined in Chapter 1.

CHAPTER 5

Element Concentration Profiles Surrounding Ilmenite Inclusions in Garnet from the Ivrea-Verbano Zone in Italy

Preface

Dr Tanya Ewing collected the samples analysed in this study from the Ivrea-Verbano Zone in northern Italy during her PhD candidature (Ewing, 2011). Dr Jörg Hermann proposed these samples to extend this study. He also assisted with the petrological and analytical work as well as the interpretation of the results. The analysis of the samples was carried out using the Cameca SX100 electron probe microanalyser (EPMA) at the Research School of Earth Sciences, ANU with the assistance of Dr Robert Rapp. All of the research presented in this chapter is my own work except where otherwise indicated.

5.0 Synopsis

Mn diffusion profiles have been observed and measured adjacent to ilmenite inclusions in garnet from natural samples from the Ivrea-Verbano Zone in Italy. The Mn concentration profiles show a peak adjacent to ilmenite inclusion in garnet before decreasing to the background Mn concentration. Additionally, inverse concentration profiles are observed in Mg with concentration decreasing towards ilmenite inclusions. The lengths of these features are proportional to the peak temperatures attained by the samples. Therefore, the features have been attributed to diffusional processes. These profiles match what was expected from the garnet-ilmenite system, where Fe and Mn exchange at the interface between garnet and ilmenite and subsequent diffusion of the concentration change produced leaves stranded diffusion profiles in garnet. However, in these samples ilmenite inclusions have an excess of Mn compared to the host garnet. This excess Mn is inferred to be related to net-transfer reactions that occurred during cooling, specifically the reaction of garnet and melt to form biotite. This implies that the ilmenite inclusions are an open system and have exchanged with minerals outside of the host garnet via cracks that have provided diffusion pathways. Despite the inconsistencies, the measured diffusion profiles could be used to broadly constrain the duration of the thermal event. This was done by calculating the expected length of diffusion profiles assuming linear cooling from peak temperatures at different cooling rates. From this the duration of the thermal event associated with the emplacement of magma in the Ivrea-Verbano Zone can be constrained to between 100 000 years and 1 Ma.

5.1 Introduction

The garnet-ilmenite system exchanges Fe and Mn between the two phases. The partition coefficient for Fe and Mn between garnet and ilmenite controls the efficiency of exchange. Then subsequent diffusion, within the two phases, creates concentration gradients at the boundary. The slow rate of diffusion within garnet means that garnet may preserve diffusion profiles surrounding ilmenite inclusions. Specifically during cooling, Mn is expelled from ilmenite into garnet and from the consequent diffusion of Mn, profiles can be preserved as the rate of diffusion decreases with decreasing temperature. The evolution of this system and the diffusion profile expected from this process is shown in Figure 5.1. The lengths of the diffusion profiles are proportional to the duration of the thermal event and therefore if the temperature is known, the profile length provides constraints on the duration of the thermal event associated with metamorphism.

To determine if the garnet-ilmenite system is viable for diffusion modelling purposes, diffusion profiles must be observed in natural samples. Previous attempts to measure diffusion profiles adjacent to ilmenite inclusions in samples from the Barrovian metamorphic series in Scotland yielded inconclusive results (Chapter 4). This study was intended to observe and measure the resulting diffusion profiles adjacent to ilmenite inclusions in garnet from the Ivrea-Verbano Zone. The Ivrea-Verbano Zone is proposed as a useful terrane to investigate this system because of the high temperatures attained during metamorphism. Therefore, growth zoning will not be preserved within garnet in the samples selected and the diffusion profiles surrounding ilmenite inclusions will be relatively long. Growth zoning is, however, preserved in the garnet-amphibolite samples of Henk et al. (1997) that recorded peak temperatures only 30 °C cooler than the lowest grade sample analysed in this study.

Three samples from the Ivrea-Verbano Zone were selected that span different metamorphic grades, with peak temperatures between 650 °C and 1000 °C. The peak metamorphic conditions of these samples are well constrained from previous petrological studies (e.g. Ewing et al., 2012; Henk et al., 1997; Luvizotto and Zack, 2009; Redler et al., 2012). The samples were analysed using electron probe microanalysis (EPMA) to determine if diffusion profiles are preserved.

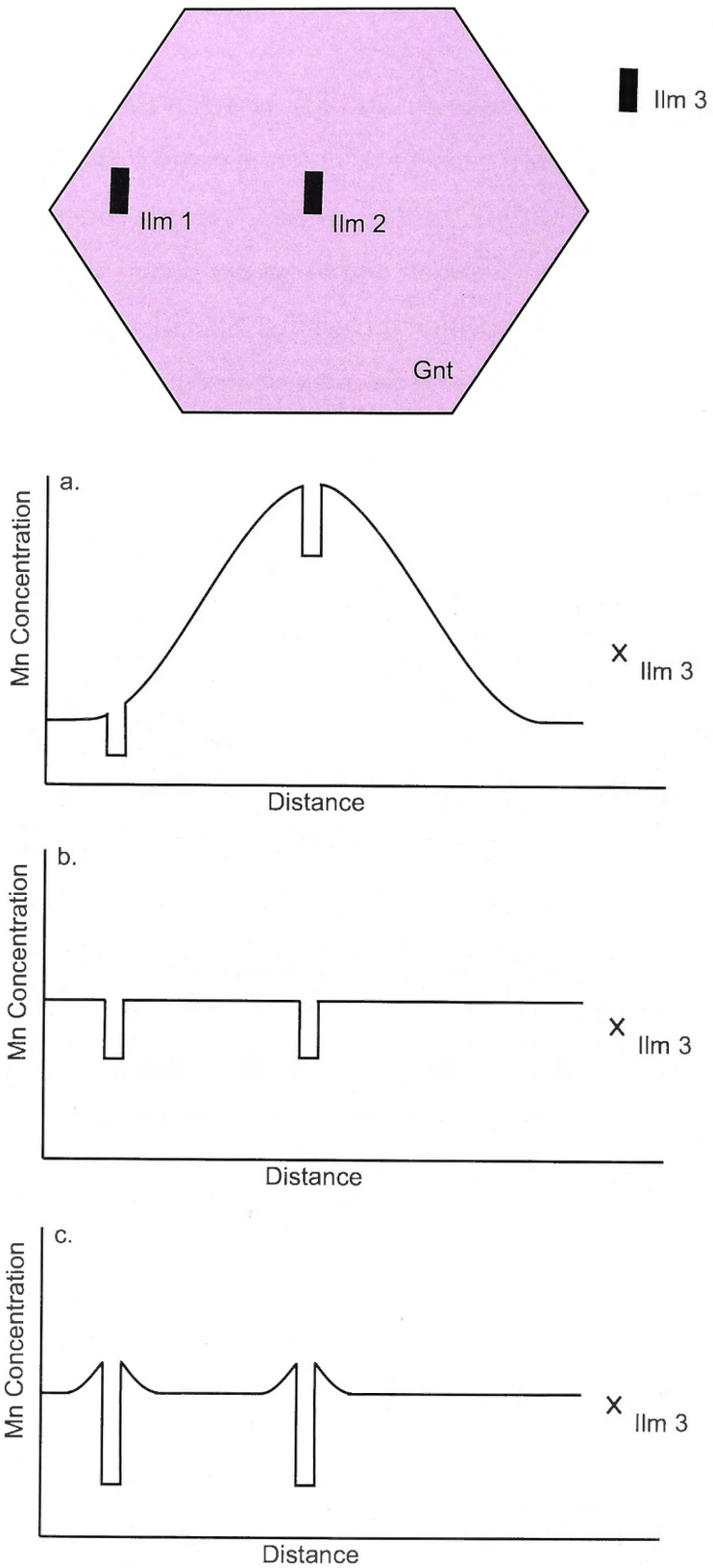

Figure 5.1: Schematic diagram of the hypothesized evolution of Mn concentration profiles in garnet surrounding ilmenite inclusions throughout the metamorphic history of the rock; (a) Mn concentration profile after garnet growth; (b) Mn concentration profile at peak metamorphic conditions and (c) Mn concentration profile after cooling.

5.2 Geological Setting

The Ivrea-Verbano Zone of the Southern Alps in northern Italy is broadly subdivided into the mafic and ultramafic rocks of the Mafic Complex and the metamorphosed pelites, psammites and basites of the so-called Kinzigite Formation (Henk et al., 1997). It is bounded by the Insubric Line (IL) to the northwest and the Cossato-Mergozzo-Brissago (CMB) and Pogallo Lines to the southeast (e.g. Boriani et al., 1990; Rivalenti et al., 1984; Schmid et al., 1987). A map of the area, including the large-scale faults that bound the terrane, is shown in Figure 5.2.

The Kinzigite Formation is heterogeneous interlayered pelite, psammites and basites that have been metamorphosed. It shows a continuous sequence of high-grade metamorphic rocks, which increases towards the northwest from amphibolite to granulite facies (e.g. Henk et al., 1997; Zingg, 1980).

The mafics and ultramafics of the Mafic Complex have been intruded into the Kinzigite Formation (Rivalenti et al., 1975). The Mafic Complex has been split into an upper and lower segment by some authors (e.g. Barboza and Bergantz, 2000; Peressini et al., 2007; Sinigoi et al., 2011). It is divided as shown in Figure 5.2. Barboza and Bergantz (2000) inferred from geochemical analysis that the upper and lower parts of the complex intruded at different times and were produced from compositionally different parent magma.

The Ivrea-Verbano Zone is significant as it shows a continuous progression through attenuated lower continental crust (Burke and Fountain, 1990) and was often referred to as an example of mantle-derived magma causing high-grade regional metamorphism. This may be true, however, Barboza et al. (1999) produced petrological evidence for the peak regional metamorphism occurring before the emplacement of the Mafic Complex. This was corroborated by later studies of Barboza and Bergantz (2000) and Redler et al. (2012) who observed cordierite, present within the rocks of Val Sesia and Val Strona di Postua, which overprints the regional metamorphic peak assemblages at lower pressure. The cordierite growth is inferred to be related to contact metamorphism. Ewing et al. (2012) presented a T-t path, constrained by Zr-in-rutile thermometry and zircon dating, that reflects this complexity in the thermal history (Fig. 5.3).

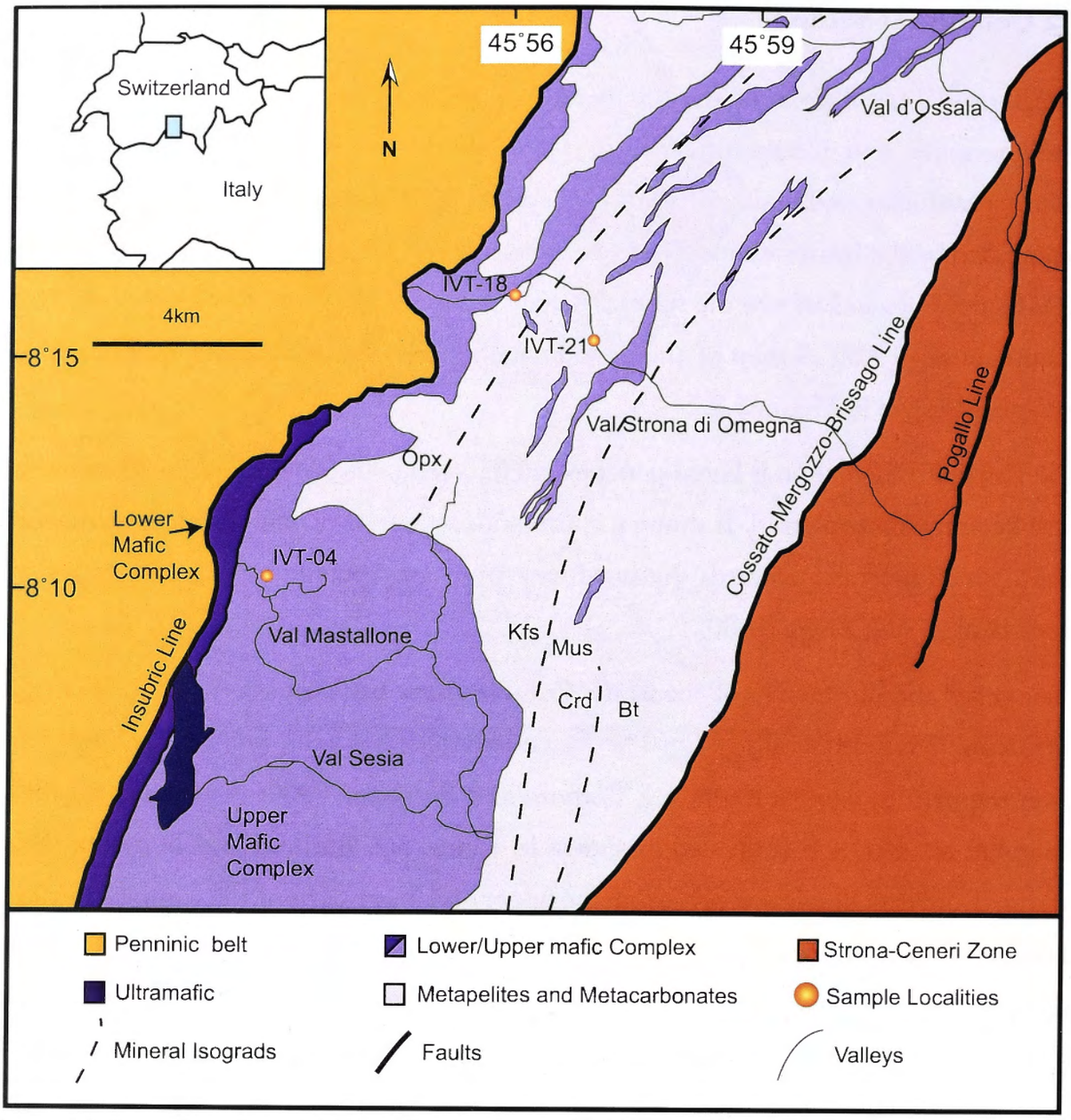

Figure 5.2: Map of the Ivrea-Verbano Zone, Southern Alps in northern Italy, with major structural constraints, contacts between adjacent terranes and the mineral isograds after Barboza and Bergantz (2000). The mineral abbreviations are as follows Bt: biotite, Crd: cordierite, Ksp: K-Feldspar, Mus: muscovite and Opx: orthopyroxene.

5.3 Ivrea-Verbano Zone Samples

For this study three samples from the Ivrea-Verbano Zone were analysed, IVT-21, IVT-18 and IVT-04. The samples were selected based on suitable mineral assemblages, namely garnet with ilmenite inclusions. Samples IVT-21 and IVT-18 were collected from Val Strona di Omegna and IVT-04 from Val Mastallone. The sample localities are as shown in Figure 5.2 and listed in Table 5.1. Peak metamorphic conditions including pressure

and temperature estimates have been made in these areas by various authors (e.g. Ewing et al., 2012; Henk et al., 1997; Luvizotto and Zack, 2009; Redler et al., 2012).

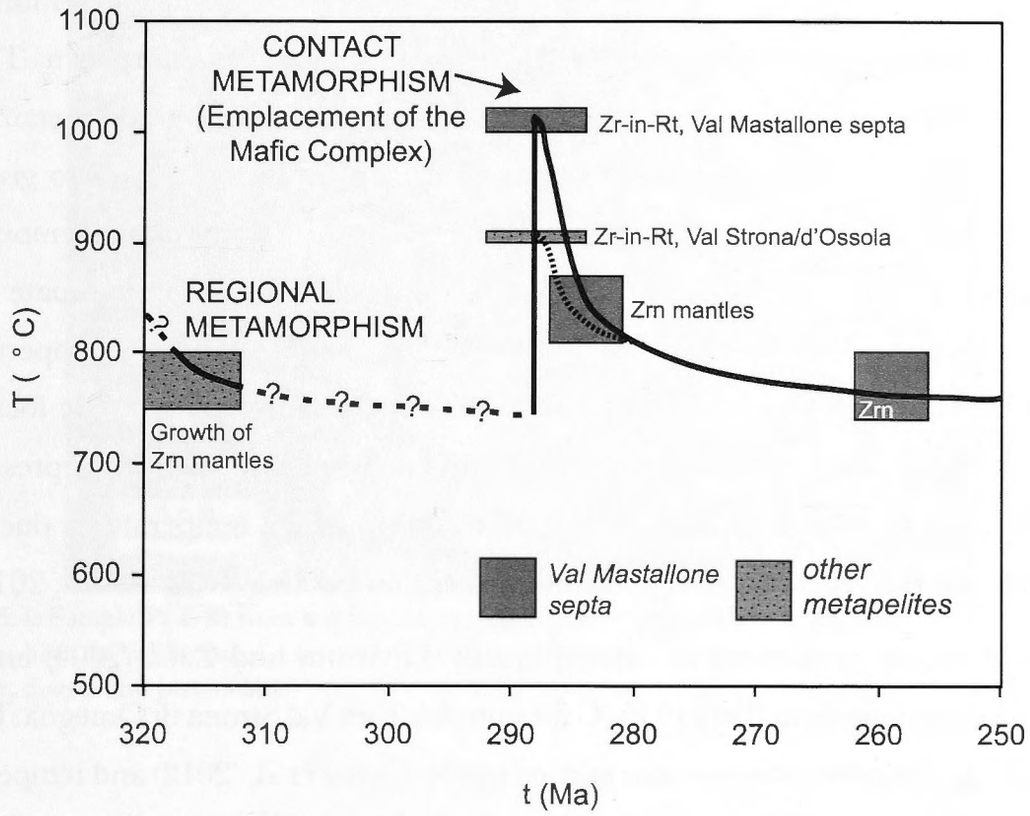

Figure 5.3: Interpretation of the T-t history of the Ivrea-Verbano Zone presented by Ewing et al. (2012) that was constrained by Zr-in-rutile (Zr-in-Rt) thermometry and zircon (Zrn) dating.

Sample	Latitude (N)	Longitude (E)
IVT-21	45° 55.247	8° 17.734
IVT-18	45° 55.973	8° 15.568
IVT-04	45° 53.161	8° 10.710

Table 5.1: Localities of samples analysed in this chapter.

Henk et al. (1997) determined temperatures and pressures along Val Strona di Omegna using various geothermobarometry techniques. A sample near the locality IVT-21 gave a temperature of 657 ± 30 °C from garnet-biotite thermometry and a pressure of 6.0 ± 0.5 kbar from GASP-barometry. A sample near the locality of IVT-18 gave a temperature of 762 ± 30 °C from garnet-orthopyroxene thermometry and a pressure of 7.6 ± 1.0 kbar from Gnt-Opx-Pl-Qtz-barometry. From the results of Henk et al. (1997)

a general trend is observed across the Ivrea-Verbano Zone where temperatures and pressures increase from the southeast towards the northwest. However, it is worth noting that the temperatures of Henk et al. (1997) are likely to underestimate temperatures and pressures due to resetting of mineral compositions post-peak metamorphism. This has been investigated by Pattison et al. (2003) and is common in high-grade metamorphic rocks. Temperatures determined by other methods (e.g. Zr-in-rutile) tend to give peak temperatures approximately 100 °C higher. Redler et al. (2012) determined temperatures in Val Strona di Omegna using THERMOCALC. Their temperature estimate nearby sample IVT-21 was 815 °C with a pressure of 6 kbar to 10 kbar. This temperature is almost 150 °C above those of Henk et al. (1997). For a sample nearby the locality of IVT-18, Redler et al. (2012) determined a temperature of 860 °C with a pressure of 7 kbar to 11 kbar. The significant difference in the obtained temperatures due to the retrograde resetting of mineral compositions infers slow cooling (Redler et al., 2012).

Zr-in-rutile geothermometry was carried out by Luvizotto and Zack (2009) and gave temperatures ranging from 850 to 930 °C for samples from Val Strona di Omegna. Further Zr-in-rutile geothermometry was also carried out by Ewing et al. (2012) and temperatures have been determined for granulite facies samples nearby IVT-04 and IVT-18. Samples near IVT-04 were calculated at 1010 ± 50 °C, these samples were metapelite slivers within the gabbro. Samples nearby IVT-18 were calculated at 910 ± 40 °C (Ewing et al., 2012). These temperatures are in agreement with those determined by Redler et al. (2012) from THERMOCALC estimates, which were 900 to 950 °C for the granulite facies metamorphism.

5.4 Petrology

Samples IVT-04 and IVT-18 are granulite facies metapelites, IVT-04 is a sliver of metapelite from within the Mafic Complex. Sample IVT-21 is a metapelite from the transition zone between the amphibolite and granulite facies (Redler et al., 2012). Photomicrographs showing the representative mineralogy for each sample are shown in Figures 5.4 to 5.6 and a summary of the mineral assemblages of the samples is shown in Table 5.2.

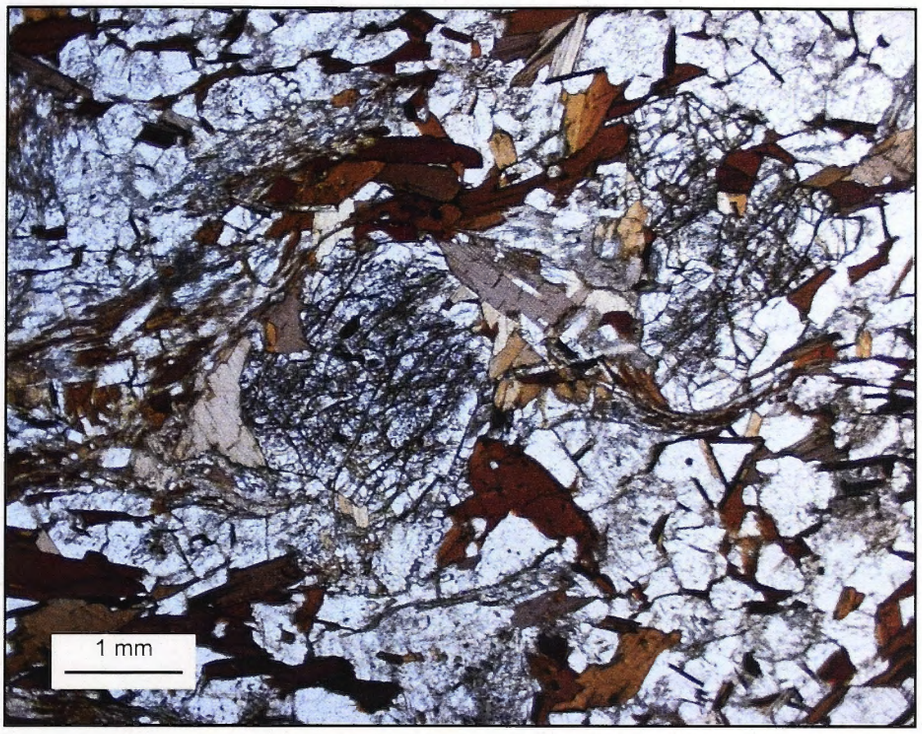

Figure 5.4: Sample IVT-21 from the transition zone between amphibolite and granulite facies metamorphism in Val Strona di Omegna. The photomicrograph shows garnet porphyroblasts in a matrix of biotite, quartz and plagioclase.

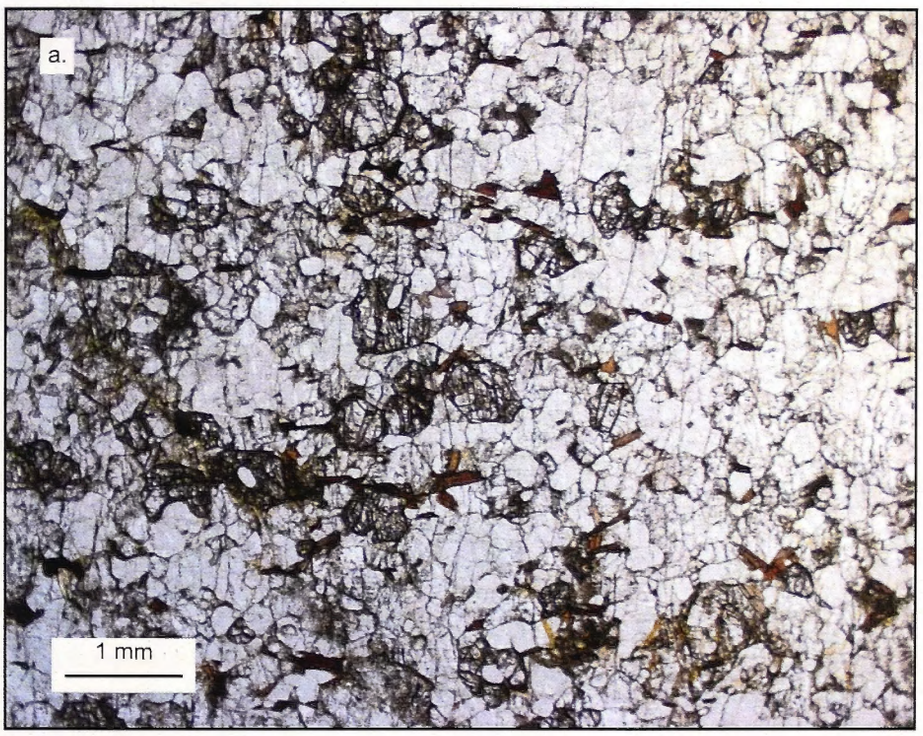

Figure 5.5: Sample IVT-18 from the granulite facies in Val Strona di Omegna. The photomicrograph shows garnet porphyroblasts in relation to the matrix minerals.

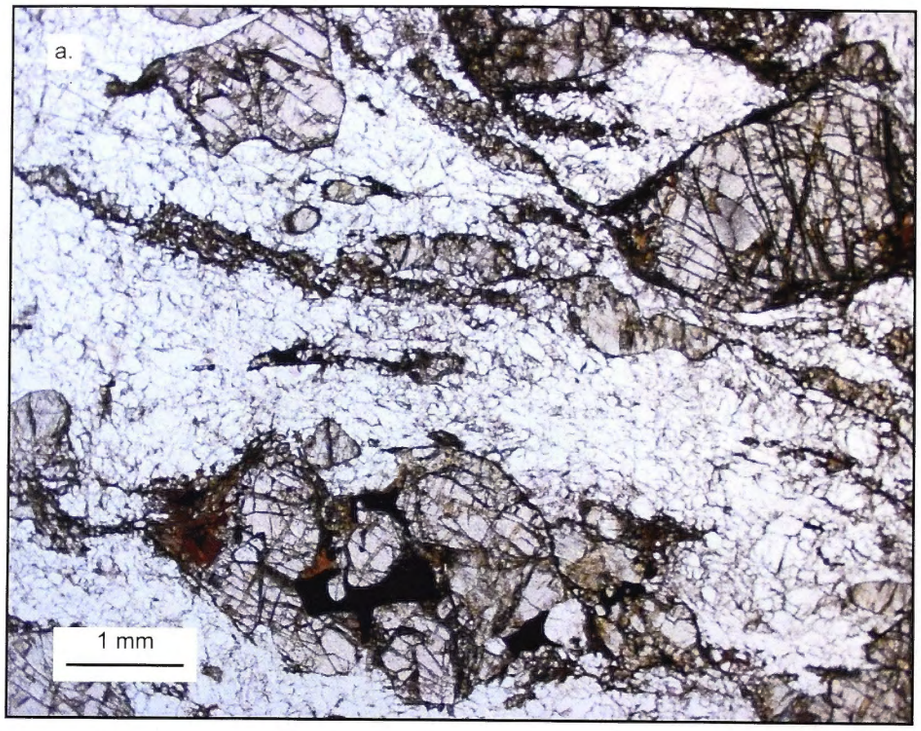

Figure 5.6: Sample IVT-04 from Val Mastallone, showing garnet porphyroblasts in relation to the matrix minerals.

Sample	Metamorphic Zone	Qtz	Plag	Kfs	Sil	Gnt	Opx	Bt	Ilm
IVT-21	transition amphibolite/ granulite	x	x	x	x	x		x	x
IVT-18	granulite	x	x	x		x	x	x <5%	x
IVT-04	granulite	x	x	x		x	x	x <5%	x

Table 5.2: Mineralogy of the samples IVT-21, IVT-18 and IVT-04 with the mineral abbreviations Qtz: Quartz, Plag: Plagioclase, Kfs: K-feldspar, Sil: Sillimanite, Gnt: Garnet, Opx: Orthopyroxene, Bt: Biotite and Ilm: Ilmenite after Kretz (1983).

5.5 Analytical Technique

The Cameca SX100 electron probe microanalyser (EPMA) at RSES, ANU was used to obtain quantitative transects from ilmenite into garnet. Point analyses of the ilmenite inclusions and host garnet were also obatined as well as point analyses of ilmenites surrounded by a non-reactive matrix of plagioclase and quartz. The concentrations of Na, Mg, Al, Mn, Fe, Ca, Ti, Si and P were measured. Samples were analysed with an accelerating voltage of 15 keV and a 20 nA beam current using wavelength-dispersive spectrometers (WDS). The beam size was approximately 1 μm with an activation volume three times this size. Nine transects were measured across ilmenite inclusions in garnet. For transects the step size was 1.5 to 5 μm. The majority of transects were started at the centre of the inclusion and traversed into the garnet, with the exception of garnet 3 in sample IVT-04, which traversed the entire garnet. For all transects the beam traversed perpendicular to the interface between the two minerals across the short axis of the ilmenite into the garnet.

5.6 Results

Back-scattered electron images were obtained for each garnet and ilmenite inclusion analysed, these images are shown in Figures 5.7 to 5.12. An average composition for each garnet and ilmenite pair was obtained from the point analyses. These compositions were then normalised. The compositions of garnets and ilmenite inclusions measured in this study are shown in Tables 5.3 and 5.4 (p.133-134). Quantitative transects across ilmenite inclusions into the surrounding garnet were performed and the results for Mg, Mn, and Fe are shown in Figures 5.12 to 5.14 (p. 136-138).

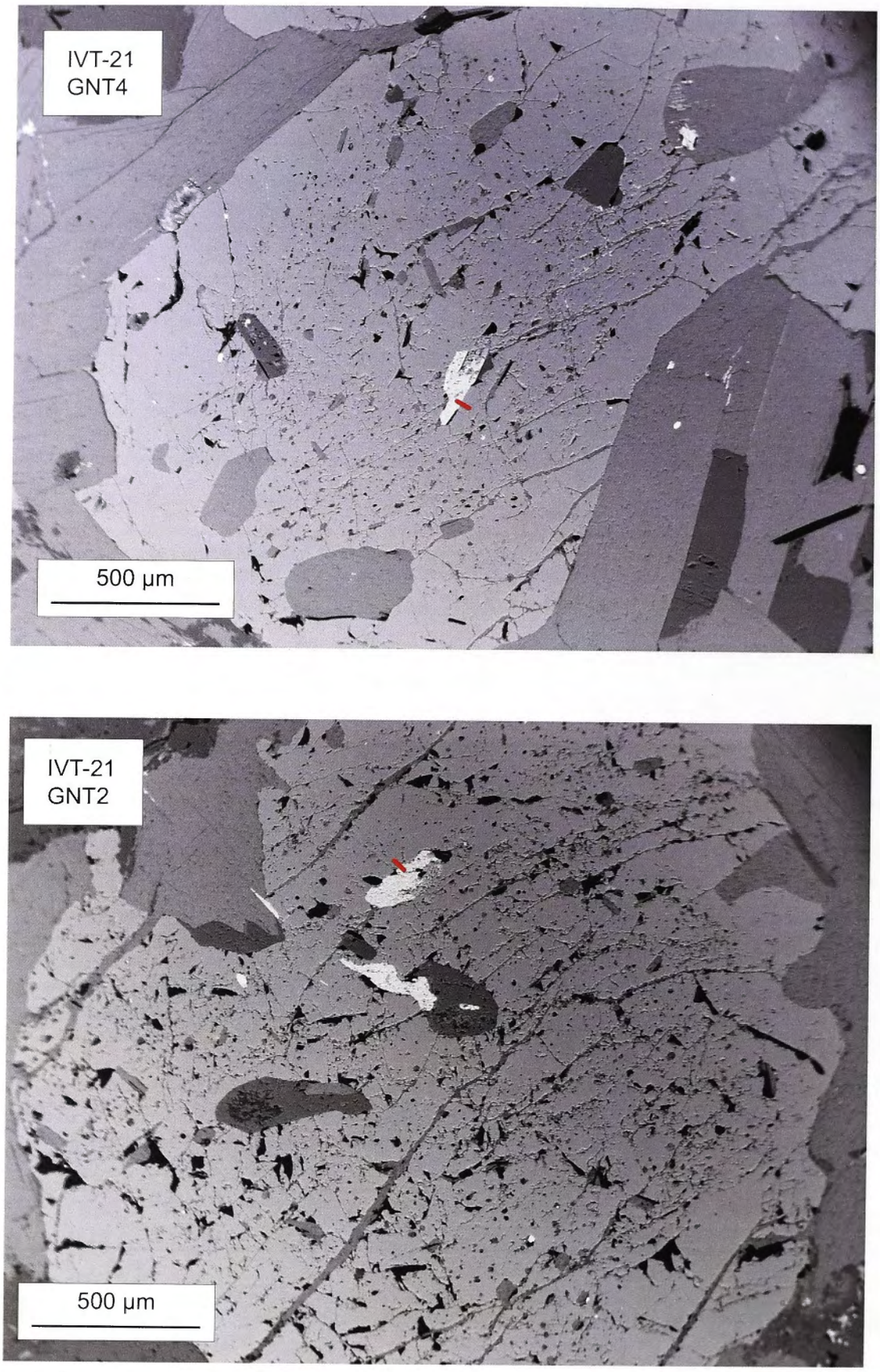

Figure 5.7: Back-scattered electron images from EPMA of the garnet and ilmenite measured in sample IVT-21, Gnt4 and Gnt2, with the transects shown.

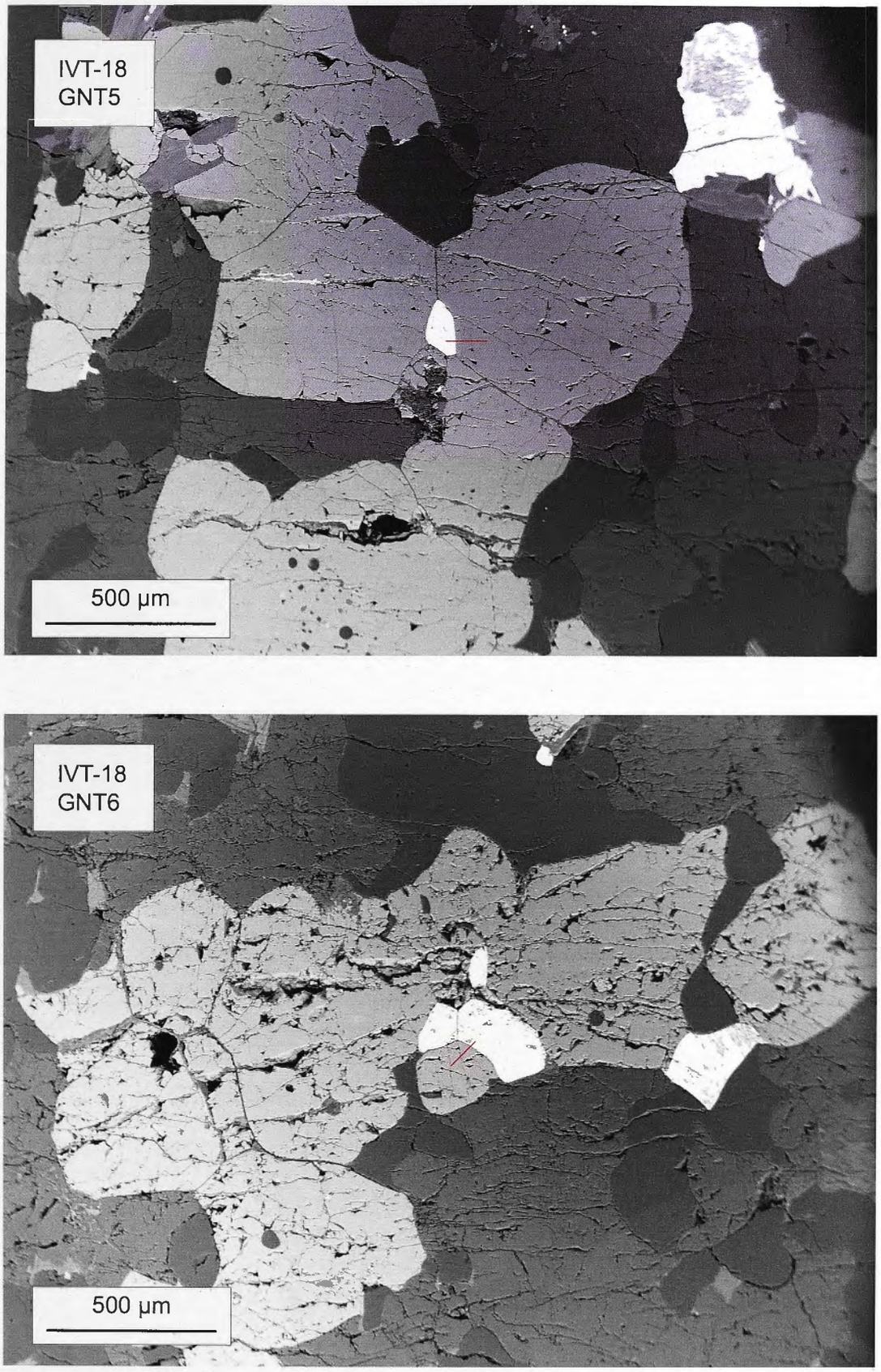

Figure 5.8: Back-scattered electron images from EPMA of the garnet and ilmenite measured in sample IVT-18, Gnt5 and Gnt6, with the transects shown.

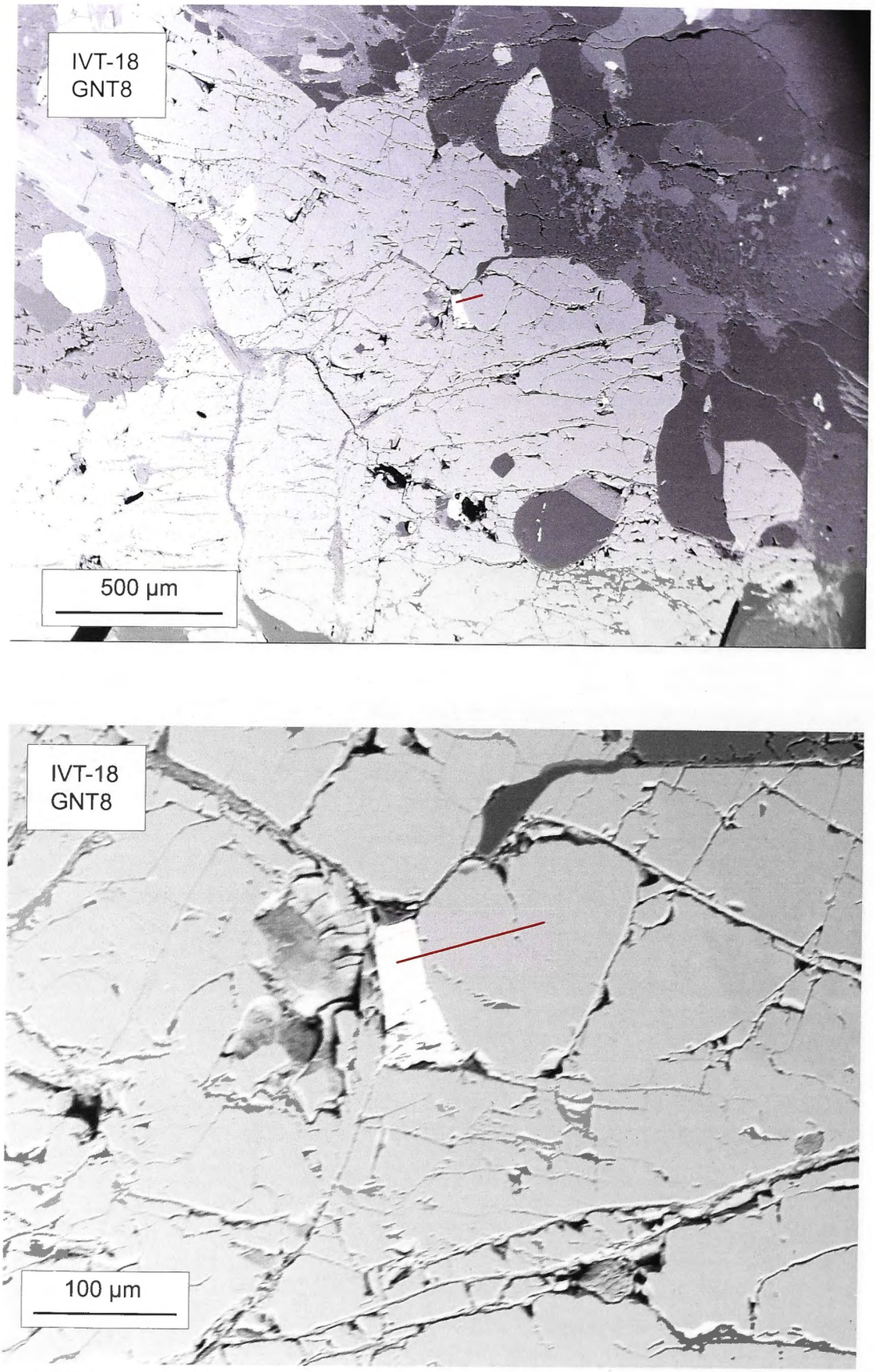

Figure 5.9: Back-scattered electron images from EPMA of the garnet and ilmenite measured in sample IVT-18, Gnt8, with the transect shown. The bottom image shows the ilmenite inclusion at a higher magnification.

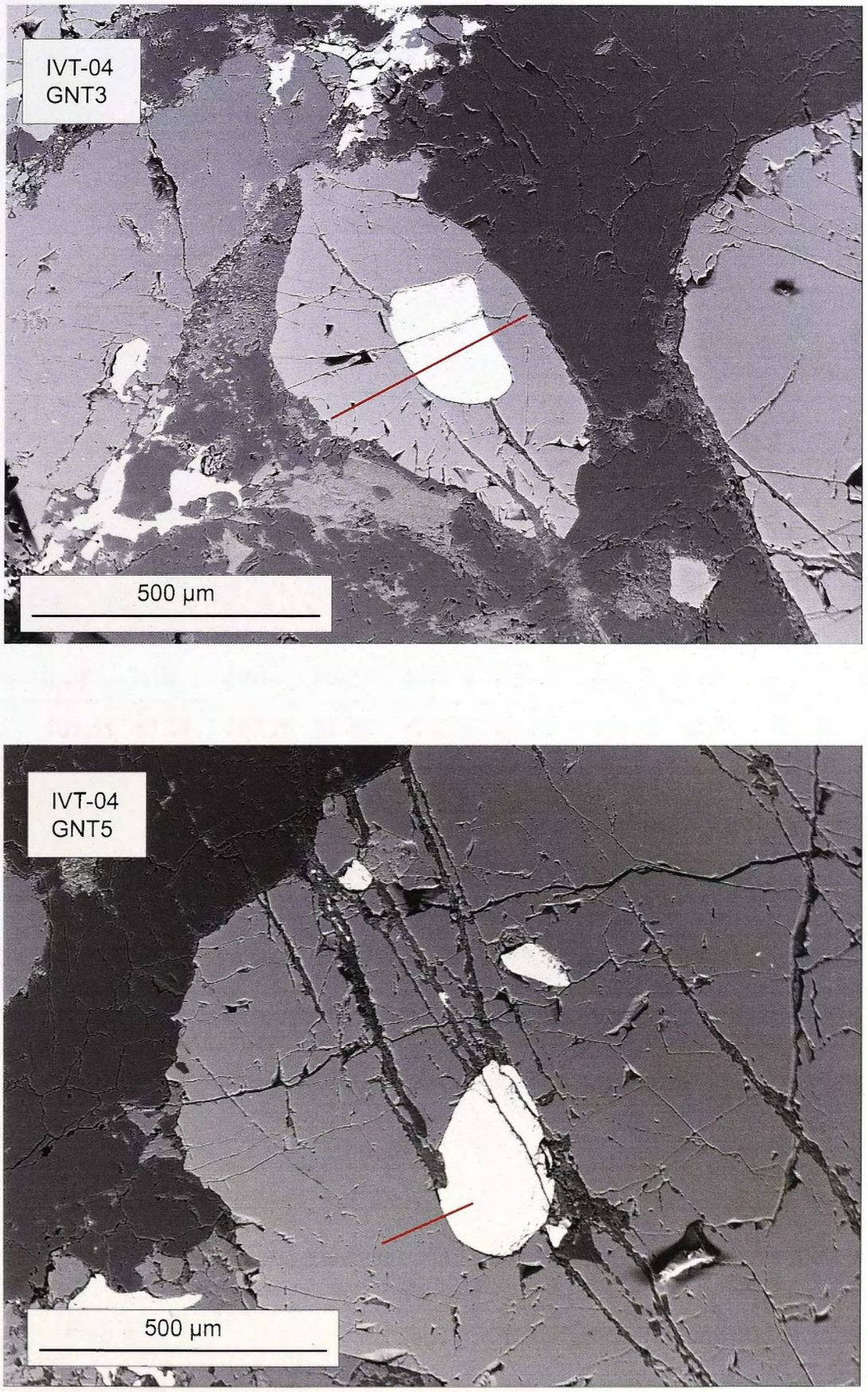

Figure 5.10: Back-scattered electron images from EPMA of the garnet and ilmenite measured in sample IVT-04, Gnt3 and Gnt5, with the transects shown.

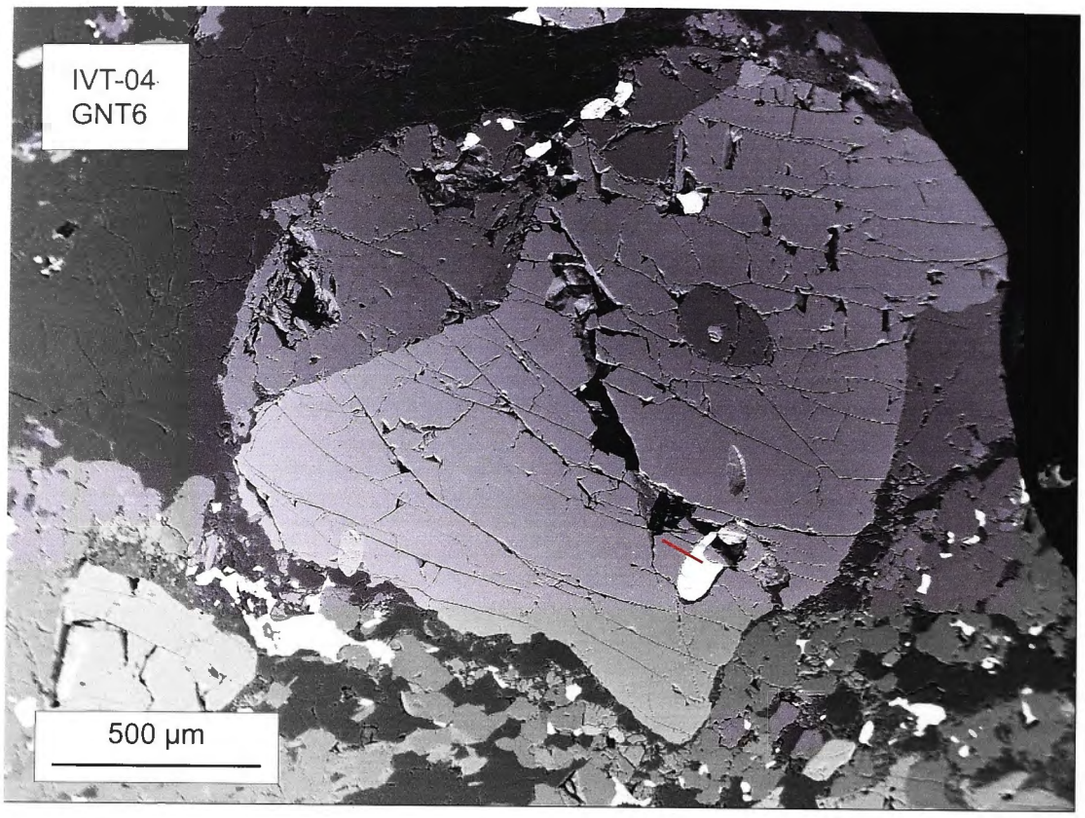

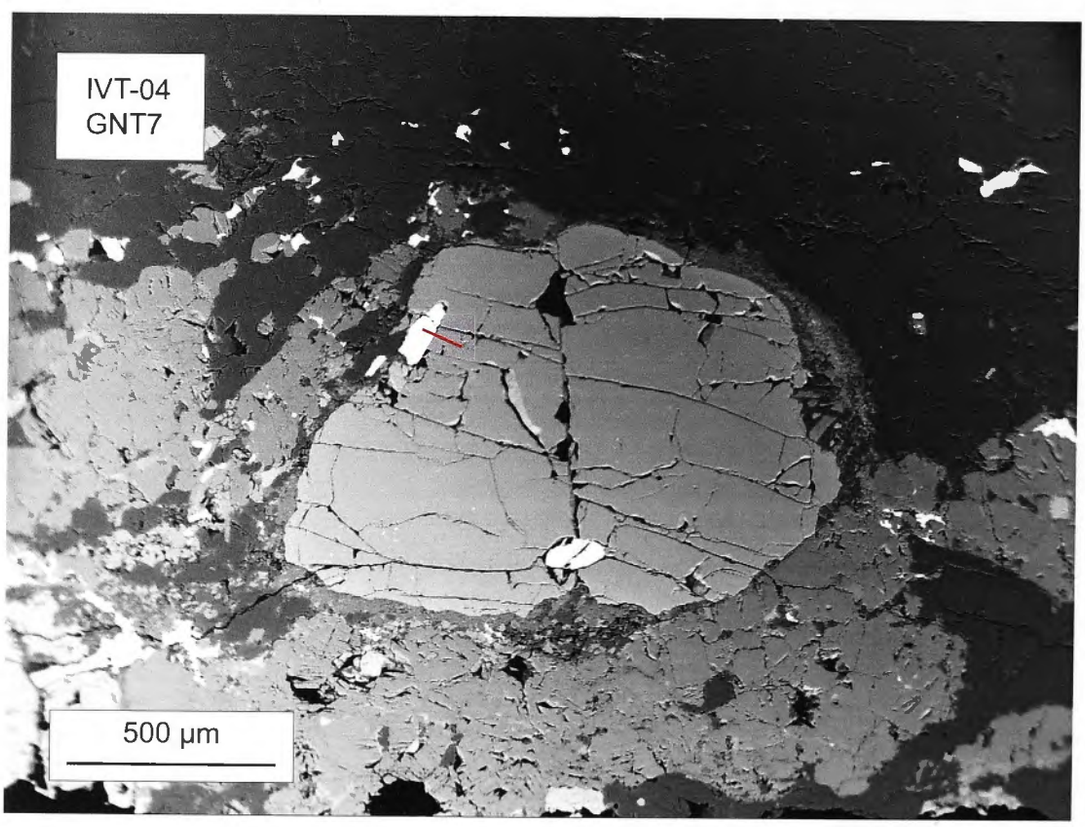

Figure 5.11: Back-scattered electron images from EPMA of the garnet and ilmenite measured in sample IVT-04, Gnt6 and Gnt7, with the transects shown.

	IVT-18						IVT-21			
Oxide	**Gnt 5**	**Ilm 5**	**Gnt 6**	**Ilm 6**	**Gnt 8**	**Ilm 8**	**Gnt 2**	**Ilm 2**	**Gnt 4**	**Ilm 4**
SiO_2	39.12	b.d	39.46	b.d	39.60	b.d	36.80	0.2	37.44	0.10
TiO_2	0.05	49.82	0.07	49.94	0.04	51.97	0.05	50.54	0.14	51.50
Al_2O_3	22.02	0.05	22.28	b.d	22.45	b.d	22.90	0.08	23.02	b.d
Cr_2O_3	0.03	0.03	0.02	0.03	0.05	0.03	n.a	n.a	n.a	n.a
Fe_2O_3	3.04	5.29	2.67	5.05	3.13	2.77	2.78	0.87	2.84	1.37
FeO	24.62	41.46	24.86	41.48	25.36	43.40	30.00	41.14	30.50	40.66
MnO	0.58	0.75	0.62	0.84	0.56	0.69	1.40	2.08	1.42	3.31
MgO	9.41	0.07	9.31	0.08	9.32	0.05	4.88	b.d	5.07	b.d
CaO	2.53	0.03	2.97	b.d	2.68	0.02	1.69	0.03	1.66	0.03
Na_2O	b.d	b.d	b.d	b.d	b.d	0.00	b.d	b.d	b.d	b.d
P_2O_5	0.04	0.00	0.04	0.00	0.05	b.d	b.d	0.00	b.d	0.00
Total	**101.51**	**97.48**	**102.29**	**97.42**	**103.25**	**98.93**	**100.49**	**94.93**	**102.08**	**96.97**
Atom										
Si	2.936	0.000	2.939	b.d	2.927	b.d	2.865	0.005	2.870	0.003
Ti	0.003	0.949	0.004	0.952	0.002	0.974	0.003	0.985	0.008	0.984
Al	1.948	0.001	1.955	b.d	1.955	b.d	2.101	0.002	2.079	b.d
Cr	0.002	0.001	0.001	0.001	0.003	0.001	n.a	n.a	n.a	n.a
Fe^{3+}	0.172	0.101	0.149	0.096	0.174	0.052	0.163	0.017	0.164	0.026
Fe^{2+}	1.637	0.929	1.640	0.931	1.660	0.957	2.068	0.944	2.070	0.915
Mn	0.037	0.016	0.039	0.018	0.035	0.015	0.092	0.046	0.092	0.071
Mg	1.053	0.003	1.033	0.003	1.027	0.002	0.566	b.d	0.580	b.d
Ca	0.203	0.001	0.237	b.d	0.213	0.001	0.141	0.001	0.136	0.001
Na	0.000	0.000	b.d	b.d	b.d	0.000	b.d	b.d	b.d	b.d
P	0.003	0.000	0.003	0.000	0.003	b.d	b.d	0.000	b.d	0.000
Cations	**8.000**	**2.000**	**8.000**	**2.000**	**8.000**	**2.000**	**8.000**	**2.000**	**8.000**	**2.000**

Table 5.3: Compositions of garnet and ilmenite in samples IVT-18 and IVT-21 obtained from EPMA analyses. Garnet analyses are normalised to 12 oxygens and ilmenite analyses are normalised to 3 oxygens. Abbreviations used: b.d: below detection limit and n.a: not measured in analysis.

	IVT-04									
Oxide	**Gnt 3**	**Ilm 3**	**Gnt 4**	**Ilm 4**	**Gnt 5**	**Ilm 5**	**Gnt 6**	**Ilm 6**	**Gnt 7**	**Ilm 7**
SiO_2	38.57	0.11	38.15	0.00	38.30	0.00	38.29	0.05	38.30	0.06
TiO_2	0.10	52.87	0.08	53.32	0.22	53.06	0.06	53.26	0.09	53.01
Al_2O_3	22.55	0.08	22.34	0.04	22.29	0.05	23.36	b.d	23.28	b.d
Cr_2O_3	b.d	0.02	b.d	b.d	0.02	0.02	n.a	n.a	n.a	n.a
Fe_2O_3	4.88	4.14	5.03	2.82	4.19	3.97	2.74	2.10	1.46	0.00
FeO	22.35	44.39	22.20	44.64	22.46	44.40	22.63	44.72	22.10	42.51
MnO	0.57	0.39	0.62	0.43	0.60	0.46	0.57	0.40	0.53	0.40
MgO	7.45	0.13	7.32	0.13	7.43	0.12	7.30	0.09	7.55	0.14
CaO	6.91	0.04	6.77	0.02	6.71	0.03	6.46	0.03	6.65	0.03
Na_2O	b.d	0.00	b.d	b.d	b.d	b.d	b.d	b.d	b.d	b.d
P_2O_5	0.08	0.00	0.08	0.00	0.12	0.00	b.d	b.d	b.d	b.d
Total	**103.46**	**102.16**	**102.61**	**101.40**	**102.33**	**102.11**	**101.43**	**100.65**	**99.99**	**96.15**
Atom										
Si	2.864	0.003	2.859	0.000	2.873	0.000	2.883	0.001	2.909	0.002
Ti	0.005	0.959	0.005	0.974	0.012	0.963	0.004	0.980	0.005	1.020
Al	1.974	0.002	1.973	0.001	1.970	0.001	2.072	b.d	2.084	b.d
Cr	b.d	0.000	b.d	b.d	0.001	0.000	n.a	n.a	n.a	n.a
Fe^{3+}	0.273	0.075	0.284	0.052	0.236	0.072	0.155	0.039	0.084	0.000
Fe^{2+}	1.470	0.948	1.473	0.960	1.492	0.949	1.509	0.968	1.487	0.963
Mn	0.036	0.008	0.040	0.009	0.038	0.009	0.037	0.008	0.034	0.009
Mg	0.824	0.005	0.818	0.005	0.831	0.004	0.820	0.003	0.855	0.005
Ca	0.550	0.001	0.544	0.001	0.539	0.001	0.521	0.001	0.541	0.001
Na	b.d	0.000	b.d	b.d	b.d	b.d	b.d	b.d	b.d	b.d
P	0.005	0.000	0.006	0.000	0.007	0.000	b.d	b.d	b.d	b.d
Cations	**8.000**	**2.000**	**8.000**	**2.000**	**8.000**	**2.000**	**8.000**	**2.000**	**8.000**	**2.000**

Table 5.4: Compositions of garnet and ilmenite in samples IVT-04 obtained from EPMA analyses. Garnet analyses are normalised to 12 oxygens and ilmenite analyses are normalised to 3 oxygens. Abbreviations used: b.d: below detection limit and n.a: not measured in analysis.

The composition of ilmenite inclusions in garnet was compared to ilmenites in a non-reactive matrix. The latter are assumed to reflect the initial compositions of the ilmenite inclusions that have not participated in Fe and Mn exchange with garnet. The results are shown in Table 5.5 for samples IVT-18 and IVT-04. These values are averages of several point analyses on the same ilmenite. Sample IVT-21 did not contain any suitable ilmenite surrounded by non-reactive matrix minerals for analysis.

Ilm in Qtz	Sample			Sample	
Oxide	**IVT-18**	**IVT-04**	**Atom**	**IVT-18**	**IVT-04**
SiO_2	b.d	0.09	Si	b.d	0.002
TiO_2	50.52	52.25	Ti	0.951	0.974
Al_2O_3	b.d	0.17	Al	b.d	0.005
Cr_2O_3	0.03	n.a	Cr	0.001	n.a
Fe_2O_3	5.18	2.29	Fe^{3+}	0.098	0.043
FeO	42.19	43.58	Fe^{2+}	0.935	0.957
MnO	0.50	0.27	Mn	0.011	0.006
MgO	0.12	0.30	Mg	0.004	0.011
CaO	0.04	0.05	Ca	0.001	0.001
Na_2O	b.d	b.d	Na	b.d	b.d
K_2O	b.d	n.a	K	b.d	n.a
P_2O_5	b.d	b.d	P	b.d	b.d
Total	**98.58**	**99.01**	**Cations**	**2.000**	**2.000**

Table 5.5: Compositions of ilmenites in a non-reactive matrix of plagioclase and quartz from samples IVT-18 and IVT-04. Abbreviations used: b.d: below detection limit and n.a: not measured in analysis.

These analyses show that the concentration of Mn in the ilmenite surrounded by a non-reactive matrix is lower than the Mn concentration in ilmenite inclusions within garnet. For sample IVT-04 the concentration of Mg is higher in the ilmenite in a non-reactive matrix than ilmenite inclusions. This result is reflected in sample IVT-18 although the difference in Mg concentrations is not as great between the ilmenite inclusions and ilmenite in a non-reactive matrix.

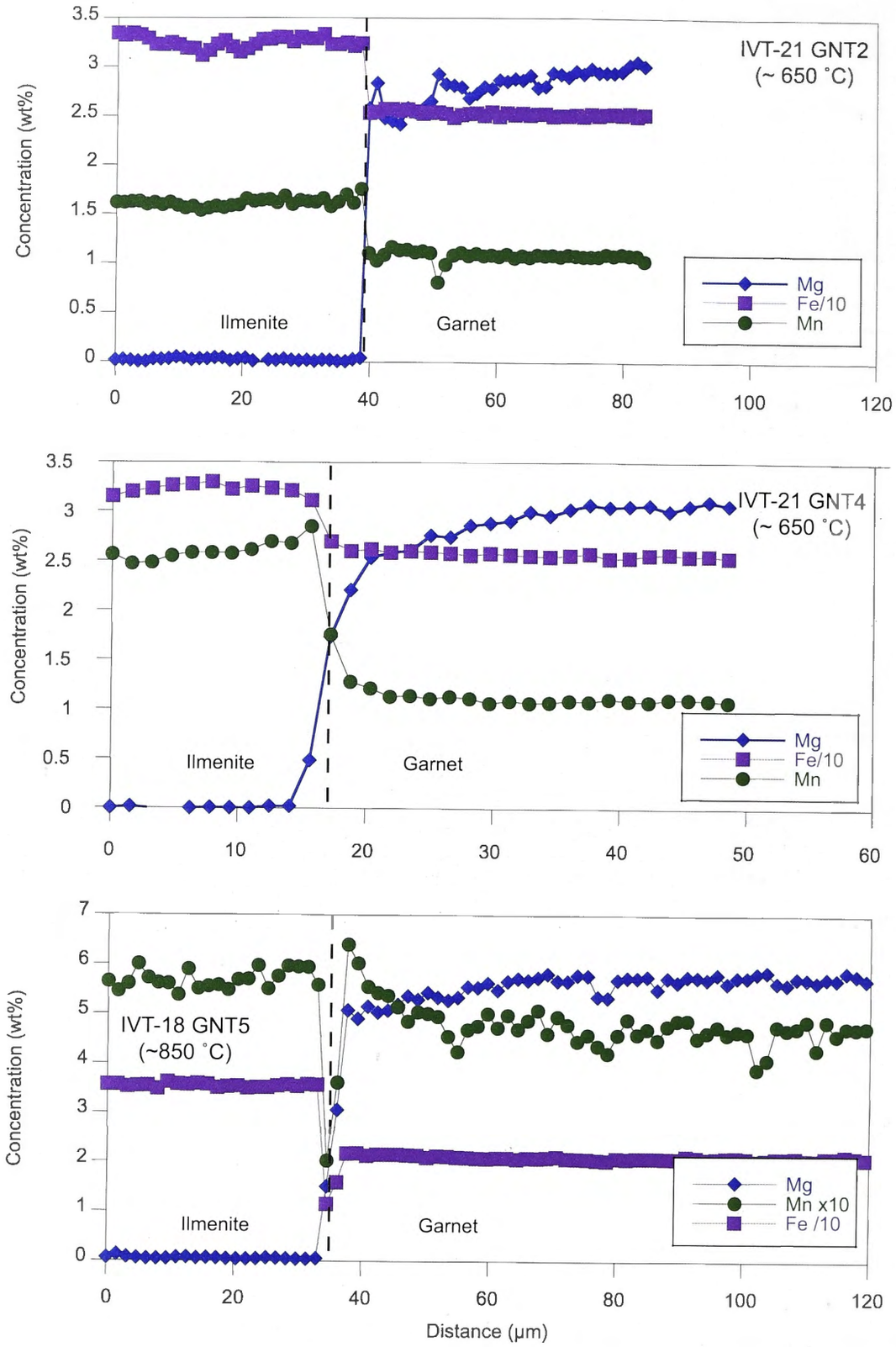

Figure 5.12: EPMA transect from an ilmenite inclusion into garnet from samples IVT-21 and IVT-18. The boundary is marked by a dotted line. The concentrations have been scaled for comparison, with Fe concentrations divided by 10 and Mn concentrations in IVT-18 Gnt5 multiplied by 10.

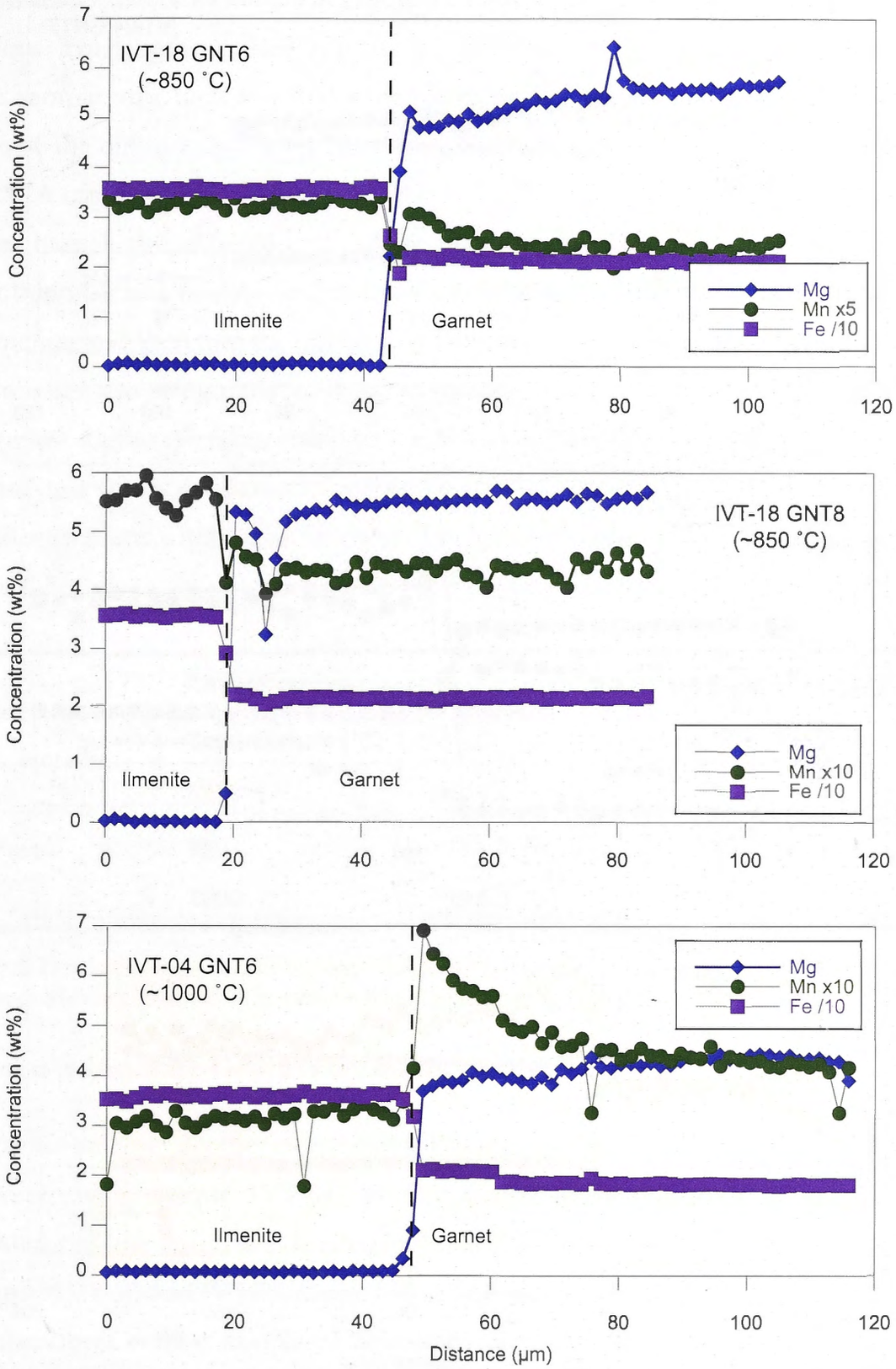

Figure 5.13: EPMA transect from an ilmenite inclusion into garnet from sample IVT-18 and IVT-04. The boundary between the two phases is marked by a dotted line. The concentrations have been scaled for comparison, with Fe concentrations divided by 10 and Mn concentrations in IVT-18 Gnt6 multiplied by 5 and in IVT-18 Gnt8 and IVT-04 Gnt6 multiplied by 10.

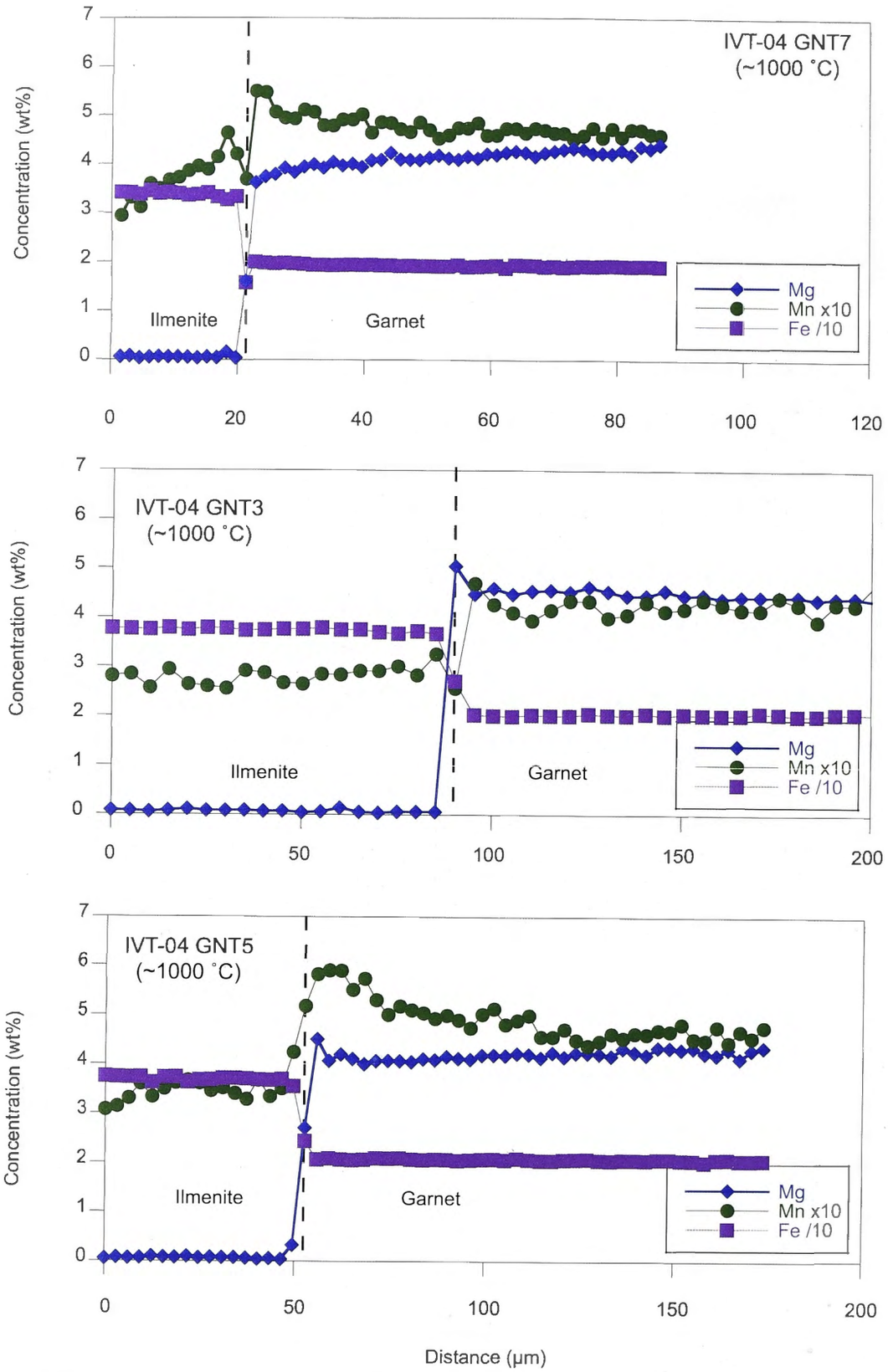

Figure 5.14: EPMA transect from an ilmenite inclusion into garnet from sample IVT-04. The boundary between the two phases is marked by a dotted line. The concentrations have been scaled for comparison, with Fe concentrations divided by 10 and Mn concentrations multiplied by 10.

In the transects Mn concentration gradients are observed in garnet adjacent to ilmenite inclusions. The lengths of these features are proportional to peak temperatures attained by the sample, this indicates that these features are diffusion related. The estimated lengths of the diffusion profiles observed in this study are shown in Table 5.6. However, the EPMA transects (Figs 5.12 to 5.14) show that the ilmenites in the lower temperature samples have higher Mn concentrations than the adjacent garnet. This higher Mn concentration is inconsistent with expected partitioning of Fe and Mn between garnet and ilmenite and therefore the garnet and ilmenite are not in equilibrium. The ilmenite inclusions are also being replaced by other phases. In addition, the concentration profiles of Mg show an inverse relationship to the Mn indicating that exchange of Mg with Mn may also be a significant part of this system. This is likely to be a result of relatively high Mg concentrations within these garnets. These observations will be discussed further in Section 5.8.

Sample	Estimated Peak Temperature (°C)	Analysis	Length of Diffusion Profile (~µm)
IVT-21	650	Gnt 2	6
IVT-18	850	Gnt 5, Gnt 6	25
IVT-04	1000	Gnt 5	55

Table 5.6: Estimated lengths of the obtained diffusion profiles. The lengths show a trend of longer diffusion profiles being preserved in samples that attained higher peak temperatures.

5.7 Garnet-Ilmenite Geothermometry

The garnet-ilmenite geothermometer of Pownceby et al. (1987) was used to calculate temperatures for sample IVT-04, as this sample does not show incongruous Mn concentrations; the results are detailed in Table 5.7. The partitioning behaviour observed in samples IVT-18 and IVT-21 meant this system was unable to be used for determination of temperatures in these samples. The temperatures calculated for sample IVT-04 range from 957 °C to 1103 °C. The temperatures calculated from this one sample vary over a 150 °C range. The wide range of temperatures determined could be related to the Mn concentration of the sample as garnet-ilmenite geothermometry often shows erratic temperatures when Mn concentrations are low.

Analysis	Xgnt Mn	Xgnt Fe	Xilm Mn	Xilm Fe	ln Kd	T(°C)
Gnt 3	0.013	0.510	0.008	0.985	1.065	971.9
Gnt 4	0.014	0.512	0.009	0.985	1.064	973.0
Gnt 5	0.013	0.514	0.009	0.985	0.988	1028.0
Gnt 6	0.013	0.523	0.008	0.988	1.088	956.8
Gnt 7	0.012	0.510	0.009	0.985	0.895	1102.8

Table 5.7: Temperatures determined from the garnet-ilmenite geothermometer by Pownceby et al. (1987) for sample IVT-04 from Val Mastallone, Ivrea-Verbano Zone.

All concentration profiles measured in sample IVT-04 across ilmenite inclusions in garnet showed a Mn diffusion profile surrounding ilmenite inclusions (Figs. 5.13 and 5.14). These profiles are assumed to be due to diffusion after peak metamorphic temperatures have been reached. Therefore, the change in concentrations will affect the calculated temperatures by changing the composition of the ilmenite. During cooling Mn is expelled from ilmenite into the garnet this results in the Mn concentration in the ilmenite being lower than at peak temperature. It can be assumed that the concentrations measured in garnet away from the ilmenite inclusion will represent concentrations at peak temperature As a result the temperatures calculated from the average compositions of garnet and ilmenite (Table 5.7) will be minimum estimates of peak temperatures (Fig. 5.15).

Temperatures calculated using the concentration of the garnet adjacent to the boundary between ilmenite and garnet are shown in the Table 5.8. The calculated temperatures range from 783 to 969 °C. The average temperature calculated for garnet adjacent to ilmenite is 888.1 ± 68 °C and for average garnet compositions is 1006.5 ± 54 °C. The errors are statistical errors of one standard deviation.

Analysis	Xgnt Mn	Xgnt Fe	Xilm Mn	Xilm Fe	ln Kd	T(°C)
Gnt 3	0.014	0.518	0.008	0.985	1.150	915.8
Gnt 5	0.017	0.527	0.009	0.985	1.200	884.6
Gnt 6	0.019	0.564	0.008	0.988	1.387	782.8
Gnt 7	0.015	0.563	0.009	0.985	1.069	969.2

Table 5.8: Temperatures calculated from the composition of the garnet directly adjacent to ilmenite inclusions using garnet-ilmenite geothermometry (Pownceby et al 1987). A transect was not carried out Gnt 4 and therefore a temperature for the adjacent garnet could not be calculated.

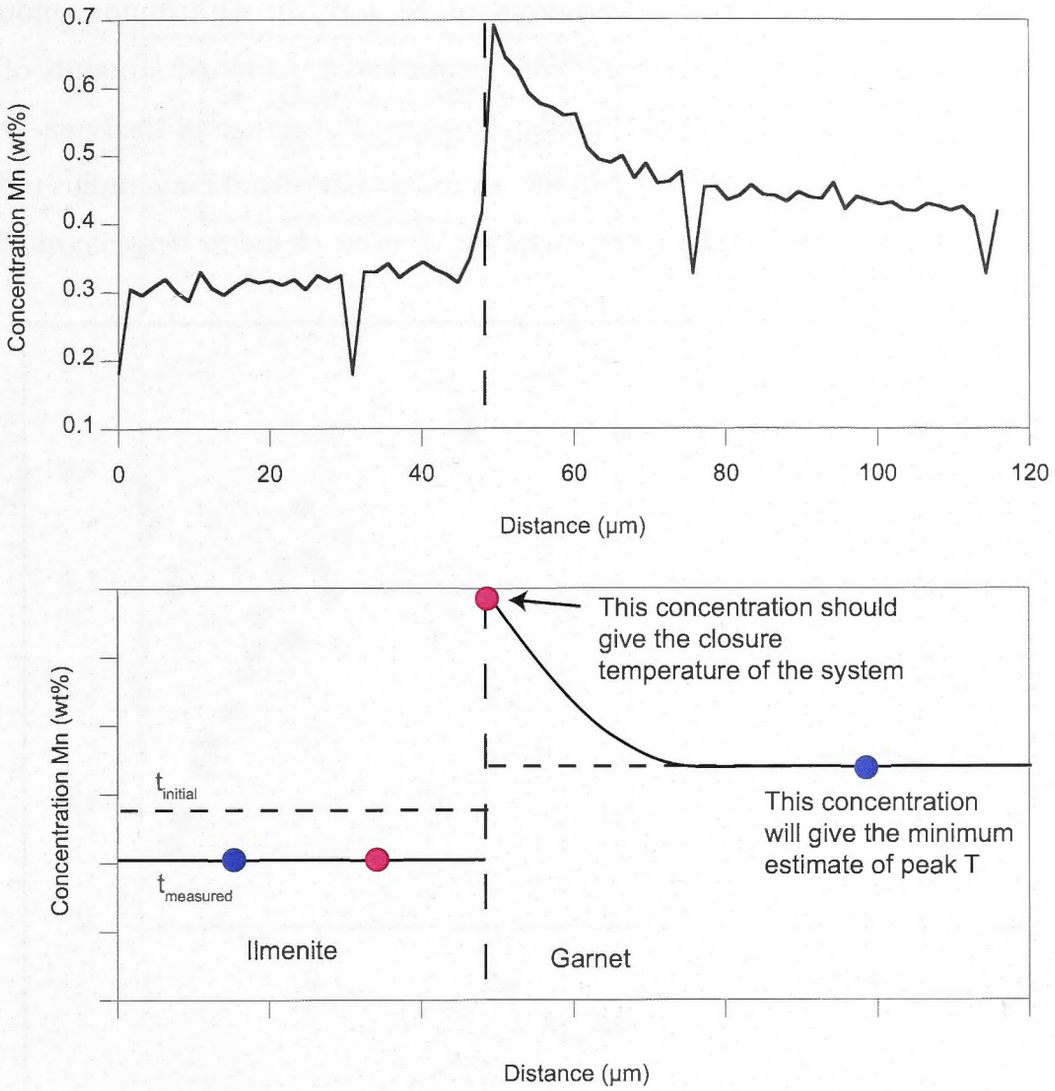

Figure 5.15: A schematic representation of a Mn concentration profile across an ilmenite-garnet boundary and the temperatures calculated from different compositions of garnet.

5.8 Discussion

In this study diffusion profiles in Mn concentration profiles were observed and measured in garnet surrounding ilmenite inclusions. However, Mg concentration profiles show the inverse diffusion profiles and evidence of unusual partitioning behaviour between garnet and ilmenite has also been observed in the Ivrea-Verbano Zone samples.

5.8.1 Mg Concentration Profiles

A feature of the concentration profiles measured in the Ivrea-Verbano Zone samples is an observable decrease in Mg concentration towards the ilmenite inclusion (Figs. 5.12 to 5.14), which is opposite to Mn concentration profiles. The Mg concentration profiles suggest that Mg is also involved in the exchange reaction. The garnet and ilmenite

system generally contains high concentrations of Fe and Mn with minor amounts of other components Mg, Ca and Fe^{3+} (O'Neill et al., 1989). Minimal amounts of other components make it a simpler system to model. However, the garnets of the Ivrea-Verbano Zone samples are Mg-rich (Fig. 5.16). Mn has a similar charge and ionic radius to Fe, Mg and Ca (Kretz, 1959) and this allows for exchange of these elements between minerals.

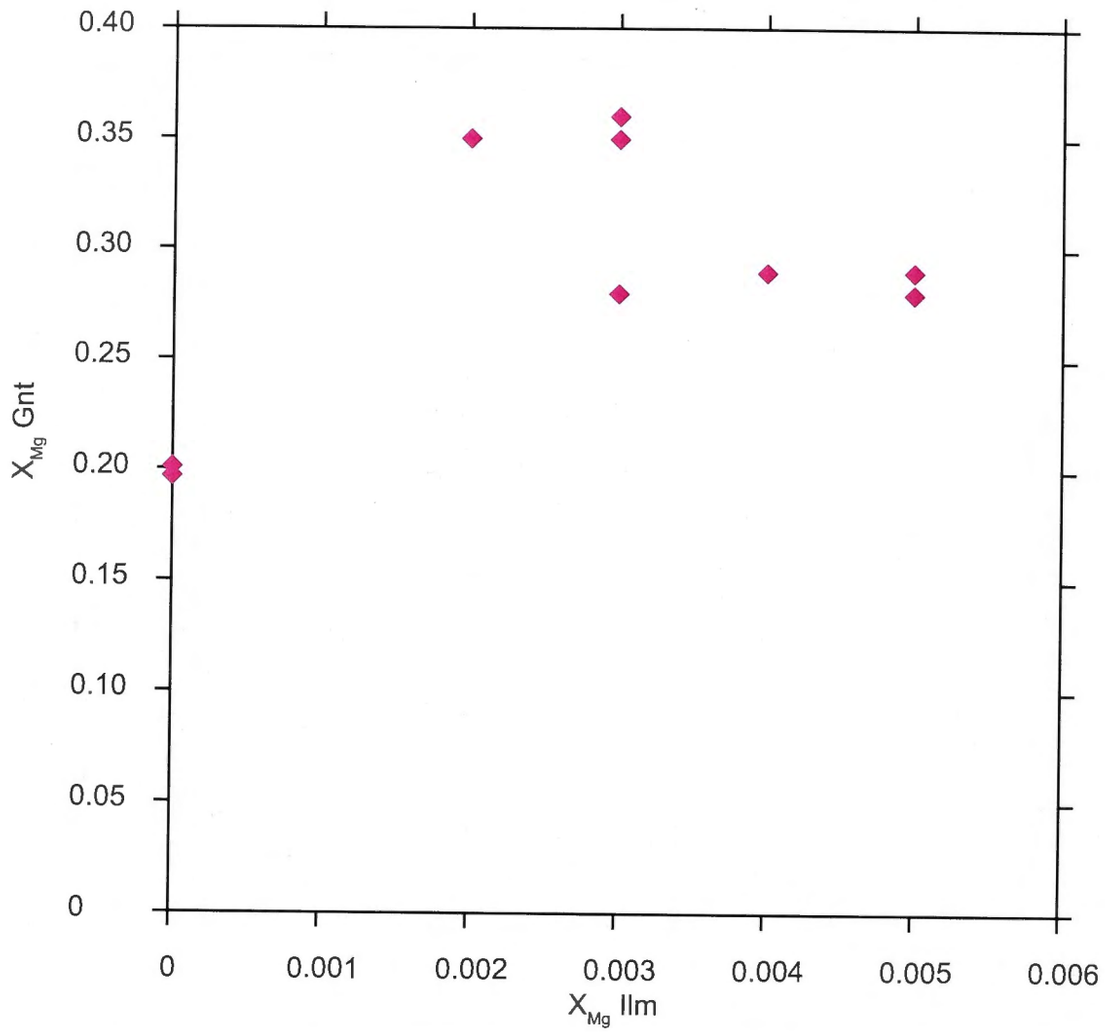

Figure 5.16: Mg concentration in ilmenite against the Mg concentration in garnet, where X_{Mg} = Mg/ (Mg+Fe).

The partitioning of Mg and Fe has been calibrated experimentally. The partition coefficient for Fe and Mg between garnet and ilmenite has been inferred to not vary with temperature, pressure or composition (Green and Sobolev, 1975). This result was corroborated by a later study (Koziol and Bohlen, 1992). When the compositions of Ivrea-Verbano Zone samples are compared to the experimental results of partitioning of Mg and Fe between garnet and ilmenite (Green and Sobolev, 1975; Koziol and Bohlen 1992) it is observed that the Ivrea-Verbano Zone ilmenite inclusions are depleted in Mg for samples IVT-18 and IVT-04 (Fig. 5.17).

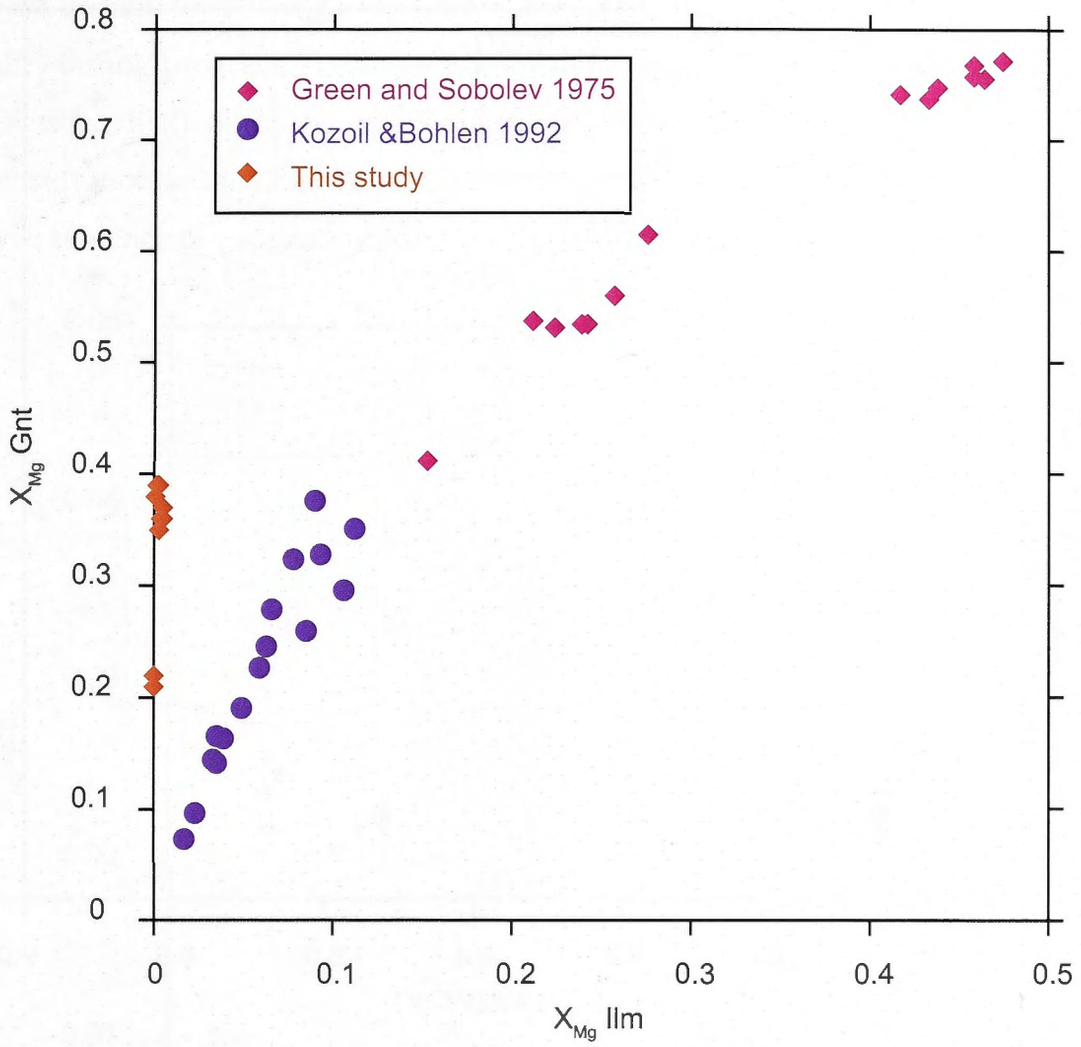

Figure 5.17: Mg concentration in ilmenite against Mg concentration in garnet from this study compared to experimental data (Green and Sobolev, 1975; Koziol and Bohlen, 1992).

In the Arrhenius plot the partition coefficient of Fe and Mg in samples IVT-18 and IVT-04 is compared to the experimental studies of Koziol and Bohlen (1992) as shown in Figure 5.18. Mg concentrations in ilmenite are below detection limits in sample IVT-21, therefore the partition coefficient cannot be calculated. The partition coefficient for IVT-18 is higher than the partition coefficient for IVT-04. Previous experimental studies showed the partition coefficient may be positively correlated with Fe_2O_3 substitution in ilmenite (Green and Sobolev, 1975). From the composition (Tables 5.3 and 5.4) of these samples this trend would be consistent with the correlation between Fe^{3+} concentrations in ilmenite and the partition coefficient.

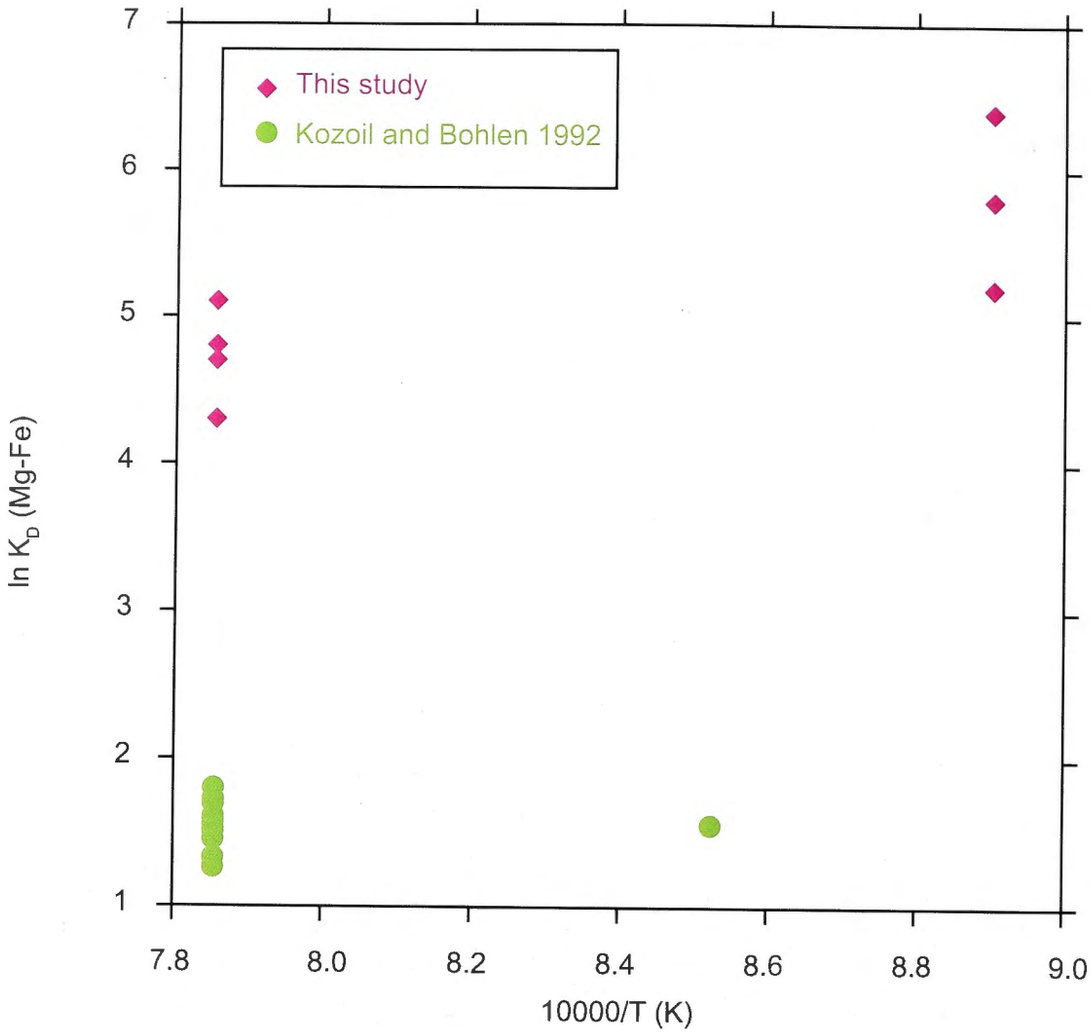

Figure 5.18: Arrhenius plot of inverse temperature against the K_D for Mg and Fe between garnet and ilmenite compared to experimental data (Koziol and Bohlen, 1992).

5.8.2 Fe and Mn Partitioning

Previous studies have shown that compared to coexisting phases garnet strongly concentrates Mn (Hollister, 1966) with Mn/(Mn+Fe) decreasing in the order of Gar>Ilm>St>Crd>Bt (Thompson, 1976; Woodsworth 1977). However, it is observed that in samples IVT-18 and IVT-21 the ilmenite inclusions have higher Mn concentrations than the host garnet (see Tables 5.3 and 5.4). The Mn concentrations of ilmenites and garnets are plotted in Figure 5.19. A previous study by Woodsworth (1977) observed a similar phenomenon where ilmenite inclusions had higher concentrations of Mn than expected based on the Mn concentrations in the host garnet. This study by Woodsworth (1977) inferred that the ilmenite inclusions were preserving relict zoning of the garnet as the Mn/(Mn+Fe) ratios in ilmenite inclusions decreased from core to rim (Woodsworth, 1977). While garnets analysed from the Ivrea-Verbano Zone do not have multiple ilmenite inclusions.

It is well documented that garnet exchanges cations with other phases, e.g. biotite and ilmenite, during prograde (Whitney and Ghent, 1993) and retrograde reactions (Tracy and Dietsch, 1982). Since the rate of diffusion in ilmenite is fast (Chapter 2) any changes in concentration in the ilmenite will quickly re-equilibrate. Thus making it impossible to preserve evidence of prograde garnet zoning in ilmenite inclusions.

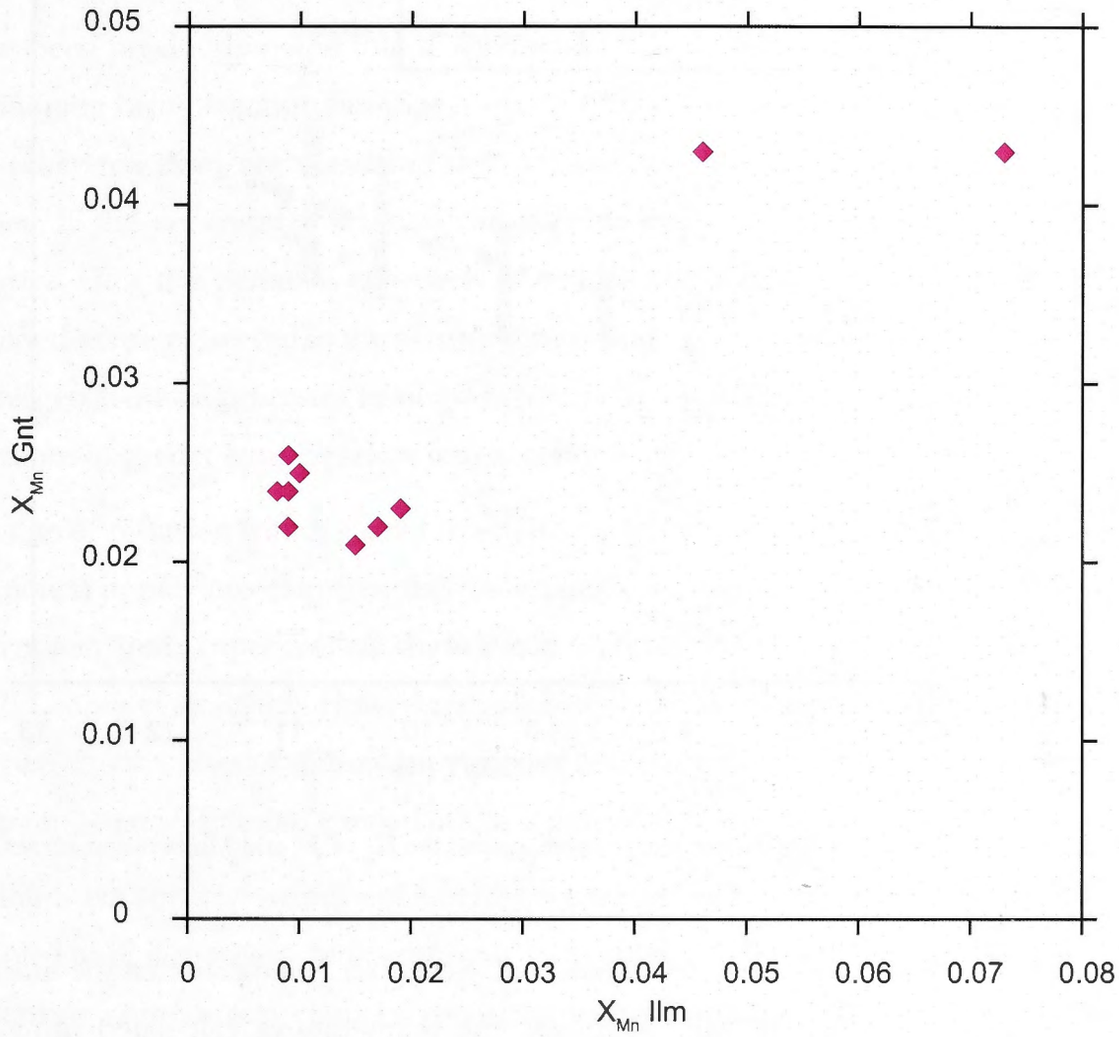

Figure 5.19: Mn concentration in ilmenite plotted against the Mn concentration in garnet. where X_{Mn} = Mn/(Mn+Fe).

The Mn/(Mn+Fe) ratio in garnet and ilmenite can be compared to the ratios obtained from experimental partitioning data. Experiments on the partitioning of Fe and Mn between garnet and ilmenite have been carried out by several studies (e.g. Ono, 1980; Pownceby et al., 1987; 1991; Feenstra and Engi, 1998; Săbău and Massonne, 2003). When plotted on an Arrhenius plot with the inverse temperature against the natural logarithm of the partition coefficient of Fe and Mn between garnet and ilmenite the Ivrea-Verbano Zone samples show an inverse trend to the experimental partitioning data (Fig. 5.20).

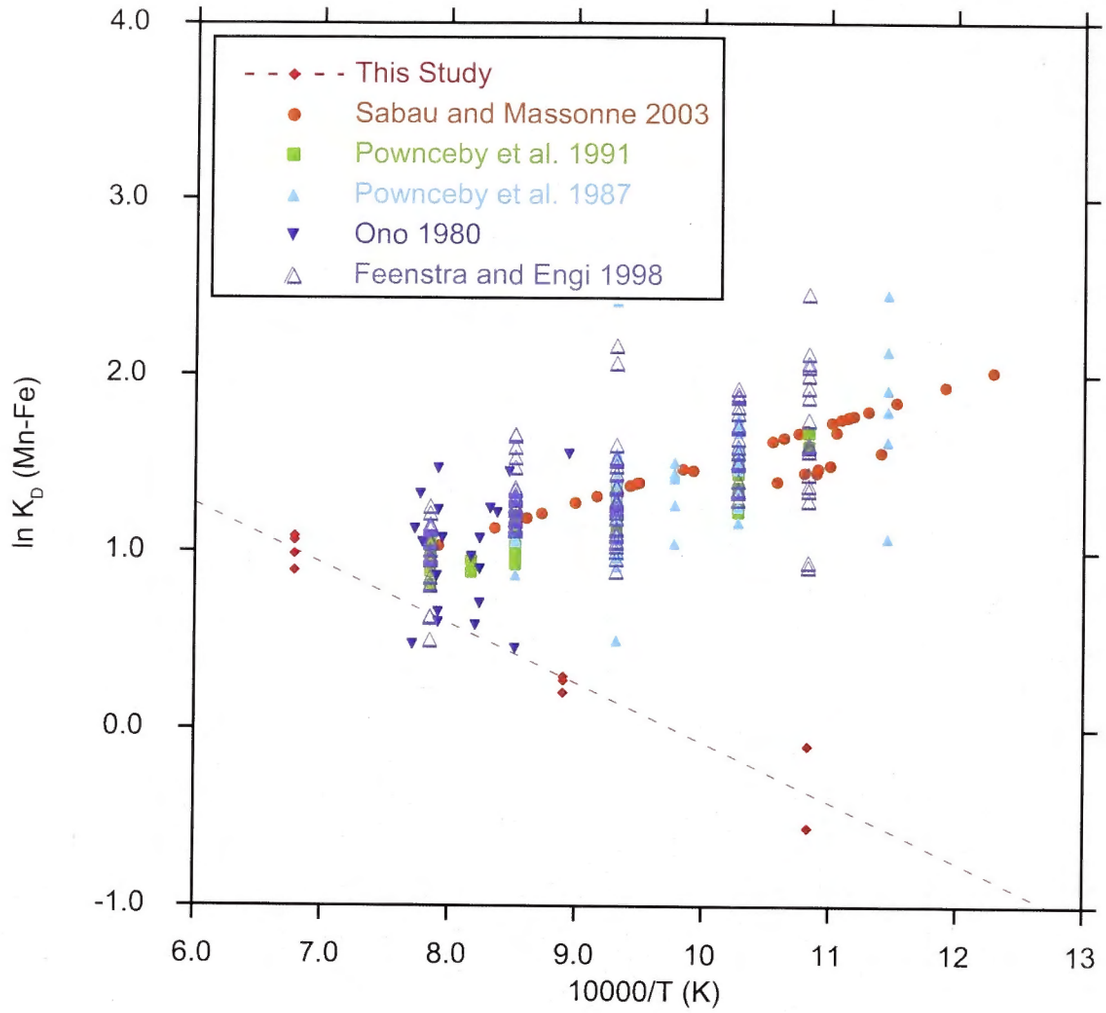

Figure 5.20: Arrhenius plot of the inverse temperature against the K_D of Fe and Mn between garnet and ilmenite.

The results from the geothermometry carried out (Section 5.7) indicate that the ilmenite in IVT-04 is also enriched in Mn. Although, the temperatures calculated using the garnet-ilmenite geothermometer appear to be in agreement with temperatures obtained from the previous study by Ewing et al. (2012). However, at these temperatures diffusion within garnet is fast enough to allow re-equilibration of Fe and Mn concentrations. Therefore, it is implausible that the garnet has actually preserved geochemical evidence of temperatures at 1000 °C. The preservation of these high temperatures indicates that the same process that has caused Mn concentrations in ilmenite to be higher than surrounding garnet in samples IVT-18 and IVT-21 has also modified the composition of the ilmenite in IVT-04 and produced the incongruent temperatures. Additionally, the ilmenites from the Ivrea-Verbano Zone samples in a non-reactive matrix compared

to the ilmenite inclusions in garnet have higher Mg concentrations and lower Mn concentrations. Based purely on the diffusion profiles observed in samples that show evidence that ilmenite inclusions have expelled Mn into the surrounding garnet this is an unexpected result.

5.8.3 Excess Mn in Ilmenite

It has been previously noted that if net transfer reactions have occurred it results in the partitioning being incongruent (Spear et al., 1991). The partitioning behaviour suggests that other reactions are occurring that are effecting the composition of ilmenite and garnet. If the net-transfer reaction causing this was a late retrograde reaction, which occurred after the garnet is effectively closed; it would have no effect on the diffusion profiles that are preserved in the surrounding garnet. Otherwise the effect of this reaction on the geochemical processes involved in producing the diffusion profiles around ilmenite inclusions in garnet must be taken into account when modelling the system.

The rate of diffusion within garnet is well documented in the literature. Although, as was mentioned in previous chapters, there is a significant amount of spread in the diffusivity determined from experimental studies (e.g. Carlson, 2006; Chakraborty and Ganguly, 1992; Loomis et al., 1985). However, regardless of the absolute magnitude, it is slow when compared to the rates of diffusion in ilmenite and this was confirmed by the experimental study on ilmenite diffusion carried out as a part of this project (Chapter 2).

Equilibration between garnet and ilmenite occurs during heating and continues as the rock is cooled until it reaches a temperature where diffusion is less effective and can no longer equilibrate composition changes produced by partitioning, i.e. a closure temperature (Dodson, 1973). The closure temperature varies depending on the cooling rate, grain size and other variables. The closure temperature for garnet is higher than ilmenite as garnet diffusion is relatively slow. Therefore, ilmenite can exchange cations with other phases after the garnet is effectively closed. It was noted by Pownceby et al. (1987) the garnet-ilmenite geothermometer would give erroneously high temperatures if ilmenite were free to react with other Fe and Mn rich phases, e.g. biotite, below the temperature at which the garnet is effectively closed. This is due to the rapid rate of diffusion in ilmenite (Chapter 2). It is also reason that ilmenite inclusions were selected for analysis in this study and are recommended for use with the geothermometer (Pownceby et al., 1987).

The ilmenites within samples IVT-18 and IVT-21 show evidence of reactions occurring. This evidence is seen in the BSE images obtained for these samples (Fig. 5.21). The EPMA results of the other phases are shown in Table 5.9. It is observed that ilmenite is replaced by rutile (TiO_2) and titanite ($CaTiSiO_5$).

Oxide	**IVT-18**		
SiO_2	-	14.548	21.746
TiO_2	99.078	71.272	56.464
Al_2O_3	-	0.860	1.998
Cr_2O_3	0.065	0.055	0.083
FeO	-	-	0.514
MnO	-	-	-
MgO	-	-	-
CaO	0.471	12.455	18.892
K_2O	-	0.016	0.018
P_2O_5	-	0.191	0.213
Total	**99.62**	**99.37**	**99.93**

Table 5.9: The analysis of other phases associated with the ilmenite inclusions observed in sample IVT-18.

It has been observed in previous studies that incomplete transformation of ilmenite during metasomatism can leave symplectic intergrowths of rutile and titanite in ilmenite (Engvik, 2011). In a study by Milos (2008) titanite reaction rims were observed around ilmenite from the Bohemian Massif, Czech Rebuplic. In some cases an enrichment of the $MnTiO_3$ component of ilmenite was measured. This reaction is related to higher oxygen or water fugacities (Milos, 2008). As the TiO_2 is removed to form titanite the residual ilmenite becomes enriched in hematite component (Milos, 2008). For the samples from the Ivrea-Verbano Zone there are higher concentrations of Fe^{3+} measured in ilmenites from IVT-21 that shows greater percentage of replacement than IVT-18. To examine if there is a relationship between the retrogressive phases and the enrichment of ilmenite in Mn the percentage of ilmenite replaced was plotted against the MnO concentration (Fig 5.22). It is observed that the amount of replacement seen in the ilmenite inclusions is not sufficient to account for the large increase in Mn content of the ilmenites.

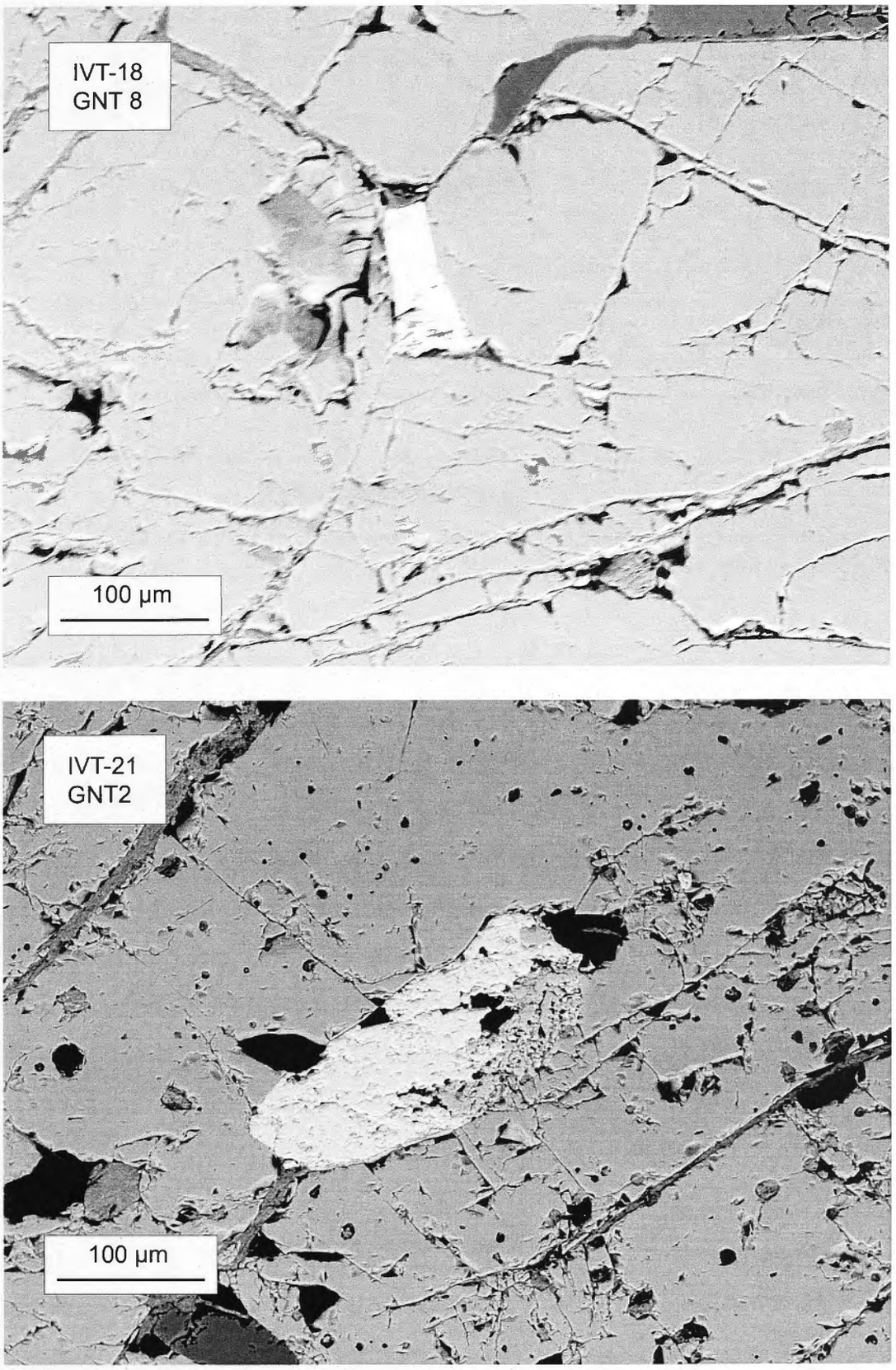

Figure 5.21: High magnification back-scattered electron image of ilmenite inclusions in samples IVT-18 and IVT-21 with different degrees of replacement. These images both show possible diffusion pathways for the ilmenite inclusions, with cracks through the garnet.

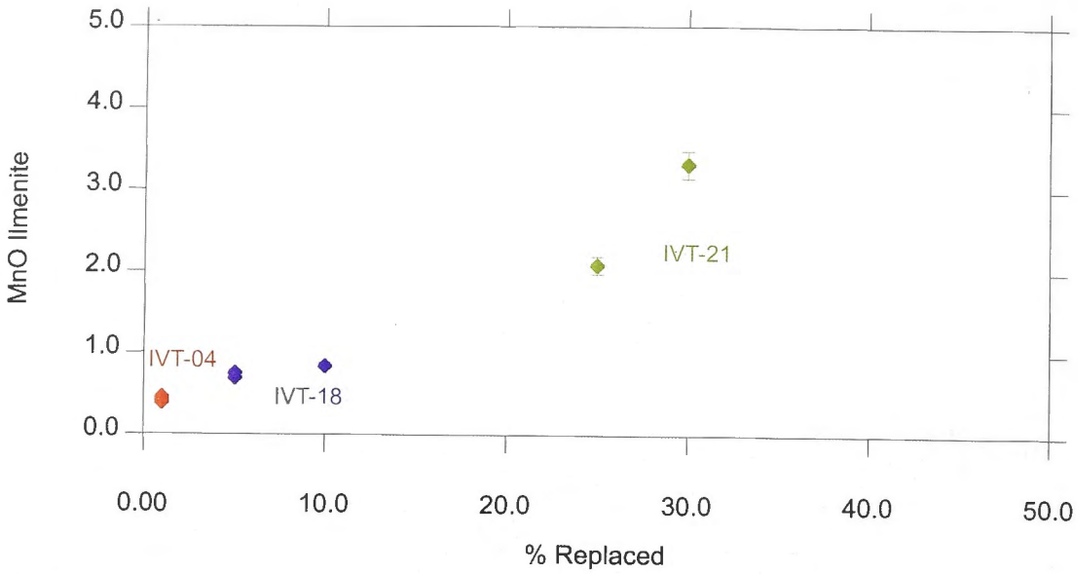

Figure 5.22: The estimated percentage of the area of ilmenite replaced against the MnO concentration of the ilmenite in all three samples.

Garnets also show evidence of net-transfer reactions occurring in all Ivrea-Verbano Zone samples. An indication of this reaction can been seen in the Fe, Mg and Mn concentration profiles from the IVT-04 Gnt3 EPMA transect. This transect was the only one carried out across the whole garnet (Fig. 5.10). Gnt3 in sample IVT-04 has a large ilmenite inclusion in the centre, approximately 150 μm wide. Fe and Mn concentrations increase towards the edge of the garnet and Mg decreases as would be expected from the garnet-biotite reaction (Fig. 5.23), as biotite will not readily incorporate Mn and thus leaves the garnet rims enriched. In this case, however, ilmenite appears to have acted as a sink for the excess Mn. Therefore, the partitioning of Fe and Mn between garnet and ilmenite is incongruent due to ilmenite inclusions exchanging with other phases outside of the garnet it is included in.

Replacement textures are observed in the thin sections of these samples, with biotite growing on embayed rims of garnet. This replacement texture is shown in Figures 5.24 and 5.25. The samples analysed in this study have undergone partial melting (e.g. Schnetger, 1994) and the replacement textures observed in the thin sections for the samples are indicative of the back-reaction of garnet and melt (Nystrom and Kreigsman, 2003).

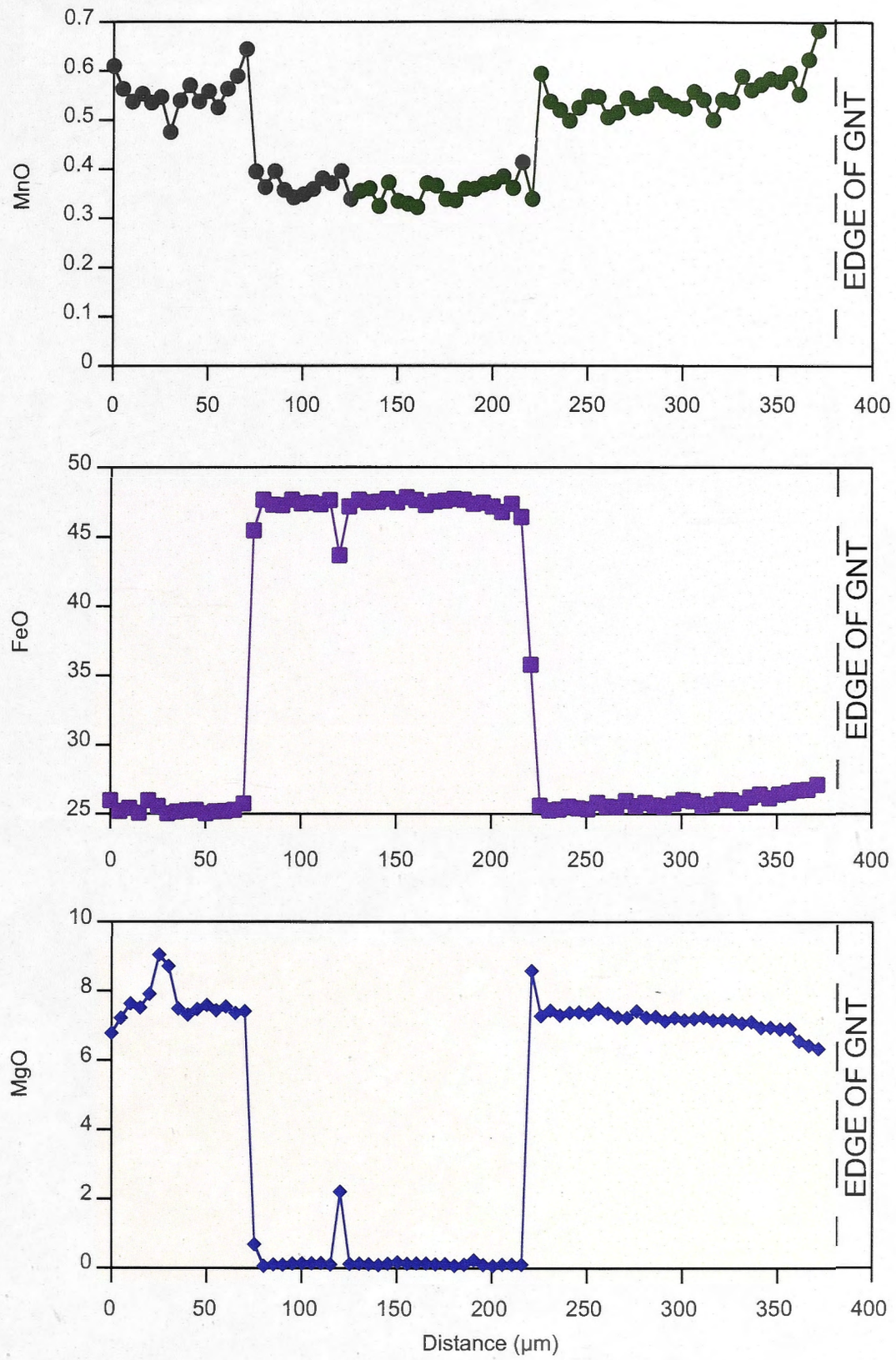

Figure 5.23: EPMA transect across the garnet with an ilmenite inclusion in the centre approximately 150 μm with concentration profiles of MnO, FeO and MnO for sample IVT-04 Gnt3.

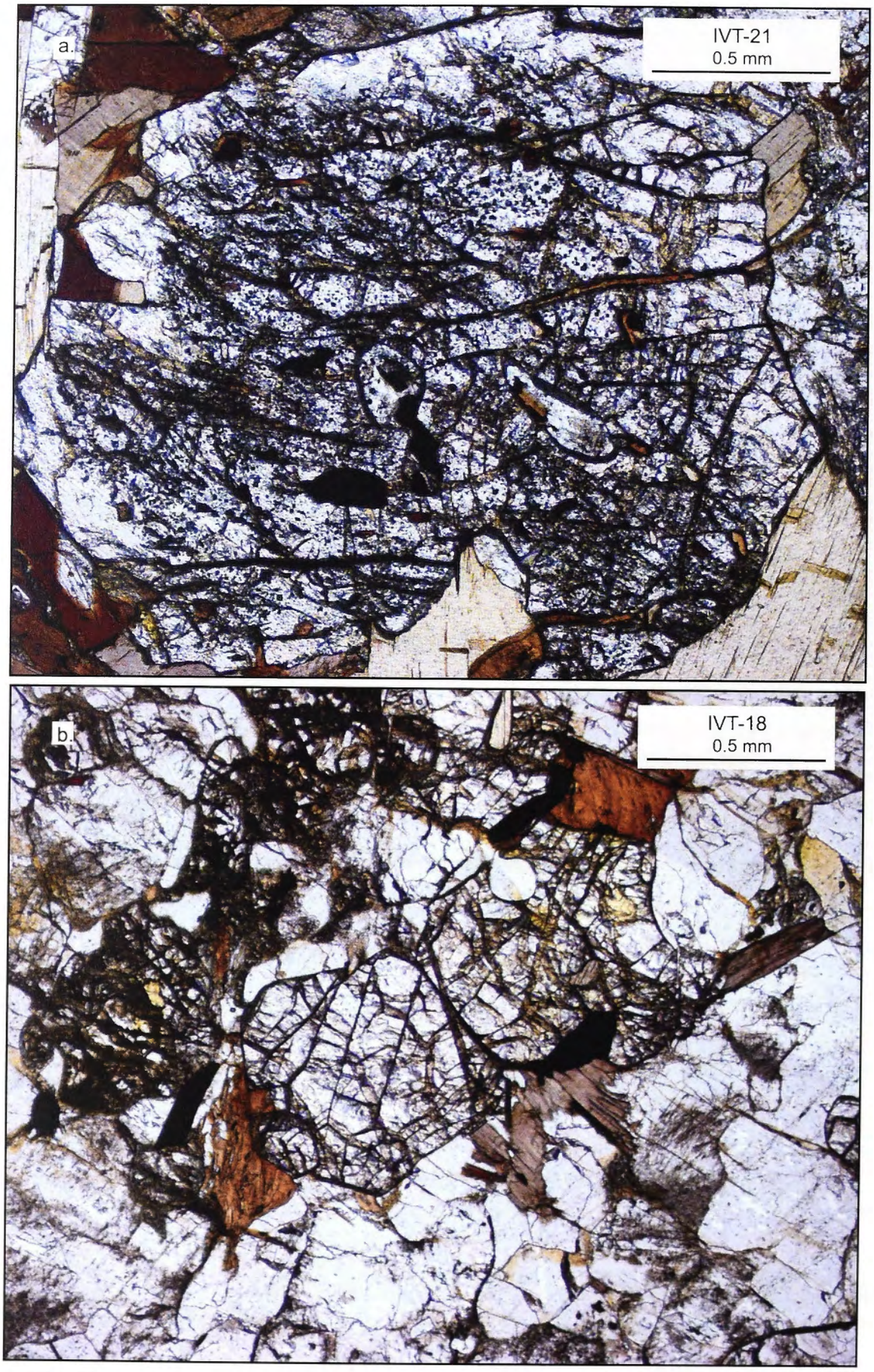

Figure 5.24: Photomicrographs of embayed rims of garnet showing replacement by biotite, (a) IVT-21 and (b) IVT-18.

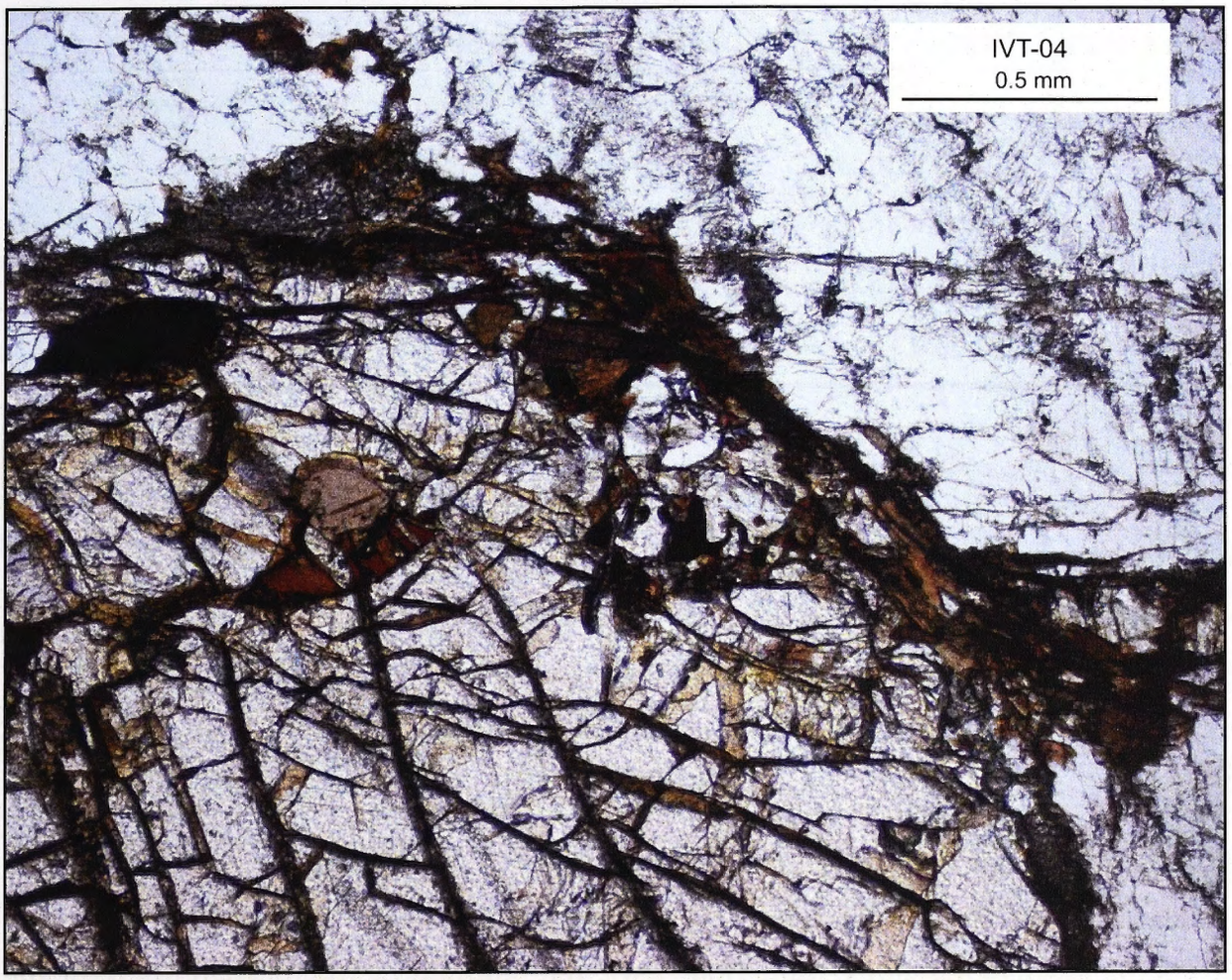

Figure 5.25: Photomicrographs from sample IVT-04 of biotite replacing garnet on embayed rims.

5.8.4 Implications for the Garnet-Ilmenite Diffusion Model

In Section 5.6 the lengths of the diffusion profiles preserved in the different samples were estimated (Table 5.6). The lengths of these profiles can be related to the duration of cooling from peak temperatures based on the rate of diffusion in garnet. At a particular temperature the diffusion coefficient (D) can be calculated from the diffusion parameters of Chakraborty and Ganguly (1992). Assuming that the concentration gradient observed is a product of diffusion, the profiles can be fitted to a solution of the diffusion equation using the curve fitting function of Kaleidagraph, as shown in Chapter 2. These results show a broad range of timescales from 0 to 950 Ma (Table 5.10).

Temperature	D (m^2s^{-1})	Duration (Ma) to produce:		
		6 μm profile	25 μm profile	55 μm profile
450	2.52 × 10-26	11	196	950
650	2.33 × 10-22	0.0012	0.0212	0.1028
850	8.34 × 10-20	-	0.0001	0.0003
1000	2.04 × 10-18	-	-	0.0000

Table 5.10: Estimates of the duration required to produce a diffusion profile of length 6 μm, 25μm and 55 μm at a specified temperature.

Using the method described by Cape and Lehmann (1963) a T-t path of a rock mass that is heated by emplacement of a hot body can be approximated (Viete et al., 2011a). For this T-t curve the duration of the thermal event is based on the thermal diffusivity of the material and the distance from the heat source, for metapelites a thermal diffusivity of 10^{-6} m^2s^{-1} is assumed.

The duration being determined is related to the thermal event that is associated with the intrusion of the Mafic Complex into the Kinzigite Formation. Considering the nature of conductive heating and cooling (Fig. 5.26), the duration of the thermal event for the sample that reaches the highest peak temperature is not significantly longer then the sample that reaches the lowest peak temperature. This is shown schematically in Figure 5.26, with the conductive T-t paths reaching peak temperatures of 650 °C, 850 °C and 1000 °C. Therefore, the duration of 11 Ma years obtained for the production of a 6 μm profile at 450 °C for places an upper limit on the duration for all samples.

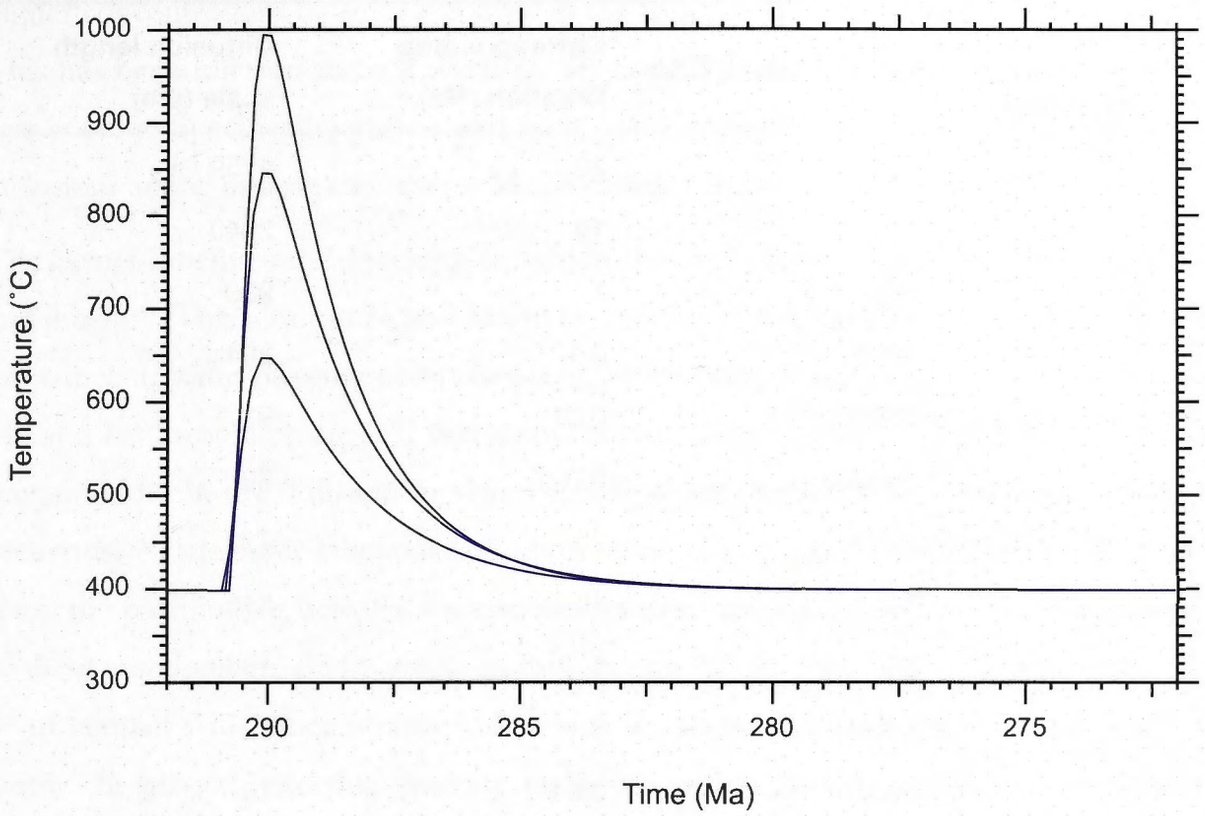

Figure 5.26: Conductive heating and cooling curve example for T-t paths reaching peak temperatures of 650 °C, 850 °C and 1000 °C.

To provide better constraints a model for linear cooling at a specified cooling rate was used. While this is still not an accurate reflection of the actual T-t path it does give a closer approximation of duration. The estimates of the lengths of diffusion profiles using this method are shown in Table 5.11. The results show that the duration required for producing the diffusion profiles as measured in the Ivrea-Verbano Zone samples is from 1000 years to 1 Ma. The higher temperature samples give shorter durations for the thermal event. This result reflects the fact that at high temperatures fast diffusion will erase any concentration gradients produced. Therefore, the lower temperature sample provides the best estimate of duration, as at this temperature it is unlikely that the garnet would have had time to equilibrate and erase diffusion profiles. This places a constraint on the duration of the thermal event of 100 000 years to 1 Ma. The samples from the Ivrea Verbano Zone are in close proximity (0 to 2 km) to the heat source. Therefore, a duration of the thermal event of 100 000 years to 1 Ma would allow sufficient time for cooling of the rock mass as indicated from the conductive T-t paths produced using the formulation of Cape and Lehmann (1963).

Peak T (˚C) (Tminimum 450 ˚C)	Cooling Rate (˚C/Ma)	Corresponding Duration (Ma)	Diffusion length scale (μm)
1000	30	20	4159
	60	10	2940
	600	1	930
	6000	0.1	294
	60000	0.01	93
	600000	0.001	29
850	30	20	732
	60	10	518
	600	1	164
	6000	0.1	52
	60000	0.01	16
	600000	0.001	5.2
650	30	20	32
	60	10	23
	600	1	7.4
	6000	0.1	2.3
	60000	0.01	0.8
	600000	0.001	0.2

Table 5.11: Calculated diffusion length scale produced for a specified duration using the diffusion parameters determined by Chakraborty and Ganguly (1992).

5.9 Conclusions

Diffusion profiles surrounding ilmenite inclusions in garnet were observed and measured in this study. The diffusion profiles increased in length with increasing peak temperature as would be expected from diffusional processes. However, the Mg showed inverse diffusion to Mn, with Mg concentrations in garnet decreasing towards the ilmenite inclusions. Also observed was unusual partitioning behaviour of Fe and Mn between garnet and ilmenite. This was especially prominent in the lower grade samples where ilmenite inclusions had

higher concentrations of Mn compared to the concentrations in the surrounding garnet. This has been inferred to be a result of net-transfer reactions that occurred as the rock was cooling. Specifically, garnet and melt being replaced by biotite with the ilmenite inclusions acting as a sink for excess Mn, indicating that the ilmenite is an open system.

The garnet-ilmenite model is characterised by the exchange of Fe and Mn between garnet and ilmenite. This requires Fe and Mn to be the only exchanging components. Therefore, low concentrations of other components in the system that are able to be exchanged, e.g. Mg and Fe^{3+}, would be ideal. If this is not the case the behaviour of Mg and Fe^{3+} must be accounted for in the diffusion model. The system also requires no net-transfer reactions occurring. Net-transfer reactions including phase changes and decomposition of phases cause the partitioning between the two phases to be incongruent. The reactant products of these reactions should be visible in thin section (Spear et al., 1991). Ilmenite must not be in contact with other phases with which it can readily exchange elements, such as biotite. In general, selecting ilmenite inclusions within garnet is sufficient for ensuring that it is not participating in reactions/exchange with other minerals after the garnet is effectively 'closed'. However, results from this study show ilmenite acting as a sink for Mn as biotite replaces garnet. This shows that even though ilmenite inclusions were selected for analysis this is still an open system and diffusion pathways, such as, cracks in the garnet have allowed the inclusion to exchange with minerals other than the garnet.

The presence of diffusion profiles adjacent to ilmenite inclusions in garnet demonstrates that the garnet-ilmenite system is a viable option for application of diffusion modelling technique. Constraints on the duration of the thermal event associated with metamorphism in the Ivrea-Verbano zone were determined based on the diffusion coefficients of Chakraborty and Ganguly (1992), with the thermal event lasting between 100 000 years to 1 Ma. However, the method does not account for the effect partitioning on the rate of this process. In Chapter 3, it was shown the rate of diffusion is significantly reduced in this system compared to the previously determined garnet diffusion parameters. Thus the constraint is a minimum duration estimate. More accurate diffusion modelling requires a numerical model that describes the partitioning and diffusion in the garnet-ilmenite system.

CHAPTER 6

$^{40}Ar/^{39}Ar$ Geochronology of the Northeast Coast of Scotland

Preface

The fieldwork component of this project consisted of a traverse across the metamorphic isograds of the Buchan and Barrovian metamorphic sequence on the northeast coast of Scotland, which was carried out over three weeks. This was conducted under the supervision of Professor Gordon Lister, who also directed the sample collection process, with Adam Bragg providing field assistance and Dr Daniel Viete gave me advice on sampling localities. An ANU Vice-Chancellor's travel grant provided partial funding for this field work. For argon geochronology, samples were crushed and white mica was separated using magnetic separation techniques with the help of Shane Paxton. Samples were dated using the argon geochronology facility at RSES, ANU, with analysis carried out under the supervision of Dr Marnie Forster and with the assistance of Davood Vasegh and Clemens Augenstein. All of the research presented in this chapter is my own work except where indicated.

6.0 Synopsis

New $^{40}Ar/^{39}Ar$ geochronological data from the Buchan and Barrovian metamorphic sequences on the northeast coast of Scotland has been obtained from *in vacuo* step-heating experiments conducted on white mica extracted from seven samples. Results confirm the synchronous formation of the Barrovian and Buchan metamorphic sequences, with the $^{40}Ar/^{39}Ar$ apparent age spectra obtained for samples of andalusite grade and higher recording a range of ages between 470.4 ± 1.8 Ma to 464.6 ± 1.3 Ma. These ages are close to the accepted age for peak metamorphism during the Grampian Orogeny, *c.* 470 Ma. Whereas, $^{40}Ar/^{39}Ar$ apparent age spectra of white mica from the lower grade cordierite zone near Banff preserve pre-Grampian detrital ages. In these spectra an age is recorded at *c.* 560 Ma. This indicates that the sediment source for the Upper Dalradian endured a thermal or deformational event at *c.* 560 Ma and therefore sedimentation occurred after that time. These samples also preserved evidence of an age older than 750 Ma.

6.1 Introduction

The Grampian Terrane in Scotland consists of the Dalradian sediments that were metamorphosed during the Grampian Orogeny (Lambert and McKerrow, 1976). This event produced the Barrovian and Buchan metamorphic sequences (Oliver, 2001). However, there is still significant uncertainty as to the age of deposition of the sediments as well as the age of the subsequent metamorphism (Dempster et al., 2002). Therefore, to obtain an accurate tectonothermal history of the terrane detailed geochronological constraints are needed.

Previous geochronology has constrained the entire Grampian orogenic event to start at 480 Ma and finish at 465 Ma, in Scotland (Oliver et al., 2000) and Ireland (Friedrich et al., 1999). The start of the Grampian Orogeny in Scotland is marked by the obduction of the Ballantrae Ophiolite (Bluck et al., 1980). K-Ar dating of hornblende from the metamorphic sole gives an age of 478 ± 8 Ma (Bluck et al., 1980). Whereas, the undeformed Kennethmont Granite in the Buchan Block gives an age of 457 ± 0.9 Ma (Oliver et al., 2000) constraining the end of the Grampian Orogeny. These ages are reflected in Connemara, Ireland where the start of the Grampian Orogeny is placed prior to 474.5 ± 1 Ma (Friedrich et al., 1999), which is the oldest age recorded by the syn-orogenic Currywongaun Gabbro. Friedrich et al. (1999) also determined a xenotime U-Pb age of 462.5 ± 1.2 Ma for the undeformed Oughterard granite, which provides an estimate constraining the end of the Grampian Orogeny in Connemara.

The Barrovian and Buchan metamorphic sequences are inferred to have formed contemporaneously during the Grampian Orogeny, with peak metamorphism at *c.* 470 Ma (Oliver et al., 2000). The metamorphism in the Barrovian has been dated directly via Sm-Nd garnet ages (e.g. Baxter et al., 2002; Oliver et al., 2000) and argon geochronology (e.g. Viete et al., 2011a). The timing of the Buchan metamorphism has been dated indirectly via a zircon U-Pb age of 467 ± 6 Ma for the syn-metamorphic Strichen granite that intruded the Buchan zones (Oliver et al., 2000). The Buchan metamorphism has also been dated using Rb-Sr biotite-whole rock techniques, but this provided erratic ages ranging from 460 to 570 Ma in the Buchan zones (Dempster et al., 1995). This spread in ages may be due to an unknown detrital component (Cliff, 1985). The argon geochronology step-heating technique provides a way for evaluating the effect of detrital components since multiple ages can be resolved from one sample using the

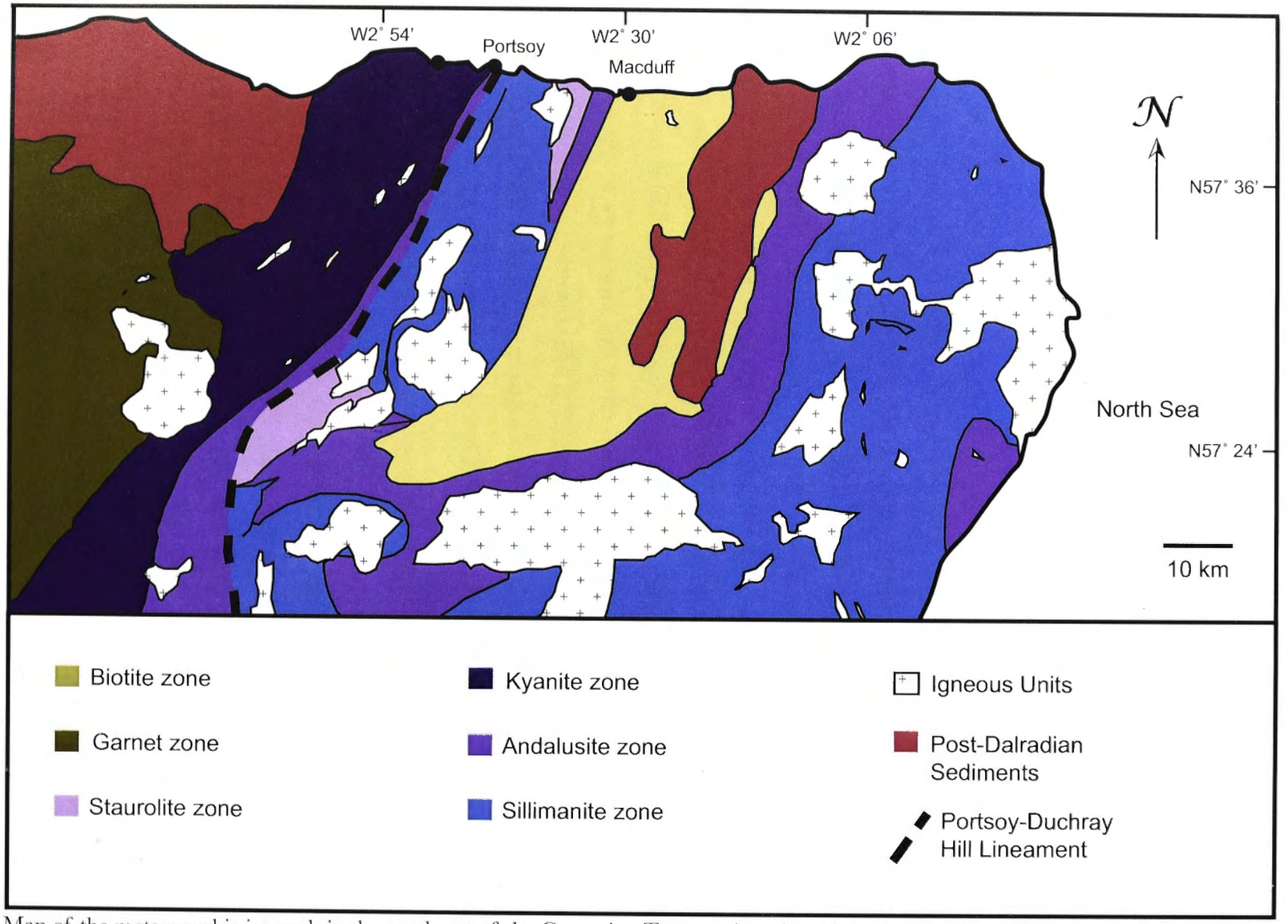

Figure 6.1: Map of the metamorphic isograds in the northeast of the Grampian Terrane. Associated intrusions and post-Dalradian sediments are also displayed. The Portsoy-Duchray Hill lineament of Fettes et al. (1986) is marked. This lineament is the western boundary of the Buchan Block. This Figure was modified from Viete et al. (2010).

method of asymptotes and limits (Forster and Lister, 2004). This method was applied to $^{40}Ar/^{39}Ar$ white mica apparent age spectra obtained from seven samples across the metamorphic zones of the northeast coast of Scotland, as presented in this chapter.

6.2 Geological Background

The Grampian Terrane in northeast Scotland is bounded by the Great Glen Fault (GGF) in the northwest and the Highland Boundary Fault (HBF) in the southeast (Chapter 4, Fig. 4.1). It contains the Buchan and Barrovian Metamorphic sequences that were produced when the Dalradian sediments were metamorphosed. The Buchan Metamorphic sequence is separated from the Barrovian sequence in the west and south by regional scale shear zones (Ashcroft et al., 1984). The Buchan metamorphic sequence was first characterised by Read (1952) and is distinguished by the presence of high-temperature/low-pressure metamorphic assemblages (Harte and Hudson, 1979; Hudson, 1980; Read, 1952). It is best observed along the Banffshire coast, where the metamorphic grade increases to the west from Banff (Atherton, 1977) and displays biotite, cordierite, andalusite, staurolite and sillimanite zones that mark a progressive increase in metamorphic grade (Hudson, 1980). The metamorphic isograds display complicated patterns as a result of syn- and post metamorphic deformation (Harte and Hudson, 1979); the isograds are illustrated in Figure 6.1.

Structurally, the northeast coast is dominated by the Boyndie Syncline, as is shown in the cross section after Treagus and Roberts (1981) in Figure 6.2. The cross section shows the flat lying Macduff Slates to the east and a steep belt to the west of the hinge. The axial trace of the Boyndie Syncline and the line of cross section are marked on the structural map in Figure 6.3.

The relative timing of the shortening event that formed the Boyndie Syncline has been debated. Treagus and Roberts (1981) argue for it being an early event, pre-metamorphism, with a second set of coaxial folds folding the metamorphic isograds. Others claim the Boyndie Syncline formed in a later event that folded the isograds (Fettes, 1970; Johnson, 1962). This latter interpretation is corroborated by the microstructural evidence presented by Viete et al. (2010) from the cordierite zone of the Buchan sequence that suggests the Boyndie Syncline was syn- to post-metamorphic in agreement with Fettes (1970) and Johnson (1962).

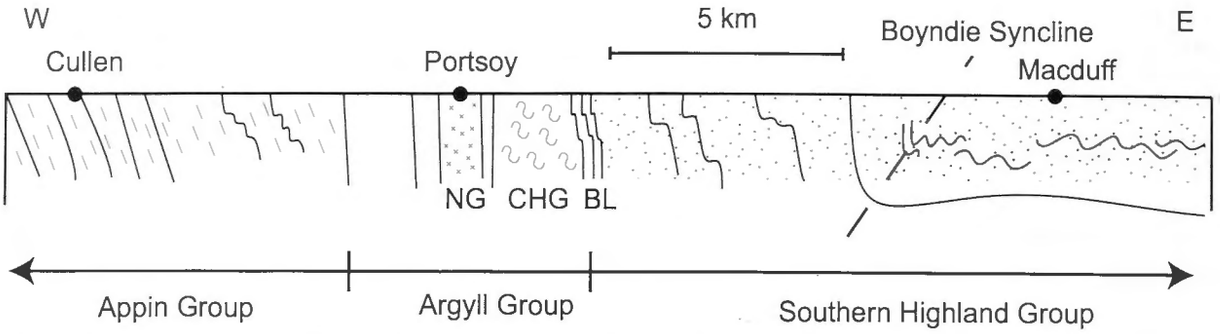

Figure 6.2: Cross section of the northeast coast of Scotland after Treagus and Roberts (1981) and Dempster et al. (1995). The units approaching Portsoy are the Boyne Limestone (BL) Cowhythe Gneiss (CHG) and the so-called Newer Gabbro (NG), which is also known in this particular location as the Portsoy Gabbro.

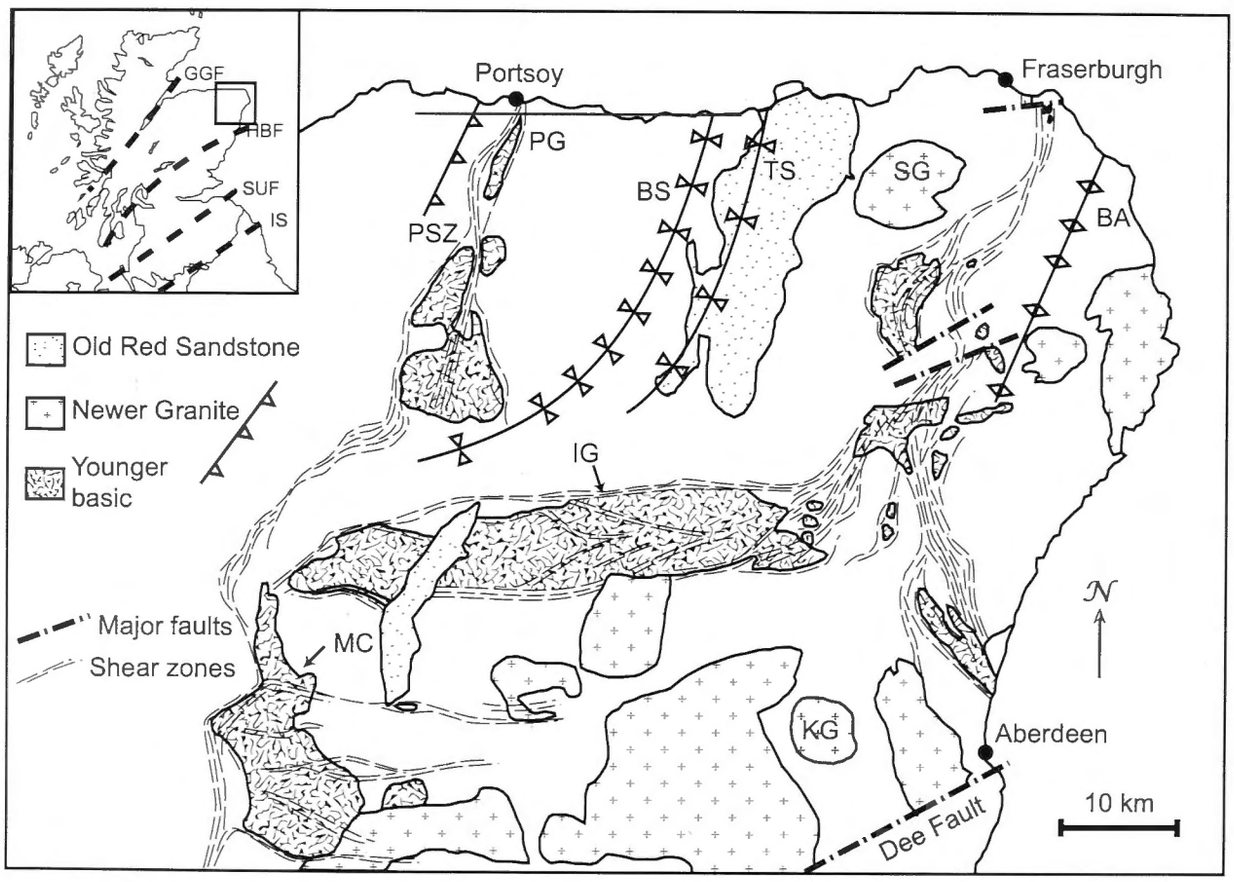

Figure 6.3: Structural map of major shear zones, structural features and intrusions of the Buchan Block. Figure after the shear zone map of Ashcroft (1984) and structural maps of the eastern Dalradian of Baker (1987) and Kneller (1987). The red line marks the cross section shown in Figure 6.2. The abbreviations on the map are the Portsoy Shear Zone (PSZ), Portsoy Gabbro (PG), Boyndie Syncline (BS), Turriff Syncline (TS), Buchan Anticline (BA), Insch Gabbro (IG), Strichen Granite (SG), Kennthmont Granite (KG) and Morven Crabach (MC).

The Cowhythe Gneiss that outcrops at Links Bay to the east of Portsoy has been inferred to be part of the pre-Dalradian basement that is of Grenville age (*c.* 1050 Ma; Oliver et al., 2000). It is suggested that the slice of basement was thrust into its current position after the folding event that formed the Boyndie Syncline (Ramsey and Sturt, 1979). Viete et al. (2010) referred to an unpublished U-Pb zircon age of G.J.H Oliver that corroborated this hypothesis and proposed that high-strain zones with opposing sense of movement that bound the gneissic unit may have facilitated emplacement of a slice of basement into the Dalradian.

Regional shear zones in the west and south (Ashcroft et al., 1984) mark the boundaries to the Buchan Block and switch to Barrovian metamorphism. The Portsoy Duchray Hill lineament (PDHL) of Fettes et al. (1986), which is shown in Figure 6.1, is the western boundary to the Buchan Block. The PDHL is coincident with the syn-metamorphic Portsoy Gabbro and Portsoy Shear Zone as described by Ashcroft et al. (1984). They carried out a detailed study on the shear zones of the northeast Dalradian and inferred large vertical displacements of approximately 5km across the western (PDHL) and southern shear belts with the Buchan Block as the hanging-wall, localities shown in Figure 6.3. Later structural analysis has demonstrated that the PDHL records both top-to-the-east and top-to-the-west movement (Carty, 2001).

The uncertainty in the relative timing of structural and intrusive events in the Dalradian and continued contention as to the sedimentation age has made reconstructing the tectonic history of the Grampian Orogeny and associated metamorphism complicated. To resolve this detailed and microstructurally focused geochronology is required.

6.3 Existing Geochronological Constraints

The Buchan metamorphic sequence in Scotland formed contemporaneously with the Barrovian metamorphic sequence during the Grampian Orogeny which is constrained to have started at *c.* 480 Ma and ended by *c.* 465 Ma (Oliver et al., 2000). The age of peak metamorphism for the Buchan and Barrovian zones is generally accepted as *c.* 470 Ma. This is consistent with Sm-Nd garnet ages of Baxter et al. (2002) and Oliver et al. (2000) as well as the Rb-Sr biotite ages of Dempster et al. (1995). This age also places several of the intrusions in the Buchan Block (Fig. 6.3) within the tectonometamorphic event, in particular the Insch Gabbro, 468 Ma, the Morven-Crabach, 472 Ma (Rogers et al., 1994)

and the Portsoy Gabbro *c.* 471 Ma (Carty, 2001). A summary of previous geochronological evidence for the age of events that occurred within the Grampian Orogeny is contained in Table 6.1, as well as a description as to how these ages were interpreted by the various studies. The ages presented here provide a broad constraint on the overall timescale of the metamorphism.

Biostratigraphical evidence provides constraints on the timing of metamorphism for the Dalradian sediments by constraining the age of deposition. However, the deposition age of the Dalradian sediments has also been an issue of contention. A single fossil, *veryhachium* cf., present within the Macduff Slate would suggest an age of 485 Ma (Molyneux, 1998). This was proposed originally by Downie et al. (1971), although as the age is based on only one intact specimen and as it did not fit with the tectonic models for the Grampian orogenesis it was largely disregarded. However, the more recent model of Viete et al. (2010) incorporates syn-orogenic extension and this tectonic scenario allows for syn-metamorphic sedimentation.

Other evidence for the deposition age comes from the South of the Dalradian near Callander, Perthshire within the Leny Limestone unit. Pringle (1939) found a middle Cambrian Trilobite in the limestone, which places the deposition at *c.* 525 Ma. The Leny Limestone unit is a part of the Keltie Water Grits formation, which is proximal to the Highland Boundary Complex (Pringle, 1939). Due to this proximity the relation between the Keltie Water Grits and the Dalradian sediments was contested by Read (1961). However, more recently detailed mapping and geochronology of the Callander area by Tanner and Pringle (1999) has supported the case for continuity between the Dalradian sediments and the Keltie Water Grits re-affirming the 525 Ma age for deposition.

A maximum age for the Grampian Orogeny is provided by zircon U-Pb ages for the Ben Vuirich granite, which was intruded into the Dalradian sediments prior to the metamorphic event (Pankhurst and Pidgeon, 1976). Emplacement was originally dated at 514 ± 7 Ma (Pankhurst and Pidgeon, 1976). This age was later revised by high precision U-Pb dating to 590 ± 2 Ma (Rogers et al., 1989).

Oliver et al. (2000) obtained zircon U-Pb ages for two granitic intrusions from the Buchan area. The Strichen Granite, which is inferred to be syn-metamorphic from the structures present, provided a zircon U-Pb age of 467 ± 6 Ma (Oliver et al., 2000). The inference of synchronous formation of the Buchan and Barrovian metamorphism in the Dalradian

is largely based on this age. The zircons also preserve an older age; *c.* 845 Ma, which Oliver et al. (2000) suggests is from an older granitic protolith underlying the Dalradian, which somehow relates to the Strichen Granite. The undeformed Kennethmont Granite also from the Buchan Block has a zircon U-Pb age of 457 ± 0.9 Ma (Oliver et al., 2000). This age is interpreted as constraining the end of the Buchan tectonometamorphic event (Oliver et al., 2000). Friedrich et al. (1999) constrained the timing of the Grampian Orogeny from ages of the syn-metamorphic mafic intrusions present in Connemara, Ireland that have U-Pb zircon ages of 474.5 ± 1.0 Ma and 470 ± 1.4 Ma.

The beginning of the Grampian event is commonly reported as the ages determined from dating the metamorphic aureoles surrounding obducted ophiolites (e.g. Bluck et al., 1980). K-Ar dating of the metamorphic aureole of the Shetland ophiolite gave ages ranging between 479 and 465 Ma (Spray, 1988). $^{40}Ar/^{39}Ar$ dating of hornblende from the Ballantrae Ophiolite yields ages of 478 ± 2 Ma (Flinn et al., 1991). In Ireland Dalradian rocks overlie the Annagh Gneiss Complex that provided a 475 ± 4 Ma age from $^{40}Ar/^{39}Ar$ dating of hornblende (Daly and Flowerdew, 2005). This age is presumed to date the onset of the Grampian Orogeny in this part of Ireland (Daly and Flowerdew, 2005). However, it is worth noting that the interpretation of these ages as representing obduction has been disputed in other ophiolite belts. Ages recorded in the metamorphic aureole may in fact date later deformation events (Rawling and Lister, 2002).

The Buchan Block has a large volume of mafic intrusions that are interpreted as syn-tectonometamorphic (Chinner, 1966). The mafic intrusions (i.e. the 'Newer Gabbros') were determined to have Rb-Sr whole rock ages of 492 ± 26 Ma, 487 ± 23 Ma and 482 ± 12 Ma (Pankhurst, 1970). The Insch and Morven Crabach gabbros were dated at 468 Ma and 472 Ma, respectively (Rogers et al., 1994) which is similar to ages obtained for the Portsoy Gabbro. Carty (2001) determined a zircon U-Pb age for the Portsoy Gabbro of 471.5 ± 3 Ma, interpreted as the age of emplacement. The gabbro is cross-cut by an undeformed pegmatite with a zircon U-Pb age of 473 +5/-3 Ma. Carty (2001) noted that these ages seem incompatible without error being taken into account. Oliver et al. (2008) reported that Condon and Martin (pers. comm.) dated the Portsoy Gabbro using TIMS on magmatic zircons at 474.3 ± 2.1 Ma. Carty (2001) also reports U-Pb titanite ages of 470 ± 3 Ma and 466 ± 3 Ma that are interpreted as cooling ages, indicating rapid cooling.

Age (Ma)	Mineral and Method	Interpretation	Rock Type and Location	Reference
590 ± 2	Zircon U-Pb	Maximum age of Grampian	Ben Vuirich Granite, Perthshire	Rogers et al., 1989
525	Trilobite Fossil	Age of deposition	Leny Limestone, Perthshire	Tanner and Pringle, 1999
514 ± 7	Zircon U-Pb	Maximum age of Grampian	Ben Vuirich Granite, Perthshire	Pankhurst and Pidgeon, 1976
485	*Veryhachium* cf. Microfossil	Age of deposition	Macduff Slate, Macduff	Molyneux, 1998
492 ± 26 487 ± 23 482 ± 12	Whole rock Rb-Sr	Age of intrusion	Newer Gabbros, Buchan Block	Pankhurst, 1970
478 ± 8	Hornblende K-Ar	Obduction	Ballantrae ophiolite, Midland	Bluck et al., 1980
478 ± 2	Hornblende Ar-Ar	Obduction	Ballantrae ophiolite Midland	Flinn, 1991
479-465	Hornblende K-Ar	Obduction	Shetland ophiolite	Spray, 1988
467 ± 6	Zircon U-Pb	Age of intrusion	Strichen Granite Buchan Block	Oliver et al., 2000
473 +5/-3	Zircon U-Pb TIMS	Cessation of Portsoy shear zone deformation	Undeformed quatzofeldspathic pegmatite, Portsoy	Carty, 2001
471.5 ± 3	Magmatic zircon TIMS	Emplacement age	Meta-gabbro, Portsoy	Carty, 2001
471 ± 0.6	Zircon U-Pb	Emplacement age	Portsoy Gabbro	Carty et al., 2012
470 ± 3 466 ± 3	Titanite U-Pb	Cooling ages	Portsoy Shear Zone	Carty, 2001

Table 6.1: Summary of the geochronology of the Grampian Orogeny with the interpretations of the events these ages correspond to as were presented by the referenced study.

Age (Ma)	Mineral and Method	Interpretation	Rock Type and Location	Reference
468 472	Zircon U-Pb	Emplacement	Insch and Morven Crabach, Buchan	Rogers et al., 1994
467.1 ± 3.4 468.1 ± 3.3 467.6 ± 2.5	Garnet Sm-Nd	Cessation of garnet growth	Garnet grade Metapelites, Barrovian	Oliver et al., 2000
471.8 ± 2.0 472 ± 2	Garnet Sm-Nd	Garnet growth	Kyanite grade Metapelites, Barrovian	Oliver et al., 2000
472.9 ± 2.9 464.8 ± 2.7	Garnet Sm-Nd	Garnet growth	Sillimanite Grade Metapelites, Glen Clova	Baxter et al., 2002
c. 470-450	Monazite U-Pb	Regional metamorphism	Grampian group, Central Highlands	Barreiro quoted by Phillips et al., 1999
470-471	Graptolite age	Deposition age	Black shale Ballantrae Complex	Maletz, 2004
462 ± 8.8	Zircon U-Pb	Metamorphic overgrowth/Fluid influx	Garnet zone, Barrovian	Breeding et al., 2004
460 Ma	Ar-Ar muscovite	Cooling age	Barrovian Metamorphic sequence	Viete et al., 2011a
457 ± 0.9	Zircon U-Pb	Emplacement	Kennethmont Granite, Buchan Block	Oliver et al., 2000
475 ± 4	Hornblende Ar-Ar step heating	Grampian Deformation	Annagh gneiss complex, Ireland	Daly and Flowerdew, 2005
474.5 ± 1.0 470 ± 1.4	Zircon U-Pb	Syn-orogenic intrusion ages	Gabbroic intrusions, Connemara, Ireland	Friedrich et al., 1999

Table 6.1 (Contd.)

The timing of Barrovian metamorphism in the Grampian Terrane has been dated directly by Sm-Nd garnet ages that are inferred to mark the termination of garnet growth (Oliver et al., 2000). Oliver et al. (2000) determined Sm-Nd garnet ages of 467.6 ± 2.5 Ma and 472 ± 2 Ma for garnet and kyanite zone samples, respectively. Baxter et al. (2002) determined two stages of garnet growth in a sillimanite zone sample, at 472.9 ± 2.9 Ma and 464.8 ± 2.7 Ma. The difference between the ages determined for the garnet zone and sillimanite zone is 2.8 ± 3.7 Ma (Baxter et al., 2002) indicating that peak temperatures were reached across the zones almost contemporaneously. This is inconsistent with a crustal thickening and erosion model that requires the ages when peak temperatures were attained across the garnet to sillimanite metamorphic zones to span approximately 10 Ma (Ague and Baxter, 2007).

Breeding et al. (2004) obtained a zircon U-Pb age of a metamorphic overgrowth of 462 ± 8.8 Ma from within the garnet zone of the Barrovian. This is interpreted as the age of fluid infiltration into the Dalradian rocks and provides evidence that peak metamorphism and fluid infiltration were broadly contemporaneous.

A study of the $^{40}Ar/^{39}Ar$ apparent age spectra of the Barrovian metamorphic sequence to the south obtained ages of *c.* 460 Ma in the higher grade samples and these can be interpreted as cooling ages (Viete et al., 2011a). The lower grade samples from the biotite zone preserved pre-grampian detrital ages, which provided age ranges of 1080 to 930 Ma, 780 to 700 Ma and 560 to 510 Ma (Viete et al., 2011a). Forward modelling of the age spectra in this study constrained the duration of the Barrovian metamorphism in the biotite zone between 1 to 10 Ma.

The timing of the Buchan metamorphic event along the Banff coast has been dated using Rb-Sr whole rock ages (Dempster et al., 1995). The transect shows a general trend of decreasing age from east to west with a considerable amount of local variation. However, whole rock ages may include detrital components that would have an unknown influence on the obtained age (Cliff, 1985). Dempster et al. (1995) determined an approximate age from Rb-Sr in biotite of *c.* 460 Ma for the rocks to the west of the PDHL in the Barrovian metamorphic zones and related this to rapid cooling caused by differential uplift on the late shear zones of Ashcroft et al. (1984).

6.4 Buchan Petrography

In this study samples were collected from Banff to Cullen (Fig. 6.4). Along this section of the coast the Buchan metamorphic grade increases from east to west until the sequence is terminated at the PDHL. To the west of this lineament is the Barrovian metamorphic sequence.

The fabrics observed in these samples during microstructural analysis are named after the structural study of Viete et al. (2010). The two main fabrics observed in samples are related to a top-to-the-east shearing event (S_{TopE}) and the folding event that formed the Boyndie Syncline ($S_{Boyndie}$).

6.4.1 Biotite Zone

The biotite zone has a typical mineral assemblage of quartz, muscovite, biotite, chlorite and opaque minerals with tourmaline as a common accessory phase (Fig. 6.5). These rocks are typically fine grained. The chlorite present in the samples overgrows biotite grains indicating this is a retrograde phase. The fabric is defined in samples by the shape orientation of the fine grained minerals of the matrix with slight elongation of the quartz grains. The muscovite often contains intergrowths of biotite.

6.4.2 Cordierite Zone

As described in Hudson (1980) the presence of the cordierite zone is marked by 'spots' appearing on the rocks and these are interpreted as cordierite porphyroblasts that have been subsequently altered to a fine grained aggregate of minerals (Fig. 6.6). Detrital muscovite was observed within cordierite zone samples, as shown in Figure 6.7. Cordierite porphyroblasts increase in size towards the west of Boyndie Bay until the andalusite isograd is reached. The cordierite porphyroblasts overprint an early foliation, which is preserved in inclusion trails within larger porphyroblasts up-sequence (Fig. 6.8, p.180). Viete et al. (2010) discussed the timing of cordierite growth based on the relative timing of fabrics and placed it during top-to-the-east extension, continuing into the shortening event that formed the Boyndie Syncline.

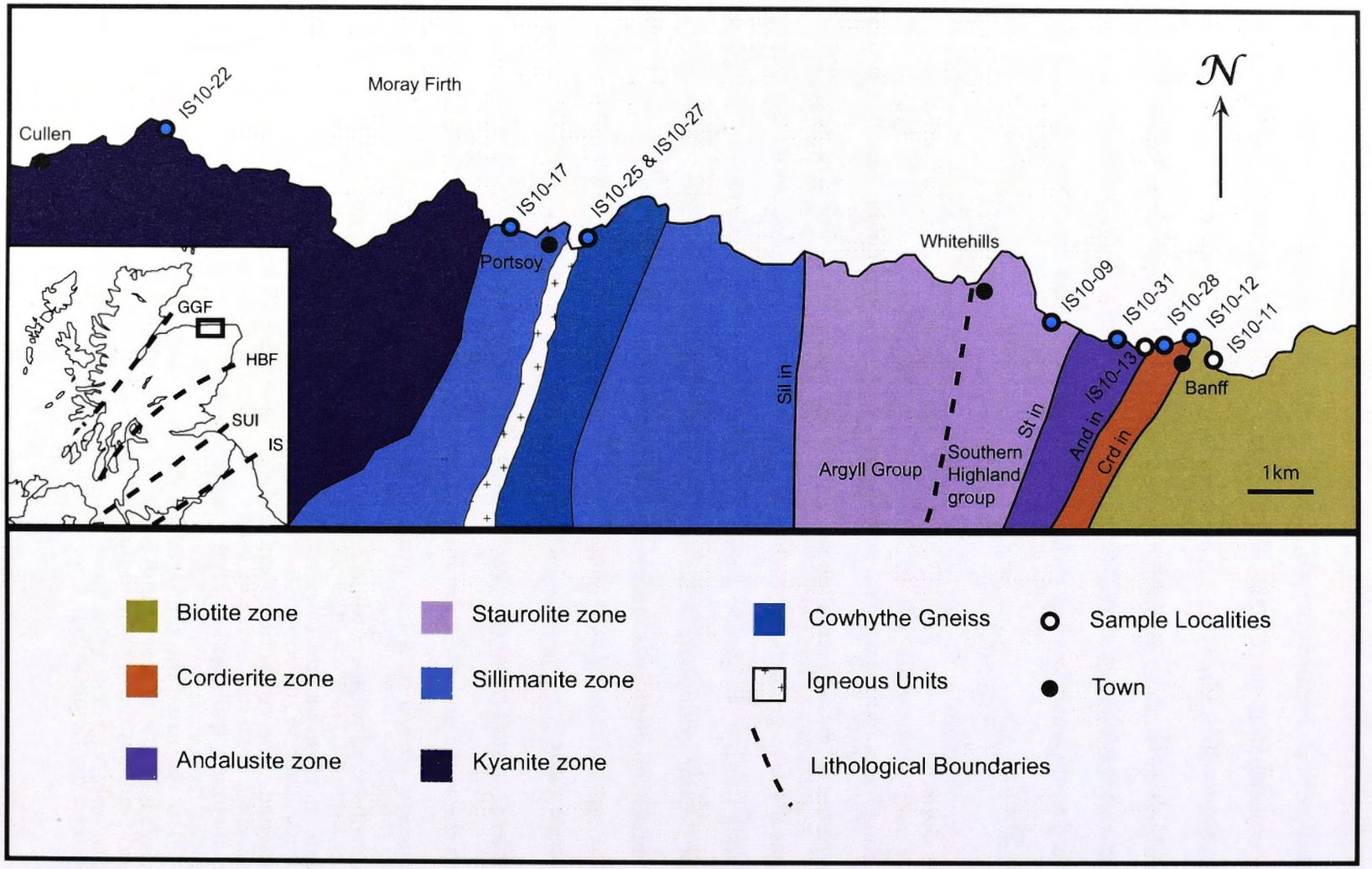

Figure 6.4: Sample localities from the northeast coast of Scotland. Filled circles show samples that were dated by $^{40}Ar/^{39}Ar$ geochronology. The mineral isograds shown are after Hudson (1985). The igneous unit near Portsoy are after Hudson (1980) and boundaries approximately follows the trend of the PDHL. The mineral abbreviations used for indicator minerals are Crd: cordierite, And: andalusite, St: staurolite, Sil: sillimanite and Ky: kyanite. The major structural boundaries in the map inset are the GGF: Great Glen Fault, HBF: Highland Boundary Fault, SUF: Southern Uplands Fault and IS: Iapetus Suture.

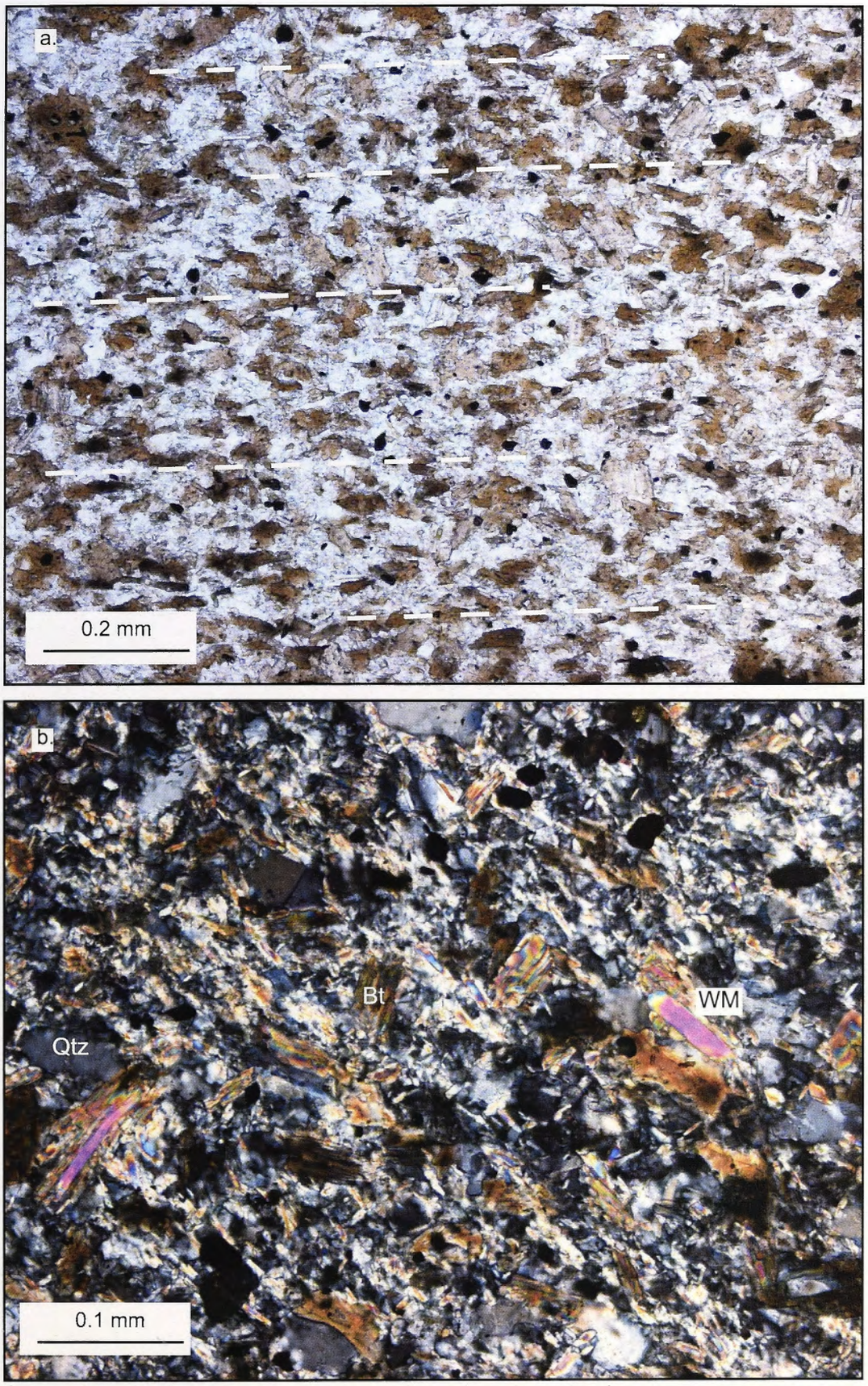

Figure 6.5: Photomicrographs of sample IS10-11 from Banff Harbour with a typical mineral assemblage of quartz, muscovite, biotite, chlorite and opaque minerals for the biotite zone samples from the Buchan metamorphic sequence; (a) Photomicrograph of the fabric defined by shape orientation of quartz, muscovite, biotite in plane polarised light and (b) photomicrograph of an area showing typical muscovite grains in cross polarised light.

Figure 6.6: Cordierite porphyroblasts in relation to minor folds from an outcrop on the beach of Boyndie Bay west of Banff.

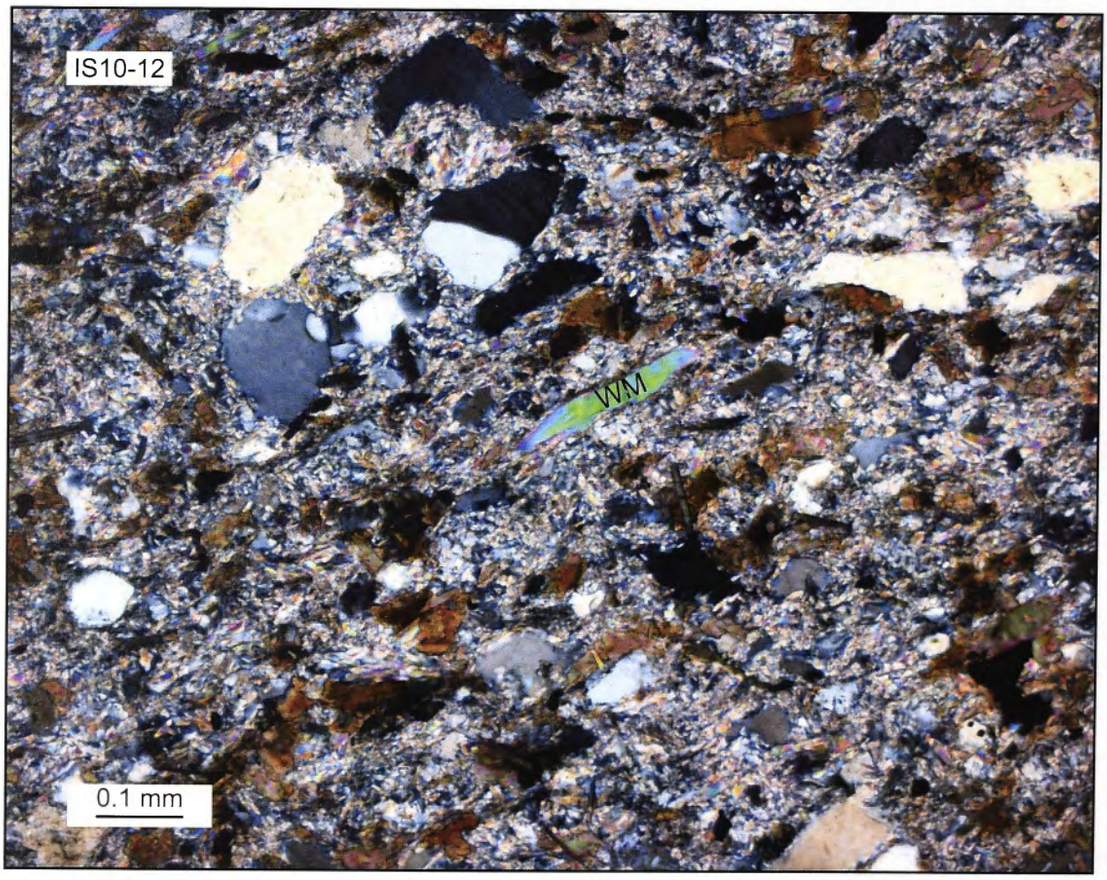

Figure 6.7: Photomicrograph of white mica grains (WM) from sample IS10-12 from the cordierite zone of the Buchan metamorphic sequence.

6.4.3 Staurolite and Andalusite Zone

Further west along Boyndie Bay the first presence of andalusite can be observed, followed by staurolite after 1 km. Sample IS10-09, shown in Figure 6.9, contains both staurolite and andalusite. The staurolites reach approximately 1 mm in diameter and display characteristic penetration twinning. Inclusion trails are present within porphyroblasts, with a later fabric wrapping the porphyroblasts. Many of the andalusite porphyroblasts have been replaced by muscovite, biotite and chlorite (Fig. 6.9b).

6.4.4 Sillimanite Zone

The sillimanite zone metamorphism along the northeast coast has previously been attributed in part to contact metamorphism as well as the regional metamorphic event (Harte and Hudson, 1979) and it is split by the PDHL. This lineament marks the termination of the Buchan metamorphic sequence (Fig. 6.1) and to the west of the PDHL is the Barrovian metamorphic sequence. Sillimanite grade samples were collected from the east and west of the PDHL. The Links Bay samples IS10-25 and IS10-27 are from the Buchan sillimanite zone.

The chiastolite schist from the Portsoy swimming pool area, which is within the sillimanite zone of the Barrovian metamorphic sequence, was sampled (IS10-17, Fig. 6.10). Within this sample is evidence of kyanite replacing andalusite, which indicates an increase in pressure during mineral growth for these rocks. Viete et al. (2010) placed the growth of andalusite prior to the main shear fabric (S_{TopE}).

Sample IS10-22 is from Logie Head within the kyanite zone of the Barrovian metamorphic sequence to the west of Portsoy and is garnet-mica schist. Pervasive mica fabric formed during top-to-the-east shearing and was subsequently folded by the Boyndie Syncline (Fig. 6.11). The inclusion trails within garnets are complicated and indicate growth during deformation.

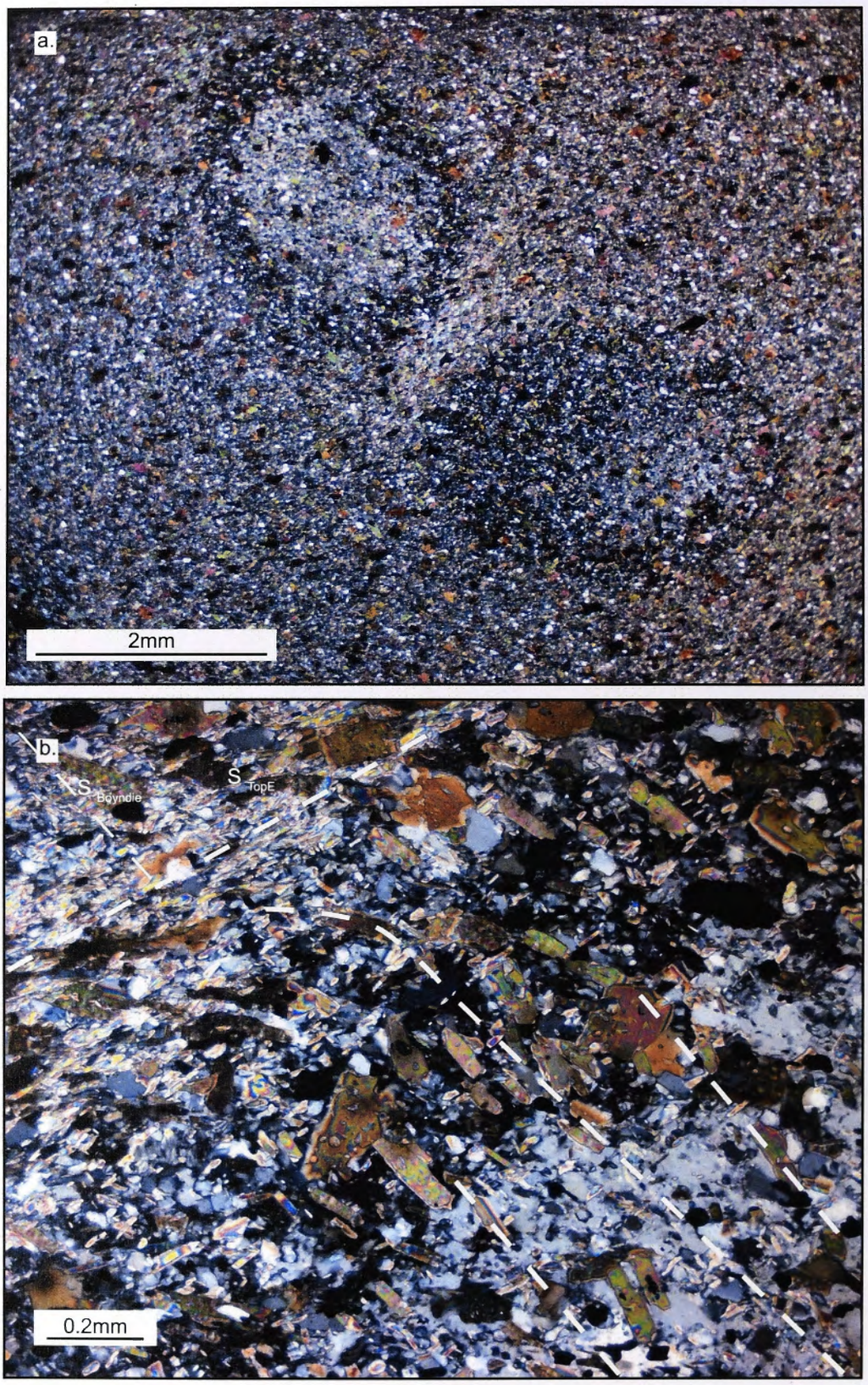

Figure 6.8: Photomicrographs in cross polarised light of sample IS10-13 from the cordierite zone. (a) Altered cordierite porphyroblasts are replaced by fine grained mica described as 'spots' by Hudson (1980). (b) Showing the edge of the cordierite as a dark rim around a lighter spot, with fabric being bent into the porphyroblast.

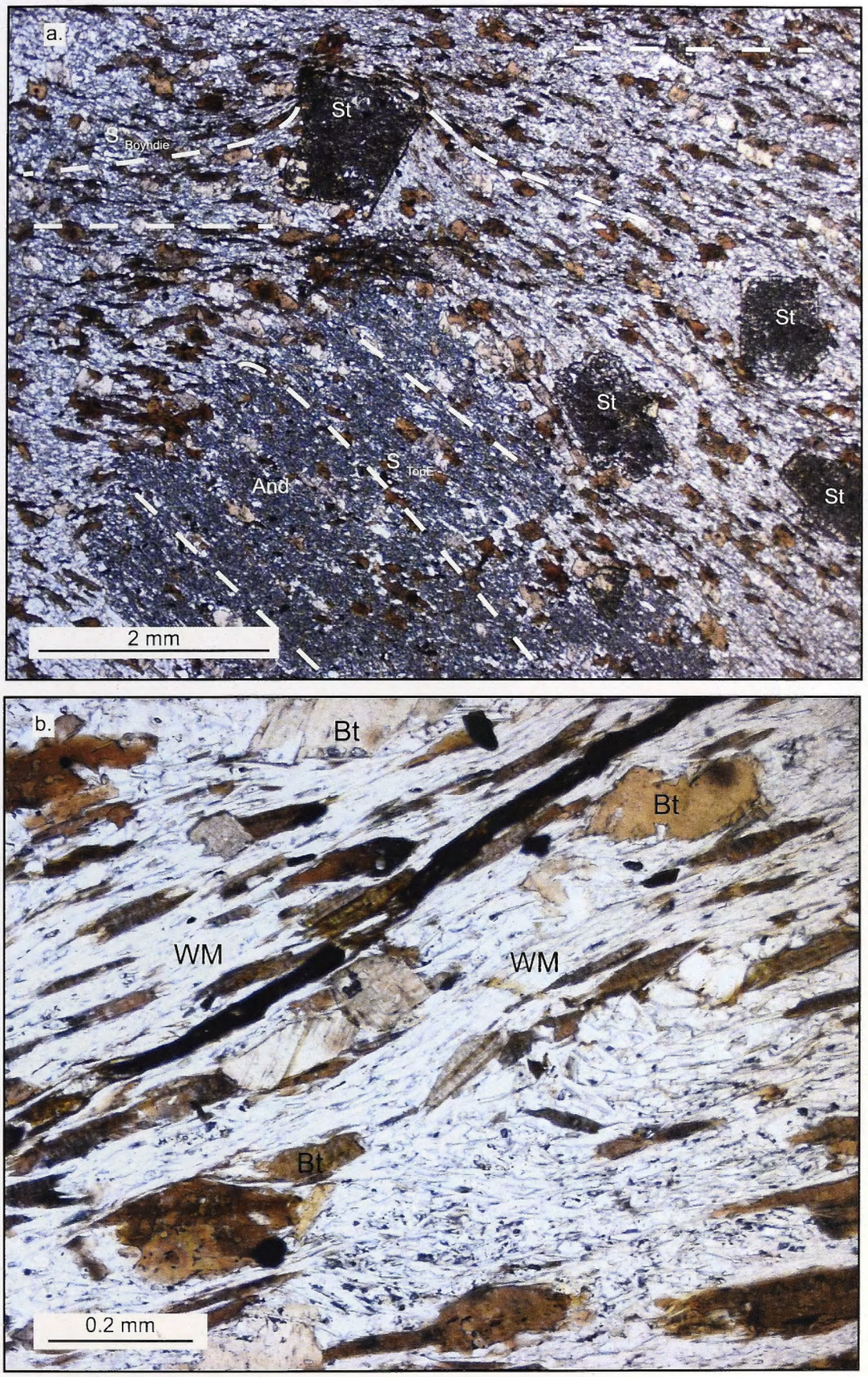

Figure 6.9: Photomicrographs in plane polarised light of sample IS10-09 from the staurolite/andalusite zone. (a) Staurolite and andalusite porphyroblasts are wrapped by the fabric. (b) The fabric is defined by the fine grained matrix minerals consisting of quartz, muscovite, biotite and opaque minerals.

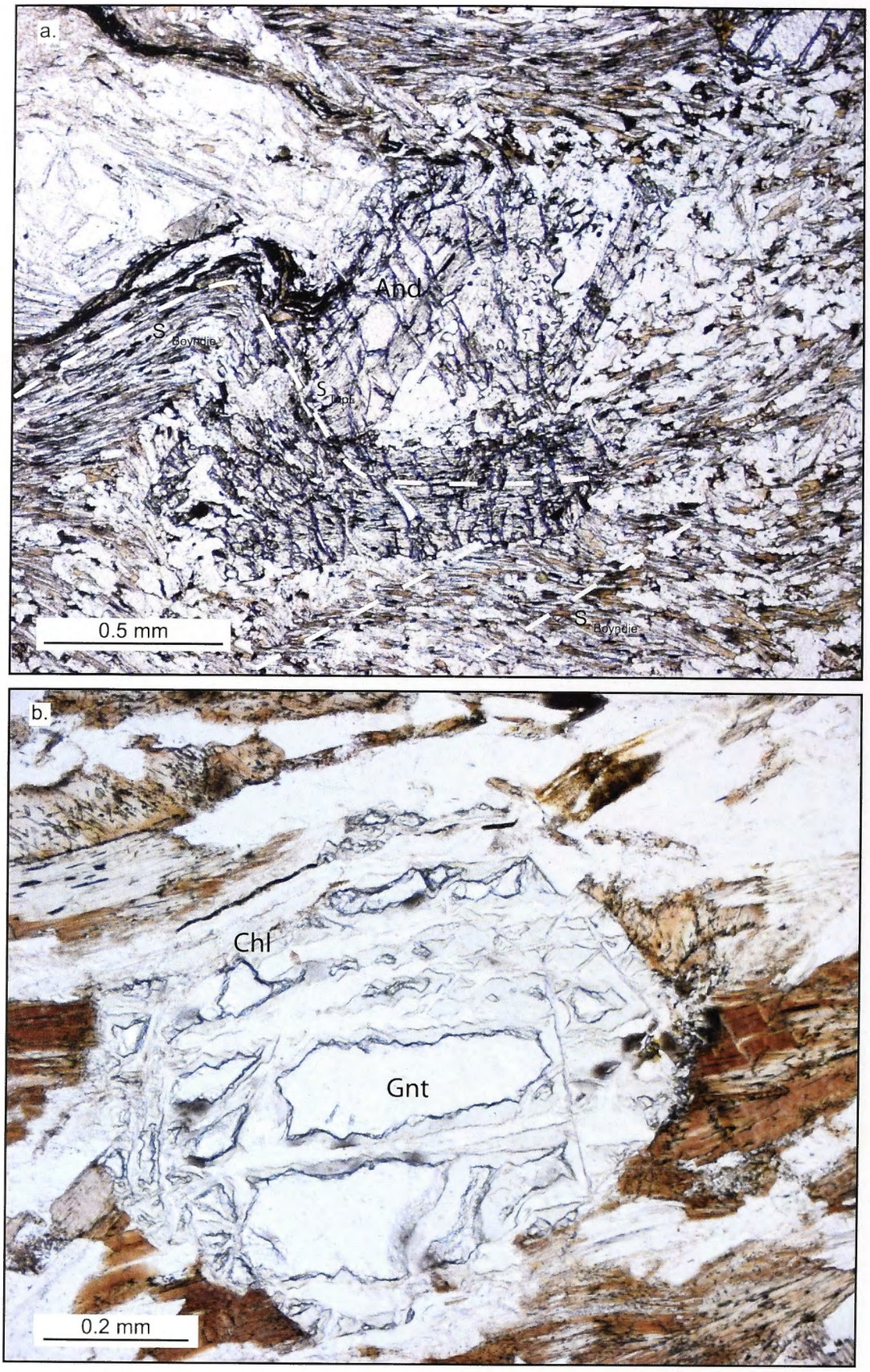

Figure 6.10: Photomicrographs in plane polarised light of samples from the sillimanite zone west and east of Portsoy (See Fig. 6.4). (a) Porphyroblast of andalusite from sample IS10-17 from the Portsoy swimming pool area. (b) Garnet from Links Bay in sample IS10-25 being replaced by chlorite.

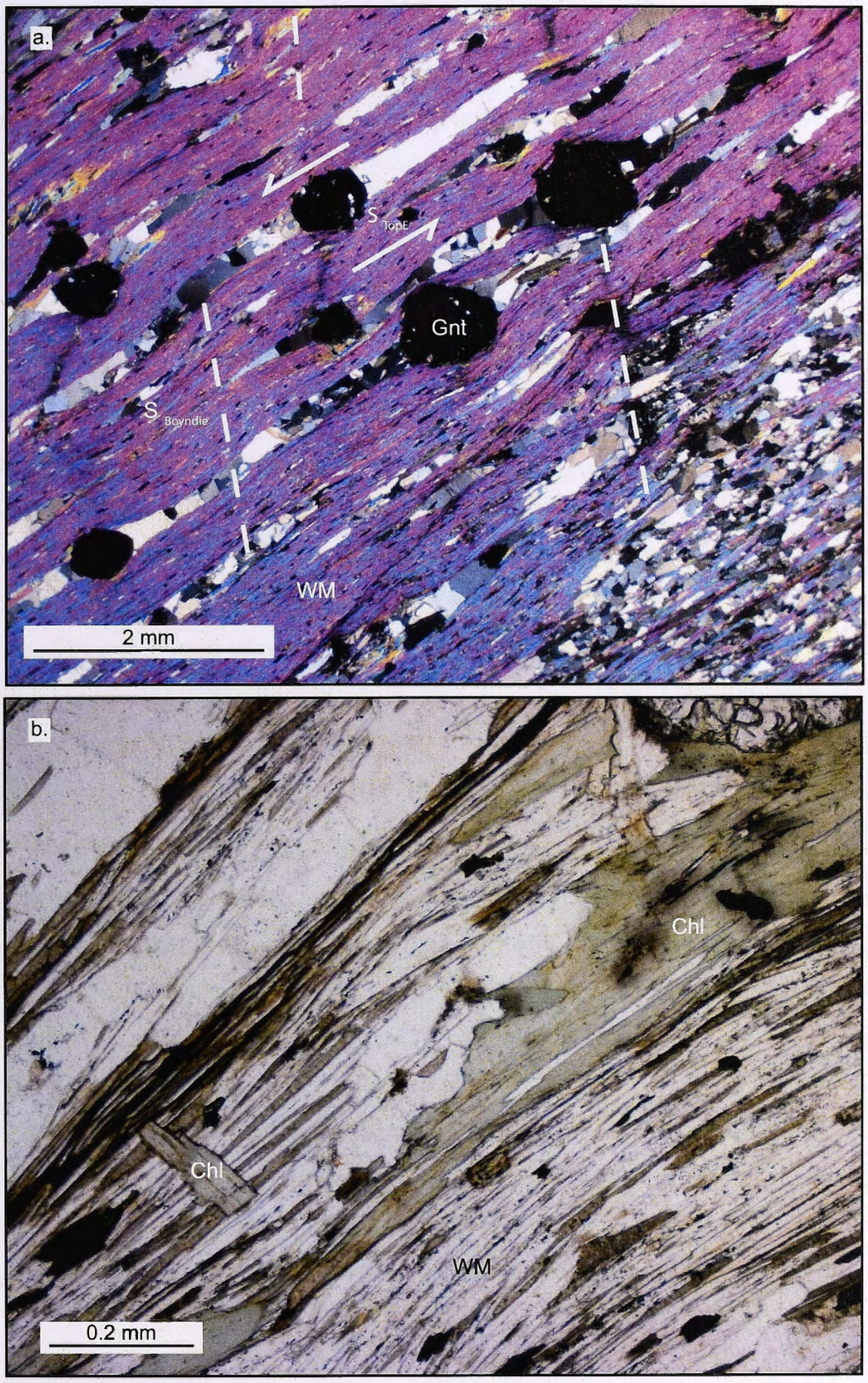

Figure 6.11: Photomicrograph of sample IS10-22 from a garnet-mica schist at Logie Head west of Portsoy. (a) Garnet porphyroblasts wrapped by a pervasive mica fabric in cross polarised light. This fabric is related to top-to-the-east shearing and has subsequently been folded by the Boyndie Syncline. (b) Fabric defined by mica with chlorite intergrowths in plane polarised light.

6.4.5 Electron Probe Microanalysis

The Cameca SX100 electron probe microanalyser (EPMA) at RSES, ANU was used to obtain the composition of white micas analysed for argon geochronology. A selection of spot analyses were performed with a beam current of 5 nA and spot size of approximately 5 μm using wave dispersive spectrometers (WDS), using phlogopite and hornblende standards. Data tables and related graphs for these analyses are provided in Appendix A. EPMA data was normalized to give per formula unit values (p.f.u) for 11 oxygen p.f.u by the method outlined in Deer et al. (1962).

Graphs illustrating the compositional variance of Si and Al in white mica are shown in Figures 6.12 and 6.13. The majority of Si values for these samples are between 3.0 and 3.2 p.f.u. Sample IS10-17 from the sillimanite zone of the Barrovian metamorphic sequence (Fig. 6.12a) shows clustered compositions compared to sample IS10-22 from the kyanite zone. The latter shows a spread in composition and a separate population of analysis points. From microstructural analysis this separate population appears to be related to later retrograde replacement of andalusite. Samples IS10-09 and IS10-25 from the higher grade zones of the Buchan metamorphic sequence show compositions that are clustered and in a similar range as for sample IS10-17 (Fig. 6.12b).

In a previous study, the Ti concentration of white micas from the Barrovian metamorphic sequence in Scotland show a trend of increasing concentration with peak metamorphic temperature (Viete et al., 2011a). This trend is not observed in samples containing detrital white mica. The Ti concentrations of white micas from the northeast coast, measured in this study, are plotted against the peak temperatures that were determined by Hudson (1985) in Figure 6.14. For sample IS10-28, from the cordierite zone, the low Ti concentrations were obtained from white mica within a cordierite porphyroblast. A change in the Ti concentrations between the lower and higher grade samples (above 500 °C) is observed. However, the correlation between temperature and Ti concentrations is not apparent. Additional samples are required for the trend to be defined for the northeast coast transect.

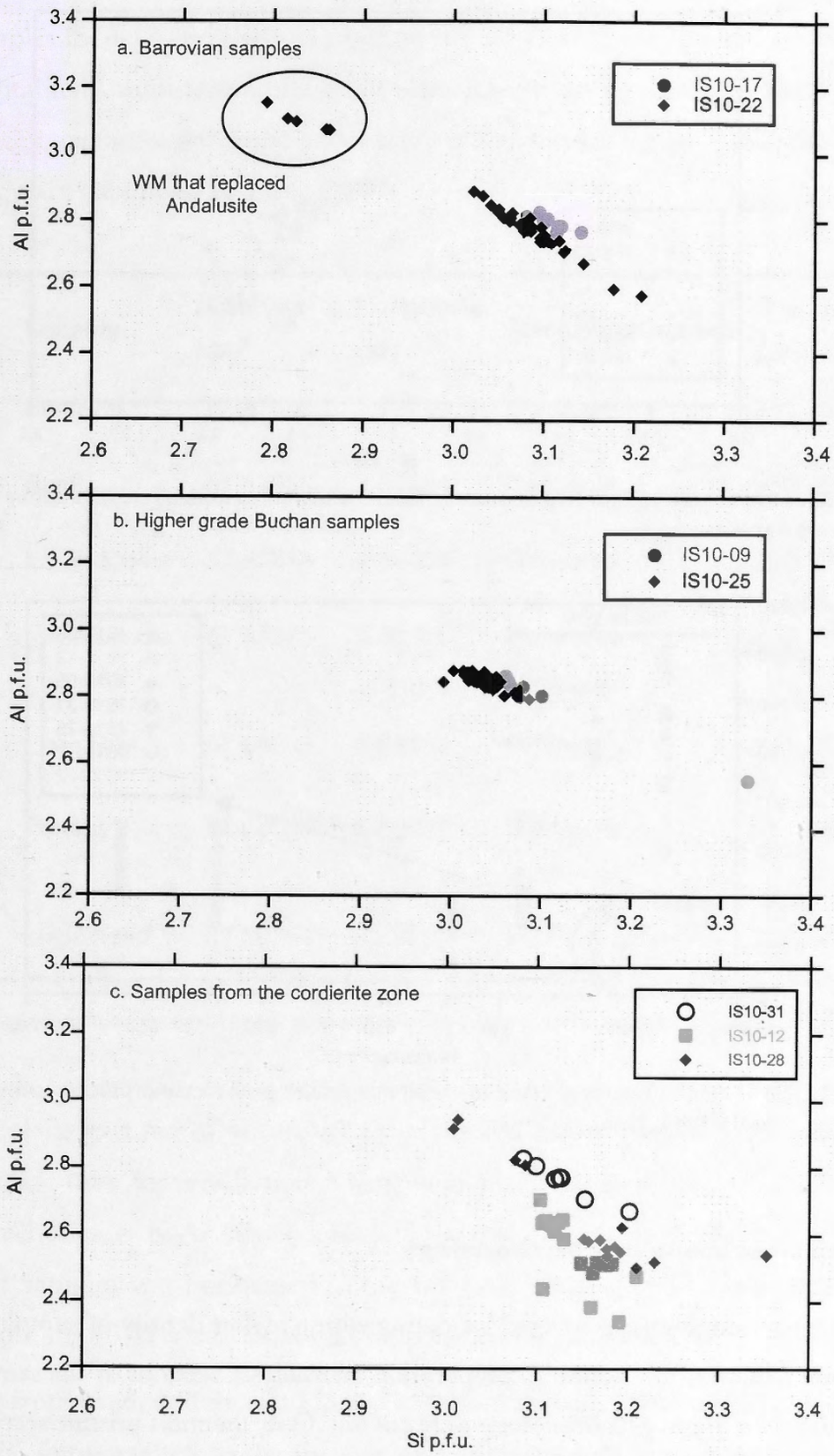

Figure 6.12: Si p.f.u is plotted against Al p.f.u for the separate sections of the northeast coast transect. (a) Barrovian metamorphic sequence samples from the west of Portsoy, IS10-17 and IS10-22. (b) Higher grade samples from the Buchan metamorphic sequence IS10-09 and IS10-25. (c) Samples from the cordierite zone of the Buchan sequence IS10-12, IS10-28 and IS10-31.

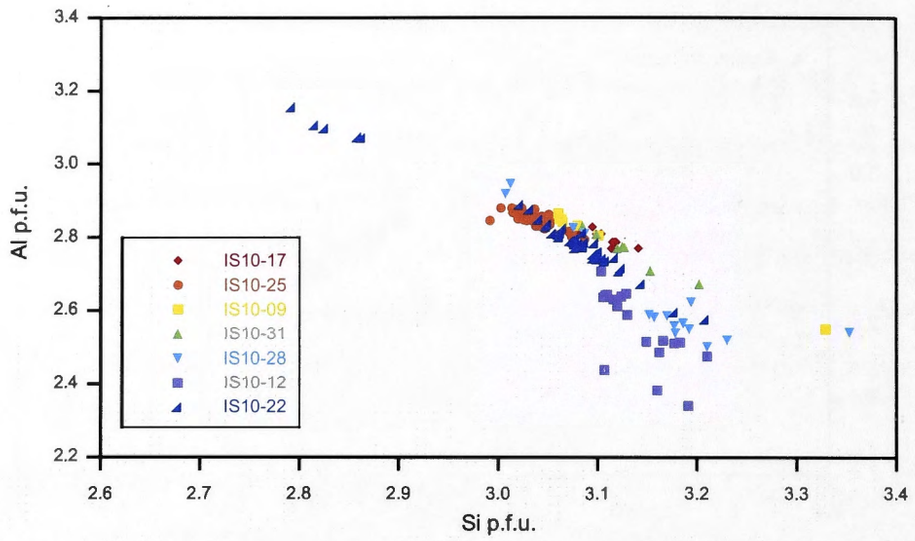

Figure 6.13: Plot of Si p.f.u against Al p.f.u content for the white micas from all samples across the northeast coast transect.

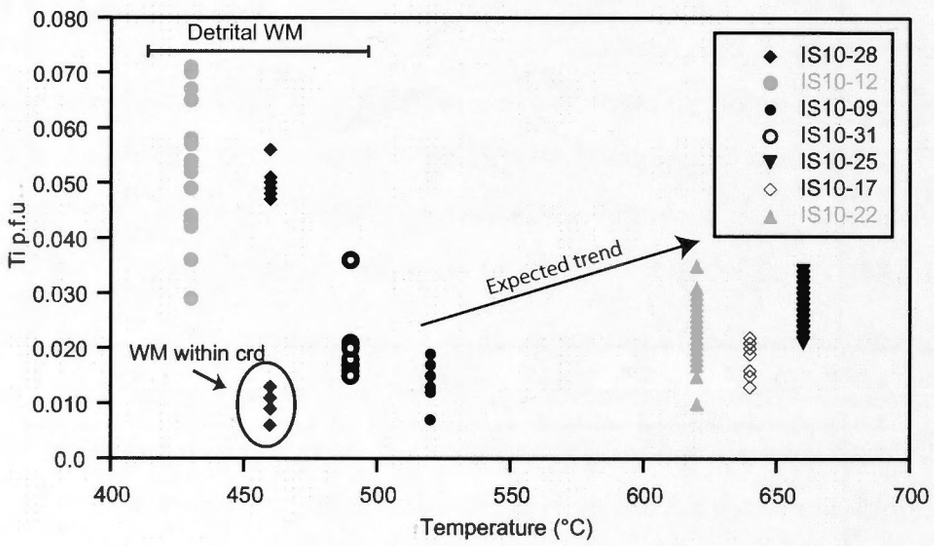

Figure 6.14: The Ti concentrations of white micas plotted against peak metamorphic temperatures that were determined by Hudson (1985).

6.5 Argon Geochronology Methodology

A total of nine samples were selected for dating with a higher density of sampling in the lower grade metamorphic zones. In preparation for analysis, sections of the samples that were the focus for argon geochronology were cut out. Only the most pristine sections were selected. These sections were then crushed using a tungsten carbide mill. Crushing was minimal to maintain whole white mica grains and to eliminate composites. The mineral separates were then sieved into separate size fractions. The size fractions of 150-250 μm

and 250-355 μm were magnetically separated to concentrate the white mica before hand picking. The white mica fractions were selected based on correlation with thin section analysis. Samples IS10-13 and IS10-11 from the biotite zone of the Buchan metamorphic sequence contained insufficient white mica after separation for analysis. Details of the sample localities, metamorphic zone and white mica grain size for samples used in argon geochronology are contained in Table 6.2.

Sample	Locality	Latitude (N)	Longitude (W)	Metamorphic zone	Grain size (μm)
IS10-12	Banff	57.67069	2.52750	Cordierite	250-150
IS10-28	Banff	57.67000	2.53364	Cordierite	250-150
IS10-31	Inverboyndie	57.67018	2.54464	Cordierite	250-150
IS10-09	Inverboyndie	57.67278	2.56114	Staurolite/ Andalusite	250-150
IS10-25	Links Bay	57.68286	2.68164	Sillimanite	250-355
IS10-17	Portsoy	57.68539	2.69897	Sillimanite (Barrovian)	250-355
IS10-22	Logie head	57.69744	2.78959	Kyanite (Barrovian)	250-355

Table 6.2: Sample localities, mineral grade and white mica grain size for samples dated by $^{40}Ar/^{39}Ar$ geochronology.

For each sample 2 to 3 mg of white mica was packed into aluminium foil packets and placed in a glass tube for irradiation, along with CaF_2, K-glass and GA 1550 biotite standard, which has a K-Ar age of 98.5 ± 0.8 Ma (Spell and McDougall, 2003). Irradiation of samples was performed in the CT position at the US Geological Survey TRIGA reactor, for 40 MWh in a canister with cadmium shielding.

After samples were irradiated the aluminium foil was removed and samples were wrapped in tin foil. The foil is melted in the furnace and contaminants are pumped away prior to analysis of the sample. All samples were analysed at the Research School of Earth Sciences (RSES) at The Australian National University (ANU) three to four months after being returned from the reactor (see Appendix B for analysis dates).

Flux monitors were analysed using a thermal diode continuous wave laser. Samples were step-heated in a temperature controlled furnace with heating schedules designed to release gas evenly from 450 °C to fusion at 1450 °C. The gas released from both of these processes, for the flux monitors and samples, was measured with the VG1200 mass spectrometer. Each heating step for samples was 15 minutes. The gas was cleaned using a liquid nitrogen trap as well as AP10 and GP50 SAES getters. The J factor was determined from measurement of the flux monitors, which were placed approximately every 2 mm and the J factors for samples were extrapolated from these values (Table 6.3).

Sample	Package	Weight (mg)	Position (mm)	J Factor	%err (1σ)
Flux Monitor	S5	3.6	12.0	8.880E-03	0.970
IS10-31	I7	1.8	13.0	8.886E-03	0.970
IS10-28	I6	0.7	13.0	8.886E-03	0.970
Flux Monitor	S4	3.8	14.0	8.892E-03	0.969
IS10-12	I5	2.8	15.0	8.897E-03	0.968
IS10-17	I4	2.6	15.0	8.897E-03	0.968
IS10-09	I3	2.2	16.0	8.902E-03	0.968
Flux Monitor	S3	3.6	16.0	8.902E-03	0.968
IS10-22	I2	2.1	17.0	8.908E-03	0.967
IS10-25	I1	2.3	18.0	8.913E-03	0.967
Flux Monitor	S2	3.5	19.0	8.918E-03	0.966

Table 6.3: The J Factor determined for each sample from extrapolation of analysis of flux monitors.

Blank analyses are undertaken at a series of increasing temperatures. These are monitored regularly and maintained an acceptable low level. Backgrounds are subtracted prior to data analysis. The mass discrimination used in data reduction was determined from measurement of the $^{40}Ar/^{36}Ar$ ratio in atmospheric argon. The $^{40}Ar/^{36}Ar$ ratio measured was 288.91 ± 2.684, which corresponds to a discrimination factor of 1.00567 ± 0.29%. The stability of the $^{40}Ar/^{36}Ar$ ratio was monitored as the samples were analysed.

Correction factors were calculated from the analyses of CaF_2 and K-glass, which were irradiated along with the samples. Data reduction was performed using Noble 1.8 with Cl correction. The calculation of correction factors was performed using a purpose built Excel spreadsheet and the correction factors used were $(^{36}Ar/^{37}Ar)_{Ca} = 2.75\times10^{-4}$, $(^{39}Ar/^{37}Ar)_{Ca} = 9.03\times10^{-3}$, $(^{40}Ar/^{39}Ar)_{K} = 1.04\times10^{-2}$ and $(^{38}Ar/^{39}Ar)_{K} = 1.32\times10^{-2}$. The abundance and decay constants of ^{40}K recommended by Steiger and Jager (1977) were used. All data tables from these analyses are in Appendix B.

6.6 Results

The results of the $^{40}Ar/^{39}Ar$ geochronology display two types of apparent age spectra as shown in Figures 6.15 and 6.16. The higher grade samples shown in Figure 6.15 display relatively flat profiles compared to the lower grade samples in Figure 6.16, which show complex apparent age spectra. The age spectra obtained from all of these samples were too complex to apply the plateau method for defining a single age for a sample. Instead, the determination of ages recorded in these samples was conducted using the method of asymptotes and limits (Forster and Lister, 2004). This method provides a means to estimate significant ages from complex apparent age spectra based on gas mixing between different microstructural/microchemical reservoirs in the white mica (Forster & Lister, 2004). The ages are determined from a single apparent age spectra obtained from step heating by identifying asymptotes and limits defined by the release of gas from different gas populations within a sample. The ages are indicated in Figures 6.15 and 6.16.

For the higher grade samples the upper and lower limits were determined (Fig. 6.15). These samples showed upper limits of 487.1 ± 5.8 Ma, 491.5 ± 5.6 Ma, 500.9 ± 0.5 Ma and 556.2 ± 8.8 Ma. The lower limits of the samples were within a smaller range with ages of 452.3 ± 6.9 Ma, 458.9 ± 2.5 Ma, 463.0 ± 2.7 Ma and 464.6 ± 8.5 Ma. An intermediate age can be interpreted from this method in the higher grade samples where the mean square weighted deviation (MSWD) of the age was close to one (Fig. 6.15, intermediate age). These intermediate ages range from 470.4 ± 1.8 Ma to 464.6 ± 1.3 Ma.

The higher grade samples reached temperatures greater than 550 °C during metamorphism (Hudson, 1985). At these temperatures the rate of diffusion of argon within white mica would be significant and the argon would be reset. Therefore the intermediate ages observed in apparent age spectra are interpreted to represent cooling

ages rather than crystallization or recrystallisation (Fig. 6.15). The later fabric associated with the Boyndie Syncline does not appear to significantly recrystallise the white mica in these samples (e.g. Fig. 6.11).

The cordierite zone samples displayed more complex apparent age spectra (Fig. 6.16). The lower limits defined in these spectra are 468.3 ± 20.4 Ma, 479.3 ± 25.0 Ma and 499.7 ± 4.7 Ma. The upper limits are defined as 720.2 ± 6.5 Ma, 757.4 ± 14.3 Ma and 765.2 ± 8.5 Ma. The intermediate age defined in the samples is *c.* 560 Ma with ages recorded at 551.9 ± 3.9 Ma, 556.1 ± 9.9 Ma, 559.3 ± 5.7 Ma, 584.3 ± 3.2 Ma. These ages match the upper limit defined in sample IS10-25 of 556.2 ± 8.8 Ma.

The lower grade samples from the cordierite zone preserve pre-Grampian ages and less than 10% of gas released is affected by the thermal event at *c.* 470 Ma. This is consistent with the white micas in the cordierite zone samples being detrital, as observed in microstructural analysis (Fig. 6.7). Samples IS10-28 and IS10-31 released only small amounts of gas during step heating, which resulted in the ages determined from these samples having larger errors. For sample IS10-28 this was a result of the sample being mica poor and only 0.7 mg of white mica could be picked for analysis. However, Sample IS10-31 did have a sufficient amount of white mica and it still only released small amounts of gas. There was nothing unusual about the sample analysis and no issues were found relating to the mass spectrometer. Additionally, this sample does not appear to have white mica with lower K content compared to the other samples (Appendix A). Although, the white mica was unclean due to intergrowths with other minerals, which might account for the low amounts of gas released.

The York and Ca/K plots for each sample are shown in Figures 6.17 to 6.23. For the higher grade samples (Figs. 6.17 to 6.20) the York plots show a cluster of steps at a single age that relates to the intermediate ages defined by the asymptotes and limits method. Whereas, the York plot for sample IS10-12 (Fig. 21) from the cordierite shows a spread of values in the $^{39}Ar/^{40}Ar$ ratio, which is indicative of mixing from different age populations. Further, the York plots of samples IS10-28 and IS10-31 (Figs. 22 and 23) from the cordierite zone show two clusters of steps, however, these analyses were affected by small amounts of gas release as stated above. The Ca/K plots (Figs. 6.17 to 6.23) for all samples show that there is no significant influence from Ca in these analyses and except for sample IS10-31, the values for Ca/K are largely below 0.1.

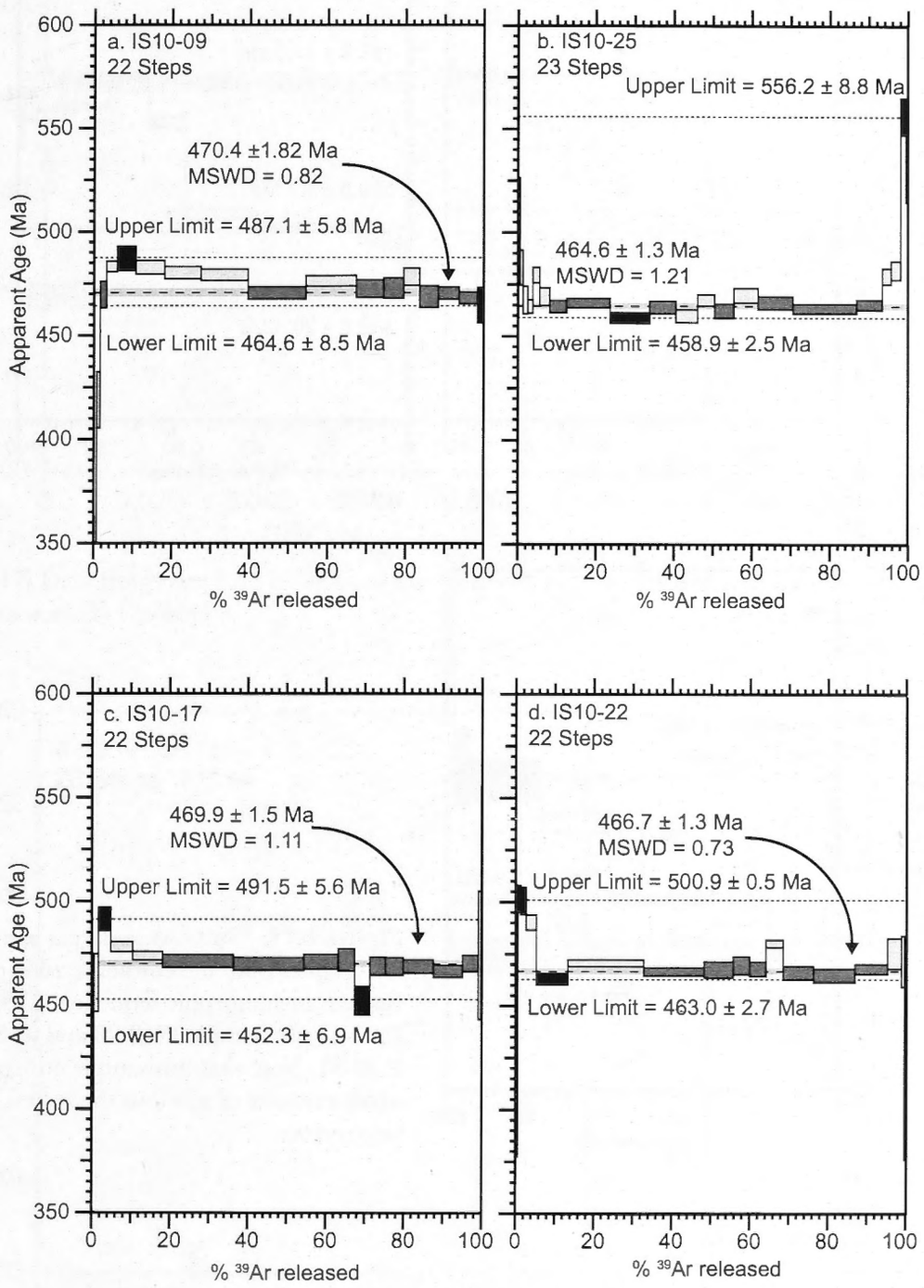

Figure 6.15: $^{40}Ar/^{39}Ar$ apparent age spectra for samples along the northeast coast Scotland from higher grade samples above the andalusite isograd. (a) Apparent age spectra for sample IS10-09 from the staurolite zone. (b) Apparent age spectra for sample IS10-25 from the sillimanite zone of the Buchan metamorphic sequence. (c) Apparent age spectra for sample IS10-17 from the sillimanite zone of the Barrovian metamorphic sequence. (d) Apparent age spectra for sample IS10-22 from the kyanite zone.

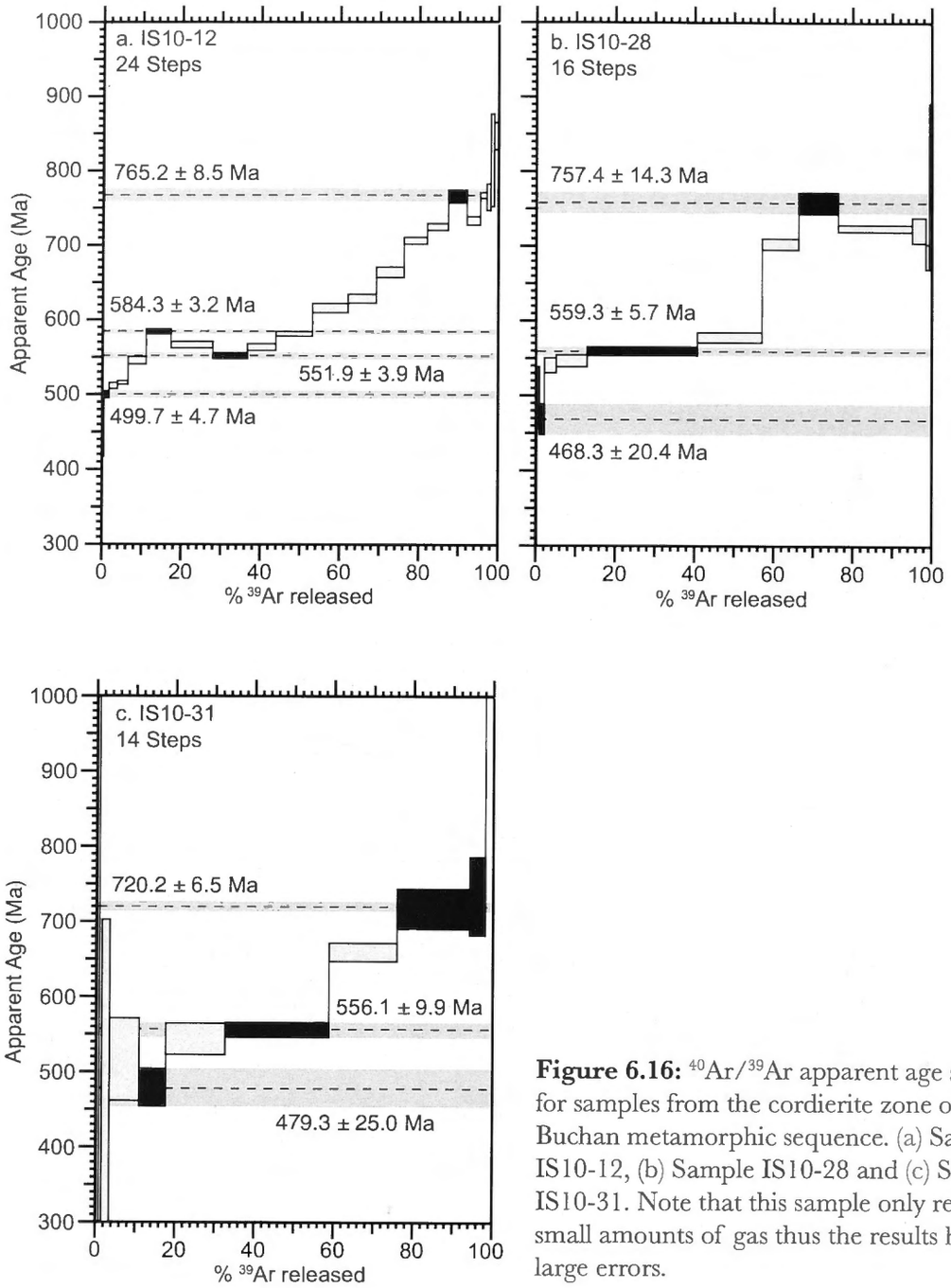

Figure 6.16: $^{40}Ar/^{39}Ar$ apparent age spectra for samples from the cordierite zone of the Buchan metamorphic sequence. (a) Sample IS10-12, (b) Sample IS10-28 and (c) Sample IS10-31. Note that this sample only released small amounts of gas thus the results have large errors.

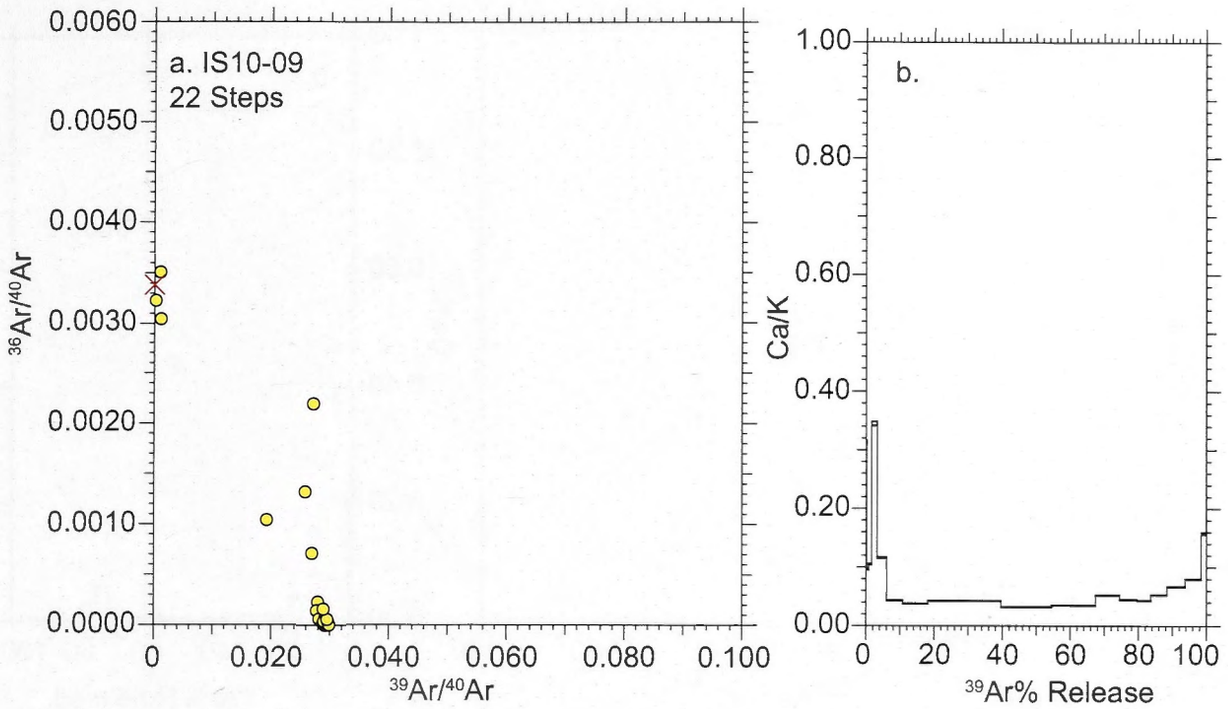

Figure 6.17: Data from sample IS10-09 from the staurolite zone of the Buchan metamorphic sequence. (a) York plot and; (b) Ca/K plot.

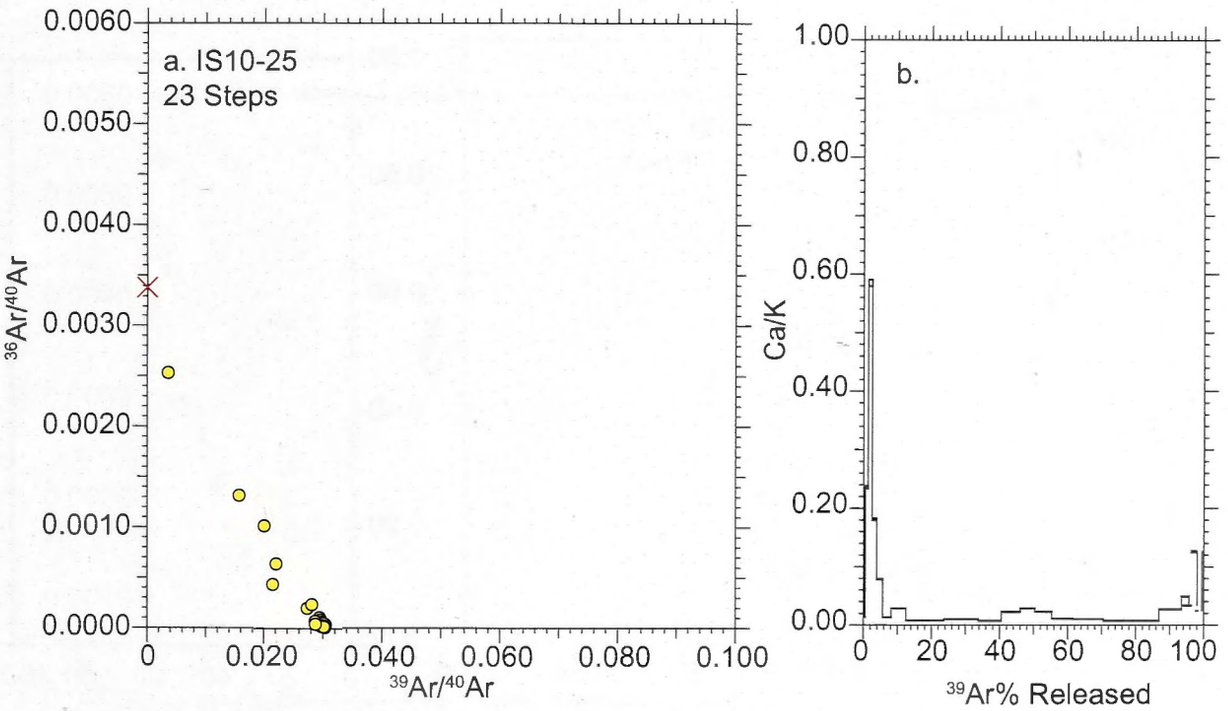

Figure 6.18: Data from sample IS10-25 from the sillimanite zone of the Buchan metamorphic sequence. (a) York plot and; (b) Ca/K plot.

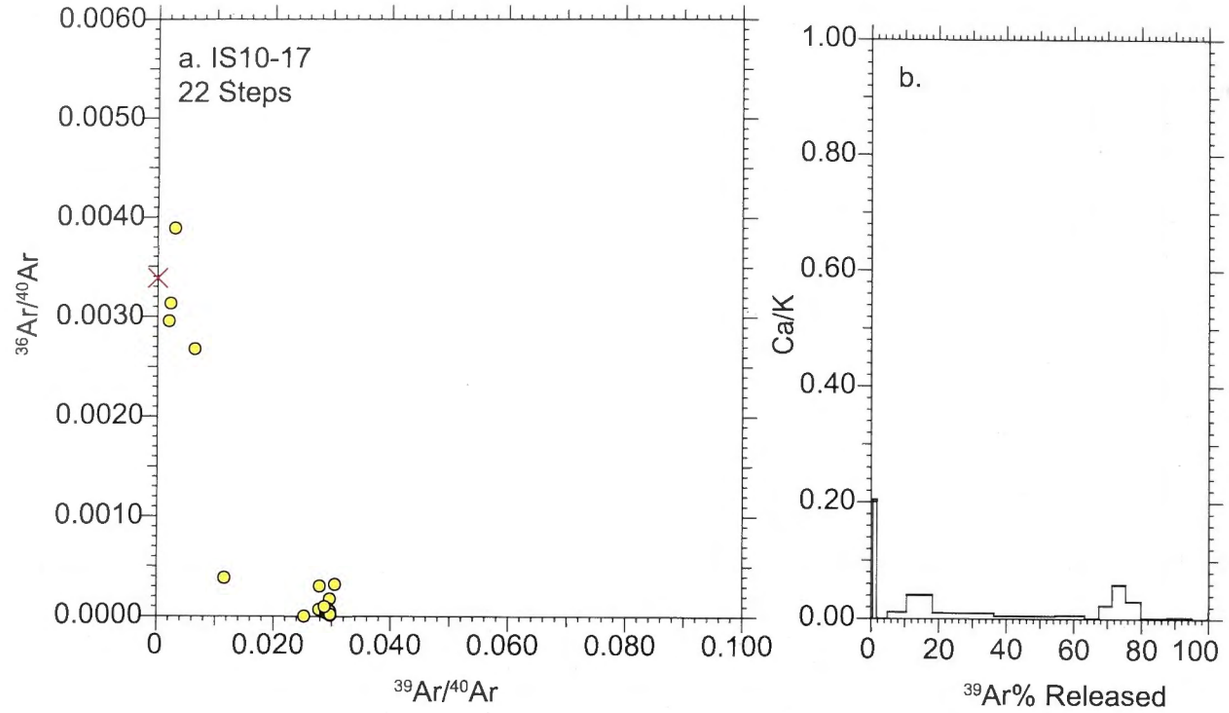

Figure 6.19: Data from sample IS10-17 from the sillimanite zone of the Barrovian metamorphic sequence. (a) York plot and; (b) Ca/K plot.

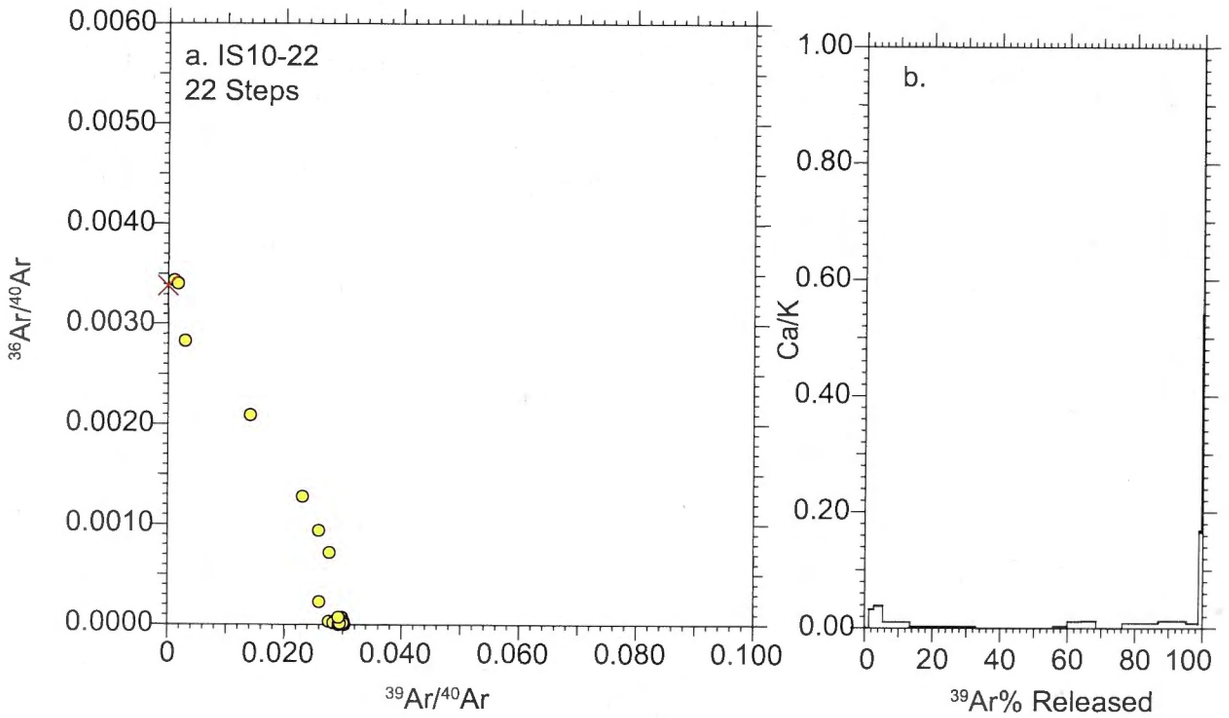

Figure 6.20: Data from sample IS10-22 from the kyanite zone of the Barrovian metamorphic sequence. (a) York plot and; (b) Ca/K plot.

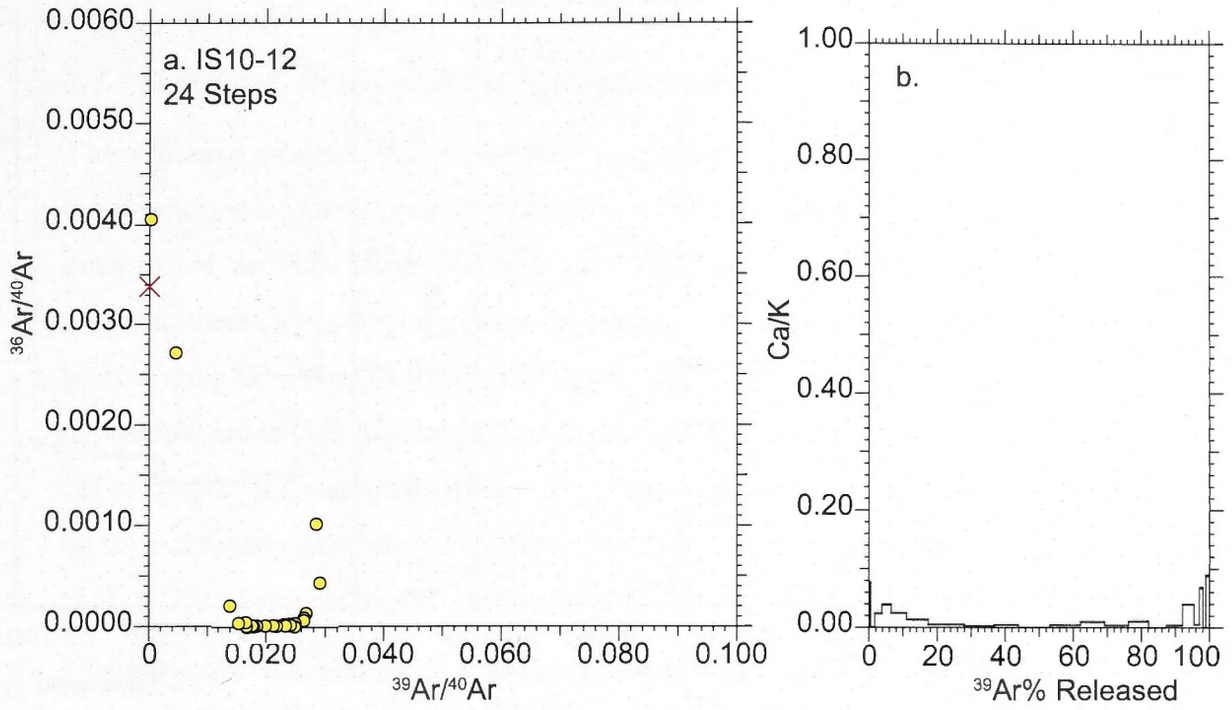

Figure 6.21: Data from sample IS10-12 from the cordierite zone of the Buchan metamorphic sequence. (a) York plot and; (b) Ca/K plot.

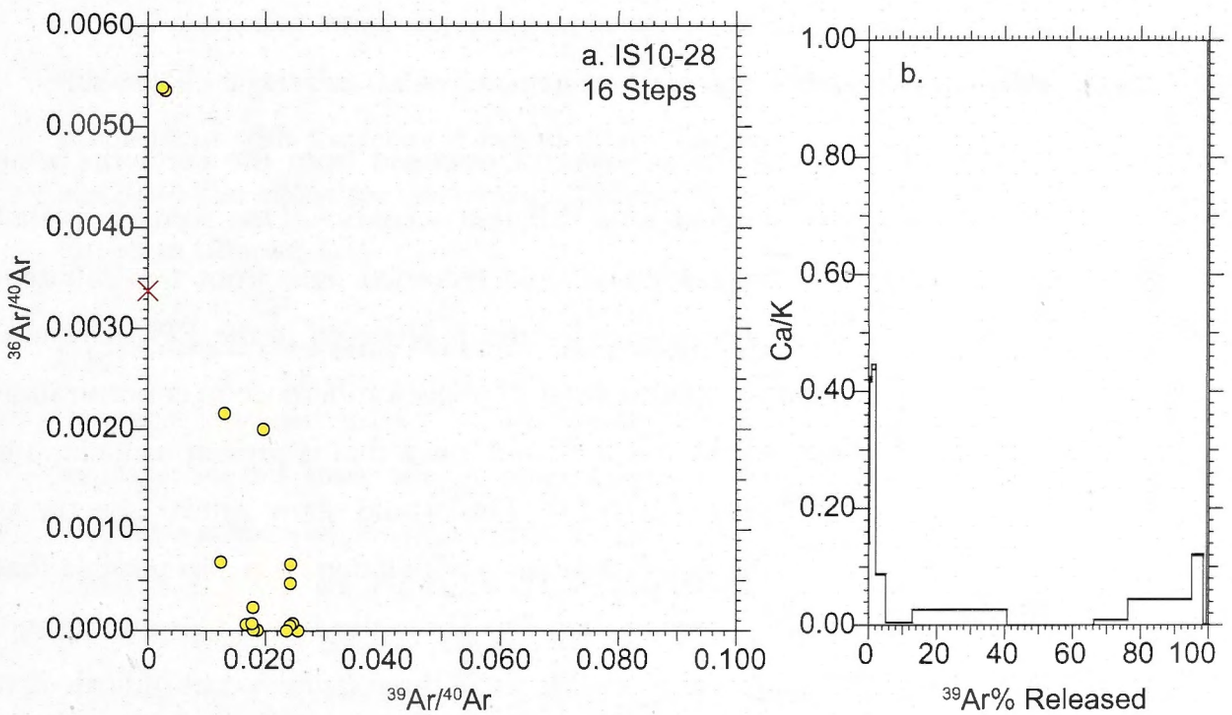

Figure 6.22: Data from sample IS10-28 from the cordierite zone of the Buchan metamorphic sequence. (a) York plot and; (b) Ca/K plot.

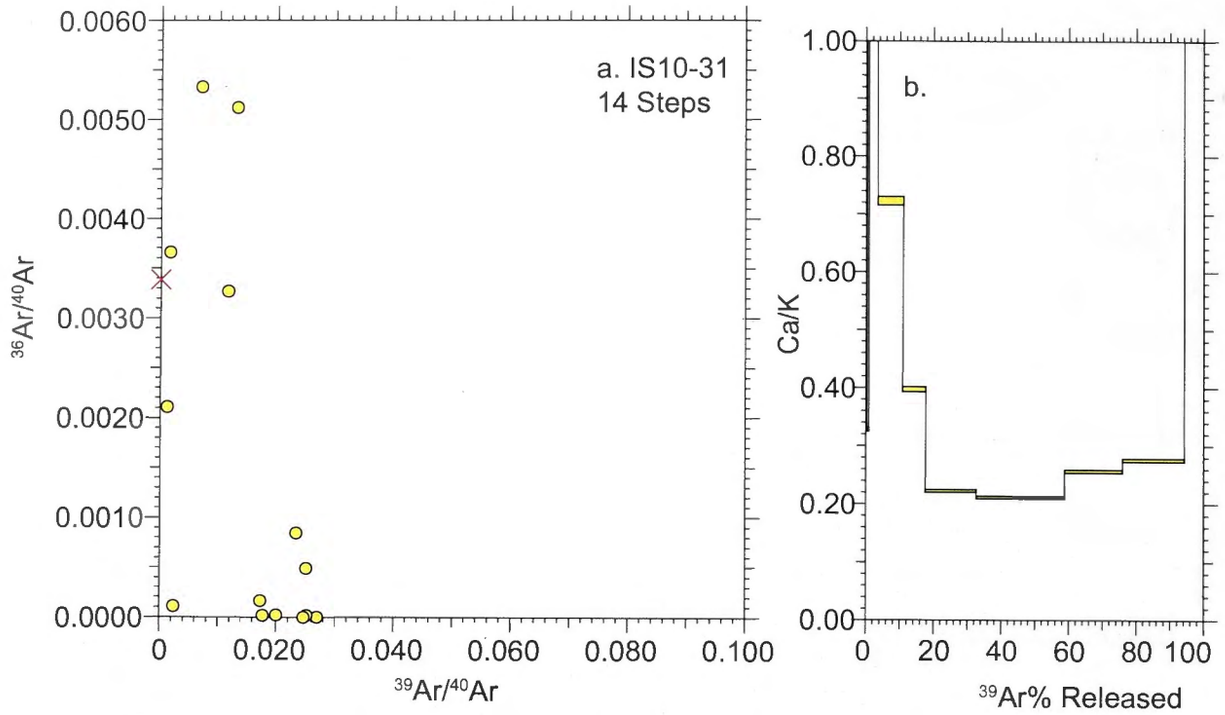

Figure 6.23: Data from sample IS10-31 from the cordierite zone of the Buchan metamorphic sequence. (a) York plot and; (b) Ca/K plot.

6.7 Discussion

6.7.1 Complex Age Spectra

The complex shape of the apparent age spectra obtained from the cordierite zone samples (Fig. 6.16) could have resulted from different scenarios. One scenario is that the spectra represent the superimposition of two recorded ages from two different populations of white mica. Possible evidence for this is observed in the EPMA results, where the Ti p.f.u concentrations in sample IS10-31 show a difference in concentration between the white mica in the matrix and the white mica that is present as inclusions within the cordierite porphyroblasts (Fig. 6.14). This would show similar spectra as mixing between two domains of the same white mica population. It is also possible that it displays mixing from an older age greater than 750 Ma to the 470 Ma Grampian age. However, the presence of the plateau at *c.* 560 Ma in all three samples does indicate that age is potentially significant. The step-wise spectra between the oldest age recorded and the age at 560 Ma also indicates diffusion loss between these two gas populations (Fig. 6.16; Sample IS10-12)

6.7.2 Sedimentation Age of the Upper Dalradian

There is some evidence in the literature (e.g. Tanner and Pringle, 1999) that indicates that the deposition of the Upper Dalradian was during the Cambrian (542 to 488 Ma). The intrusion of the Ben Vuirich Granite into the Dalradian sediments before the Grampian orogenic event gives an emplacement age of 590 ± 2 Ma (Rogers et al., 1989). The biostratigraphical evidence from the Upper Dalradian, as previously discussed, provides a deposition age of 525 Ma for the Leny Limestone (Tanner & Pringle, 1999), that out crops at Callander. Although, an Ordovician (~485 Ma) deposition age for the Macduff Slates on the northeast coast has been inferred from the presence of a single architarch (Downie et al. 1971; Molyneux, 1998). Although this conclusion has been widely debated.

The results from argon geochronology presented in this paper indicate that the sediment source of the Dalradian underwent a thermal or deformational event at 560 Ma. The presence of detrital white mica in these samples indicates that the samples are unlikely to have underwent this thermal or deformational event in situ. If an event of sufficient temperature and duration took place after sedimentation the ragged detrital appearance of the mica would have been modified by recrystallization and grain growth. Therefore, this would suggest that the sedimentation of the upper Dalradian was after 560 Ma. This is consistent with the tectonic model of the Grampian Terrane presented by Viete et al. (2010) that allows for syn-metamorphic sedimentation. This model will be discussed further in Chapter 7.

6.7.3 Comparison with Previous Geochronology

The ages obtained from $^{40}Ar/^{39}Ar$ dating techniques for the Buchan metamorphic sequence in this study are in general agreement with previously determined ages. The high grade samples record intermediate ages that range from 470.4 ± 1.8 Ma to 464.6 ± 0.3 Ma (see Fig. 6.15). This age range is close to the accepted age of peak metamorphism in the Dalradian sediments of *c.* 470 Ma (e.g. Oliver et al., 2008). However, the ages obtained in this study from the higher grade samples are interpreted as cooling ages. This result is corroborated by previous ages from the northeast coast of Scotland (Carty, 2001; Dempster et al., 1995). For instance the biotite-whole-rock and muscovite whole rock Rb-Sr ages determined in a study by Dempster et al. (1995) range

from *c.* 470 Ma to *c.* 440 Ma for samples from Portsoy to Cullen. These ages were also interpreted as cooling ages. This result indicates rapid cooling.

The Cowhythe Gneiss (see Fig. 6.1 for sample locality) sample allows a direct comparison of ages between the Dempster et al. (1995) study and this study. For the Cowhythe Gneiss Dempster et al. (1995) obtained a Rb-Sr muscovite age of 476 Ma that corresponds to cooling through 500 °C. The $^{40}Ar/^{39}Ar$ white mica age for sample IS10-25 from the same locality is 464.6 ± 1.3 Ma for cooling through 400 °C. These ages are both close to the accepted age for peak metamorphism at *c.* 470 Ma, as determined by Oliver et al. (2000) from dating the inferred syn-metamorphic Strichen Granite at 467 ± 7 Ma in the Buchan zones. This age is also reflected in the Barrovian zones from the Sm-Nd garnet ages (Baxter et al., 2002; Oliver et al., 2000), which are interpreted as ages of garnet growth. If the peak of Barrovian and Buchan metamorphism is synchronous at *c.* 470 Ma the cooling ages determined in this study correspond to a cooling rate for sample IS10-25 of approximately 47 °C Ma^{-1}.

The pre-Grampian age *c.* 560 Ma was recorded in four samples in this study, including all of the lower grade cordierite zone samples (Fig. 6.16). It closely matches an age that Dempster et al. (1995) reported from a biotite grade sample from the Buchan metamorphic sequence. An age of *c.* 570 Ma was obtained from Rb-Sr muscovite-whole rock dating. This study did not speculate as to the significance of this age.

The age ranges seen in this study are also similar to those obtained from $^{40}Ar/^{39}Ar$ dating of the Barrovian metamorphic sequence to the south in the Glen Esk/Stonehaven area (Viete et al., 2011). In the Viete et al. (2011) study, pre-Grampian age ranges of 485 Ma, 560-510 Ma, 780-700 Ma and 1080-930 Ma were obtained from biotite grade samples. In their study the 485 Ma age was attributed to an early folding event during Grampian orogenesis. The 780-700 Ma age range, which matches our *c.* 750 Ma age, is in agreement with a 737 ± 5 Ma age determined from U/Pb titanite (Tanner and Evans 2003) and the 740 ± 40 Ma Rb/Sr mineral-whole-rock age of Piasecki and Van Breemen (1983). These ages have been interpreted as dating a Knoydartian tectonothermal event. Although, this study also gave no indication as to what the c. 560 Ma age could be related too. The age is, however, also reflected in ages obtained from U-Pb zircon and Rb-Sr whole rock ages in the Northern Highlands that are ages of granite emplacement (Pankhurst & Pidgeon, 1976).

6.8 Conclusions

The $^{40}Ar/^{39}Ar$ apparent age spectra obtained from white mica with a detrital component in samples from the cordierite zone of the Buchan metamorphic sequence indicates that deposition of the Upper Dalradian took place after *c.* 560 Ma. Viete et al. (2010) proposed a new tectonic model that describes the formation of the Buchan and the adjacent Barrovian metamorphic sequence in a lithospheric-scale extensional system, which allows for syn-metamorphic sedimentation and the data presented here is consistent with that model.

The $^{40}Ar/^{39}Ar$ apparent age spectra from the higher grade samples show intermediate ages that range from 470.4 ± 1.8 Ma to 464.6 ± 1.3 Ma. These ages are interpreted to be cooling ages as the samples were at high temperatures and therefore indicate rapid cooling from peak metamorphism at *c.* 470 Ma. This provides further confirmation that the Barrovian and Buchan metamorphic sequences formed synchronously.

CHAPTER 7

The Duration of Buchan Metamorphism from Diffusion Modelling of Argon in White Mica

Preface

The argon geochronology results presented in Chapter 6 are utilised in this study for comparison to forward modelling of argon diffusion in white mica. In this study diffusion modelling was carried out using the MacArgon and eArgon computer programs, which were both developed by Professor Gordon Lister. As the argon geochronology community prefers to use the units Kcal mol^{-1} for activation energy in this chapter these values are referred to with these units followed by the value in SI units of KJ mol^{-1}. Except where otherwise indicated the research reported on in this chapter is my own work.

7.0 Synopsis

The $^{40}Ar/^{39}Ar$ geochronology of cordierite grade samples from the Buchan metamorphic sequence in Scotland yielded complex apparent age spectra that displayed pre-Grampian ages. Forward modelling of the effect of thermal events on the argon age spectra was carried out using the MacArgon computer program (Lister and Baldwin, 1996). This modelling allowed determination of the maximum duration of the Buchan thermal event that these rocks could have endured and still retain pre-Grampian ages. This modelling was undertaken using the muscovite diffusion parameters determined by Harrison et al. (2009) and simplified pressure-temperature-time (P-T-t) paths to simulate the effect of metamorphism. Results from square-wave T-t path modelling constrain a maximum duration for peak metamorphic conditions between 1000 and 10 000 years. However, square wave T-t paths, where heating to and cooling from peak conditions is instantaneous, will always underestimate actual durations of the thermal event. While modelling using a flash heating curve that describes a conductive heating and cooling T-t path indicated a duration of 1000 years or less at peak temperature (430 °C), this corresponds to a duration of 10 000 years above 300 °C and approximately 100 000 years above 100 °C. The conductive length scale for this T-t path is 1000 m, dictating that the heat source needs to be within this distance.

The duration determined from diffusion modelling is dependent on the diffusion parameters used for the simulation. However, for white mica there is only one set of experimentally determined parameters. Therefore, inverse modelling of the diffusion properties of white micas measured in this study was undertaken. This modelling was done using the eArgon computer program to model the Arrhenius parameters (D_0/r^2 and E). The analytical data can be fitted reasonably well to modelled data. However, the parameters obtained from modelling were consistently less retentive than those of Harrison et al. (2009) and therefore would result in an even shorter estimate for the duration of the Buchan thermal event. These micas were once detritus in a sandstone-shale sequence, however, and thus their crystal structure may have been substantially modified.

7.1 Introduction

The duration of the entire Grampian orogenic event has been constrained to last between 12 and 18 Ma (Friedrich et al., 1999; Oliver et al., 2000; and Dewey, 2005). Friedrich et al. (1999) presented U-Pb ages, from the Connemara region of Ireland, for the undeformed Oughterard granite. This xenotime U-Pb age of 462.5 ± 1.2 Ma provides a constraint for the end of the Grampian Orogeny. The oldest age recorded by Friedrich et al. (1999) was 474.5 ± 1 Ma for the Currywongaun Gabbro, which is an indication of the start of orogeny. Previous work had demonstrated the intrusive activity and Grampian mid-crustal deformation to be broadly synchronous (Friedrich et al., 1999).

These limits are closely matched by geochronological data from Scotland (Oliver et al., 2000; Bluck et al., 1980). Bluck et al. (1980) inferred the K-Ar hornblende age from the metamorphic sole of the Ballantrae Ophiolite Complex to be 478 ± 8 Ma and that this age marked the onset of the Grampian Orogeny. Later $^{40}Ar/^{39}Ar$ dating confirmed the age at 478 ± 2 Ma (Flinn et al., 1991). The geochronological work of Oliver et al. (2000) determined an age of 457 ± 0.9 Ma for the emplacement of the undeformed Kennethmont Granite in the Buchan Block, thus further constraining the end of the Grampian Orogeny.

During the Grampian Orogeny the Dalradian sediments were metamorphosed to form the Barrovian and Buchan metamorphic sequences (Chinner, 1966; Fig. 6.1, Chapter 6). Zircon and garnet radiometric dates from the northeast of Scotland have determined that the two metamorphic sequences formed synchronously at *c.* 470 Ma (Oliver et al., 2000). This result was corroborated by argon geochronology (Chapter 6), which provided cooling ages that ranged from 470.4 ± 1.8 Ma to 464.6 ± 1.3 Ma.

Recent studies of the Barrovian metamorphic sequence have made the argument that the maximum duration of the thermal event that produced the metamorphism in Scotland was a few million years (e.g. Viete et al., 2011a; Viete et al., 2011b). Forward modelling of $^{40}Ar/^{39}Ar$ age spectra of samples from the Barrovian metamorphic sequence, conducted by Viete et al. (2011a), suggested that heating above 50 °C in the biotite zone (peak temperature 475 °C) of the Barrovian metamorphic sequence lasted between 1 and 10 Ma. Further, Viete et al. (2011b) inferred, from diffusional modification to garnet major element zoning profiles, that small-scale local thermal excursions occurred over

durations of a few tens of thousands of years while a background regional thermal event occurred over a few million years.

Even shorter timescales were proposed by Ague and Baxter (2007) based on square wave Temperature-time (T-t) diffusion modelling of Sr in apatite. Sr diffusion in apatite is sluggish below 500 °C (Ague and Baxter, 2007) therefore their modelling was conducted with an ambient temperature of 450 °C. They determined the duration of thermal event to be between 200 000 and 300 000 years above 500 °C in the garnet, staurolite and sillimanite zones.

These short timescales determined from diffusion modelling studies have consequences for the tectonic setting in which this regional metamorphic belt formed. For example, the durations determined are incongruent with those predicted by the established crustal thickening and erosion model of metamorphism of England and Thompson (1984). This model can require up to 50 Ma to produce Barrovian mineral assemblages and it fails to predict the Buchan mineral assemblages without an added heat source. For the Grampian Terrane the additional heat required has been attributed to magmatic intrusions (e.g. Ague and Baxter, 2007). If the Buchan thermal event can be related to the same heat source for metamorphism, constraining the duration of the thermal event could possibly provide further evidence in support of magmatism as the primary heat source for metamorphism in the Grampian Terrane in Scotland.

Results from argon geochronology (Chapter 6), conducted on samples from the cordierite zone of the Buchan metamorphic sequence displayed complex $^{40}Ar/^{39}Ar$ apparent age spectra. The apparent age spectra show that the white mica has preserved pre-Grampian ages, with a correlation across the three samples for an age of *c.* 560 Ma. The spectra also record evidence of an age that is greater than *c.* 750 Ma. The preservation of these ages can be used as a constraint for diffusion modelling of argon in white mica.

For the purposes of modelling carried out in this study, it is assumed that volume diffusion is the dominant process releasing argon during step-heating *in vacuo* as well as during deformation and metamorphism (Forster and Lister, 2004). Therefore, the ability of the white mica in the samples to preserve pre-Grampian ages is dependent on the temperature and duration of the thermal event associated with Buchan metamorphism at *c.* 470 Ma, as argon in the white mica would be reset and no longer preserve older ages in samples that have been heated for a long time or at high temperatures. The peak temperature

of these samples during Buchan metamorphism has been constrained independently. Therefore, constraints can be developed as to the duration of heating that the Dalradian sediments could have endured and still preserve the pre-Grampian ages (e.g. Lister and Baldwin, 1996; Wijbrans and McDougall, 1986).

7.2 Argon Geochronology

The cordierite zone samples used in this study were collected from Boyndie Bay, where the metamorphic grade increases towards the west until the andalusite isograd is reached (Hudson, 1985). The localities for these three samples as well as the temperature estimates of Hudson (1985) are shown in Figure 7.1. The temperature estimates for the cordierite isograd and andalusite isograd presented by Hudson (1985) were determined from calc-silicate bands within the pelitic lithologies of the Southern Highland Group of the Dalradian sediments. A temperature of 430 ± 15 °C was obtained for the cordierite isograd and 490 ± 15 °C for the andalusite isograd (Hudson, 1985). These temperatures were calculated using the garnet-biotite Fe-Mg exchange thermometer of Hodges and Spear (1982) and corroborated by the garnet-hornblende Fe-Mg exchange thermometer of Graham and Powell (1984). Hudson (1985) did not constrain the pressure directly from the cordierite zone, but bracketed the possible value based on pressure estimates from the adjacent andalusite zone and biotite zone. These estimates provided a pressure range of 2 to 4 kbar for the cordierite zone (Hudson, 1985). The temperature and pressure estimates determined by Hudson (1985) are used to constrain the Pressure-Temperature-time (P-T-t) paths for modelling.

The argon geochronology conducted on samples from the northeast coast of Scotland (Chapter 6) revealed that the cordierite grade samples all preserved pre-Grampian ages. To determine the significant age ranges in these samples the method of asymptotes and limits of Forster and Lister (2004) was applied. The argon apparent age spectra of these samples show a significant age at *c.* 560 Ma and an age greater than 750 Ma (Fig. 7.2).

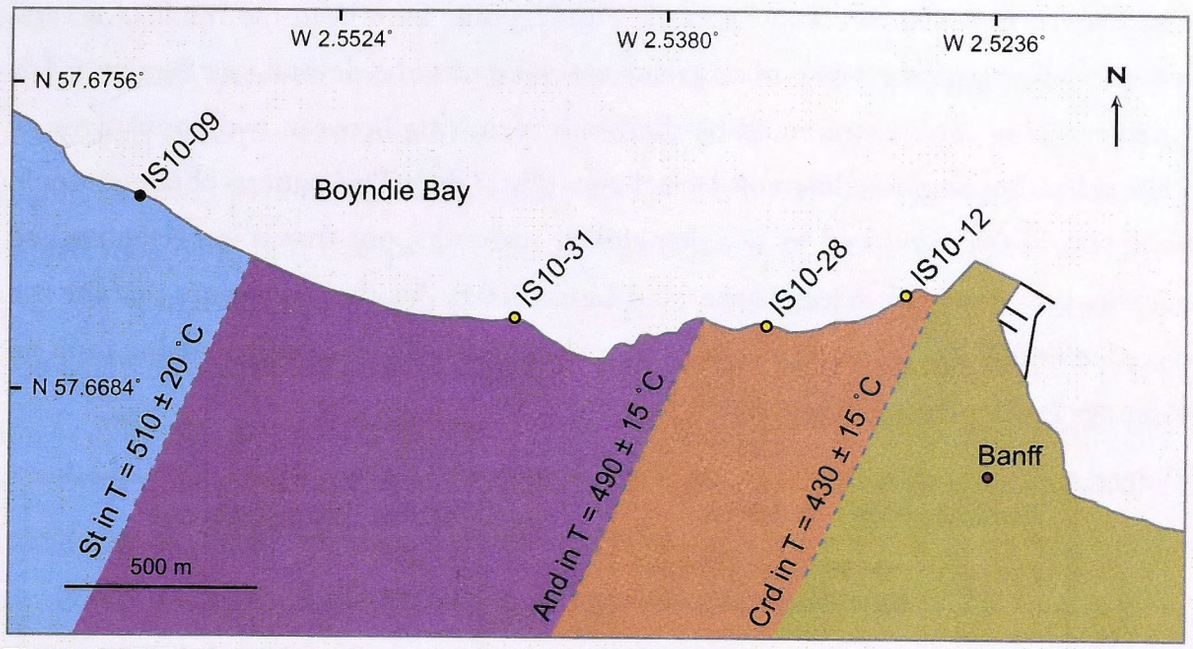

Figure 7.1: Sample localities of the three samples from the cordierite zone of the Buchan metamorphic sequence, northeast Scotland. An increase in metamorphic grade is observed towards the west of Boyndie Bay. The temperature estimates of Hudson (1985) are displayed.

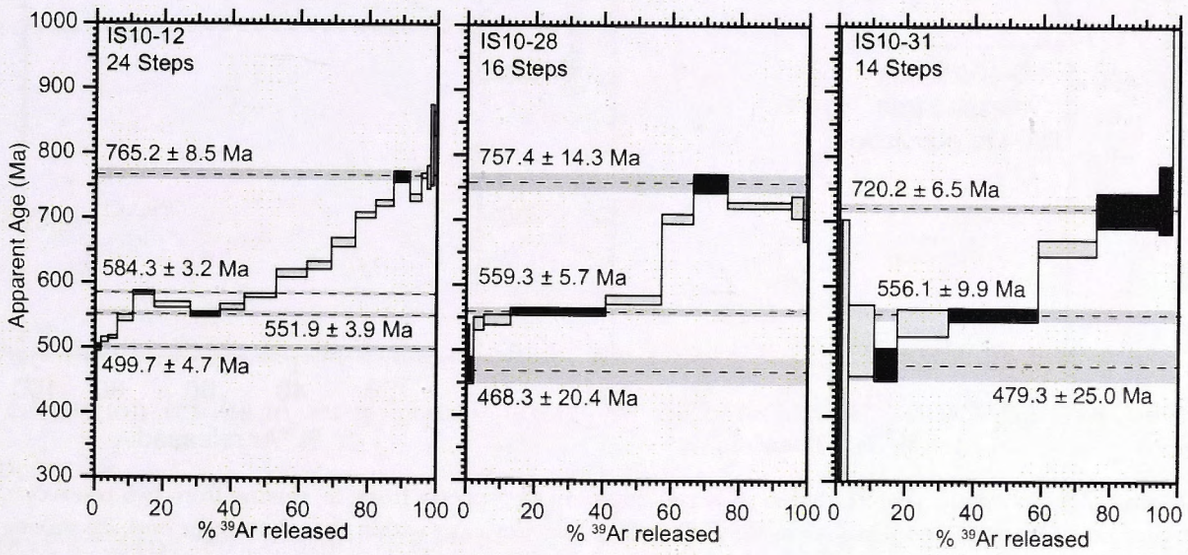

Figure 7.2: $^{40}Ar/^{39}Ar$ apparent age spectra from cordierite zone samples from the Buchan metamorphic sequence, Scotland that preserve pre-Grampian ages.

The pattern in the apparent age spectra (Fig. 7.2) may have been the result of several scenarios. Firstly, as the white mica grains are inferred to be detrital (see Section 6.4.2, Chapter 6) the age spectra could be the result of mixing between two populations of white mica that retained different detrital ages (Fig. 7.3a.). This pattern obtained would be similar to that produced by two domains or reservoirs, one that is less retentive and one that is more retentive (e.g. Forster and Lister, 2004). Another scenario is that the age recorded at 560 Ma is not significant and spectra represent progressive mixing from an older age greater than 750 Ma (Fig. 7.3b.).

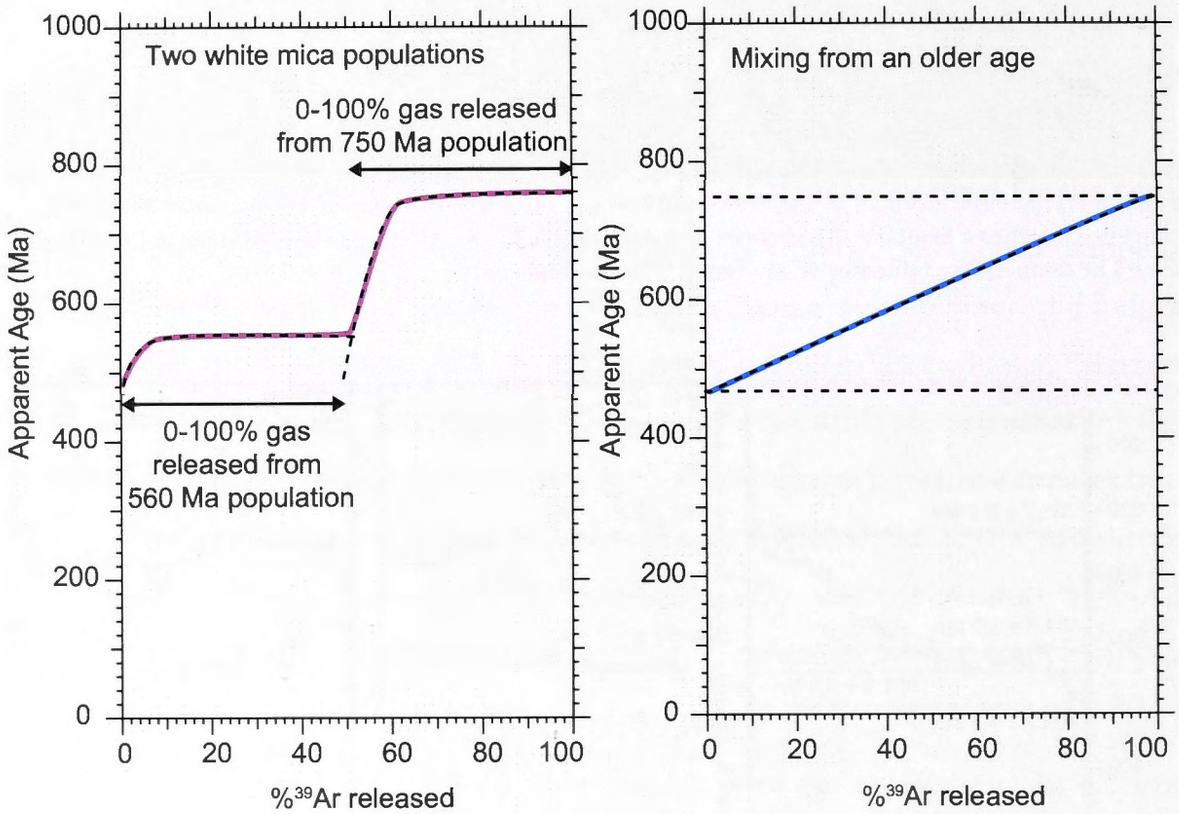

Figure 7.3: Schematic representation of argon apparent age spectra from: (a) mixing from two reservoirs, either two white mica populations in the sediment or two domains within the white mica and, (b) mixing from an older age.

The results indicate that the *c.* 560 Ma age is significant as it is obtained from all three samples. This shows it is unlikely to be the result of an inappropriate furnace schedule. Therefore, the apparent age spectra pattern seen in the cordierite samples are assumed to be a result of mixing from two reservoirs that retain different ages. However, these reservoirs could be either different domains within the same white mica population or white micas from separate sediment sources with different tectonometamorphic history.

7.3 Argon Diffusion Modelling

Diffusion modelling was carried out using MacArgon, a program that was developed to forward model the $^{40}Ar/^{39}Ar$ apparent age spectra obtained using the step-heating argon geochronology technique (Lister and Baldwin, 1996). This is achieved by input of a P-T-t history and diffusion parameters that are appropriate to the sample. The experimentally determined muscovite diffusion parameters of Harrison et al. (2009) were used. These are D_0 = 2.3 +70/-2.2 cm^2s^{-1} and Q = 63 ± 7 Kcal mol^{-1} (261.5 KJ mol^{-1}), where D_0 is the diffusion coefficient at infinite temperature and Q is a function of the activation energy (E) and the activation volume ($\bar{v}$), as described by Equation 7.1. From the published experimental data (Harrison et al., 2009) the activation volume for muscovite was calculated by linear regression of the data for experiments run at 10 kbar and 20 kbar. Using this method the activation volume was determined to be 15.4 cm^3mol^{-1}. Then using the calculated activation volume, the activation energy was corrected to zero pressure using these equations:

$$Q = E + P\bar{v} \qquad (7.1)$$

$$D = D_0 e^{-Q/RT} \qquad (7.2)$$

Where P is the Pressure, R is the universal gas constant and T is the temperature. This correction results in an activation energy of 58.8 Kcal mol^{-1} (245.8 KJ mol^{-1}) at zero pressure.

For modelling the temperature determined by Hudson (1985) for the cordierite isograd was used, which is 430 ± 15 °C. This is the minimum temperature for the cordierite grade samples. Diffusion is more effective at higher temperature; therefore, the selection of the lowest possible temperature will provide a maximum duration. Hudson (1985) did not constrain the pressure in the cordierite zone. However, from determinations of pressure in adjacent isograds it is expected to be between 2 to 4 kbar. The midpoint of 3 kbar was used for modelling purposes in this study.

7.3.1 Square Wave T-t Paths

Forward modelling was carried out using a square wave T-t path with instantaneous heating to and cooling from the peak metamorphic temperatures. The pressure increase and decrease is also instantaneous. The T-t paths input into the program had an initial condition of homogeneous $^{40}Ar/^{39}Ar$ distribution at particular ages of 550 Ma, 750 Ma and 1050 Ma as displayed in Figure 7.4. The apparent age spectra obtained from the samples were inferred to be the result of diffusion from two reservoirs retaining pre-Grampian ages. Reproducing the complexity of the age spectra obtained without any constraints on the conditions of the pre-Grampian events would be difficult. Therefore, modelling is carried out using a single domain. Thus allowing investigation of the effect the duration of the Buchan thermal event has on the argon age spectra with initial homogeneous $^{40}Ar/^{39}Ar$ distribution at various pre-Grampian ages. The results of the modelling are displayed in Figure 7.5.

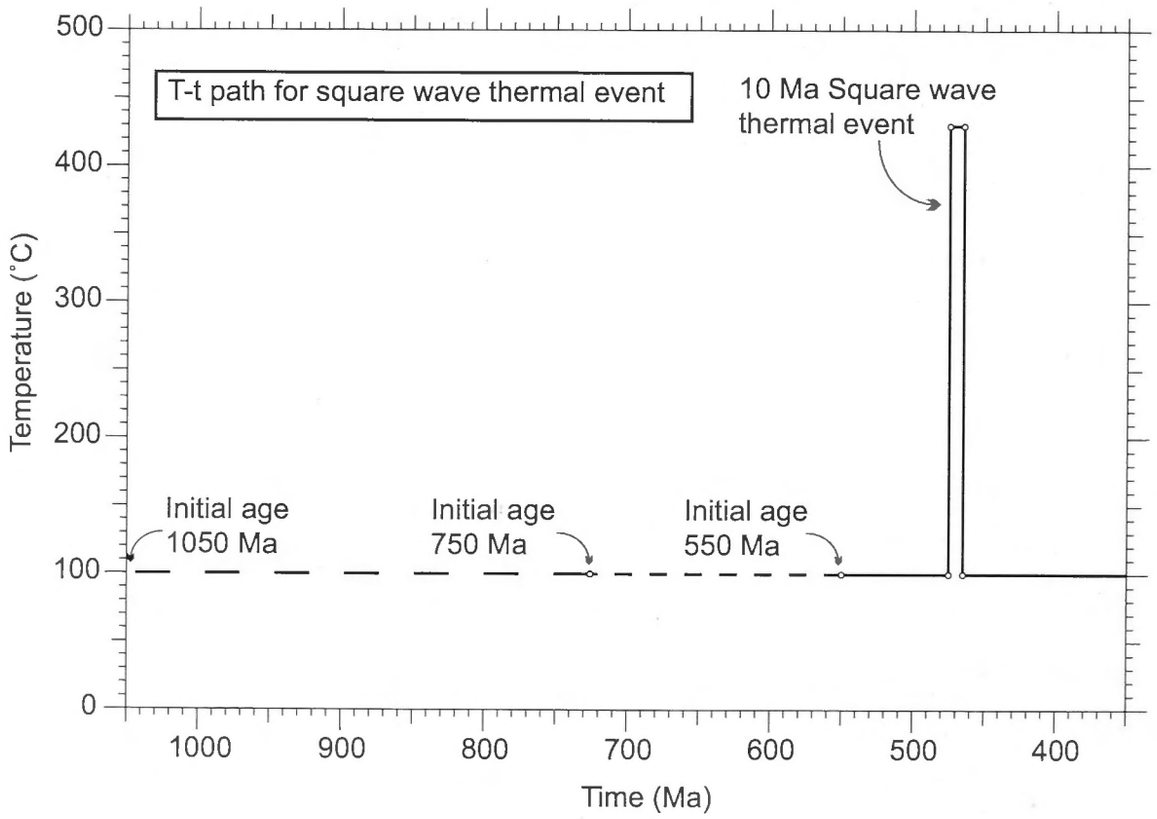

Figure 7.4: Square wave T-t paths with a 10 Ma year duration of the thermal event input for forward modelling of argon diffusion in white mica.

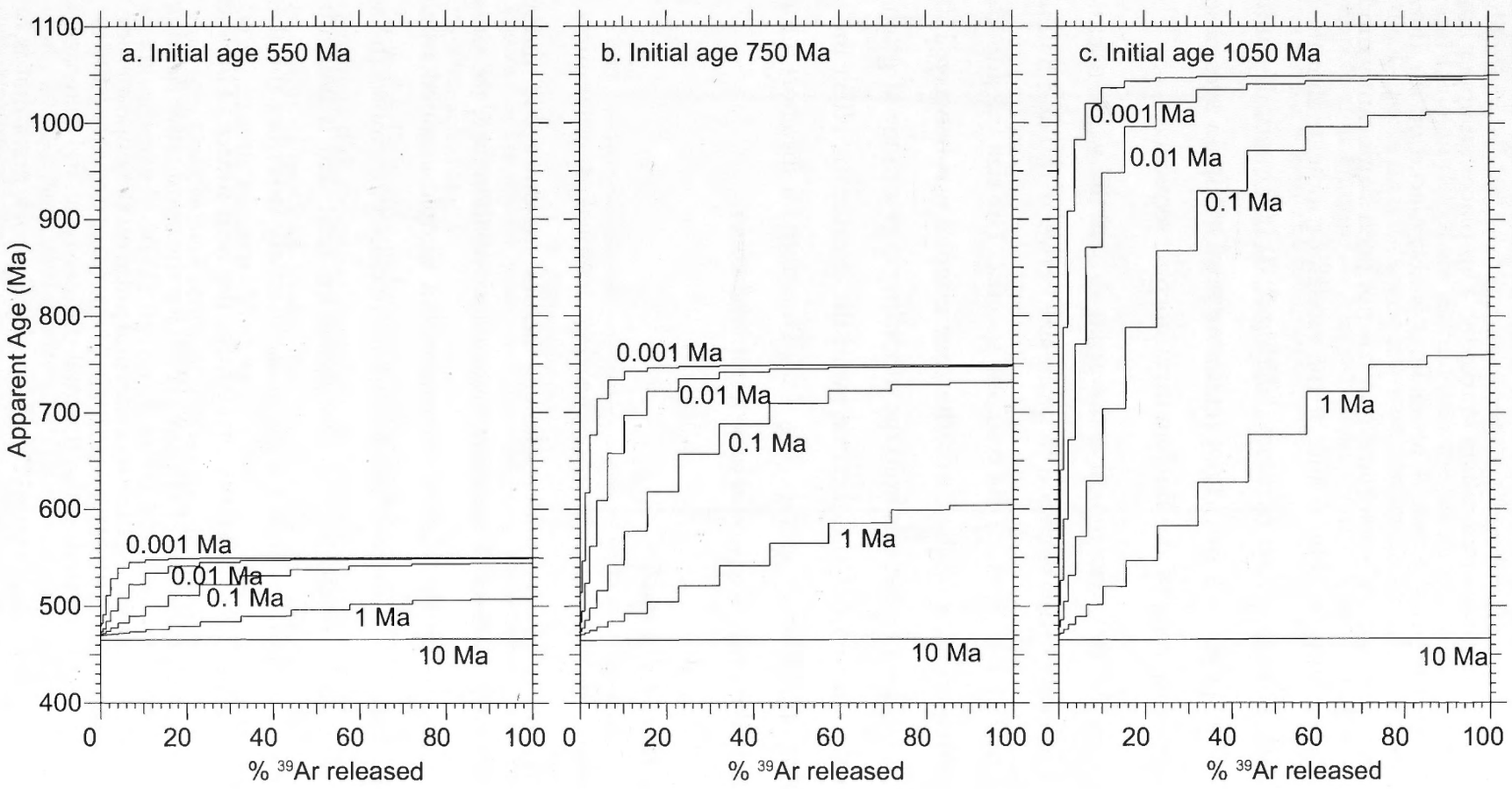

Figure 7.5: Results from modelling $^{40}Ar/^{39}Ar$ apparent age spectra undertaken using a square wave T-t path with an initial condition of homogeneous $^{40}Ar/^{39}Ar$ distribution at (a) 550 Ma (b) 750 Ma and (c) 1050 Ma. Arrhenius parameters from Harrison et al. (2009) adjusted to zero pressure from published data were used, with a spherical geometry for the white mica grains.

The modelling shows that after a thermal event with a duration of 100 000 years the initial age is no longer retained and in comparison to the apparent age spectra of the samples (Fig. 7.2) the shape of the spectra differs markedly. This places an upper limit on the duration of the Buchan thermal event. A lower limit is also placed on the duration at 1000 years as the modelled spectra show the argon has not been significantly modified by a thermal event of this duration. The results of the modelling indicate that the peak temperatures could only have persisted between 1000 and 10 000 years. If durations were longer the apparent age spectra would not retain the pre-Grampian ages observed in samples from the cordierite zone of the Buchan metamorphic sequence.

Another consideration in the diffusion model is the grain size of the white micas. Age spectra were forward modelled with variation in grain size between 150 and 350 μm to determine the magnitude of the effect on the resulting spectra. The size fraction used in this study for argon geochronology of the cordierite zone samples was between 150 and 250 μm (see Table 6.2, Chapter 6). Results from the modelling over a range of grain sizes show that the longer the duration of the thermal event the greater the effect the grain size has on the resulting apparent age spectra (Fig. 7.6). Therefore for the short durations determined in this study the grain size would have a minimal effect.

7.3.2 Flash Heating Curve T-t Path

Square wave T-t paths model instantaneous heating to peak temperatures and instantaneous cooling, so it always underestimates actual metamorphic durations. This is because at high temperatures diffusion is more effective, therefore, the duration relating to time spent entirely at the highest temperature a sample attained would be shorter than the actual duration. A thermal model that more closely resembles the actual T-t paths taken by these rocks would be one that described heat that is built up and dissipated conductively. The flash method for thermal diffusivity describes the thermal evolution of an object at a particular distance away from the heat source. This method is mathematically described by Cape and Lehman (1963) for the conductive heating and cooling of one side of a thin wafer in response to a thermal pulse on the opposite side. The duration of the thermal event is related to the thermal diffusivity of the material (Cape and Lehman, 1963). Using this 'flash method' a T-t path of a rock mass that is heated by emplacement of a hot body can be approximated (Viete et al., 2011a). A thermal

diffusivity of 10^{-6} m^2s^{-1} was assumed for this study. The necessary formulations of Cape and Lehman (1963) are in-built into the MacArgon computer program. An example of the T-t paths used for modelling with conductive length scales of 10 000 and 5000 m are displayed in Figure 7.7. The conductive length scale is indicative of the distance of the rock mass is from the heat source.

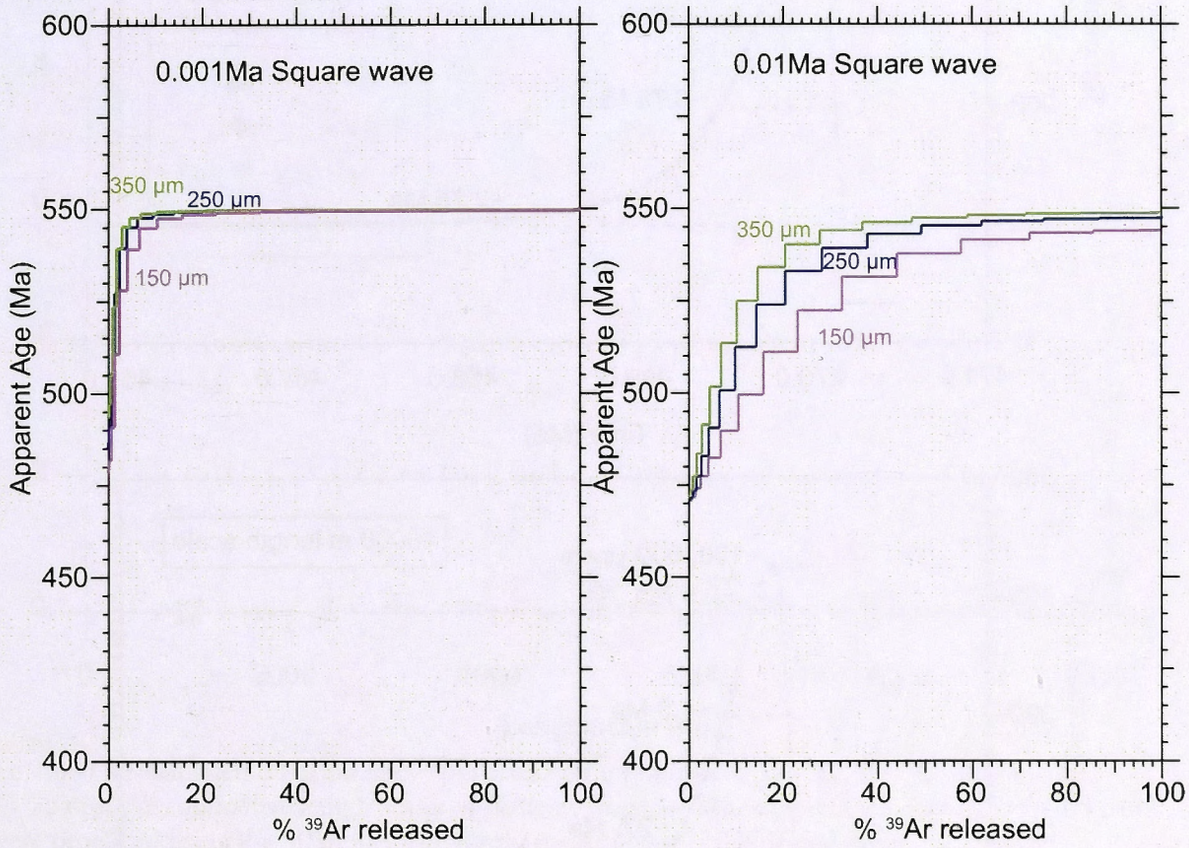

Figure 7.6: The effect of grain size (150 to 350 µm) on the apparent age spectra obtained from diffusion modelling of argon in white mica, using a square wave T-t path with a homogeneous distribution of $^{40}Ar/^{39}Ar$ at 550 Ma.

From the T-t paths produced using the flash heating method (Fig. 7.7) it is evident that the determined duration is dependent on how the thermal event is defined. For comparison to results of previous studies the definition of the thermal event those studies used must be taken into account. Viete et al. (2011a) defined the thermal event duration as the time spent above one tenth of the maximum temperature reached. This corresponds to approximately 50 °C for the 1 to 10 Ma duration obtained for the thermal event (475 °C) that produced the biotite zone of the Barrovian metamorphic sequence (Viete et al., 2011a). Ague and Baxter (2007) used a square wave T-t path that had an ambient temperature of 450 °C, below which diffusion in both of the systems used in their modelling Sr in apatite and garnet major elements would be negligible.

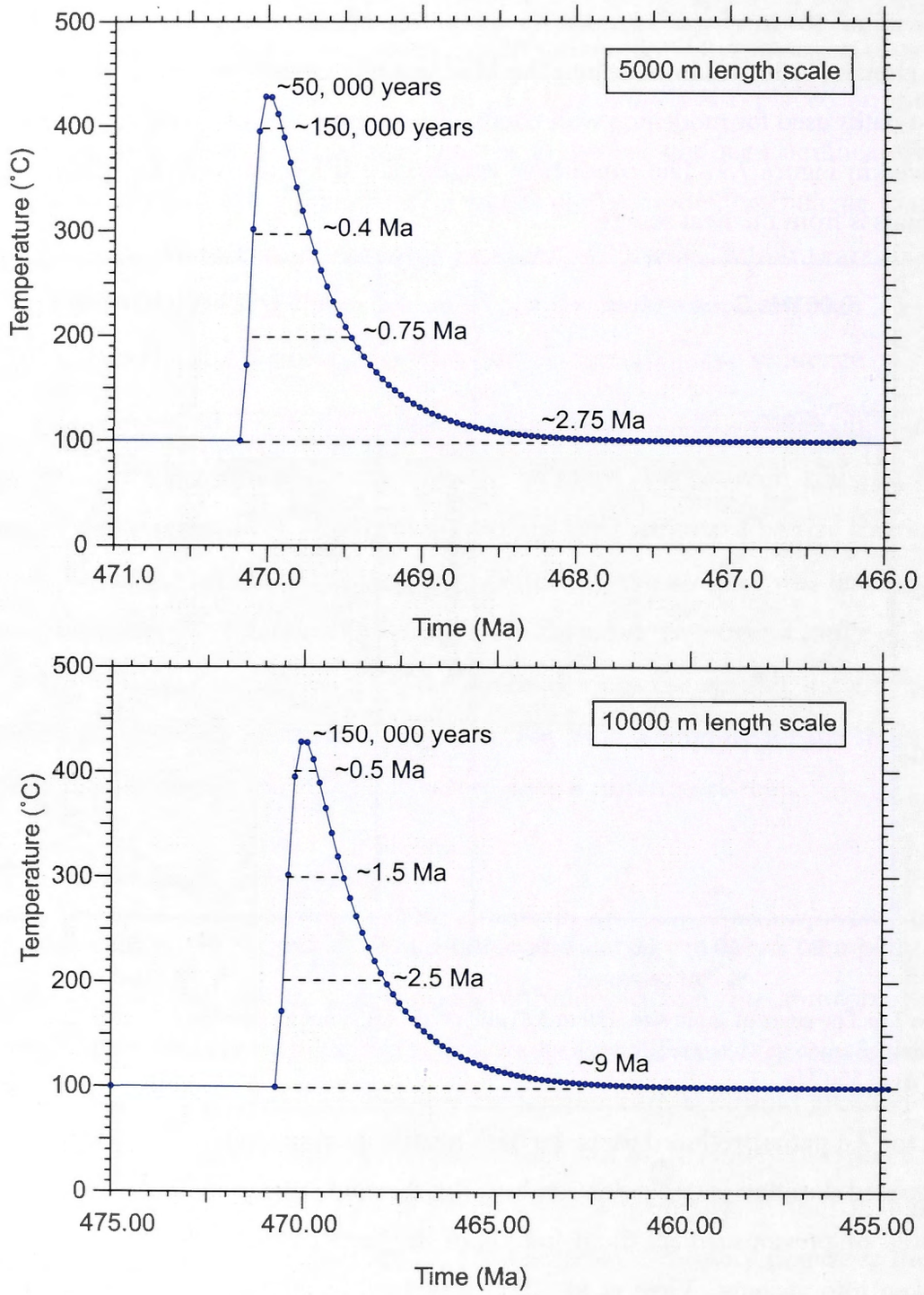

Figure 7.7: The flash heating T-t path with a peak temperature of 430 °C at 470 Ma from an ambient temperature of 100 °C for conductive length scales of 10 000 m and 5000 m and exhumation age of 440 Ma. The approximate duration spent above certain temperatures are labelled.

The duration of the thermal event is largely dependent on the distance from the heat source (Fig. 7.8). T-t paths for modelling were produced by forcing the curve to reach the peak temperature, which was previously constrained (Hudson, 1985) and varying the conductive length scale to modifiy the duration of the thermal event. These length scales

are effectively the distance of the sample locality from the heat source. Therefore, the upper limit for this length scale is constrained by the total thickness of the Dalradian sequence which has been estimated at 10 000 m (Rast, 1963). The results of the forward modelling using a flash heating and cooling curve (Fig. 7.7) can be seen in Figure 7.9.

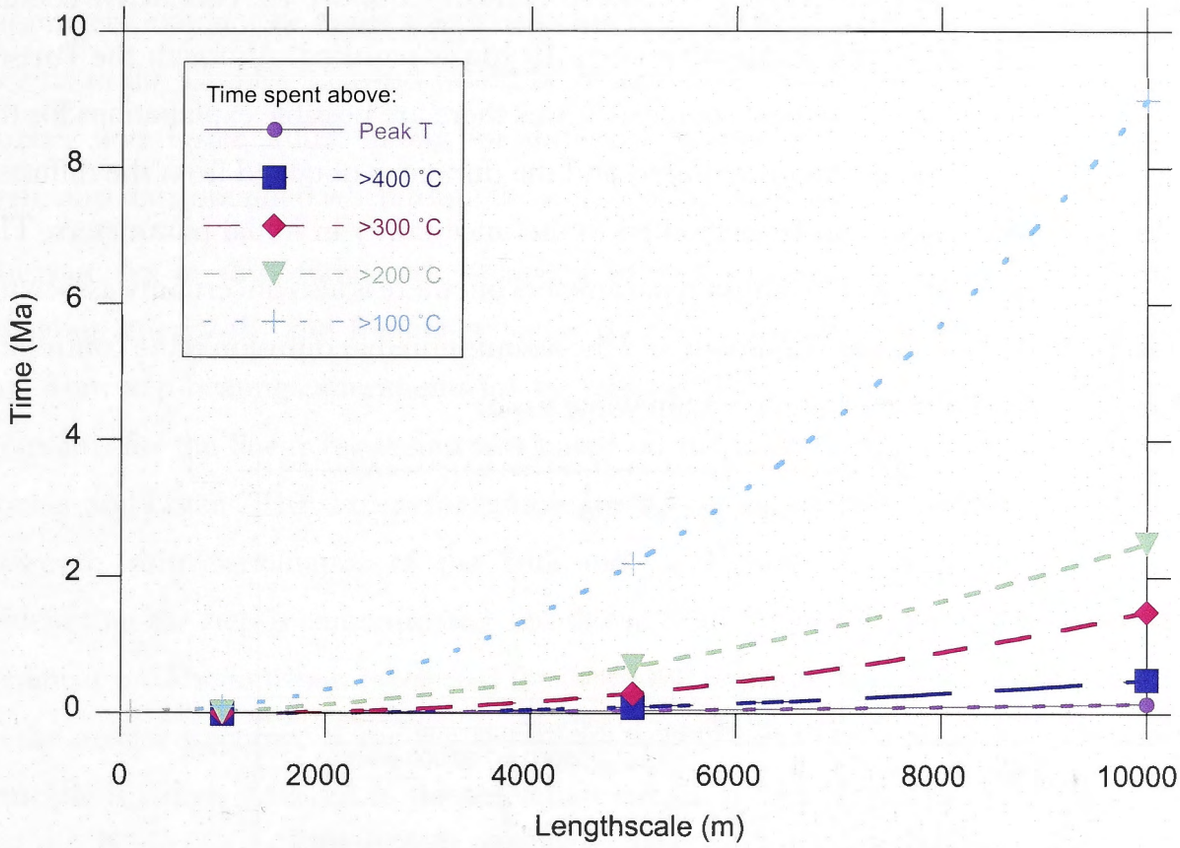

Figure 7.8: The estimated duration above particular temperatures of 100 °C, 200 °C, 300 °C and 400 °C, against the conductive length scales or distance from the heat source. Determined from T-t paths that were produced using the 'flash method' for thermal diffusivity (Cape and Lehman, 1963).

The modelling carried out using the flash heating curve provides an estimate of the duration of Buchan metamorphism that is approximately an order of magnitude longer than the results from the square wave T-t path modelling. The results are consistent with a duration of 1000 years or less at peak temperatures; this duration corresponds to a duration of 10 000 years above 300 °C and approximately 100 000 years above 100 °C. The conductive length scale for this T-t path is 1000 m, therefore dictating that the heat source needs to be within this distance.

The closest magmatic heat source of Grampian age that is present in the Buchan Block is the Portsoy Gabbro (Carty et al., 2012). This gabbro outcrops approximately 10 000 m to the west (e.g. Beddoe-Stephens, 1990; Dempster et al., 1995; Hudson, 1980; Hudson,

1985). Magmatic zircons from the Portsoy Gabbro have been dated at 471.3 ± 0.6 Ma (Carty et al., 2012; see Table 6.1, Ch.6). This age allows the Portsoy Gabbro to be considered as a possible heat source for Buchan metamorphism. If the gabbroic intrusion at Portsoy was the heat source for metamorphism that would indicate that the duration determined from forward modelling (<100 000 years) is too short. For conductive cooling of a length scale of 10 000 m approximately 10 Ma is required. Although the Portsoy Gabbro is not necessarily the heat source, if it was there are possible explanations for the difference between the durations required and the durations obtained from the diffusion model. The discrepancy can be attributed to the uncertainty in initial parameters. The largest uncertainty is from the diffusion parameters but there is also uncertainty associated with the calculation of peak conditions and the assumption that diffusion is the controlling factor in the distribution of argon within white mica.

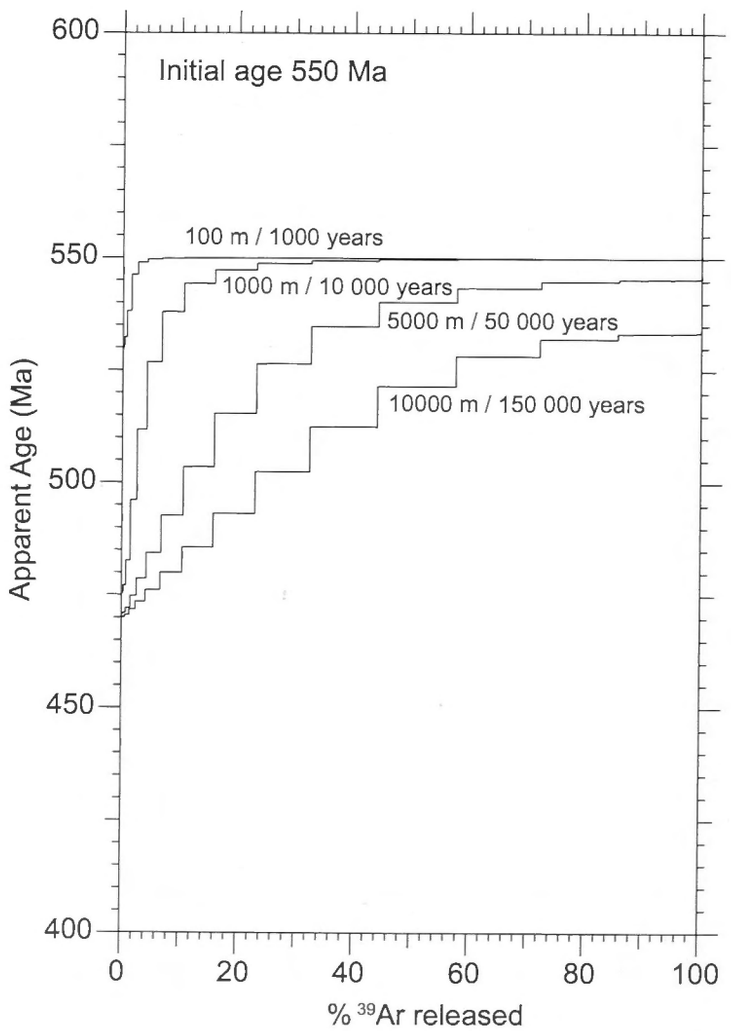

Figure 7.9: Modelled argon apparent age spectra using flash heating and cooling curve at the distance from heat source of 100 m, 1000 m, 5000 m and 10 000 m. The timescales labelled are the approximate durations at peak metamorphic conditions.

7.4 Modelling Arrhenius Data

The outcome of any diffusion model is heavily dependent on the diffusion parameters. For argon diffusion in muscovite there is only one set of experimental data available from Harrison et al. (2009). Due to differences in muscovite, such as composition, this set of parameters may not be applicable to all muscovite grains. Ideally, diffusion parameters specific to the samples analysed would be determined. The computer program eArgon (Forster and Lister, 2009) allows for diffusion parameters to be modelled from the Arrhenius data obtained when using the step-heating technique.

The samples in this study were modelled by first estimating Arrhenius parameters, activation energy (E) and frequency factor (D_0/r^2), obtained from linear regression of data from step-heating experiments for the samples (Figs. 7.10 to 7.13). The selection of the points for the linear regression was based on the fundamental asymmetry principle (Forster and Lister, 2010), except for sample IS10-28 where one step violates this principle. However, from examination of the York and Ca/K plots (Fig. 6.22; Chapter 6) it is evident that the step is contaminated and this may account for it plotting to the right of the linear fit. The four points selected for the linear regression also plot roughly together on the inverse isochron. If the last step is not selected and the fundamental asymmetry principle is strictly adhered to the activation energy is 79.5 Kcal mol^{-1} (332.3 KJ mol^{-1}) and the D_0/r^2 is 1.1×10^{13} s^{-1}. The closure temperatures for the Arrhenius parameters, determined from linear regression, indicate that these values are less retentive than the data from Harrison et al. (2009). Once points have been selected for a particular domain the r/r_0 plots provide information as to the relative volume of the domains (Figs. 7.10 to 7.13) The r/r_0 plots describe the radius of a domain in relation to a reference domain.

Modelling was undertaken using the estimates as a starting point and assuming diffusion from a semi-infinite slab with a length of 125 μm. The activation volume was kept constant in all simulations at the published value of 14 cm^3mol^{-1} (Harrison et al., 2009). The Arrhenius parameters, D_0/r^2 and E, were varied as well as the amount of diffusion domains and the relative volume taken up by the different domains until a best fit to the experimental data was obtained. The Arrhenius data obtained from the furnace step-heating experiments was compared to results of the modelling. Figure 7.14 shows the best-fit obtained from modelling using the parameters detailed in Table 7.1, combined with results from the step-heating of the cordierite zone sample, IS10-12.

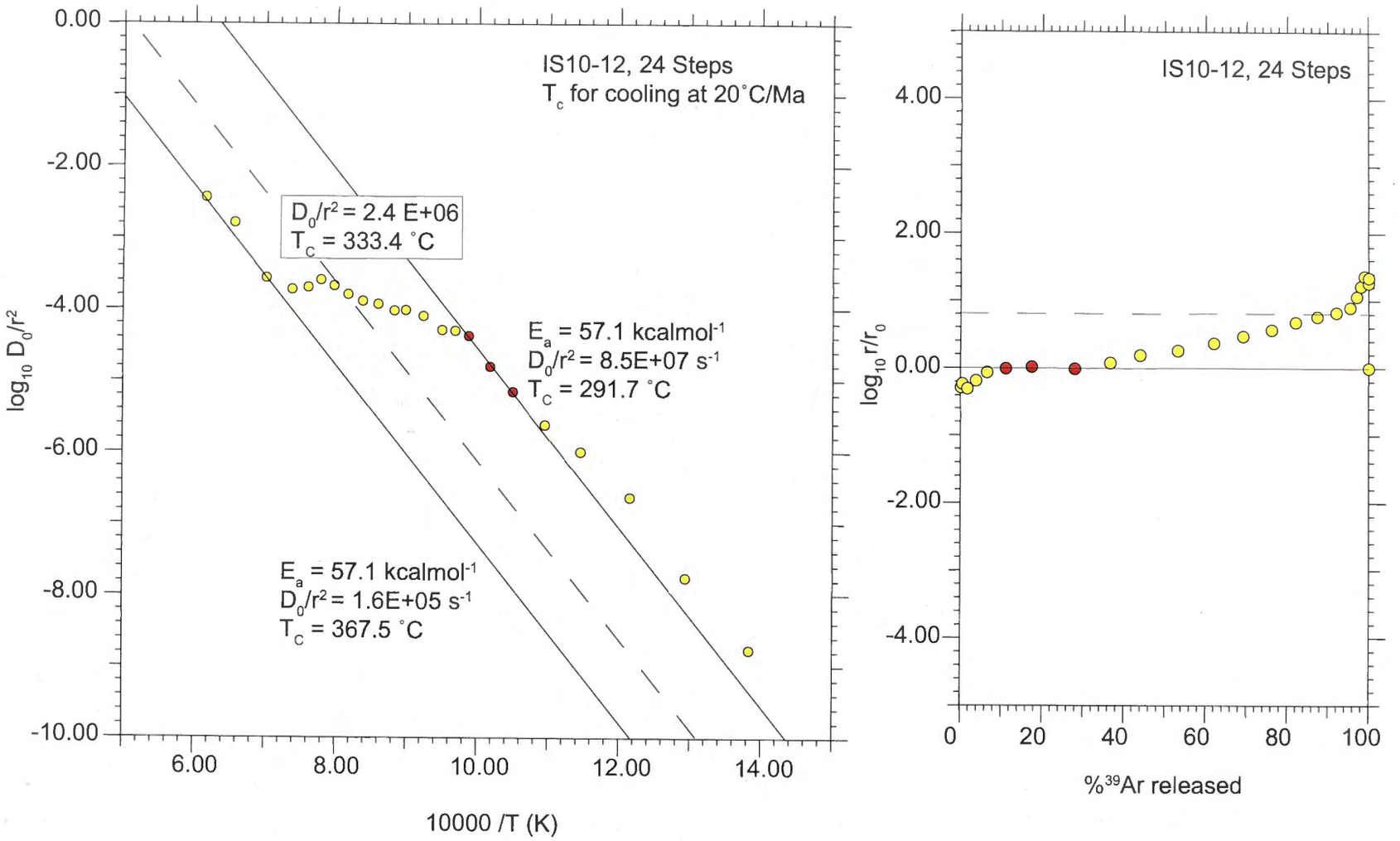

Figure 7.10: The Arrhenius plot, D_0/r^2 against E, for sample IS10-12 and the corresponding log r/r_0 plot. The dotted line in the Arrhenius plot corresponds to the domain marked by a dotted line in the r/r_0 plot.

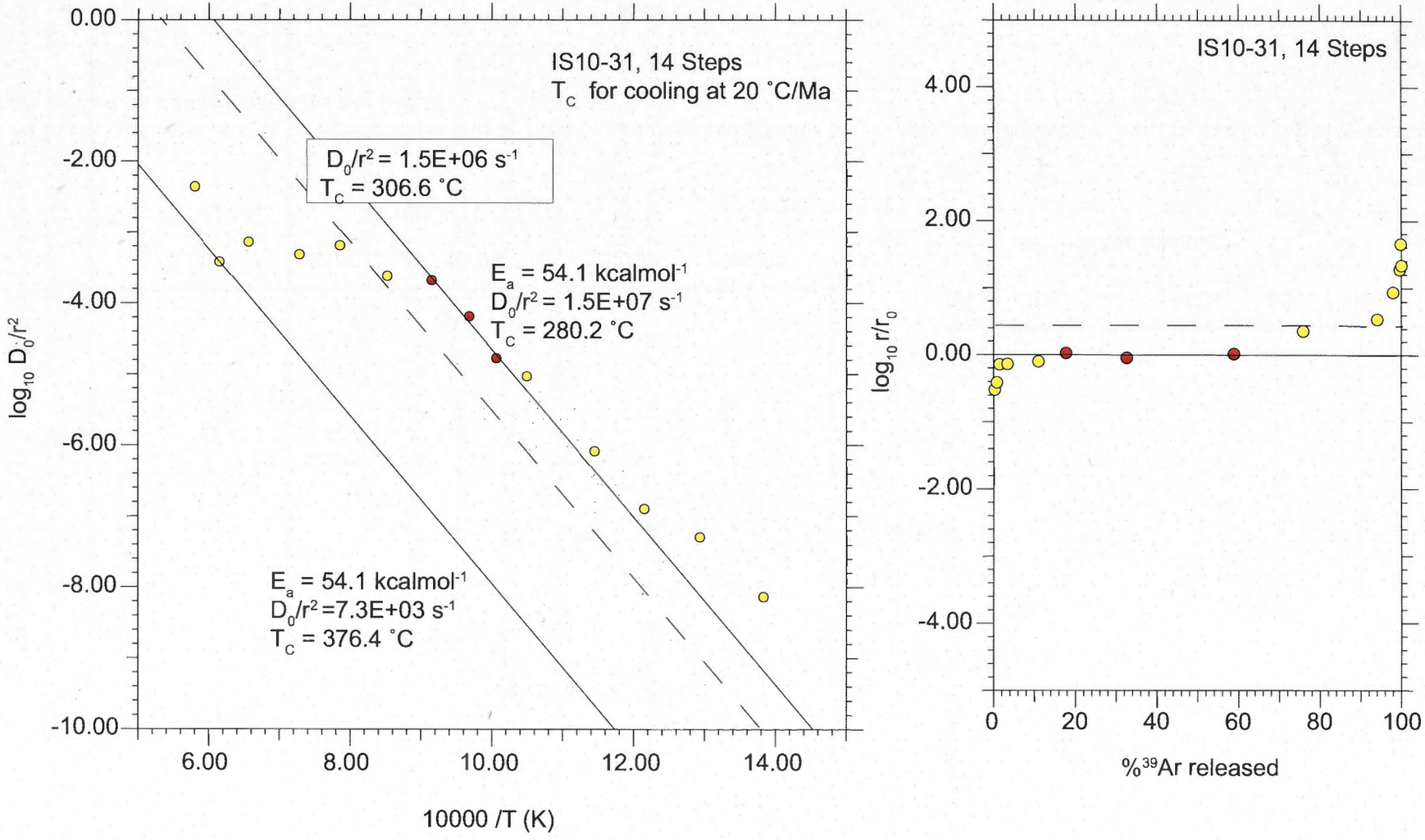

Figure 7.11: The Arrhenius plot, D_0/r^2 against E, for sample IS10-31 and the corresponding log r/r_0 plot. The dotted line in the Arrhenius plot corresponds to the domain marked by a dotted line in the r/r_0 plot.

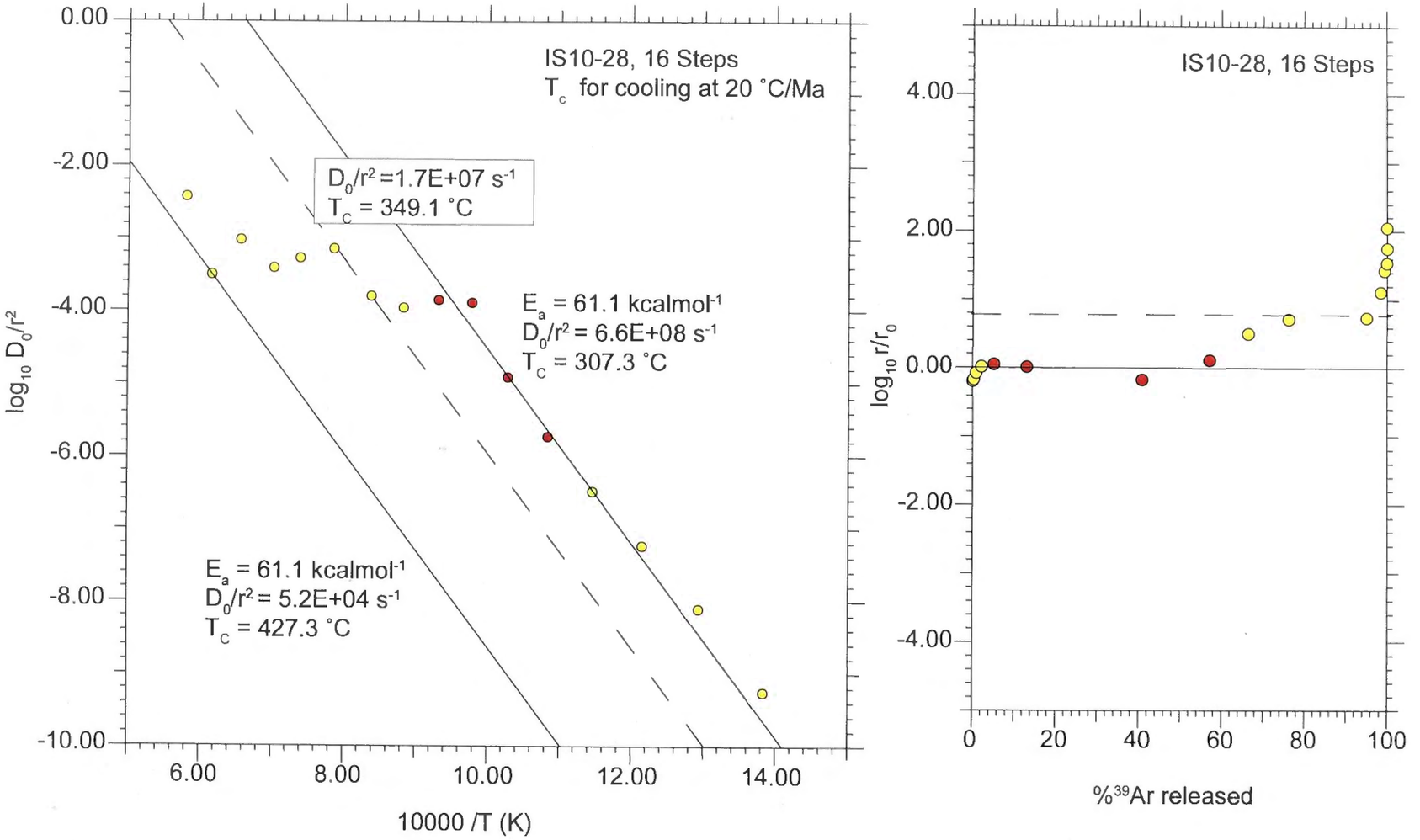

Figure 7.12: The Arrhenius plot, D_0/r^2 against E, for sample IS10-28 and the corresponding log r/r_0 plot. The dotted line in the Arrhenius plot corresponds to the domain marked by a dotted line in the r/r_0 plot.

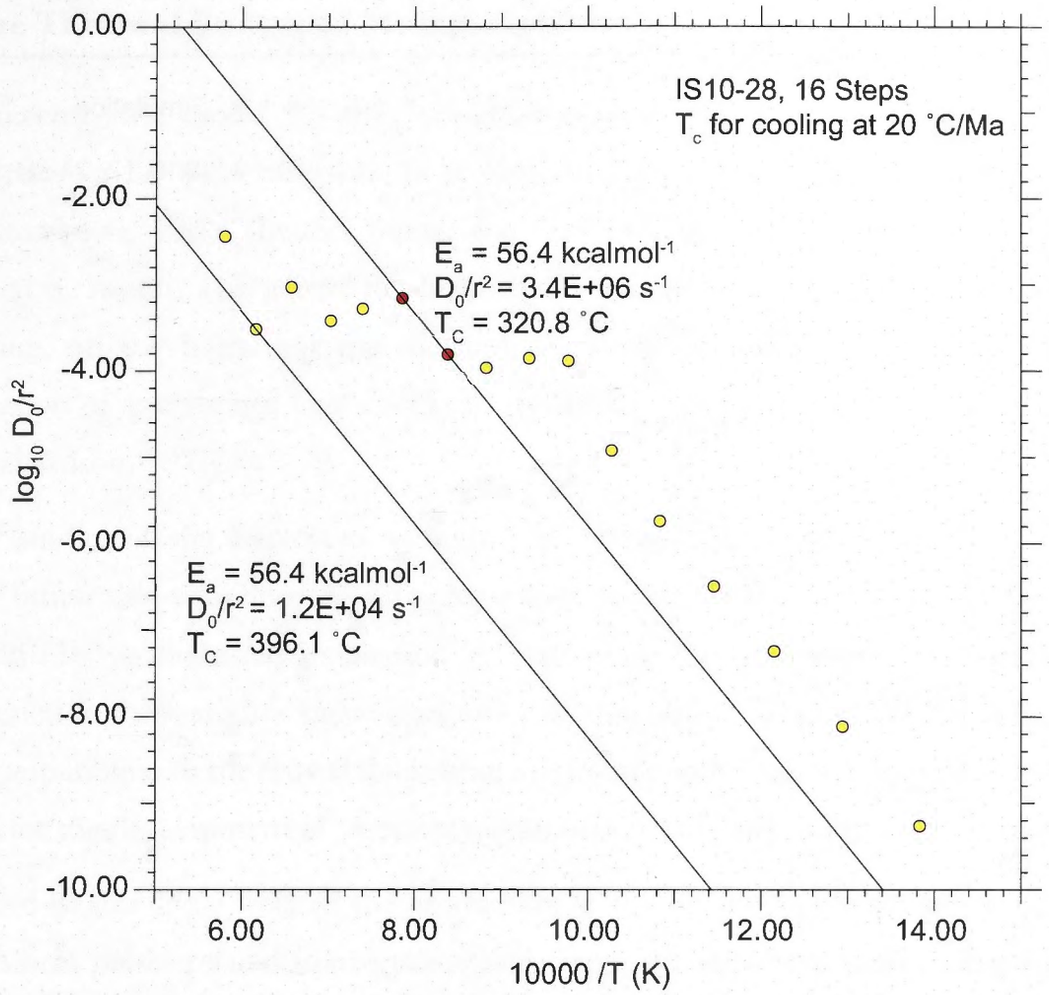

Figure 7.13: The Arrhenius plot, D_0/r^2 against E, for IS10-28 with a line of best fit with a different activation energy from Fig. 7.12.

All three of the cordierite zone samples were modelled together. This was due to IS10-28 having a low amount of white mica and IS10-31 had a low amount of gas released during step heating. This meant that the results for these two samples IS10-28 and IS10-31 had large uncertainties, however, both samples produced apparent age spectra and Arrhenius plots that closely mimicked sample IS10-12.

Domain	E (Kcal mol^{-1})	E (KJ mol^{-1})	D_0/r_2 (s^{-1})	Relative Volume (%)
1	52	231	2.0×10^5	10
2	52	231	2.0×10^8	40
3	55	218	3.0×10^6	50

Table 7.1: Diffusion parameters for best fit to the Arrhenius data. Simulation of data was carried out assuming diffusion from an infinite slab with a radius of 125 μm.

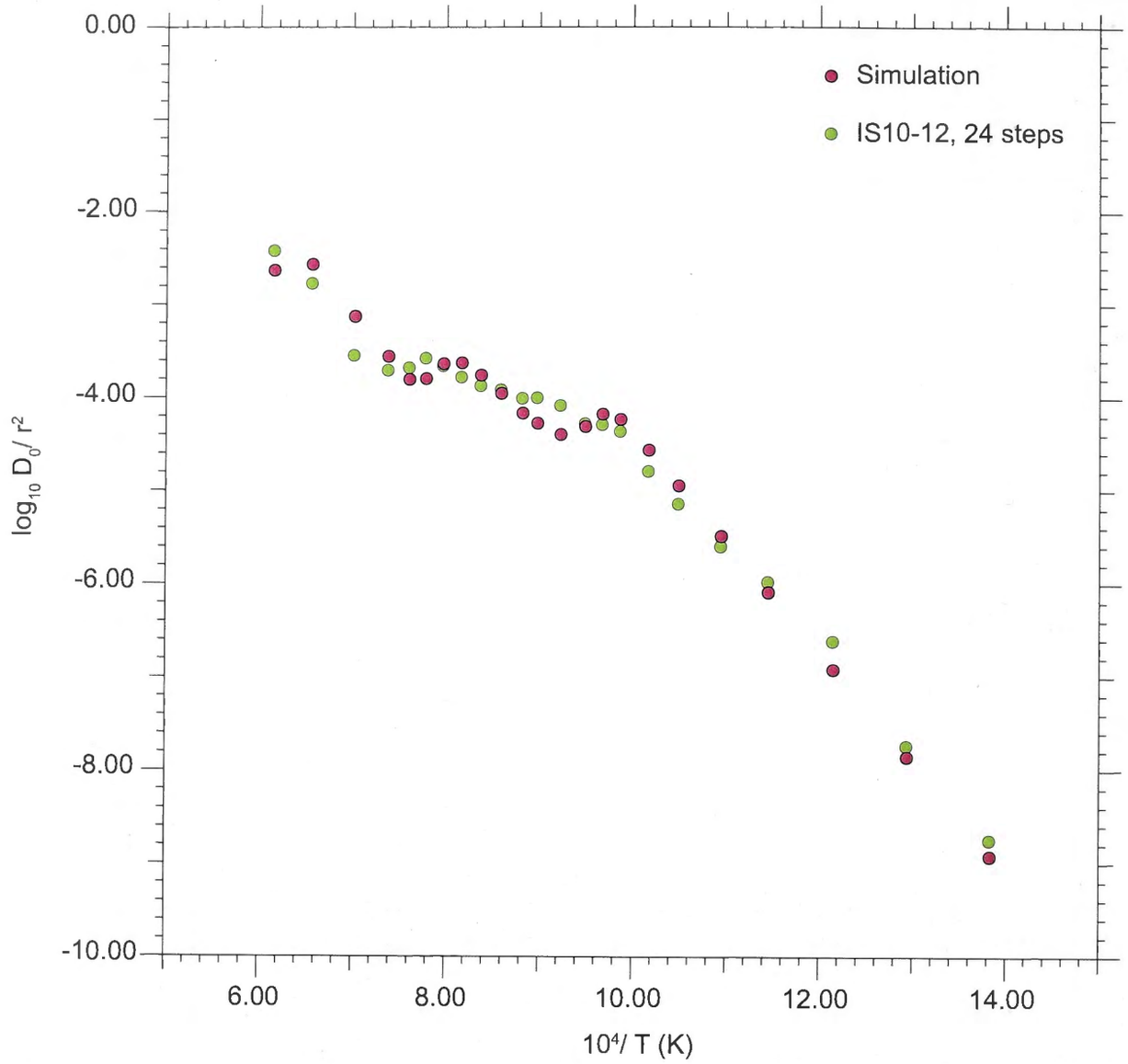

Figure 7.14: Arrhenius data obtained from $^{40}Ar/^{39}Ar$ step-heating experiments for samples IS10-12 from the cordierite zone of the Buchan metamorphic sequence with the best-fit modelled profile using the parameters shown in Table 7.1.

This best-fit solution is not unique, however, the Arrhenius parameters predicted from furnace step-heating experiments for these samples are generally less retentive than the published parameters of Harrison et al. (2009). This might be a result of the samples being exposed to weathering for a long time. Therefore, the white mica grains in the furnace during step-heating may not reflect the actual diffusion parameters of the grains at the time of metamorphism. However, as the diffusion modelling carried out utilised the more retentive values it is assumed the modelling results provide a maximum duration for the Buchan metamorphic event.

7.5 The Thermal Budget of Metamorphism in the Dalradian

Until recently the model for the formation of regional metamorphic belts involved overthickening of the crust with heat dissipated by conductive relaxation (England and Thompson, 1984). In this model the only mechanism allowing the rocks to be exhumed is erosion. This model has been challenged by recent studies utilizing diffusion modelling, on the basis that the duration required for this process is too long. For exhumation of greenschist facies rocks to the surface requires at least 30 Ma (England and Richardson, 1977).

Several studies of the Barrovian metamorphic sequence in Scotland have determined shorter timescales of metamorphism (Ague and Baxter, 2007; Viete et al., 2011a; Viete et al., 2011b) as discussed in Section 7.1, although the durations of metamorphism determined in these studies vary by an order of magnitude. Despite this, both durations are incompatible with the crustal thickening model and both studies proposed new tectonic models for the development of regional metamorphic belts over short timescales.

Ague and Baxter (2007) related the production of the Barrovian metamorphic sequence to short heat pulses related to magmatic intrusions and associated fluid during collision. They also suggest this model for the production of the Buchan metamorphic sequence. This model is shown schematically in Figure 7.15a. Alternatively, Viete et al. (2010) related the synchronous formation of the Buchan and Barrovian sequences to magmatism during large-scale extension. The metamorphism was attributed to episodic heating of shear zones with added heat from mafic magmas and associated fluid flow (Viete et al., 2010). In this model the Buchan metamorphic sequence develops in the hanging-wall and the Barrovian metamorphic sequence to the south develops in the footwall of a mid-crustal detachment. This model is also shown schematically in Figure 7.15b.

Thermal modelling for the two competing theories can be explored to illustrate some of the timescales that are involved in the tectonometamorphic processes outlined by Ague and Baxter (2007) and Viete et al. (2010).

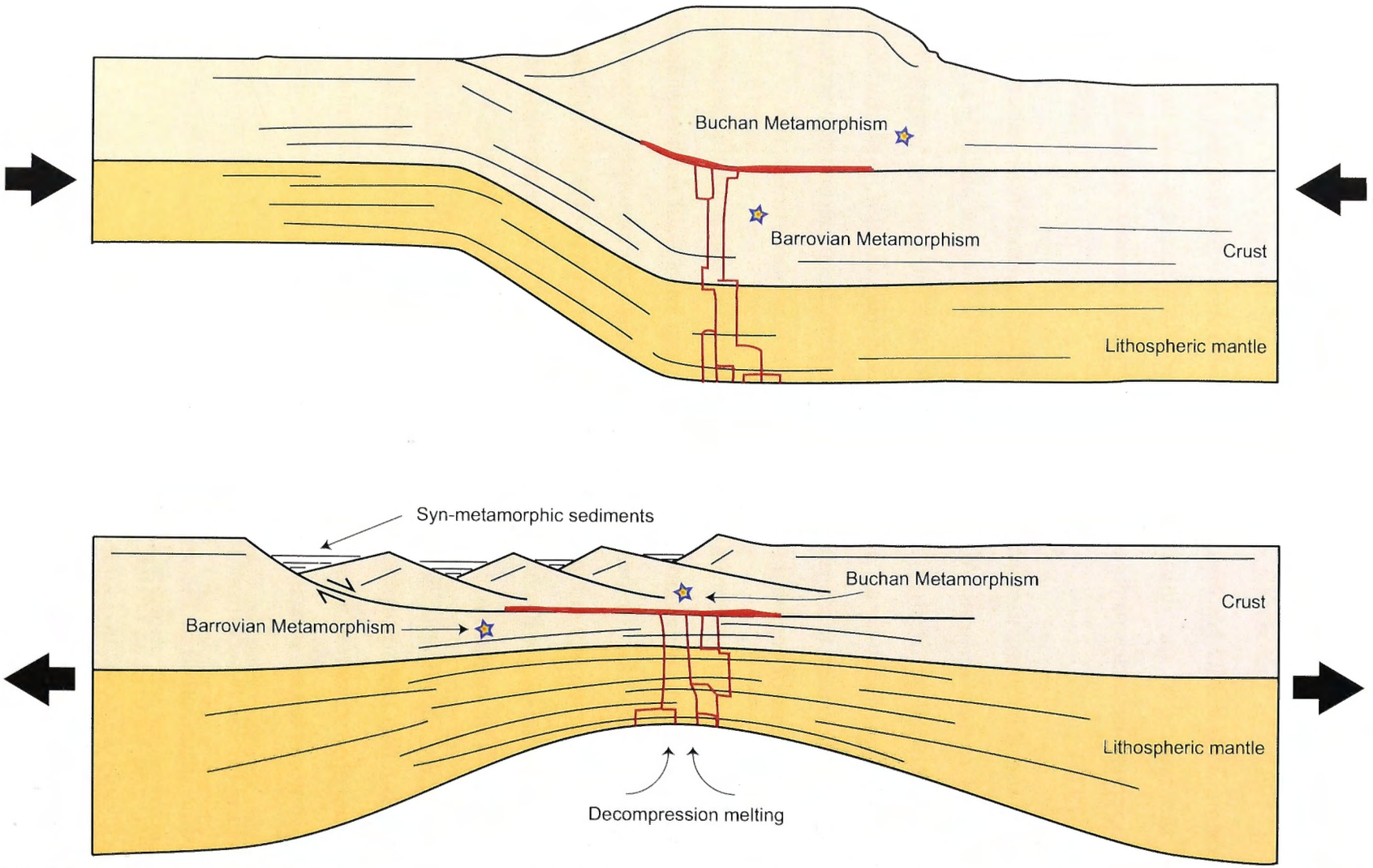

Figure 7.15: Schematic representations of the two competing models for the synchronous formation of the Barrovian and Buchan metamorphic sequences in Scotland. (a) After Ague and Baxter (2007) model for metamorphism occurring in a collisional setting. (b) After Viete et al. (2010) model for metamorphism occurring during extension.

7.5.1 Magmatic Intrusions During Collision

Thermal modelling of the tectonic setting proposed by Ague and Baxter (2007) was carried out by Lyubetskaya and Ague (2010). They produced a two dimensional thermal model of an overthrust setting with added heat from mafic intrusions. The results of the modelling determined that it is necessary to input heat from magmatic intrusions during or following collision to produce the mineral assemblages observed in northeast Scotland on the timescales predicted from diffusion modelling (Ague and Baxter, 2007). The pace at which the magma is intruded will determine the rates of heating.

Also investigated with this model was the synchronous attainment of peak temperatures across metamorphic grades as indicated by Sm-Nd garnet ages of Oliver et al. (2000) and Baxter et al. (2002). For peak temperatures to be attained at the same time across metamorphic grades the magma has to be intruded over a short time interval (Lyubetskaya and Ague, 2010). The resulting T-t paths for mid-crustal magma emplacement with rock displacement at fast and slow intrusion rates using this thermal model are reproduced in Figure 7.16.

Lyubetskaya and Ague (2010) argue against the rapid exhumation rate inherent in extensional models, based on modelling carried out with enhanced basal heat flow without magmatic intrusions. This scenario was described by Oliver et al. (2008) but the results of this modelling do not predict the mineral assemblages observed in the Barrovian. However, this does not rule out rapid exhumation during extension in conjunction with added heat as a result of magmatic intrusions.

7.5.2 Mid-Crustal Detachments

Voorhoeve and Housemann (1988) provide the relevant mathematics to model the thermal regimes associated with mid-crustal detachments. This method provides a means of partially modelling the scenario outlined in Viete et al. (2010). This thermal model has been built into the MacArgon program.

The thermal modelling for a mid-crustal detachment along the PDHL (Fig. 6.1; Chapter 6) was carried out with an ambient geothermal gradient of 20 $^{\circ}Ckm^{-1}$. Due to post-metamorphic folding in the Grampian Terrane the actual dip of the detachment is unconstrained. For modelling a dip of 30° was used and a displacement on the detachment of 20 km. The lithosphere thickness used in the model was based on an assumption made

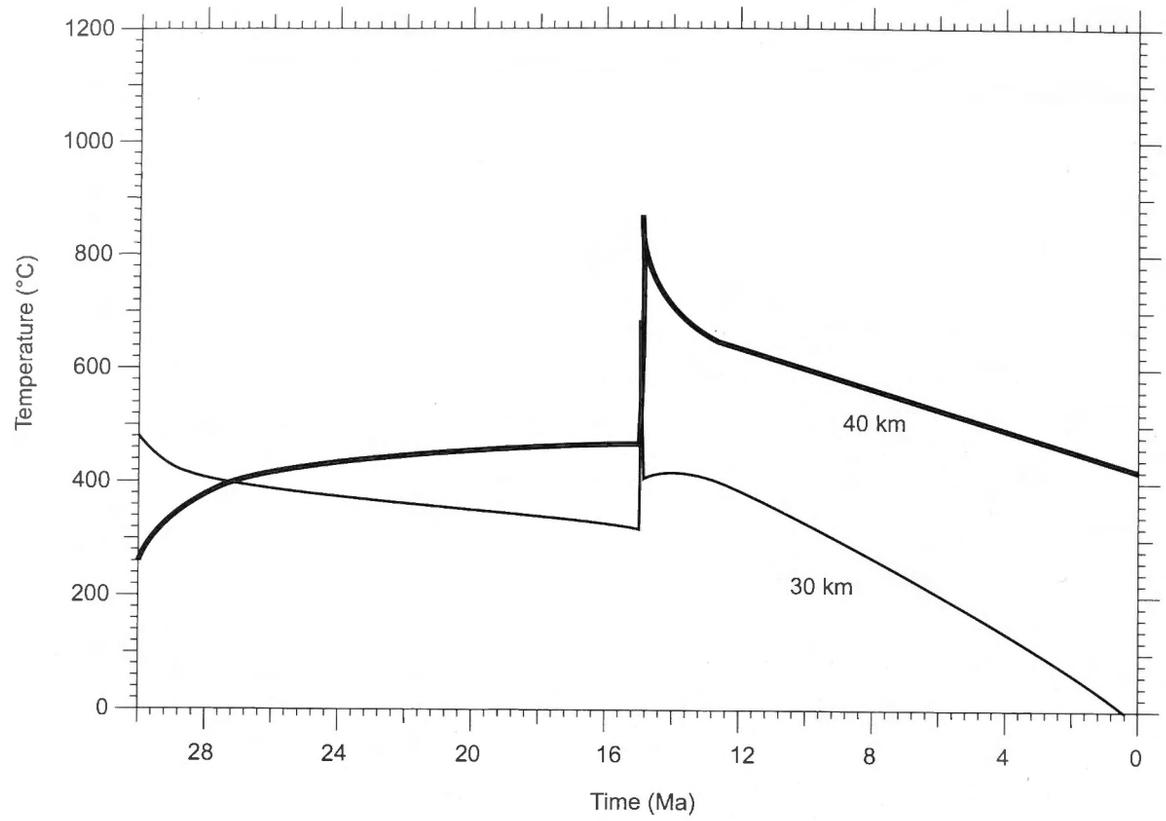

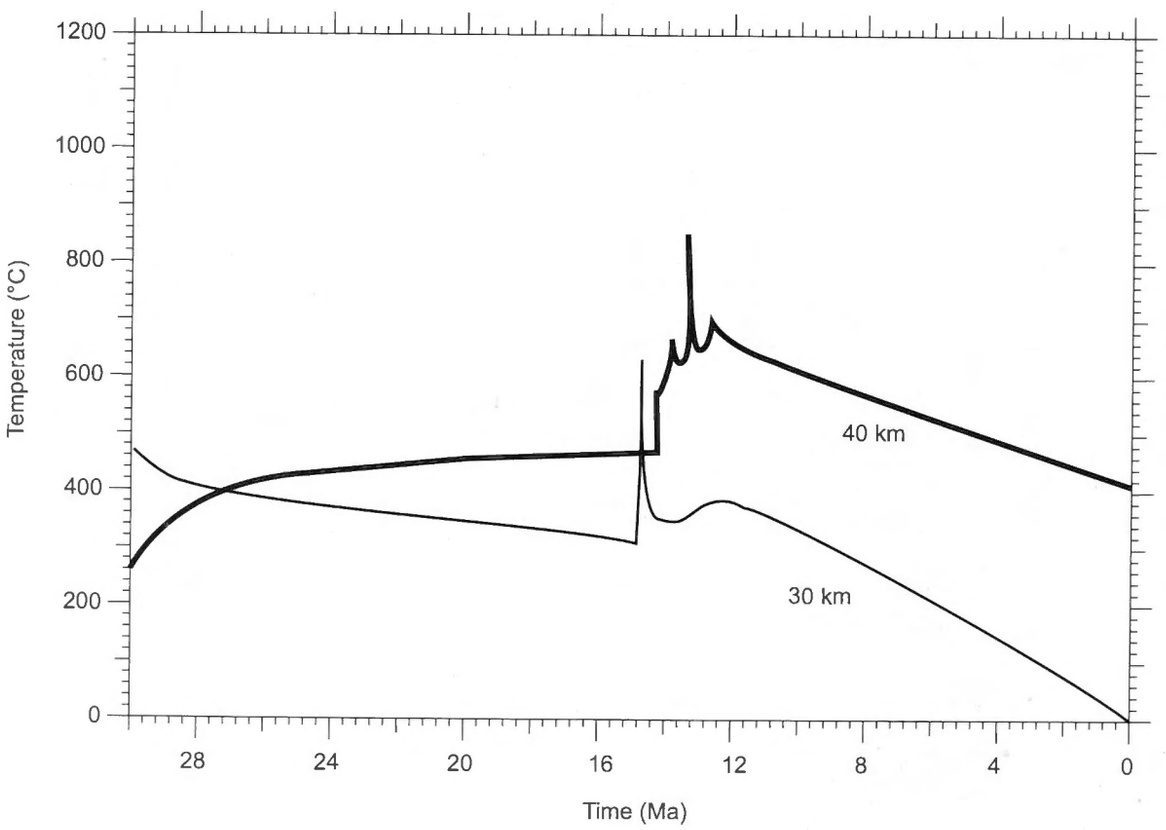

Figure 7.16: Temperature-time paths for rocks initially at 30 and 40 km depth determined from the thermal model of Lyubetskaya and Ague (2010). These paths were produced by modelling mid-crustal magma emplacement with rock displacement, for 10 sills, 0.5 km thick intruding at 15 Ma at: (a) a fast rate of intrusion of 2.5 cm yr^{-1} and (b) a slow rate of intrusion of 0.25 cm yr^{-1}.

by Oliver et al (2008) that the thickness of the Grampian crust at 470 Ma was *c.* 70 km, double the thickness it is presently. The detachment in this model is at 15 km depth based on overburden estimates of Hudson (1985) calculated from the pressure estimates, which placed the Ky/And isograd at 17 km. In the model the detachment is instantly activated at 10 Ma. The resultant temperature-time paths for both the upper and lower plate are shown in Figure 7.17.

This modelling shows the thermal regime of a detachment is such that the hanging-wall stays at high temperatures for longer while the footwall is rapidly cooled. If the Buchan and Barrovian sequences formed in this setting the similar durations of heating that have been determined for the Buchan and Barrovian metamorphic event necessitate that another detachment or similar mechanism is required to cool the Buchan Block rapidly.

7.5.3 Latent Heat of Reaction

Another consideration of the metamorphic thermal budget that was investigated is the latent heat of reaction that would affect the surrounding rock as porphyroblasts are grown. Theoretically, if growth of cordierite porphyroblasts significantly decreases the temperature of the surrounding rock to be below the closure temperature of argon in white mica, this effect may account for the short durations obtained from diffusion modelling. It was noted in a study of Lyubetskaya and Ague (2009) that latent heat of dehydration and hydration reactions might have a significant effect on the thermal budget of metamorphosing rocks (Lyubetskaya and Ague, 2009). From their modelling it was found that the maximum change in temperature was 35 to 45 °C as the cordierite zone is only approximately 30 °C above the closure temperature of argon in white mica this change would have a significant effect. The enthalpy of formation of cordierite has been experimentally determined to be -67.4 KJ mol^{-1} (Navrotsky and Kleppa, 1973). This can be converted into a temperature change for the surrounding rock and was found to have a negligible effect.

7.6 Discussion and Conclusion

The results of argon diffusion modelling indicate that peak metamorphism in the cordierite zone of the Buchan metamorphic sequence of Scotland lasted for less than 100 000 years at *c.* 470 Ma. The modelling conducted using a square wave T-t path indicated that the peak conditions were not sustained for longer than 1000 to 10 000 years. However, this

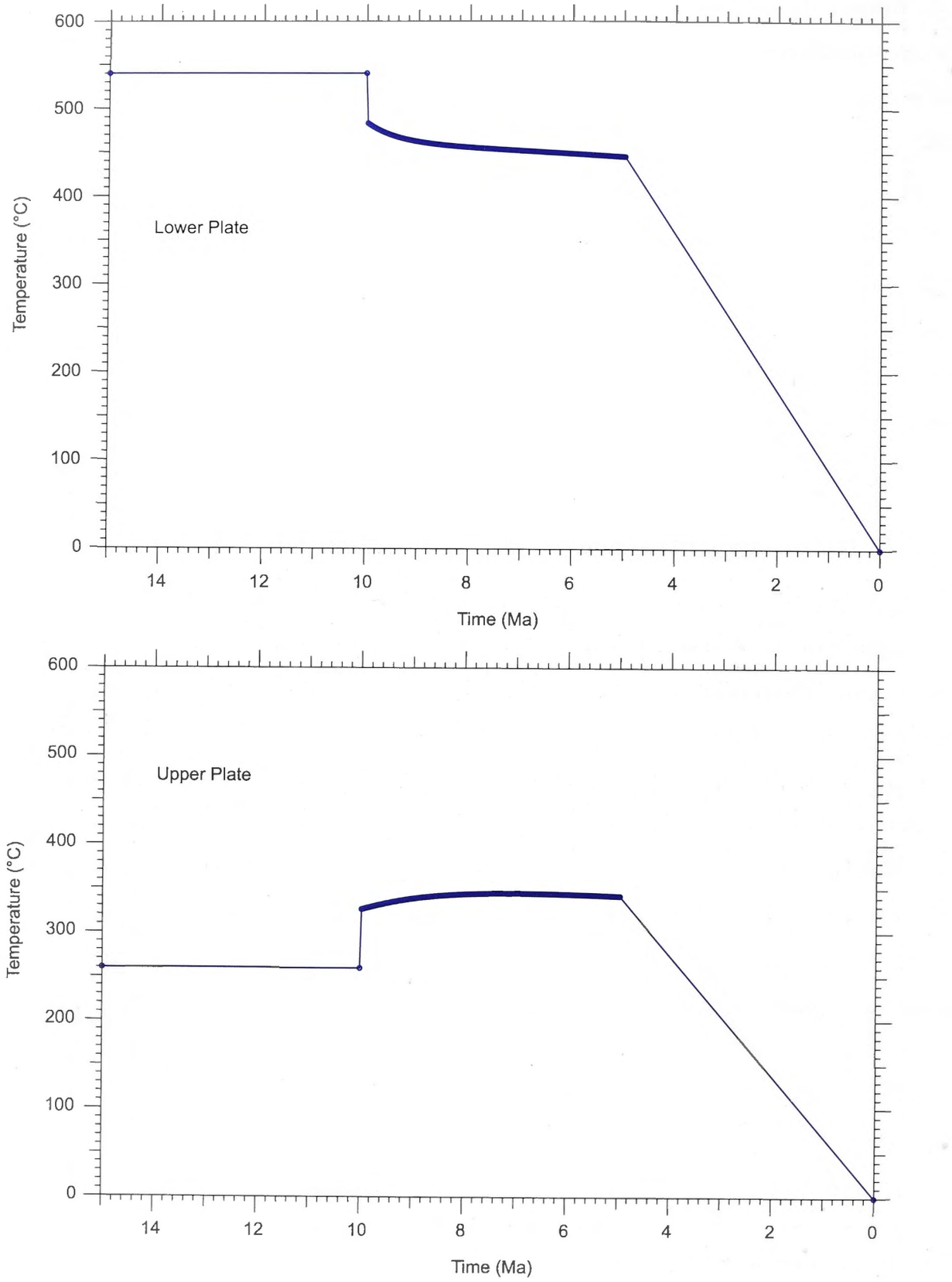

Figure 7.17: Thermal modelling of a detachment from Voorhoeve and Houseman (1988) with an ambient geothermal gradient of 20 °Ckm^{-1}, a lithosphere thickness of 70 km, with the dip of the detachment at 30° with a displacement of 20 km. The detachment in this model is at 15 km depth and is instantly activated at 10 Ma.

is an underestimate of the actual duration of the thermal event due to the nature of a square wave T-t time path. Modelling with a flash heating T-t path at different conductive length scales, provides similar constraints for the time at peak conditions of 1000 years, although the duration for the entire thermal event is on the order of 100 000 years above 100 °C. These timescales correspond to a conductive length scale of 1000 m, which constrains the distance the cordierite zone was from the heat source. Although, there is no appropriate magmatic heat source observed within this range with the closest being the Portsoy Gabbro at 10 000 m.

The issue with diffusion modelling is that determined durations are highly sensitive to the diffusion parameters. Therefore an attempt was made to extract diffusion parameters directly from the samples step-heating results. The Arrhenius parameters modelled in this study gave consistently less retentive values for D_0/r^2 and E. Thus it is evident that the diffusion modelling conducted using the experimentally determined diffusion parameters of Harrison et al. (2009) provides a maximum duration for the thermal event.

The short timescale obtained in this study is also incompatible with the crustal thickening and erosion model of England and Thompson (1984), although it is broadly consistent with the Buchan metamorphic sequence being produced by added heat from syn-metamorphic intrusions as described by various studies of the Barrovian metamorphic sequence (Viete et al. 2010; Ague and Baxter, 2007). Note that the duration determined in this study is shorter than the durations determined in the Barrovian metamorphic sequence studies carried out by Viete et al. (2011a) and Ague and Baxter (2007). These durations were 1 to 10 Ma above 50 °C for the biotite zone (Viete et al., 2011a) and 200 000 to 300 000 years at peak temperatures above 500 °C in the garnet, staurolite and sillimanite zones (Ague and Baxter, 2007). In contrast this diffusion modelling study showed detrital ages in the cordierite zone samples could only be preserved if the duration of the thermal event with a peak temperature of 430 °C lasted less than 100 000 years. Even when taking into account the large uncertainty involved in the determination of this duration the thermal event could not have lasted longer than 10 Ma. These results are therefore indicative of the timescales of the thermal events for the Barrovian and Buchan metamorphic sequences either being the same magnitude or the Buchan thermal event being of a shorter duration.

CHAPTER 8

Diffusion Modelling to Constrain the Duration of Metamorphism

Preface

The conclusions outlined in this chapter are the culmination of four years of research and discussing that research with my peers, supervisors and collaborators. This chapter is my own work except where otherwise indicated.

8.0 Synopsis

In this study the application of the diffusion modelling technique to the garnet-ilmenite system was investigated. This system was used to determine the duration of metamorphism in the Ivrea-Verbano Zone in Italy. This duration was determined from Mn diffusion profiles that were preserved in garnet surrounding ilmenite inclusions. The lengths of these profiles are proportional to the duration of the thermal event. Using this relation, constraints were placed on the duration of the thermal event associated with the emplacement of magmatic intrusions in the Ivrea-Verbano Zone of 100 000 years to 1 Ma.

Additionally, constraints were placed on the duration of the thermal event that produced the Buchan metamorphic sequence in Scotland using argon diffusion modelling. The results from this modelling indicate that peak metamorphism in the cordierite zone of the Buchan metamorphic sequence lasted for less than 100 000 years.

The determination of the duration of the thermal event that produced a metamorphic belt can provide evidence as to the heat source of metamorphism. In this chapter the implications of the short durations obtained for the production of metamorphic belts in this and other recent studies are discussed.

8.1 Introduction

This thesis investigated the application of diffusion modelling to obtain the duration of thermal events that produced metamorphic belts. Knowing the duration of the thermal event is essential when attributing the metamorphism to a particular heat source, as different heat sources operate over significantly different timescales. For instance, heating due to thickening of the crust with heat produced by the decay of radioactive isotopes requires at least 30 Ma to bring Barrovian metamorphic assemblages to the surface (England and Richardson, 1977). In contrast, adding heat from magmatic intrusions can produce the same assemblages in a much shorter duration, on the order of a few million years (Lyubetskaya and Ague, 2010).

To obtain durations of thermal events the technique of forward modelling the diffusion of major elements in garnet can be utilised. This technique is based on the measurement of the extent of diffusional modification to initial concentration profiles. However, the uncertainty in diffusion parameters and the difficulty in assigning initial conditions can impede accurate determination of durations. This difficulty is particularly problematic in garnet diffusion models as initial concentration profiles display growth zoning. This obstacle can be overcome by providing a means for independently constraining the duration, for instance, the development of a diffusion model for the garnet-ilmenite system.

The garnet-ilmenite system is characterised by the exchange of Fe and Mn between the two minerals. The efficiency of the exchange is determined by the partitioning behaviour and is dependent on temperature. This exchange reaction produces a concentration change at the interface between the two minerals that is subsequently diffused. Diffusion within ilmenite is relatively fast and therefore only garnet, with slow diffusivity, can preserve diffusion profiles. The length of the diffusion profiles adjacent to ilmenite inclusions will be proportional to the duration of the thermal event. Therefore, this provides a new and independent method for measuring the duration of thermal events. The rates of diffusional processes in the garnet-ilmenite system and the application of this system was investigated in this study.

Additionally, if durations obtained using a particular mineral system are accurate, then durations obtained via alternative mineral systems should be comparable. Therefore in this study durations constrained from Sr in apatite and garnet diffusion modelling

in the Barrovian metamorphic series (Ague and Baxter, 2007; Viete et al., 2001b) were compared to durations obtained from forward modelling of argon diffusion in white mica from the synchronous Buchan metamorphic sequence.

8.2 The Garnet-Ilmenite System

One difficulty in constraining durations using the diffusion modelling technique is the accuracy of the determined rates of diffusional processes involved. Therefore experimental constraints on the rates of the diffusional processes involved in the garnet-ilmenite system are required for this system to be utilised effectively. In this study diffusion experiments were conducted to further constrain rates of diffusion in ilmenite and garnet.

Diffusion parameters for Mn, Co, Ni, Ga, Mg, Y, Al, Cr and Hf in ilmenite were determined, with the diffusivity at 1000 °C determined to be on the order of 10^{-13} to 10^{-16} m^2s^{-1} for the range of elements measured. These results validate the assumption that diffusivity within ilmenite is orders of magnitude faster than in garnet and thus in a garnet-ilmenite diffusion model ilmenite diffusivity can be treated as infinite. However, the rapidity of diffusion in ilmenite also needs to be taken into account when selecting garnet-ilmenite pairs for analysis because if ilmenite is in contact with other minerals with which it can exchange cations, either directly or via cracks that provide diffusion pathways, it will no longer retain accurate information. Therefore, for the purposes of geothermometry, geobarometry or diffusion modelling ilmenite inclusions that are isolated from other minerals in three dimensions should be selected.

Experiments to constrain the rate of the diffusional processes in the garnet-ilmenite system at lower temperatures than previous garnet diffusion experiments (e.g. Chakraborty and Ganguly, 1992; Loomis et al. 1985) were also undertaken. These experiments were carried out on garnet with an ilmenite thin film as a diffusant source. It was shown that this methodological approach is valid, however, these experiments failed to produce measurable diffusion profiles. To produce diffusion profiles modifications would need to be made to the method, in particular, running experiments over longer annealing times as well as production of the thin film from a synthetic ilmenite to avoid contamination. Nonetheless, the results allowed a maximum and minimum constraint to be placed on the rate of diffusion in garnet at these temperatures. The results show that the diffusivity is at least one order of magnitude slower than the diffusivity extrapolated from previously

determined diffusion parameters at higher temperatures (Chakraborty and Ganguly, 1992) but no more than two orders of magnitude slower.

Additionally, in this study evidence of diffusion profiles preserved in garnet surrounding ilmenite inclusions in natural samples was obtained. The preservation of the diffusion profiles demonstrates that the garnet-ilmenite system can record information regarding the T-t history of a rock. Therefore, it is a viable system for the diffusion modelling technique.

Possible diffusional features were observed in Mn surrounding ilmenite inclusions in garnet from the sillimanite zone of the Barrovian metamorphic sequence in Scotland. However, the lengths of these possible diffusion profiles were shorter than the observed Ti concentration profiles in garnet that are known to be a result of analytical interferences. These diffusional features also varied significantly across samples. Therefore more substantial evidence was required.

This evidence was obtained from high-grade metamorphic rocks from the Ivrea-Verbano Zone in Italy. In these samples Mn diffusion profiles were observed and measured adjacent to ilmenite inclusions in garnet. The lengths of the profiles are proportional to the peak temperature attained by the sample. Also, in these samples Mg displayed an inverse concentration profile to Mn indicating that this component was participating in the exchange reaction. However, retrograde reactions involving ilmenite acting as a sink for excess Mn caused the partitioning between the two phases to be incongruent. This partitioning behaviour was most notable in the lower grade samples where Mn concentrations are higher in the ilmenite than in garnet. This evidence of ilmenite participating in reactions with minerals outside of the garnet host again highlights the need to select ilmenites that are isolated from other minerals in three dimensions, including diffusion pathways, such as cracks in the garnet host. Despite these inconsistencies with the model, the diffusion profiles that were measured provide a broad constraint on the duration of the thermal event associated with metamorphism in the Ivrea-Verbano Zone in Italy of 100 000 years to 1 Ma.

8.3 $^{40}Ar/^{39}Ar$ Diffusion Modelling

In this study $^{40}Ar/^{39}Ar$ geochronology was carried out on samples from the northeast coast of Scotland. The apparent age spectra of samples from the cordierite zone of the Buchan metamorphic sequence in Scotland showed pre-Grampian ages were preserved in detrital white mica. In these samples an age is recorded at *c.* 560 Ma, which indicates that the sediment source for the Upper Dalradian endured a thermal or deformational event at *c.* 560 Ma and therefore sedimentation occurred after that time. These samples also preserved evidence of an age older than 750 Ma.

Forward modelling the effect of thermal events on the apparent age spectra was carried out using the MacArgon program (Lister and Baldwin, 1996). This modelling allowed a constraint to be placed on the maximum duration of the Buchan thermal event that these rocks could have endured and still retain pre-Grampian ages by comparing the simulated $^{40}Ar/^{39}Ar$ apparent age spectra to the $^{40}Ar/^{39}Ar$ apparent age spectra obtained from step-heating of the samples. The result of this modelling indicated that the cordierite zone of the Buchan metamorphic sequence could not have endured peak metamorphic conditions (430 °C) for longer than 100 000 years. This duration for the thermal event is broadly consistent with recent studies that have utilised the diffusion modelling technique on various mineralogical systems for determining the duration of the Barrovian metamorphic sequence to the south (e.g. Ague and Baxter, 2007; Viete et al., 2011a).

These recent studies have proposed tectonic models for the synchronous production of the Buchan and Barrovian metamorphic sequences to account for this shorter duration (Ague and Baxter, 2007; Viete et al., 2011b). Both of these models utilise added heat input from magmatic intrusions to form the mineral assemblages that are observed. The difference between the models is the tectonic setting in which the magmatic intrusions are emplaced, for instance, Viete et al. (2011b) proposed emplacement of magmatic intrusions during regional extension (Fig. 7.15; Chapter 7).

The results from the $^{40}Ar/^{39}Ar$ geochronology for higher grade samples from the northeast coast of Scotland are also consistent with magmatic heating models (Chapter 6). In these samples ages were recorded at *c.* 470 Ma, which can be interpreted as cooling ages. These ages are close to the age inferred for peak metamorphism in the Barrovian and Buchan sequences and therefore indicate rapid exhumation of the Barrovian and Buchan metamorphic sequences.

8.4 The Duration of Metamorphism

This study has determined relatively short durations for thermal events that produced metamorphic belts compared with the established model for the production of regional metamorphic belts proposed by England and Richardson (1977). Similarly short durations have also been determined for other regional metamorphic belts in previous studies (e.g. Ague and Baxter, 2007; O'Brien and Vrána, 1995; Viete et al., 2011a; Viete et al., 2011b) and the long duration required for the England and Richardson (1977) model is even incompatible with broad geochronological constraints that have been placed on orogenesis (e.g. Dewey, 2005; Friedrich et al., 1999; Oliver et al., 2000). In particular, the duration of the Grampian orogenic event, during which the Barrovian and Buchan metamorphic sequences were produced, has been constrained to have lasted *c.* 15 Ma (Oliver et al., 2000).

In conclusion, from diffusion modelling it is known that the duration over which metamorphic belts are produced is short. However, for the diffusion modelling method to provide better constraints on the duration of metamorphism accurate rates of the diffusional processes need to be determined. This obstacle is apparent in all mineral systems that are used for diffusion modelling and in this thesis it has been discussed in relation to major-element diffusion in garnet and argon diffusion in white mica. Additionally, this study showed the garnet-ilmenite system is a viable system for application to the diffusion modelling technique. The inter-calibration of systems, such as grain-scale garnet diffusion with the garnet-ilmenite system, can provide a valuable method for discerning information on the tectonometamorphic history of a terrane.

References

Ague, J., and Baxter, E., 2007, Brief thermal pulses during mountain building recorded by Sr diffusion in apatite and multicomponent diffusion in garnet: Earth and Planetary Science Letters, v. 261, p. 500-516.

Anderson, D.E., and Olimpio, J.C., 1977, Progressive homogenization of metamorphic garnets, south Morar, Scotland: Evidence for volume diffusion Canadian Mineralogist, v. 15, p. 205-216.

Ashcroft, W., Kneller, B., Leslie, A., and Munro, M., 1984, Major shear zones and autochthonous Dalradian in the northeast Scottish Caledonides: Nature, v. 310, p. 760-762.

Atherton, M., 1977, The Metamorphism of the Dalradian rocks of Scotland: Scottish Journal of Geology, v. 13, p. 331-370.

Atherton, M., and Ghani, A., 2002, Slab breakoff: a model for Caledonian, Late Granite syn-collisional magmatism in the orthotectonic (metamorphic) zone of Scotland and Donegal, Ireland: Lithos, v. 62, p. 65-85.

Ayres, M., and Vance, D., 1997, A comparative study of diffusion profiles in Himalayan and Dalradian garnets: Constraints on diffusion data and the relative duration of the metamorphic events: Contributions to Mineralogy and Petrology, v. 128, p. 66-80.

Baker, A., 1987, Models for the tectonothermal evolution of the eastern Dalradian of Scotland: Journal of Metamorphic Geology, v. 5, p. 101-118.

Barboza, S., and Bergantz, G., 2000, Metamorphism and anatexis in the mafic complex contact aureole, Ivrea zone, northern Italy: Journal of Petrology, v. 41, p. 1307-1327.

Barboza, S.A., Bergantz, G.W., and Brown, M., 1999, Regional granulite facies metamorphism in the Ivrea zone: Is the Mafic Complex the smoking gun or a red herring?: Geology, v. 27, p. 447.

Barrow, G., 1893, On an Intrusion of Muscovite-biotite Gneiss in the South-eastern Highlands of Scotland, and its accompanying Metamorphism: Quarterly Journal of the Geological Society, v. 49, p. 330-358.

Barthelmy, D., 2010, Mineralogy database: webmineral.com (accessed July 2010).

Baxter, E., Ague, J., and Depaolo, D., 2002, Prograde temperature-time evolution in the Barrovian type-locality constrained by Sm/Nd garnet ages from Glen Clova, Scotland: Journal of the Geological Society, v. 159, p. 71-82.

Beddoe-Stephens, B., 1990, Pressures and temperatures of Dalradian metamorphism and the andalusite-kyanite transformation in the northeast Grampians: Scottish Journal of Geology, v. 26, p. 3-14.

Bluck, B., Halliday, A., Aftalion, M., and Macintyre, R., 1980, Age and origin of Ballantrae ophiolite and its significance to the Caledonian orogeny and Ordovician time scale: Geology, v. 8, p. 492-495.

Boriani, A.C., Burlini, L., and Sacchi, R., 1990, The Cossato-Mergozzo-Brissago Line and the Pogallo Line (Southern Alps, Northern Italy) and their relationships with the late-Hercynian magmatic and metamorphic events: Tectonophysics, v. 182, p. 91-102.

Breeding, C., Ague, J., Grove, M., and Rupke, A., 2004, Isotopic and chemical alteration of zircon by metamorphic fluids: U-Pb age depth-profiling of zircon crystals from Barrow's garnet zone, northeast Scotland: American Mineralogist, v. 89, p. 1067-1077.

Briggs, R.A., and Sacco, A., 1993, The oxidation of Ilmenite and its relationship to the FeO-Fe_2O_3-TiO_2 phase diagram at 1073 and 1140 K: Metallurgical Transactions A, v. 24, p. 1257-1264.

Burke, M.M., and Fountain, D.M., 1990, Seismic properties of rocks from an exposure of extended continental crust - new laboratory measurements from the Ivrea Zone: Tectonophysics, v. 182, p. 119-146.

Brady, J., 1995, Diffusion data for silicate minerals, glasses, and liquids, Mineral Physics and Crystallography; A Handbook of Physical Constants, American Geophysical Union, p. 269-290.

Camacho, A., Yang, P., and Frederiksen, A., 2009, Constraints from diffusion profiles on the duration of high-strain deformation in thickened crust: Geology, v. 37, p. 755-758.

Cape, J.A., and Lehman, G.W., 1963, Temperature and Finite Pulse-Time Effects in the Flash Method for Measuring Thermal Diffusivity: Journal of Applied Physics, v. 34, p. 1909.

Carlson, W.D., 2006, Rates of Fe, Mg, Mn and Ca diffusion in garnet: American Mineralogist, v. 91, p. 1-11.

Carty, J.P., 2001, Deformation, magmatism and metamorphism in the Portsoy shear zone, North-East Scotland: PhD Thesis, p. 1-323.

Carty, J.P., Connelly, J.N., Hudson, N.F.C., and Gale, J.F.W., 2012, Constraints on the timing of deformation, magmatism and metamorphism in the Dalradian of NE Scotland: Scottish Journal of Geology, v. 48, p. 103-117.

Chakraborty, S., 1995, Diffusion in silicate melts: Reviews in Mineralogy and Geochemistry, v. 32, p. 411-503.

Chakraborty, S., 2008, Diffusion in solid silicates: A tool to track timescales of processes comes of age: Annual Review of Earth and Planetary Sciences, v. 36, p. 153-190.

Chakraborty, S., and Ganguly, J., 1992, Cation diffusion in aluminosilicate garnets - experimental-determination in spessartine-almandine diffusion couples, evaluation of effective binary diffusion-coefficients, and applications: Contributions to Mineralogy and Petrology, v. 111, p. 74-86.

Chatterjee, N.D., 1991, Applied mineralogical thermodynamics- selected topics: Heidelberg, Germany, Springer.

Chinner, G.A., 1966, The distribution of pressure and temperature during Dalradian metamorphism: Quarterly Journal of the Geological Society, v. 122, p. 159-181.

Clark, A.M., and Long, J.V.P., 1971, The anisotropic diffusion of nickel in olivine, in Sherwood, J.N., Chadwick, A.V., and Muir, W., eds., Thomas Graham Memorial Symposium on Diffusion Processes: New York, Gordon and Breach, p. 511-521.

Cliff, R., 1985, Isotopic dating in metamorphic belts: Journal of the Geological Society, v. 142, p. 97-110.

Crank, J., 1975, The Mathematics of Diffusion, Oxford University Press.

Dachs, E., and Proyer, A., 2002, Constraints on the duration of high-pressure metamorphism in the Tauern Window from diffusion modelling of discontinuous growth zones in eclogite garnet: Journal of Metamorphic Geology, v. 20, p. 769-780.

Daly, J.S., and Flowerdew, M.J., 2005, Grampian and late Grenville events recorded by mineral geochronology near a basement-cover contact in north Mayo, Ireland: Journal of the Geological Society, v. 162, p. 163-174.

Deer, W.A., Howie, R.A., Zussman, J., 1962, Rock forming minerals: New York, John Wiley and Sons.

Dempster, T., Rogers, G., Tanner, P., Bluck, B., Muir, R., Redwood, S., Ireland, T., and Paterson, B., 2002, Timing of deposition, orogenesis and glaciation within the Dalradian rocks of Scotland: constraints from U-Pb zircon ages: Journal of The Geological Society, v. 159, p. 83.

Dempster, T.J., Hudson, N.F.C., and Rogers, G., 1995, Metamorphism and cooling of the NE Dalradian: Journal of the Geological Society, v. 152, p. 383-390.

Dewey, J.F., 2005, Orogeny can be very short: Procedings of the National Academy of Sciences, v. 102, p. 15286-15293.

Dieckmann, R., and Schmalzried, H., 1977a, Defects and cation diffusion in magnetite (i): Berichte Der Bunsen-Gesellschaft-Physical Chemistry Chemical Physics, v. 81, p. 344-347.

Dieckmann, R., and Schmalzried, H.,1977b, Defects and cation diffusion in magnetite (ii): Berichte Der Bunsen-Gesellschaft-Physical Chemistry Chemical Physics, v. 81, p. 414-419.

Docka, J.A., 1984, Ilmenite-garnet Mn-Fe exchange: calibration from naturally occuring pairs: Geological Society of America Abstracts with Programs, v. 16, p. 491.

Docka, J.A., Berg, J.H., and Klewin, K.W., 1986, Geothermometry in the Kiglapait aureole .2. Evaluation of exchange thermometry in a well-constrained thermal setting: Journal of Petrology, v. 27, p. 605-626.

Dodson, M., 1973, Closure temperature in cooling geochronological and petrological systems: Contributions to Mineralogy and Petrology, v. 40, p. 259-274.

Dohmen, R., 2008, A new experimental thin film approach to study mobility and partitioning of elements in grain boundaries: Fe-Mg exchange between olivines mediated by transport through an inert grain boundary: American Mineralogist, v. 93, p. 863-874.

Dohmen, R., Becker, H., Meissner, E., and Etzel, T., 2002, Production of silicate thin films using pulsed laser deposition (PLD) and applications to studies in mineral kinetics: European Journal of Mineralogy, v. 14, p. 1155-1168.

Downie, C., Lister, T.R., Harris, A.L., Fettes, D.J., 1971, A palynological investigation of the Dalradian rocks of Scotland: Institute of Geological Sciences, Reports, v. 71/9.

Drouin, D., Couture, A.R., Joly, D., Tastet, X., Aimez, V., and Gauvin, R., 2007, CASINO V2.42 - A fast and easy-to-use modeling tool for scanning electron microscopy and microanalysis users: Scanning, v. 29, p. 92-101.

Eggins, S.M., Kinsley, L., and Shelley, J., 1998, Deposition and element fractionation processes during atmospheric pressure laser sampling for analysis by ICP-MS: Applied Surface Science, v. 127, p. 278-286.

Ehlers, K., Powell, R., and Stüwe, K., 1994, Cooling rate histories from garnet plus biotite equilibrium: American Mineralogist, v. 79, p. 737-744.

Eiler, J.M., Baumgartner, L.P., and Valley, J.W., 1992, Intercrystalline stable isotope diffusion: a fast grain boundary model: Contributions to Mineralogy and Petrology, v. 112, p. 543-557.

England, P., and Thompson, A., 1984, Pressure-temperature-time paths of regional metamorphism I. Heat transfer during the evolution of regions of thickened continental crust: Journal of Petrology, v. 25, p. 894-928.

England, P., and Thompson, A., 1986, Some thermal and tectonic models for crustal melting in continental collision zones, in Coward, M.P., Ries, A. C., ed., Collision Tectonics, Volume 19: London, Geological Society of London Special Publication, p. 83-94.

England, P.C., and Richardson, S.W., 1977, The influence of erosion upon the mineral fades of rocks from different metamorphic environments: Journal of the Geological Society, v. 134, p. 201-213.

Engvik, A.K., Mezger, K., Wortelkamp, S., Bast, R., Corfu, F., Korneliussen, A., Ihlen, P., Bingen, B., and Austrheim, H., 2011, Metasomatism of gabbro - mineral replacement and element mobilization during Sveconorwegian metamorphic event: Journal of Metamorphic Geology, v. 29, p. 399-423.

Ewing, T., 2011, Hf isotope analysis and U-Pb geochronology of rutile: Technique development and application to a lower crustal section (Ivrea-Verbano Zone, Italy): Canberra, The Australian National University.

Ewing, T., Hermann, J., and Rubatto, D., 2012, The robustness of the Zr-in-rutile and Ti-in-zircon thermometers during high-temperature metamorphism (Ivrea–Verbano Zone, northern Italy): Contributions to Mineralogy and Petrology, v. 165, p. 757-779.

Faryad, S., and Chakraborty, S., 2005, Duration of Eo-Alpine metamorphic events obtained from multicomponent diffusion modeling of garnet: a case study from the Eastern Alps: Contributions to Mineralogy and Petrology, v. 150, p. 306-318.

Feenstra, A., and Engi, M., 1998, An experimental study of the Fe-Mn exchange between garnet and ilmenite: Contributions to Mineralogy and Petrology, v. 131, p. 379-392.

Fettes, D.J., 1970, The structural and metamorphic state of the Dalradian rocks and their bearing on the age of emplacement of the basic sheet: Scottish Journal of Geology, v. 6, p. 108-118.

Fettes, D.J., Graham, C.M., Harte, B., Plant, J.A., 1986, Lineaments and basement domains: an alternative view of Dalradian evolution: Journal of the Geological Society, London, v. 143, p. 453-464.

Flinn, D., Miller, J.A., Roddom, D., 1991, The age of the Norwick hornblendic schists of Unst and Fetlar and the obduction of the Shetland ophiolite: Scottish Journal of Geology, v. 27, p. 11-19.

Florence, F., and Spear, F., 1995, Intergranular diffusion kinetics of Fe and Mg during retrograde metamorphism of a pelitic gneiss from the Adirondack mountains: Earth and Planetary Science Letters, v. 134, p. 329-340.

Forster, M.A., and Lister, G.S., 2004, The interpretation of $^{40}Ar/^{39}Ar$ apparent age spectra produced by mixing: application of the method of asymptotes and limits: Journal Of Structural Geology, v. 26, p. 287-305.

Forster, M., and Lister, G., 2009, Core-complex-related extension of the Aegean lithosphere initiated at the Eocene-Oligocene transition: Journal of Geophysical Research, v. 114, p. B02401.

Forster, M.A., and Lister, G.S., 2010, Argon enters the retentive zone: reassessment of diffusion parameters for K-feldspar in the South Cyclades Shear Zone, Ios, Greece: Geological Society, v. 332, p. 17-34.

Friedrich, A., Bowring, S., Martin, M., and Hodges, K., 1999, Short-lived continental magmatic arc at Connemara, western Irish Caledonides: Implications for the age of the Grampian orogeny: Geology, v. 27, p. 27-30.

Frost, B.R., 1991, Introduction to oxygen fugacity and its petrological importance, in Lindsley, D.H., ed., Oxide minerals: Petrological and magnetic significance, Volume 25: New York, USA, Reviews in Mineralogy.

Fuhrman, M.L., Lindsley, D.H., 1988, Ternary-feldspar modeling and thermometry: The American Mineralogist, v. 73, p. 201-216.

Ganguly, J., 2002, Diffusion kinetics in minerals: principles and applications to tectono-metamorphic processes: EMU notes in Mineralogy, v.4, p. 271-309.

Ganguly, Y., Chakraborty, S., Sharp, T., and Rumble III, D., 1996a, Constraint on the time scale of biotite-grade metamorphism during Acadian orogeny from a natural garnet-garnet diffusion couple: American Mineralogist, v. 81, p. 1208-1216.

Ganguly, J., Cheng, W., and Chakraborty, S., 1998, Cation diffusion in aluminosilicate garnets: experimental determination in pyrope-almandine diffusion couples: Contributions to Mineralogy and Petrology, v. 131, p. 171-180.

Ganguly, J., Cheng, W., and Tirone, M., 1996b, Thermodynamics of aluminosilicate garnet solid solution: new experimental data, an optimized model, and thermometric applications: Contributions to Mineralogy and Petrology, v. 126, p. 137-151.

Ghiorso, M.S., 1997, Thermodynamic analysis of the effect of magnetic ordering on miscibility gaps in the FeTi cubic and rhombohedral oxide minerals and the FeTi oxide geothermometer: Physics and Chemistry of Minerals, v. 25, p. 28-38.

Giletti, B., 1986, Diffusion effects on oxygen isotope temperatures of slowly cooled igneous and metamorphic rocks: Earth and Planetary Science Letters, v. 77, p. 218-228.

Goldstein, J., Newbury, D.E., Joy, D.C., Lyman, C.E., Echlin, P., Lifshin, E., Sawyer, L., Michael, J.R., 2003, Scanning electon microscopy and X-ray microanalysis, Springer, p. 411.

Goodman, S., 1994, The Portsoy-Duchray Hill lineament - a review of the evidence: Geological Magazine, v. 13, p. 407-415.

Graham, C.M., Powell, R., 1984, A garnet-hornblende thermometer: calibration, testing and application to the Pelona Schist S. California: Journal of Metamorphic Geology, v. 2, p. 13-31.

Green, D.H., and Sobolev, N.V., 1975, Coexisting garnets and ilmenites synthesized at high-pressures from pyrolite and olivine basanite and their significance for kimberlitic assemblages: Contributions to Mineralogy and Petrology v. 50, p. 217-229.

Hamblock, J., Andronicos, C., Miller, K., Barnes, C., Ren, M., Averill, M., and Anthony, E., 2007, A composite geologic and seismic profile beneath the southern Rio Grande rift, New Mexico, based on xenolith mineralogy, temperature, and pressure: Tectonophysics, v. 442, p. 14-48.

Harrison, T.M., Celerier, J., Aikman, A.B., Hermann, J., and Heizler, M.T., 2009, Diffusion of ^{40}Ar in muscovite: Geochimica et Cosmochimica Acta, v. 73, p. 1039-1051.

Harte, B., and Hudson, N.F.C., 1979, Pelite facies series and the temperatures and pressures of Dalradian metamorphism in E Scotland, in Harris, A.L., Holland, C.H., and Leake, B.E., eds., The Caledonides of the British Isles - A Review, Volume 8: London, Geological Society London Special Publications, p. 323-337.

Henk, A., Franz, L., Teufel, S., and Oncken, O., 1997, Magmatic underplating, extension, and crustal reequilibration: Insights from a cross-section through the Ivrea Zone and Strona-Ceneri Zone, northern Italy: The Journal of Geology, v. 105, p. 367-377.

Hodges, K.V., Spear, F. S., 1982, Geothermometry, geobarometry and the Al_2SiO_5 triple point at Mt. Mossilauke, New Hampshire: American Mineralogist, v. 67, p. 1118-1134.

Hofmann, S., and Schubert, J., 1998, Determination and application of the depth resolution function in sputter profiling with secondary ion mass spectroscopy and Auger electron spectroscopy: Journal of Vacuum Science & Technology A: Vacuum, Surfaces, and Films, v. 16, p. 1096.

Hofmann, S., and Schubert, J., 2004, Sputter-depth profiling for thin-film analysis: Philosophical Transactions of the Royal Society A: Mathematical, Physical and Engineering Sciences, v. 362, p. 55-75.

Hollister, L.S., 1966, Garnet zoning: an interpretation based on the Rayleigh fractionation model: Science, v. 154, p. 1647-1651.

Hollister, L.S., Hargraves, R.B., James, T.S., and Renne, P.R., 2004, The paleomagnetic effects of reheating the Ecstall pluton, British Columbia: Earth And Planetary Science Letters, v. 221, p. 397-407.

Hudson, N., 1980, Regional metamorphism of some Dalradian pelites in the Buchan area, NE Scotland: Contributions to Mineralogy and Petrology, v. 73, p. 39-51.

Hudson, N., 1985, Conditions of Dalradian metamorphism in the Buchan area, NE Scotland: Journal of the Geological Society, v. 142, p. 63-76.

Ishikawa, Y., and Akimoto, S., 1958, Magnetic Property and Crystal Chemistry of Ilmenite ($MeTiO_3$) and Hematite (αFe_2O_3) System II. Magnetic Property: Journal of the Physical Society of Japan, v. 13, p. 1298-1310.

Jaoul, O., and Sautter, V., 1999, A new approach to geospeedometry based on the 'compensation law': Physics of the Earth and Planetary Interiors, v. 110, p. 95-114.

Jiang, J., and Lasaga, A., 1990, The effect of postgrowth thermal events on growth-zoned garnet - implications for metamorphic P-T history calculations: Contributions to Mineralogy and Petrology, v. 105, p. 454-459.

Johnson, M.R.W., 1962, Relations of movement and metamorphism in the Dalradians of Banffshire: Transactions of the Edinburgh Geological Society, v. 19, p. 29-64.

Kneller, B.C., 1987, A geological history of north-east Scotland, in Trewin, N.H., Kneller, B.C., Gillen, C., ed., Geology of the Aberdeen area: Edinburgh, Scottish Academic Press, p. 1-50.

Koziol, A., and Bohlen, S., 1992, Solution properties of almandine-pyrope garnet as determined by phase-equilibrium experiments: American Mineralogist, v. 77, p. 765-773.

Krabbendam, M., Leslie, A.G., Crane, A., and Goodman, S., 1997, Generation of the Tay Nappe, Scotland, by large-scale SE-directed shearing: Journal Of The Geological Society, v. 154, p. 15-24.

Kress, V.C., Bohlen, S.R., and Lindsley, D.H., 1985, Experimental calibration of Fe-Mn exchange between coexisting garnet and ilmenite: EOS, v. 66, p. 388.

Kress, V.C., 1986, Iron-manganese exchange in coexisting garnet and ilmenite. MSc thesis, State University of New York at Stony Brook.

Kretz, R., 1959, Chemical study of garnet, biotite and hornblende from gneisses of S.W. Quebec, with emphasis on distribution of elements in coexisting minerals: The Journal of Geology, v. 67, p. 371-402.

Kretz, R., 1983, Symbols for rock-forming minerals: American Mineralogist, v. 68, p. 277-279.

Lambert, R.S.J., and McKerrow, W.S., 1976, The Grampian Orogeny: Scottish Journal of Geology, v. 12, p. 271-292.

Lancaster, P.J., Baxter, E.F., Ague, J.J., Breeding, C.M., and Owens, T.L., 2008, Synchronous peak Barrovian metamorphism driven by syn-orogenic magmatism and fluid flow in southern Connecticut, USA: Journal of Metamorphic Geology, v. 26, p. 527-538.

Lindström, R., Viitanen, M., Juhanoja, J., and Hölttä, P., 1991, Geospeedometry of metamorphic rocks: examples in the Rantasalmi-Sulkava and Kiuruvesi areas, eastern Finland. Biotite-garnet diffusion couples: Journal of Metamorphic Geology, v. 9, p. 181-190.

Lister, G.S., and Baldwin, S.L., 1996, Modelling the effect of arbitrary P-T-t histories on argon diffusion in minerals using the MacArgon program for the Apple Macintosh: Tectonophysics, v. 253, p. 83-109.

Lo, V.C., and Sun, J.Z., 1996, Simulation of uphill diffusion behaviour of Si-implanted GaAs: Modelling and Simulation in Materials Science and Engineering, v. 4, p. 613-621.

Loomis, T., Ganguly, J., and Elphick, S., 1985, Experimental determination of cation diffusivities in aluminosilicate garnets: Contributions to Mineralogy and Petrology, v. 90, p. 45-51.

Luvizotto, G.L., and Zack, T., 2009, Nb and Zr behavior in rutile during high-grade metamorphism and retrogression: An example from the Ivrea-Verbano Zone: Chemical Geology, v. 261, p. 303-317.

Lyubetskaya, T., and Ague, J.J., 2009, Modeling the Magnitudes and Directions of Regional Metamorphic Fluid Flow in Collisional Orogens: Journal of Petrology, v. 50, p. 1505-1531.

Lyubetskaya, T., and Ague, J.J., 2010, Modeling metamorphism in collisional orogens intruded by magmas: II. Fluid flow and implications for Barrovian and Buchan metamorphism, Scotland: American Journal of Science, v. 310, p. 459-491.

Maaskant, P., and Kaper, H., 1991, Fluorescence effects at phase boundaries: petrological implications for Fe-Ti oxides: Mineralogical Magazine, v. 55, p. 277-279.

Magee, C., and Honig, R., 1982, Depth profiling by SIMS-depth resolution, dynamic range and sensitivity: Surface and Interface Analysis, v. 4, p. 35-41.

Maletz, J., 2004, Late Castlemainian (Ca 4, Arenig) graptolites from the Ballantrae Complex, SW Scotland: Scottish Journal of Geology, v. 40, p. 185-186.

Martin, A.J., Ganguly, J., and Decelles, P.G., 2010, Metamorphism of Greater and Lesser Himalayan rocks exposed in the Modi Khola valley, central Nepal: Contributions to Mineralogy and Petrology, v. 159, p. 203-223.

McEnroe, S.A., Harrison, R.J., Robinson, P., and Langenhorst, F., 2002, Nanoscale haematite-ilmenite lamellae in massive ilmenite rock: an example of 'lamellar magnetism'with implications for planetary magnetic anomalies: Geophysical Journal International, v. 151, p. 890-912.

McKenzie, D., 1984, A possible mechanism for epeirogenic uplift: Nature, v. 307, p. 616-618.

Miloš, R., Titanite-ilmenite-magnetite phase relations in amphibolites of the Chýnov area (Bohemian Massif, Czech Republic): Acta Geodynamica et Geomaterialia, v. 5, p. 239-246.

Molyneux, S., 1998, An upper Dalradian microfossil reassessed: Journal of the Geological Society, v. 155, p. 741-743.

Morioka, M., and Nagasawa H., 1991, Diffusion in single crystals of melilite: II. Cations: Geochimica et Cosmochimica Acta, v. 55, p. 751-759.

Muncill, G.E., Chamberlain, C. P., 1988, Crustal cooling rates inferred from homogenization of metamorphic garnets: Earth and Planetary Science Letters, v. 87, p. 390-396.

Navrotsky, A., and Kleppa, O.J., 1973, Estimate of enthalpies of formation and fusion of cordierite: Journal of the American Ceramic Society, v. 56, p. 198-199.

Nystrom, A.I., and Kriegsman, L.M., 2003, Prograde and retrograde reactions, garnet zoning patterns, and accessory phase behaviour in SW Finland migmatites, with implications for geochronology: Geological Society, London, Special Publications, v. 220, p. 213-230.

O'Brien, P., 1997, Garnet zoning and reaction textures in overprinted eclogites, Bohemian Massif, European Variscides: a record of their thermal history during exhumation: Lithos, v. 41, p. 119-133.

O'Brien, P.J., and Vrána, S., 1995, Eclogites with a short-lived granulite facies overprint in the Moldanubian Zone, Czech Republic: petrology, geochemistry and diffusion modelling of garnet zoning: Geologische Rundschau, v. 84, p. 473-488.

Oliver, G.J.H., 2001, Reconstruction of the Grampian episode in Scotland: its place in the Caledonian Orogeny: Tectonophysics, v. 332, p. 23-49.

Oliver, G.J.H., Chen, F., Buchwaldt, R., and Hegner, E., 2000, Fast tectonometamorphism and exhumation in the type area of the Barrovian and Buchan zones: Geology, v. 28, p. 459-462.

Oliver, G.J.H., Wilde, S.A., and Wan, Y., 2008, Geochronology and geodynamics of Scottish granitoids from the late Neoproterozoic break-up of Rodinia to Palaeozoic collision: Journal of Geological Society, v. 165, p. 165-674.

Olker, B., Altherr, R., and Paquin, J., 2003, Fast exhumation of the ultrahigh-pressure Alpe Arami garnet peridotite (Central Alps, Switzerland): constraints from geospeedometry and thermal modelling: Journal of Metamorphic Geology, v. 21, p. 395-402.

O'Neill, H.St.C., Pownceby, M.I., and Wall, V.J., 1989, Activity-composition relations in $FeTiO_3$-$MnTiO_3$ ilmenite solid-solutions from EMF-measurements at 1050-1300 K: Contributions to Mineralogy and Petrology, v. 103, p. 216-222.

Ono, A., 1980, Partitioning of Fe and Mn between garnet an ilmenite: An Experimental study: Journal of the Japanese Association of Mineralogy, Petrology and Economic Geology, v. 75, p. 160-163.

Pankhurst, R.J., 1970, The geochronology of the basic igneous complexes: Scottish Journal of Geology, v. 6, p. 83-107.

Pankhurst, R.J., and Pidgeon, R.T., 1976, Inherited isotope systems and source region pre-history of early Caledonian granites in Dalradian series of Scotland: Earth and Planetary Science Letters, v. 31, p. 55-68.

Pattison, D., Chacko, T., Farquhar, J., and McFarlane, C., 2003, Temperatures of granulite-facies metamorphism: Constraints from experimental phase equilibria and thermobarometry corrected for retrograde exchange: Journal of Petrology, v. 44, p. 867-900.

Pearce, N.J.G., Perkins, W.T., Westgate, J.A., Gorton, M.P., Jackson, S.E., Neal, S.E., Chenery, S.P., 1997, A compilation of new and published major and trace element data for NIST SRM 610 and NIST SRM 612 glass reference materials: Geostandards and Geoanalytical Research, v. 21, p. 115-144.

Perchuk, A.L., and Philippot, P., 2000, Geospeedometry and time scales of high-pressure metamorphism: International Geology Review, v. 42, p. 207-223.

Peressini, G., Quick, J.E., Sinigoi, S., Hofmann, A.W., and Fanning, M., 2007, Duration of a Large Mafic Intrusion and Heat Transfer in the Lower Crust: a SHRIMP U-Pb zircon study in the Ivrea-Verbano zone (Western Alps, Italy): Journal of Petrology, v. 48, p. 1185-1218.

Philippot, P., Blichert-Toft, J., Perchuk, A., Costa, S., and Gerasimov, V., 2001, Lu–Hf and Ar–Ar chronometry supports extreme rate of subduction zone metamorphism deduced from geospeedometry: Tectonophysics, v. 342, p. 23-38.

Phillips, E.R., Highton, A.J., Hyslop, E.K., and Smith, M., 1999, The timing and P-T conditions of regional metamorphism in the Central Highlands, Scotland: Journal of the Geological Society, v. 156, p. 1183-1193.

Pownceby, M.I., Wall, V.J., and O'Neill, H.S.C., 1987, Fe-Mn partitioning between garnet and ilmenite: experimental calibration and applications: Contributions to Mineralogy and Petrology, v. 97, p. 116-126.

Pownceby, M.I., Wall, V.J., and O'Neill, H.S.C., 1987, Erratum: Fe-Mn partitioning between garnet and ilmenite: experimental calibration and applications: Contributions to Mineralogy and Petrology, v. 97, p. 539.

Pownceby, M.I., Wall, V.J., and O'Neill, H.S.C., 1991, An experimental-study of the effect of Ca upon garnet-ilmenite Fe-Mn exchange equilibria: American Mineralogist, v. 76, p. 1580-1588.

Pringle, M., 1939, The discovery of Cambrian trilobites in the Highland Border rocks near Callander, Perthshire: Report of the British Association for the Advancement of Science, v. 1, p. 252.

Ramsey, D.M., and Sturt, B.A., 1979, The status of the Banff nappe, in Harris, A.L., Holland, C.H., and Leake, B.E., eds., The Caledonides of the British Isles - A Review, Volume 8: London, Geological Society London Special Publications, p. 145-151.

Rast, N., 1963, Structure and metamorphism of the Dalradian rocks of Scotland, The British Caledonides: Edinburgh, Oliver and Boyd Ltd., p. 123-142.

Rawling, T.J., and Lister, G.S., 2002, Large-scale structure of the eclogite–blueschist belt of New Caledonia: Journal Of Structural Geology, v. 24, p. 1239-1258.

Read, H.H., 1952, Metamorphism and Migmatisation in the Ythan valley, Aberdeenshire: Transactions of the Edinburgh Geological Society, v. 15, p. 265-279.

Read, H.H., 1961, Aspects of Caledonian magmatism in Britain: Geological Journal, v. 2, p. 653-683.

Redler, C., Johnson, T.E., White, R.W., and Kunz, B.E., 2012, Phase equilibrium constraints on a deep crustal metamorphic field gradient: metapelitic rocks from the Ivrea Zone (NW Italy): Journal of Metamorphic Geology, v. 30, p. 235-254.

Riciputi, L.R., Paterson, B.A., and Ripperdan, R.L., 1998, Measurement of light stable isotope ratios by SIMS: Matrix effects for oxygen, carbon and sulfur isotopes in minerals: International Journal of Mass Spectrometry, v. 178, p. 81-112.

Rivalenti, G., Garuti, G., and Rossi, A., 1975, The origin of the Ivrea-Verbano basic formation (western Italian Alps); whole rock geochemistry: Bollettino della Societa Geologica Italiana, v. 94, p. 1149-1186.

Rivalenti, G., Rossi, A., Siena, F., and Sinigoi, S., 1984, The layered series of the Ivrea-Verbano igneous complex, western Alps, Italy: Mineralogy and Petrology, v. 33, p. 77-99.

Robl, J., Hergarten, S., Stüwe, K., and Hauzenberger, C., 2007, THERMAL HISTORY: A new software to interpret diffusive zoning profiles in garnet: Computers & Geosciences, v. 33, p. 760-772.

Rogers, G., Dempster, T., Bluck, B., and Tanner, P., 1989, A high precision U-Pb age for the Ben Vuirich granite: implications for the evolution of the Scottish Dalradian supergroup: Journal of the Geological Society London, v. 146, p. 789-798.

Rogers, G., Paterson, B.A., Dempster, T.J., and Redwood, S.D., 1994, U-Pb geochronology of the 'Newer' Gabbros, NE Grampians (abstract), Caledonian Terrane Relationships in Britain: Keyworth.

Săbău, G., and Massonne, H.-J., 2003, Relationships among eclogite bodies and host rocks in the Lotru metamorphic suite (south Carpathians, Romania): Petrological evidence for multistage tectonic emplacement of eclogites in a medium-pressure domain: International Geology Review, v. 45, p. 225-262.

Sautter, V., Duchêne, S., and Marques, F.O., 2001, New analytical and numerical geospeedometers tested on garnet pyroxenites from Bragança Nappe Complex (NE Portugal): Tectonophysics, v. 342, p. 39-59.

Schmid, S.M., Zingg, A., and Handy, M., 1987, The kinematics of movements along the Insubric Line and the emplacement of the Ivrea Zone: Tectonophysics, v. 135, p. 47-66.

Schnetger, B., 1994, Partial melting during the evolution of the amphibolite-to granulite-facies gneisses of the Ivrea Zone, northern Italy: Chemical Geology, v. 113, p. 71-101.

Sills, J., and Tarney, J., 1984, Petrogenesis and tectonic significance of amphibolites interlayered with metasedimentary gneisses in the Ivrea Zone, Southern Alps, Northwest Italy: Tectonophysics, v. 107, p. 187-206.

Sinigoi, S., Quick, J.E., Demarchi, G., and Klötzli, U., 2011, The role of crustal fertility in the generation of large silicic magmatic systems triggered by intrusion of mantle magma in the deep crust: Contributions to Mineralogy and Petrology, v. 162, p. 691-707.

Spandler, C., O'Neill, H.S.C., and Kamenetsky, V.S., 2007, Survival times of anomalous melt inclusions from element diffusion in olivine and chromite: Nature, v. 447, p. 303-306.

Spandler, C., and O'Neill, H.S.C., 2010, Diffusion and partition coefficients of minor and trace elements in San Carlos olivine at 1,300° C with some geochemical implications: Contributions to Mineralogy and Petrology, v. 159, p. 791-818.

Spear, F., 1991, On the interpretation of peak metamorphic temperatures in light of garnet diffusion during cooling: Journal of Metamorphic Geology, v. 9, p. 379-388.

Spear, F.S., and Parrish, R.R., 1996, Petrology and cooling rates of the Valhalla complex, British Columbia, Canada: Journal of Petrology, v. 37, p. 733-765.

Spell, T., and McDougall, I., 2003, Characterization and calibration of $^{40}Ar/^{39}Ar$ dating standards: Chemical Geology, v. 198, p. 189-211.

Spray, J.G., 1988, Thrust-related metamorphism beneath the Shetland Islands oceanic fragment, northeast Scotland: Canadian Journal of Earth Sciences, v. 25, p. 1760-1776.

Steiger, R.H., and Jager, E., 1977, Subcommission on Geochronology - Convention on Use of Decay Constants in Geochronology and Cosmochronology: Earth And Planetary Science Letters, v. 36, p. 359-362.

Tanner, P.W.G., and Pringle, M.S., 1999, Testing for the presence of a terrane boundary within Neoproterozoic (Dalradian) to Cambrian siliceous turbidites at Callander, Perthshire, Scotland: Journal of the Geological Society, London, v. 156, p. 1205-1216.

Thompson, A.B., 1976, Mineral reactions in pelitic rocks; II, Calculation of some P-T-X(Fe-Mg) phase relations: American Journal of Science, v. 276, p. 425-454.

Tracy, R.J., and Dietsch, C.W., 1982, High-temperature retrograde reactions in pelitic gneiss, central Massachusetts: Canadian Mineralogist, v. 20, p. 425-437.

Treagus, J.E., and Roberts, J.L., 1981, The boyndie syncline, a D1 structure in the Dalradian of Scotland: Geological Journal, v. 16, p. 125-135.

Trepmann, C.A., Stockhert, B., and Chakraborty, S., 2004, Oligocene trondhjemitic dikes in the Austroalpine basement of the Pfunderer Berge, Sudtirol-level of emplacement and metamorphic overprint: European Journal of Mineralogy, v. 16, p. 641-659.

Vielzeuf, D., Champenois, M., Valley, J.W., Brunet, F., and Devidal, J.L., 2005, SIMS analyses of oxygen isotopes: Matrix effects in Fe–Mg–Ca garnets: Chemical Geology, v. 223, p. 208-226.

Vielzeuf, D., and Saúl, A., 2011, Uphill diffusion, zero-flux planes and transient chemical solitary waves in garnet: Contributions to Mineralogy and Petrology, v. 161, p. 683-702.

Viete, D.R., 2009, The nature and origin of regional metamorphism: observations from the Barrovian metamorphic series of Scotland. PhD Thesis, The Australian National University.

Viete, D.R., Forster, M.A., and Lister, G.S., 2011a, The nature and origin of the Barrovian metamorphism, Scotland: Ar-40/Ar-39 apparent age patterns and the duration of metamorphism in the biotite zone: Journal of the Geological Society, London, v. 168, p. 133-146.

Viete, D.R., Hermann, J., Lister, G.S., and Stenhouse, I.R., 2011b, The nature and origin of the Barrovian metamorphism, Scotland: diffusion length scales in garnet and inferred thermal time scales: Journal of the Geological Society, v. 168, p. 115-132.

Viete, D.R., Richards, S.W., Lister, G.S., Oliver, G.J.H., and Banks, G.J., 2010, Lithospheric-scale extension during Grampian orogenesis in Scotland: Geological Society, London, Special Publications, v. 335, p. 121-160.

Voorhoeve, H., and Houseman, G., 1988, The thermal evolution of lithosphere extending on a low-angle detachment zone: Basin research, v. 1, p. 1-9.

Wechslar, B.A., and Prewitt, C.T., 1984, Ilmenite at high temperature and pressure: American Mineralogist, v. 69, p. 176-185.

Weyer, S., Jarick, J., and Mezger, K., 1999, Quantitative temperature-time information from retrograde diffusion zoning in garnet: constraints for the P-T-t history of the Central Black Forest, Germany: Journal of Metamorphic Geology, v. 17, p. 449-461.

Whitney, D.L., and Ghent, E.D., 1993, Prograde reactions and garnet zoning reversals in staurolite schist, British Columbia: significance for thermobarometric interpretations: Journal of Metamorphic Geology, v. 11, p. 779-788.

Wijbrans, J.R., and McDougall, I., 1986, $^{40}Ar/^{39}Ar$ dating of white micas from an Alpine high-pressure metamorphic belt on Naxos (Greece): the resetting of the argon isotopic system: Contributions to Mineralogy and Petrology, v. 93, p. 187-194.

Wilson, N.C., Russo, S.P., Muscat, J., and Harrison, N.M., 2005, High-pressure phases of $FeTiO_3$ from first principles: Physical Review B, v. 72, p. 1-8.

Woodsworth, G.J., 1977, Homogenization of zoned garnets from peletic schists: Canadian Mineralogist, v. 15, p. 230-242.

Yardley, B.W.D., 1977, An empirical study of diffusion in garnet: American Mineralogist, v. 62, p. 793-800.

Zingg, A., 1980, Regional metamorphism in the Ivrea Zone (Southern Alps, N-Italy): Field and microscopic investigations: Schweizerische mineralogische und petrographische mitteilungen, v. 60, p. 153-179.

APPENDIX A

White Mica Geochemistry
(Chapter 6)

Electron Probe Microanalysis

The Cameca SX100 electron probe microanalyser (EPMA) at RSES, ANU was used to obtain the composition of white micas analysed for argon geochronology. A selection of spot analyses were performed with a beam current of 5 nA, an accelerating voltage of 15 keV, a spot size of approximately 5 μm using wave dispersive spectrometers (WDS). Standards of phlogopite and hornblende were used. Data tables and graphs of Si concentration against Mg concentration are provided below. The EPMA data was normalized to give per formula unit values (p.f.u) for 11 oxygen p.f.u by the method outlined in Deer et al. (1962).

Normalised Concentration (p.f.u)												
Na	Mg	Al	Si	Fe	Mn	K	Ca	Ti	Total	Na/ Na+K	Mg/ Mg+Fe	Comment
IS10-12 [57.67069N, 2.52750W]												
0.093	0.161	2.511	3.177	0.132	0.000	0.847	0.000	0.058	6.980	0.099	0.550	Detrital
0.101	0.159	2.476	3.210	0.132	0.001	0.835	0.000	0.053	6.967	0.108	0.547	Detrital
0.099	0.176	2.518	3.166	0.127	0.000	0.819	0.000	0.065	6.969	0.107	0.582	Detrital
0.103	0.088	2.706	3.104	0.081	0.000	0.832	0.000	0.049	6.962	0.111	0.521	Detrital
0.083	0.270	2.384	3.160	0.238	0.001	0.821	0.000	0.071	7.029	0.092	0.532	Detrital
0.083	0.276	2.342	3.191	0.234	0.002	0.821	0.002	0.070	7.021	0.092	0.542	Detrital
0.102	0.296	2.439	3.107	0.242	0.000	0.807	0.000	0.067	7.061	0.112	0.550	Detrital
0.104	0.172	2.514	3.183	0.116	0.000	0.831	0.000	0.054	6.974	0.111	0.598	Detrital
0.096	0.194	2.516	3.149	0.158	0.002	0.822	0.000	0.058	6.995	0.105	0.551	Detrital
0.107	0.208	2.487	3.162	0.146	0.001	0.840	0.001	0.057	7.010	0.113	0.587	Detrital
0.132	0.141	2.588	3.130	0.105	0.000	0.822	0.000	0.067	6.986	0.139	0.573	Detrital
0.152	0.143	2.643	3.110	0.111	0.000	0.800	0.001	0.042	7.002	0.160	0.563	Detrital
0.149	0.122	2.611	3.120	0.109	0.001	0.812	0.000	0.065	6.989	0.155	0.528	Detrital
0.146	0.131	2.636	3.106	0.111	0.000	0.827	0.001	0.052	7.010	0.150	0.542	Detrital
0.127	0.132	2.646	3.129	0.108	0.002	0.821	0.000	0.029	6.993	0.134	0.550	Detrital
0.140	0.136	2.630	3.116	0.122	0.000	0.819	0.000	0.043	7.005	0.146	0.527	Detrital
0.142	0.140	2.641	3.108	0.117	0.000	0.816	0.000	0.044	7.007	0.148	0.546	Detrital
0.147	0.134	2.638	3.124	0.112	0.000	0.804	0.000	0.036	6.996	0.155	0.545	Detrital
IS10-31 [57.67018N, 2.54464W]												
0.163	0.056	2.769	3.120	0.051	0.000	0.761	0.003	0.016	6.941	0.177	0.524	Detrital
0.182	0.044	2.829	3.085	0.039	0.003	0.742	0.006	0.017	6.946	0.197	0.527	Detrital
0.137	0.075	2.708	3.153	0.064	0.000	0.762	0.002	0.021	6.922	0.153	0.538	Detrital
0.126	0.055	2.068	3.688	0.037	0.000	0.585	0.002	0.036	6.597	0.178	0.593	Detrital
0.157	0.047	2.773	3.125	0.060	0.002	0.731	0.004	0.017	6.916	0.177	0.438	Detrital
0.168	0.054	2.772	3.127	0.046	0.001	0.733	0.008	0.015	6.923	0.186	0.542	Detrital
0.157	0.043	2.807	3.099	0.050	0.003	0.756	0.002	0.018	6.936	0.172	0.464	Detrital
0.130	0.079	2.672	3.202	0.046	0.000	0.710	0.002	0.020	6.862	0.155	0.632	Detrital

Na	Mg	Al	Si	Fe	Mn	K	Ca	Ti	Total	Na/ Na+K	Mg/ Mg+Fe	Comment
IS10-28 [57.67000N, 2.53364W]												
0.110	0.164	2.502	3.210	0.107	0.000	0.800	0.005	0.048	6.946	0.121	0.606	Detrital
0.120	0.126	2.520	3.230	0.086	0.002	0.781	0.000	0.048	6.913	0.133	0.593	Detrital
0.124	0.138	2.566	3.186	0.088	0.001	0.781	0.000	0.050	6.934	0.137	0.611	Detrital
0.134	0.138	2.589	3.152	0.093	0.001	0.804	0.000	0.056	6.967	0.143	0.596	Detrital
0.122	0.149	2.558	3.177	0.100	0.002	0.786	0.000	0.051	6.946	0.134	0.599	Detrital
0.149	0.157	2.539	3.178	0.107	0.001	0.797	0.000	0.049	6.976	0.157	0.595	Detrital
0.141	0.141	2.582	3.157	0.101	0.000	0.799	0.000	0.050	6.972	0.150	0.584	Detrital
0.135	0.126	2.586	3.170	0.097	0.000	0.783	0.000	0.050	6.946	0.147	0.566	Detrital
0.122	0.148	2.550	3.192	0.099	0.000	0.774	0.003	0.047	6.934	0.136	0.599	Detrital
0.178	0.042	2.944	3.013	0.052	0.000	0.713	0.001	0.009	6.951	0.200	0.448	Detrital
0.191	0.066	2.917	3.008	0.067	0.001	0.714	0.000	0.011	6.975	0.211	0.495	Detrital
0.155	0.040	2.541	3.353	0.046	0.000	0.609	0.001	0.006	6.752	0.203	0.466	Detrital
0.571	0.025	2.623	3.194	0.044	0.000	0.449	0.076	0.011	6.993	0.560	0.358	Detrital
0.180	0.054	2.824	3.076	0.065	0.000	0.751	0.000	0.013	6.964	0.194	0.454	Detrital
0.183	0.054	2.808	3.087	0.059	0.001	0.765	0.000	0.013	6.970	0.193	0.477	Detrital
IS10-09 [57.67278N, 2.56114W]												
0.184	0.061	2.803	3.101	0.050	0.000	0.732	0.000	0.012	6.943	0.200	0.551	
0.201	0.038	2.863	3.061	0.044	0.000	0.735	0.000	0.017	6.959	0.215	0.461	
0.167	0.036	2.549	3.329	0.039	0.000	0.662	0.000	0.015	6.796	0.201	0.480	
0.188	0.050	2.830	3.080	0.056	0.000	0.736	0.001	0.013	6.953	0.203	0.471	
0.194	0.050	2.847	3.062	0.064	0.001	0.732	0.002	0.013	6.964	0.209	0.442	
0.131	0.105	2.092	3.626	0.165	0.001	0.511	0.004	0.007	6.642	0.204	0.390	
0.171	0.048	2.840	3.065	0.067	0.001	0.743	0.000	0.019	6.953	0.187	0.420	
0.183	0.045	2.847	3.064	0.068	0.000	0.736	0.000	0.015	6.958	0.199	0.395	

Na	Mg	Al	Si	Fe	Mn	K	Ca	Ti	Total	Na/ Na+K	Mg/ Mg+Fe	Comment
IS10-17 [57.68539N, 2.69897W]												
0.239	0.049	2.769	3.141	0.039	0.000	0.608	0.008	0.022	6.876	0.282	0.556	
0.292	0.043	2.786	3.119	0.025	0.000	0.654	0.000	0.021	6.940	0.309	0.634	
0.271	0.057	2.797	3.100	0.040	0.002	0.656	0.001	0.020	6.945	0.292	0.589	
0.293	0.035	2.827	3.095	0.036	0.000	0.639	0.002	0.016	6.942	0.315	0.494	
0.271	0.050	2.785	3.117	0.037	0.000	0.653	0.001	0.019	6.933	0.293	0.575	
0.327	0.057	2.814	3.081	0.043	0.002	0.651	0.001	0.013	6.989	0.335	0.565	
0.295	0.051	2.768	3.114	0.046	0.001	0.665	0.001	0.021	6.962	0.307	0.525	
0.288	0.039	2.807	3.099	0.045	0.000	0.662	0.000	0.016	6.957	0.303	0.468	
0.284	0.042	2.785	3.115	0.039	0.001	0.651	0.003	0.021	6.939	0.304	0.522	
0.284	0.048	2.808	3.104	0.035	0.000	0.646	0.002	0.015	6.942	0.305	0.580	
IS10-25 [57.68286N, 2.68164W]												
0.070	0.069	2.847	3.055	0.054	0.001	0.817	0.001	0.026	6.939	0.079	0.562	
0.064	0.076	2.878	3.014	0.071	0.001	0.848	0.000	0.025	6.978	0.070	0.518	
0.061	0.067	2.815	3.071	0.062	0.001	0.851	0.000	0.026	6.952	0.067	0.517	
0.070	0.059	2.854	3.046	0.056	0.000	0.861	0.000	0.024	6.969	0.075	0.514	
0.062	0.060	2.853	3.038	0.070	0.000	0.846	0.000	0.030	6.960	0.069	0.459	
0.071	0.066	2.857	3.026	0.071	0.002	0.858	0.000	0.030	6.981	0.076	0.481	
0.075	0.072	2.863	3.027	0.068	0.000	0.840	0.000	0.027	6.972	0.082	0.516	
0.062	0.073	2.801	3.074	0.067	0.002	0.827	0.003	0.031	6.939	0.070	0.522	
0.064	0.089	2.848	3.020	0.101	0.002	0.810	0.001	0.029	6.964	0.073	0.468	
0.067	0.073	2.831	3.047	0.070	0.001	0.845	0.000	0.029	6.964	0.073	0.511	
0.069	0.070	2.856	3.034	0.061	0.002	0.850	0.000	0.027	6.970	0.075	0.534	
0.057	0.108	2.844	2.992	0.176	0.000	0.786	0.001	0.022	6.985	0.067	0.380	
0.058	0.059	2.875	3.037	0.051	0.001	0.861	0.001	0.021	6.964	0.063	0.539	
0.058	0.070	2.862	3.024	0.070	0.000	0.865	0.000	0.029	6.978	0.063	0.501	
0.074	0.065	2.878	3.024	0.066	0.001	0.845	0.000	0.022	6.974	0.080	0.498	
0.070	0.043	2.861	3.051	0.056	0.000	0.854	0.000	0.022	6.958	0.075	0.436	
0.054	0.075	2.793	3.087	0.053	0.000	0.831	0.003	0.031	6.928	0.061	0.585	

Na	Mg	Al	Si	Fe	Mn	K	Ca	Ti	Total	Na/ Na+K	Mg/ Mg+Fe	Comment
0.058	0.068	2.856	3.044	0.059	0.001	0.823	0.000	0.030	6.938	0.066	0.535	
0.058	0.065	2.821	3.076	0.057	0.000	0.837	0.003	0.022	6.939	0.065	0.532	
0.060	0.064	2.833	3.052	0.076	0.000	0.864	0.000	0.021	6.972	0.065	0.456	
0.075	0.066	2.874	3.019	0.075	0.002	0.848	0.001	0.023	6.982	0.081	0.467	
0.064	0.088	2.866	3.015	0.087	0.001	0.833	0.002	0.022	6.979	0.071	0.504	
0.072	0.084	2.831	3.045	0.080	0.000	0.836	0.001	0.022	6.971	0.079	0.514	
0.080	0.084	2.844	3.034	0.076	0.000	0.823	0.000	0.026	6.969	0.088	0.523	
0.072	0.071	2.829	3.038	0.083	0.000	0.849	0.001	0.033	6.976	0.078	0.458	
0.067	0.074	2.837	3.041	0.068	0.002	0.851	0.000	0.029	6.970	0.073	0.519	
0.073	0.071	2.837	3.038	0.077	0.000	0.835	0.001	0.033	6.965	0.081	0.480	
0.074	0.076	2.857	3.026	0.067	0.000	0.846	0.000	0.029	6.976	0.081	0.529	
0.058	0.070	2.836	3.051	0.084	0.001	0.832	0.001	0.022	6.954	0.065	0.455	
0.069	0.073	2.841	3.037	0.080	0.000	0.834	0.000	0.030	6.964	0.076	0.477	
0.068	0.070	2.849	3.034	0.083	0.000	0.849	0.003	0.022	6.978	0.074	0.458	
0.073	0.090	2.846	3.026	0.077	0.001	0.841	0.000	0.027	6.981	0.079	0.538	
0.071	0.081	2.829	3.042	0.076	0.000	0.827	0.000	0.033	6.959	0.079	0.515	
0.058	0.077	2.844	3.029	0.082	0.000	0.838	0.001	0.034	6.963	0.064	0.483	
0.053	0.072	2.798	3.077	0.084	0.002	0.812	0.002	0.028	6.928	0.061	0.463	
0.071	0.083	2.805	3.060	0.092	0.003	0.830	0.001	0.022	6.966	0.079	0.475	
0.072	0.080	2.822	3.047	0.069	0.003	0.840	0.001	0.032	6.965	0.079	0.537	
0.063	0.078	2.878	3.003	0.082	0.000	0.843	0.008	0.028	6.984	0.070	0.488	

Na	Mg	Al	Si	Fe	Mn	K	Ca	Ti	Total	Na/ Na+K	Mg/ Mg+Fe	Comment
IS10-22 [57.69744N, 2.78959W]												
0.123	0.073	2.785	3.076	0.088	0.002	0.776	0.007	0.026	6.956	0.137	0.453	
0.131	0.088	2.755	3.100	0.085	0.000	0.763	0.000	0.023	6.946	0.147	0.507	
0.099	0.090	2.733	3.108	0.114	0.000	0.788	0.000	0.018	6.951	0.112	0.440	
0.114	0.077	2.757	3.100	0.090	0.000	0.780	0.000	0.025	6.943	0.128	0.463	
0.126	0.084	2.741	3.096	0.097	0.000	0.785	0.001	0.029	6.959	0.138	0.466	
0.142	0.046	2.887	3.022	0.072	0.000	0.771	0.000	0.026	6.966	0.156	0.389	
0.118	0.085	2.754	3.098	0.089	0.002	0.772	0.003	0.025	6.945	0.133	0.488	
0.130	0.072	2.794	3.078	0.086	0.000	0.767	0.000	0.023	6.950	0.145	0.457	
0.111	0.078	2.751	3.096	0.102	0.002	0.760	0.002	0.031	6.933	0.128	0.435	
0.121	0.084	2.784	3.078	0.087	0.001	0.778	0.000	0.023	6.956	0.134	0.490	
0.126	0.075	2.786	3.077	0.090	0.000	0.789	0.000	0.022	6.965	0.138	0.456	
0.110	0.088	2.714	3.124	0.101	0.000	0.774	0.001	0.024	6.936	0.124	0.467	
0.111	0.078	2.759	3.101	0.091	0.002	0.774	0.001	0.023	6.939	0.125	0.463	
0.123	0.070	2.784	3.087	0.081	0.000	0.769	0.000	0.027	6.940	0.138	0.465	
0.123	0.084	2.741	3.105	0.086	0.000	0.771	0.001	0.030	6.941	0.138	0.492	
0.110	0.085	2.739	3.100	0.092	0.000	0.775	0.001	0.035	6.938	0.125	0.480	
0.135	0.076	2.779	3.078	0.093	0.001	0.769	0.002	0.026	6.959	0.150	0.449	
0.104	0.120	2.672	3.144	0.099	0.000	0.780	0.000	0.022	6.940	0.118	0.547	
0.115	0.059	2.810	3.085	0.084	0.000	0.770	0.000	0.015	6.938	0.130	0.410	
0.113	0.076	2.798	3.062	0.099	0.001	0.755	0.009	0.030	6.943	0.130	0.436	
0.130	0.073	2.771	3.086	0.082	0.000	0.776	0.001	0.031	6.951	0.144	0.470	
0.131	0.080	2.775	3.082	0.093	0.000	0.757	0.002	0.027	6.947	0.148	0.461	
0.095	0.132	2.595	3.177	0.150	0.001	0.776	0.001	0.017	6.943	0.109	0.467	
0.072	0.132	2.576	3.208	0.116	0.000	0.797	0.000	0.019	6.919	0.083	0.532	
0.122	0.089	2.769	3.078	0.093	0.003	0.774	0.000	0.029	6.956	0.136	0.489	
0.115	0.080	2.809	3.055	0.091	0.000	0.775	0.000	0.031	6.955	0.129	0.468	
0.149	0.072	3.072	2.858	0.086	0.000	0.810	0.000	0.020	7.066	0.155	0.457	Late
0.129	0.069	3.070	2.862	0.087	0.001	0.813	0.003	0.020	7.054	0.137	0.444	Late

Na	Mg	Al	Si	Fe	Mn	K	Ca	Ti	Total	Na/ Na+K	Mg/ Mg+Fe	Comment
0.146	0.061	3.153	2.792	0.094	0.000	0.813	0.001	0.025	7.085	0.152	0.395	Late
0.155	0.071	3.105	2.815	0.094	0.000	0.829	0.000	0.028	7.097	0.158	0.429	Late
0.141	0.072	3.096	2.825	0.104	0.000	0.811	0.000	0.027	7.076	0.148	0.409	Late
0.139	0.072	2.806	3.061	0.095	0.000	0.783	0.001	0.020	6.977	0.150	0.432	Early
0.133	0.078	2.778	3.085	0.073	0.001	0.795	0.000	0.024	6.967	0.144	0.517	Early
0.098	0.097	2.706	3.122	0.111	0.001	0.795	0.001	0.020	6.952	0.110	0.465	Early
0.111	0.079	2.781	3.081	0.085	0.000	0.788	0.002	0.026	6.952	0.124	0.483	Early
0.128	0.073	2.790	3.075	0.086	0.000	0.775	0.000	0.027	6.954	0.141	0.461	Early
0.113	0.058	2.823	3.065	0.085	0.000	0.788	0.001	0.021	6.953	0.126	0.405	
0.127	0.073	2.808	3.063	0.089	0.000	0.781	0.000	0.023	6.964	0.140	0.453	
0.124	0.072	2.834	3.050	0.100	0.001	0.788	0.000	0.010	6.979	0.136	0.417	
0.115	0.058	2.846	3.041	0.107	0.000	0.777	0.002	0.018	6.965	0.129	0.351	
0.131	0.061	2.874	3.032	0.079	0.000	0.768	0.000	0.018	6.963	0.145	0.435	
0.121	0.077	2.827	3.049	0.105	0.000	0.742	0.001	0.023	6.946	0.140	0.421	
0.113	0.066	2.783	3.097	0.081	0.001	0.781	0.000	0.019	6.940	0.126	0.452	
0.112	0.084	2.788	3.073	0.088	0.000	0.784	0.000	0.025	6.956	0.126	0.487	
0.116	0.065	2.743	3.117	0.085	0.000	0.770	0.002	0.028	6.926	0.131	0.436	

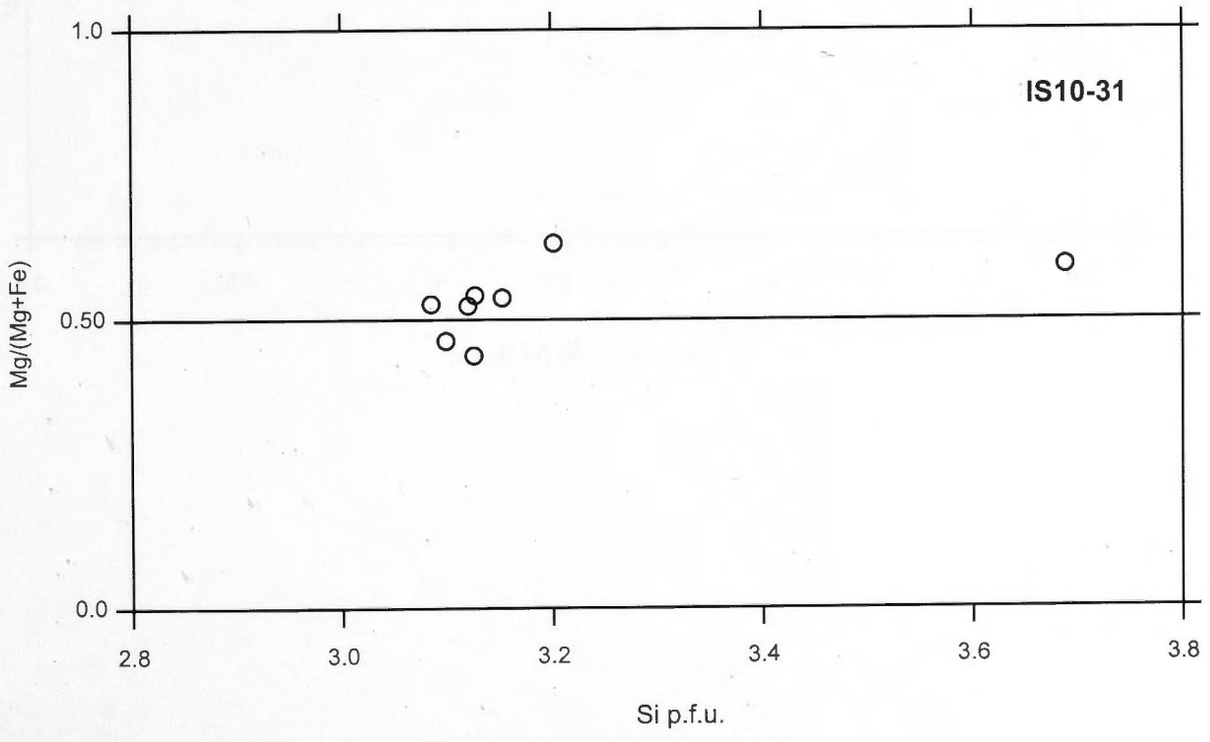

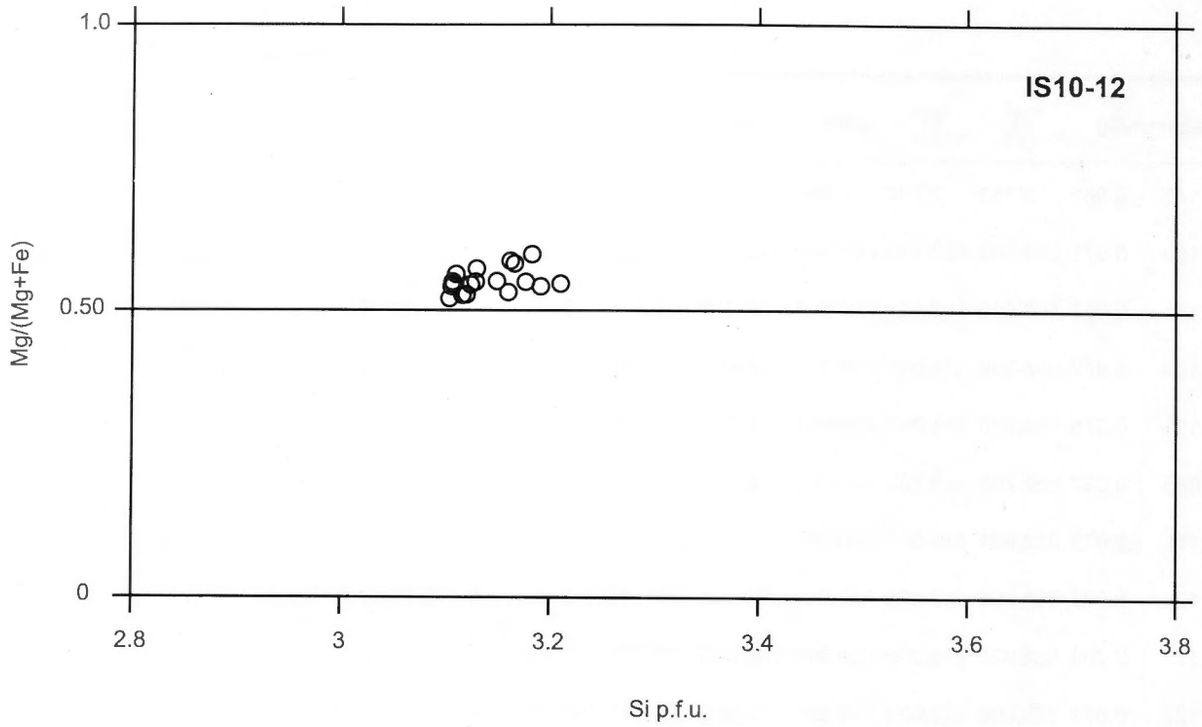
IS10-12
1.0
0.50
0
Mg/(Mg+Fe)
2.8
3
3.2
3.4
3.6
3.8
Si p.f.u.

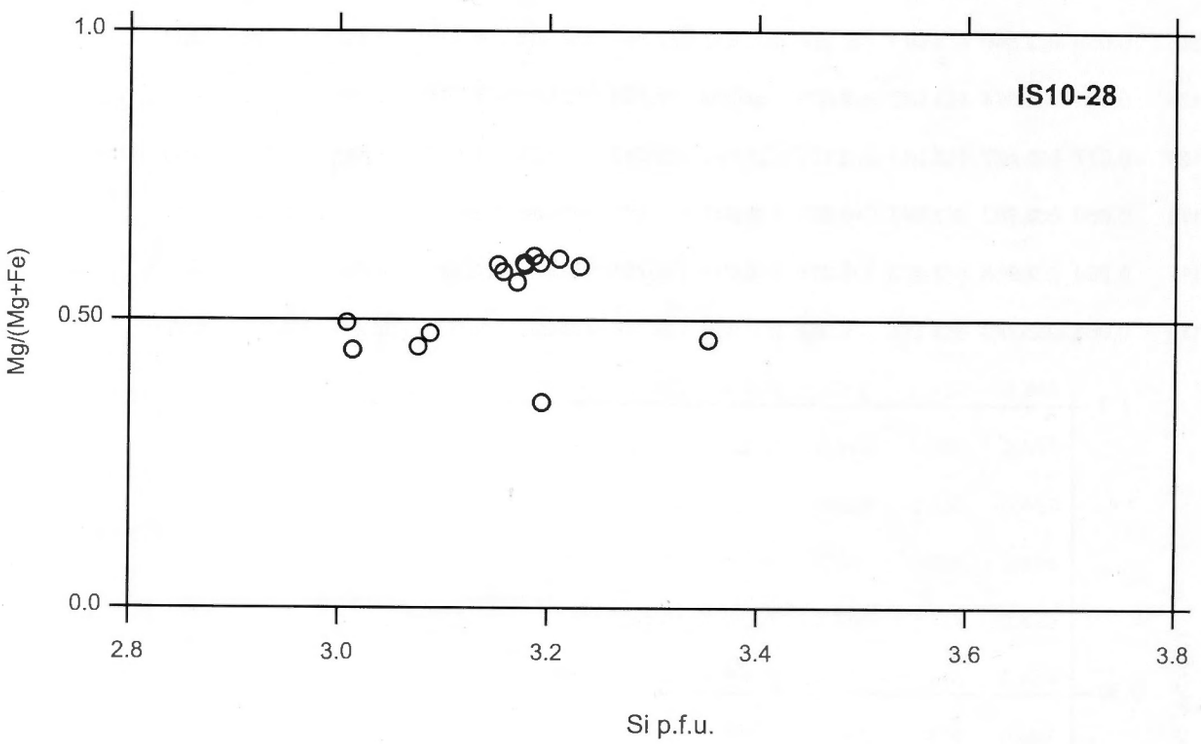
IS10-28
1.0
0.50
0.0
Mg/(Mg+Fe)
2.8
3.0
3.2
3.4
3.6
3.8
Si p.f.u.

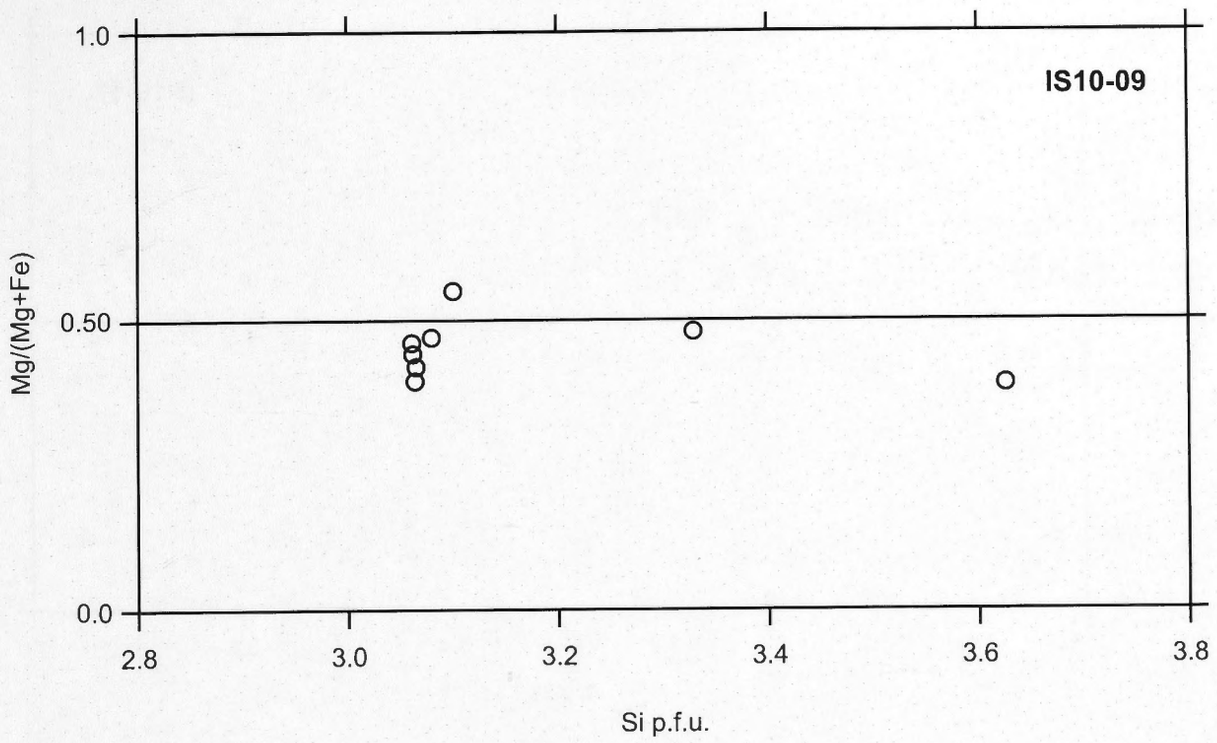
IS10-09
1.0
0.50
0.0
Mg/(Mg+Fe)
2.8
3.0
3.2
3.4
3.6
3.8
Si p.f.u.

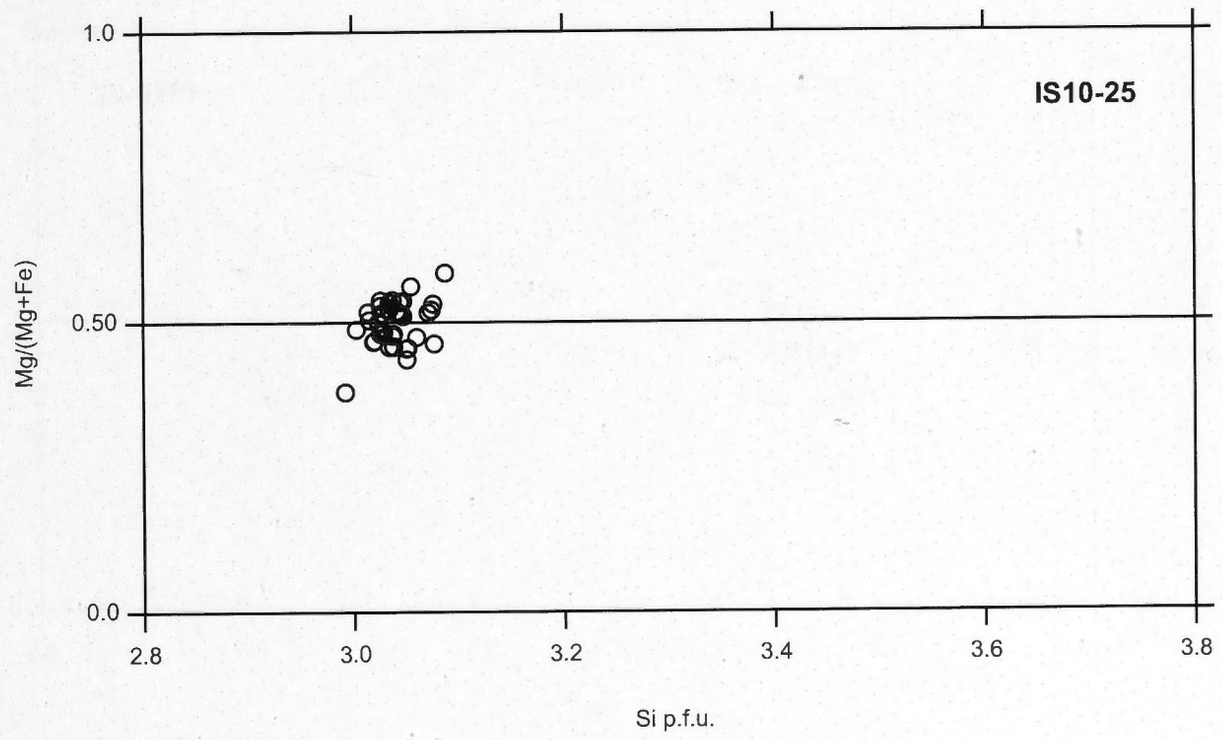
IS10-25
1.0
0.50
0.0
Mg/(Mg+Fe)
2.8
3.0
3.2
3.4
3.6
3.8
Si p.f.u.

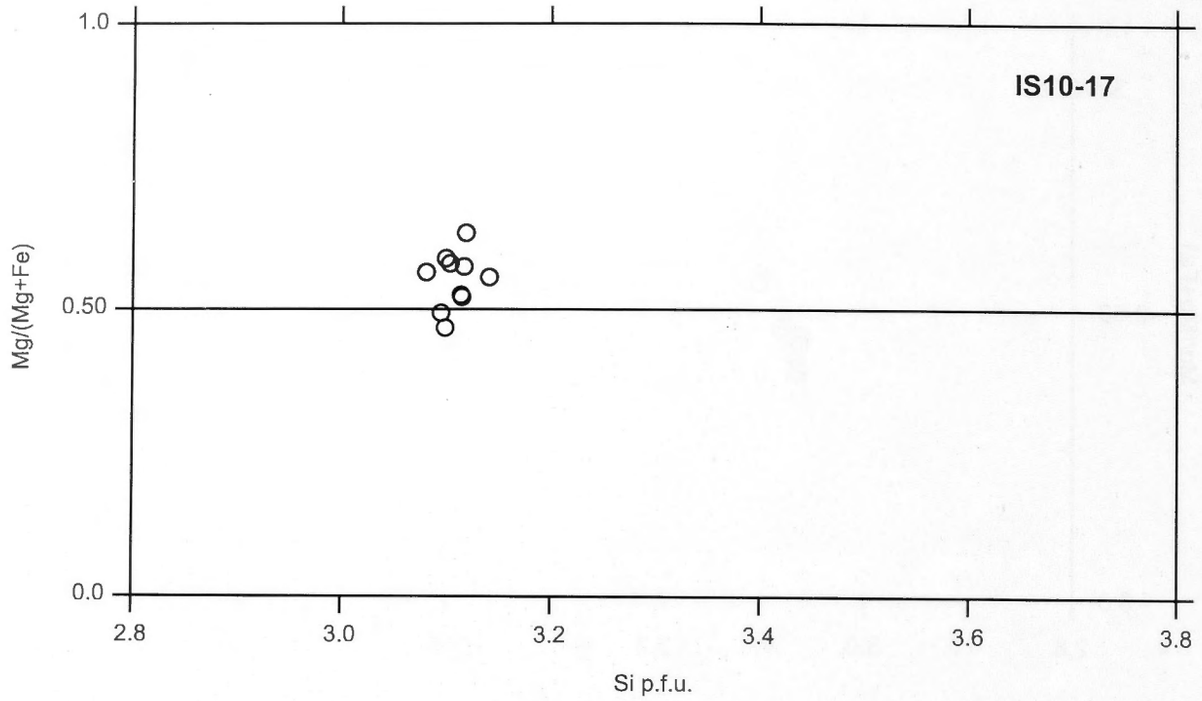
IS10-17
1.0
0.50
0.0
Mg/(Mg+Fe)
2.8
3.0
3.2
3.4
3.6
3.8
Si p.f.u.

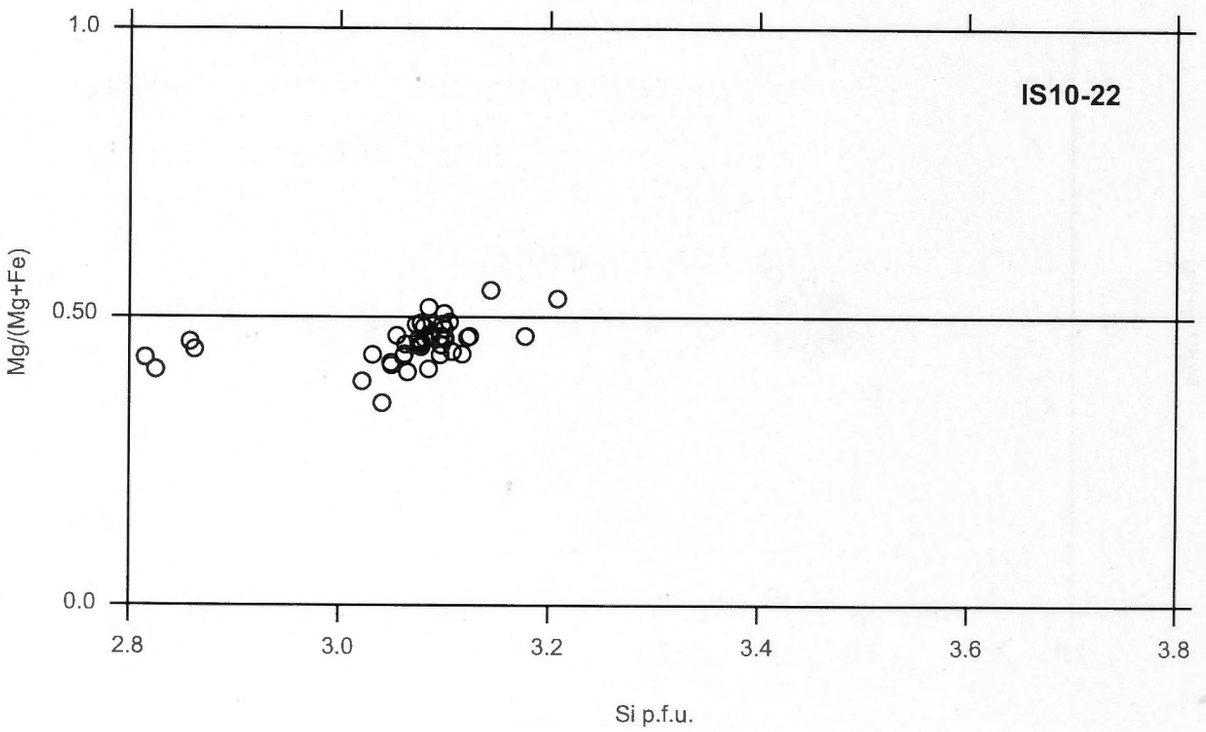
IS10-22
1.0
0.50
0.0
Mg/(Mg+Fe)
2.8
3.0
3.2
3.4
3.6
3.8
Si p.f.u.

APPENDIX B

$^{40}Ar/^{39}Ar$ Step Heating Data
(Chapter 6)

CAN #10 ANU, Sample I1 IS10-25, Muscovite

Analysed: 30th May, 2012

Temp (C)	Ar36 (mol)	err (%)	Ar37 (mol)	err (%)	Ar38 (mol)	err (%)	Ar39 (mol)	err (%)	Ar40 (mol)	err (%)	Ar40* (%)	Ar40*/ Ar39(K) (%)	Cumula-tive Ar39%	Calculated age (Ma)	Error (1σ)	Ca/K
450	3.20E-17	8.21	7.44E-17	41.09	2.31E-17	21.05	6.25E-16	4.58	3.14E-14	4.59	69.90	35.18	0.18	491.99	32.09	2.26E-1
500	3.65E-17	13.52	9.09E-18	146.86	1.69E-17	24.06	1.27E-15	0.78	5.76E-14	0.92	81.20	36.78	0.55	511.57	14.78	1.36E-2
550	1.89E-17	12.48	3.21E-16	9.46	2.92E-17	19.24	2.59E-15	1.69	9.49E-14	1.73	94.10	34.45	1.31	483.04	8.45	2.36E-1
600	3.41E-17	18.89	1.25E-15	3.18	6.22E-17	11.65	4.07E-15	0.52	1.45E-13	0.74	93.10	33.18	2.50	467.44	6.68	5.85E-1
640	1.71E-17	10.41	4.42E-16	4.79	8.10E-17	17.79	4.64E-15	0.57	1.58E-13	0.70	96.80	32.94	3.85	464.35	3.26	1.81E-1
680	1.09E-17	33.58	2.51E-16	31.22	7.89E-17	9.40	6.08E-15	0.43	2.11E-13	0.72	98.50	34.16	5.62	479.48	3.77	7.86E-2
720	1.72E-17	20.51	6.03E-17	22.58	1.16E-16	4.04	8.69E-15	0.88	2.95E-13	0.95	98.20	33.32	8.16	469.12	4.27	1.32E-2
760	4.24E-17	6.21	2.24E-16	9.34	2.08E-16	4.51	1.49E-14	0.59	5.02E-13	0.67	97.50	32.94	12.51	464.36	2.89	2.86E-2
790	5.03E-17	6.50	1.62E-16	11.55	4.89E-16	1.21	3.82E-14	0.44	1.28E-12	0.53	98.80	33.07	23.66	466.04	2.22	8.07E-3
810	4.12E-17	11.76	1.80E-16	24.77	4.57E-16	1.66	3.46E-14	0.48	1.14E-12	0.61	98.90	32.50	33.77	458.93	2.54	9.91E-3
830	4.84E-17	10.90	9.21E-17	24.55	3.03E-16	3.56	2.30E-14	0.62	7.70E-13	0.70	98.10	32.90	40.47	463.95	3.02	7.63E-3
860	2.75E-17	17.74	2.26E-16	15.86	2.75E-16	7.46	1.91E-14	0.62	6.29E-13	0.71	98.70	32.57	46.04	459.81	3.08	2.25E-2
890	1.89E-17	17.52	2.23E-16	30.79	2.01E-16	1.58	1.49E-14	0.57	5.00E-13	0.63	98.90	33.19	50.39	467.51	2.75	2.85E-2
930	3.03E-17	8.21	2.00E-16	5.55	2.32E-16	3.06	1.69E-14	0.69	5.62E-13	0.80	98.40	32.77	55.32	462.29	3.35	2.26E-2
970	1.59E-17	24.95	1.24E-16	19.22	2.87E-16	6.17	2.13E-14	0.74	7.15E-13	0.81	99.30	33.38	61.54	469.82	3.45	1.11E-2
1000	2.89E-17	7.32	1.66E-16	18.50	3.97E-16	1.96	3.07E-14	0.61	1.02E-12	0.74	99.10	33.09	70.50	466.24	3.09	1.03E-2
1040	2.35E-17	9.68	2.18E-16	5.87	7.62E-16	1.52	5.58E-14	0.34	1.84E-12	0.55	99.60	32.86	86.81	463.42	2.26	7.43E-3
1070	1.42E-17	21.71	3.21E-16	3.54	3.03E-16	1.85	2.26E-14	0.42	7.49E-13	0.56	99.40	33.01	93.41	465.22	2.37	2.70E-2
1100	1.96E-17	21.26	1.98E-16	11.00	1.04E-16	5.65	7.69E-15	0.60	2.68E-13	0.77	97.80	34.13	95.65	479.08	3.84	4.89E-2
1150	1.26E-17	31.82	1.44E-16	16.48	1.26E-16	13.81	8.21E-15	0.91	2.86E-13	0.96	98.70	34.36	98.05	481.95	4.47	3.34E-2
1250	9.38E-17	5.84	3.08E-16	26.69	8.25E-17	5.64	4.66E-15	1.34	2.16E-13	1.42	87.20	40.52	99.41	556.21	8.82	1.26E-1
1350	1.59E-16	7.00	2.44E-17	49.84	4.80E-17	10.03	1.90E-15	1.33	1.21E-13	1.39	61.10	39.00	99.97	538.25	23.28	2.44E-2
1450	8.11E-17	8.12	8.27E-17	61.07	1.97E-17	55.13	1.13E-16	7.07	3.20E-14	7.09	25.10	71.50	100.00	889.41	259.16	1.40E+0
Total	**8.75E-16**		**5.30E-15**		**4.70E-15**		**3.42E-13**		**1.16E-11**			**33.20**		**467.57**	**3.31**	

Lambda K40 = 5.54E-10, J Factor = 8.913E-3, err% = 0.967%

The following pages contain the data tables for all samples analysed in the argon geochronology study detailed in Chapter 6.

CAN #10 ANU, Sample I2 IS10-22, Muscovite

Analysed: 6th June, 2012

Temp (C)	Ar36 (mol)	err (%)	Ar37 (mol)	err (%)	Ar38 (mol)	err (%)	Ar39 (mol)	err (%)	Ar40 (mol)	err (%)	Ar40* (%)	Ar40*/ Ar39(K) (%)	Cumala-tive Ar39%	Calculated age (Ma)	Error (1σ)	Ca/K
450	1.62E-17	10.17	1.89E-19	196.19	8.98E-18	19.52	2.91E-16	2.02	1.27E-14	2.05	62.20	27.04	0.19	389.30	24.54	1.23E-3
500	2.23E-17	17.27	1.89E-19	136.59	5.81E-18	34.20	6.11E-16	1.02	2.37E-14	1.16	72.20	28.03	0.58	402.12	24.67	5.88E-4
550	9.32E-18	17.79	1.90E-19	164.40	1.52E-17	18.36	1.08E-15	0.60	4.15E-14	0.71	93.30	35.98	1.28	501.57	6.46	3.35E-4
600	2.43E-18	111.80	3.70E-17	65.18	3.89E-17	10.66	2.17E-15	1.00	7.88E-14	1.06	99.10	35.90	2.69	500.52	6.49	3.23E-2
650	2.66E-18	112.71	8.27E-17	24.58	5.42E-17	7.16	4.10E-15	0.33	1.45E-13	0.59	99.40	35.05	5.35	490.21	3.69	3.83E-2
700	2.92E-17	20.45	6.79E-17	34.47	1.65E-16	1.77	1.24E-14	0.41	4.16E-13	0.49	97.90	32.85	13.37	463.00	2.69	1.04E-2
730	1.33E-17	22.04	4.35E-17	29.27	4.18E-16	4.34	3.00E-14	0.29	1.01E-12	0.38	99.60	33.46	32.81	470.62	1.60	2.75E-3
760	1.30E-17	20.44	1.91E-19	110.14	3.09E-16	2.00	2.38E-14	0.37	7.94E-13	0.47	99.50	33.13	48.26	466.49	1.99	1.52E-5
790	7.08E-18	36.21	1.91E-19	51.48	1.53E-16	3.04	1.15E-14	0.60	3.84E-13	0.90	99.40	33.21	55.71	467.48	3.81	3.15E-5
810	1.68E-18	96.97	1.06E-17	201.55	7.44E-17	6.42	6.54E-15	0.97	2.19E-13	1.01	99.70	33.36	59.94	469.39	4.30	3.08E-3
840	9.30E-18	36.76	3.90E-17	41.71	8.47E-17	6.78	6.44E-15	0.62	2.17E-13	0.68	98.70	33.23	64.12	467.77	3.43	1.15E-2
870	3.02E-20	999.00	4.26E-17	131.62	8.67E-17	5.85	6.75E-15	0.13	2.31E-13	0.42	100.00	34.22	68.49	480.02	1.77	1.20E-2
910	5.29E-19	999.00	1.92E-19	151.49	1.58E-16	3.92	1.20E-14	0.61	3.99E-13	0.68	99.90	33.08	76.30	465.93	3.21	3.03E-5
940	1.33E-17	71.87	7.40E-17	67.27	2.22E-16	5.08	1.64E-14	0.49	5.44E-13	0.58	99.20	32.98	86.91	464.62	3.21	8.58E-3
960	6.08E-18	49.31	8.34E-17	21.71	1.63E-16	2.45	1.29E-14	0.41	4.30E-13	0.53	99.60	33.22	95.25	467.67	2.34	1.23E-2
990	2.39E-18	158.38	2.45E-17	70.91	7.47E-17	4.87	5.50E-15	1.56	1.87E-13	1.63	99.60	33.83	98.82	475.19	7.27	8.46E-3
1030	2.99E-18	120.48	1.07E-16	77.81	1.25E-17	64.39	1.21E-15	1.21	4.16E-14	1.36	97.90	33.54	99.60	471.55	12.27	1.67E-1
1080	9.16E-18	30.24	9.85E-17	64.55	1.36E-17	66.92	3.50E-16	3.53	1.27E-14	3.59	78.70	28.67	99.83	410.26	34.29	5.36E-1
1150	2.04E-17	14.14	7.81E-17	20.75	1.32E-18	373.11	1.37E-16	3.16	9.74E-15	3.24	38.30	27.41	99.92	394.05	85.72	1.09E+0
1250	8.32E-17	9.88	1.79E-17	97.56	2.27E-17	17.57	8.30E-17	9.11	2.94E-14	9.12	16.40	58.27	99.97	754.24	461.39	4.10E-1
1350	6.54E-17	23.96	6.11E-17	50.99	6.30E-18	52.27	1.95E-17	23.50	1.90E-14	23.50	-1.50	0.00	99.98	0.02	5315.24	6.14E+0
1450	5.68E-17	15.19	4.56E-17	22.88	1.23E-17	41.68	2.71E-17	12.33	1.67E-14	12.33	-0.60	0.00	100.00	0.02	1941.95	3.24E+0
Total	**3.87E-16**		**9.14E-16**		**2.10E-15**		**1.54E-13**		**5.26E-12**			**33.32**		**468.89**	**4.43**	

Lambda K40=5.54E-10, J Factor =8.908E-3, err = 0.967%

CAN #10 ANU, Sample I3 IS10-09, Muscovite

Analysed: 24th May, 2012

Temp (C)	Ar36 (mol)	err (%)	Ar37 (mol)	err (%)	Ar38 (mol)	err (%)	Ar39 (mol)	err (%)	Ar40 (mol)	err (%)	Ar40* (%)	Ar40*/ Ar39(K) (%)	Cumala-tive Ar39%	Calculated age (Ma)	Error (1σ)	Ca/K
450	4.31E-17	10.75	8.76E-17	32.73	1.02E-17	118.09	5.33E-16	2.02	1.97E-14	2.08	35.20	13.00	0.24	197.54	38.60	3.13E-1
500	6.02E-17	5.87	5.94E-17	8.85	3.62E-17	6.39	1.18E-15	2.35	4.58E-14	2.40	61.10	23.77	0.78	346.28	17.06	9.58E-2
550	4.99E-17	8.39	1.04E-16	19.01	3.91E-17	23.32	1.88E-15	2.20	6.99E-14	2.23	78.90	29.37	1.63	418.97	13.47	1.05E-1
600	2.93E-17	8.23	6.53E-16	4.32	5.72E-17	9.82	3.60E-15	1.29	1.29E-13	1.33	93.30	33.40	3.26	469.67	6.38	3.45E-1
640	3.13E-17	5.41	3.69E-16	3.05	9.37E-17	12.38	6.06E-15	0.37	2.18E-13	0.52	95.70	34.50	6.01	483.20	2.53	1.16E-1
680	2.27E-17	51.39	2.37E-16	5.89	1.36E-16	4.52	1.05E-14	0.90	3.71E-13	0.96	98.20	34.82	10.75	487.11	5.81	4.31E-2
720	1.08E-17	50.94	3.22E-16	7.02	1.96E-16	3.98	1.63E-14	0.46	5.65E-13	0.70	99.40	34.47	18.15	482.81	3.23	3.75E-2
750	3.01E-20	164.09	4.58E-16	3.28	2.68E-16	3.40	2.05E-14	0.61	7.03E-13	0.69	100.00	34.25	27.45	480.17	2.93	4.24E-2
780	5.63E-18	66.65	6.00E-16	3.16	3.49E-16	2.01	2.68E-14	0.51	9.17E-13	0.63	99.80	34.17	39.59	479.17	2.72	4.26E-2
810	1.74E-17	15.39	5.53E-16	5.47	4.03E-16	2.50	3.28E-14	0.49	1.10E-12	0.70	99.50	33.47	54.46	470.46	2.93	3.20E-2
840	1.04E-17	46.88	5.23E-16	5.76	3.69E-16	3.63	2.85E-14	0.47	9.71E-13	0.59	99.70	33.94	67.39	476.28	2.54	3.49E-2
860	2.76E-17	10.26	4.26E-16	17.18	1.99E-16	3.33	1.56E-14	0.71	5.31E-13	0.98	98.40	33.63	74.44	472.41	4.18	5.21E-2
890	2.54E-17	11.54	2.64E-16	13.16	1.52E-16	3.51	1.13E-14	1.06	3.87E-13	1.13	98.00	33.66	79.55	472.78	4.91	4.45E-2
920	1.18E-17	29.94	2.04E-16	9.73	1.19E-16	3.40	9.00E-15	0.86	3.10E-13	0.91	98.90	34.10	83.63	478.26	4.13	4.31E-2
960	1.27E-17	68.92	2.93E-16	9.44	1.37E-16	3.26	1.05E-14	0.89	3.52E-13	1.00	98.90	33.32	88.37	468.61	5.19	5.32E-2
1000	1.67E-18	182.39	4.15E-16	4.18	1.51E-16	5.63	1.18E-14	0.59	3.95E-13	0.67	99.90	33.46	93.71	470.36	2.93	6.69E-2
1040	2.03E-17	22.44	4.36E-16	6.96	1.54E-16	10.57	1.04E-14	0.46	3.52E-13	0.55	98.30	33.27	98.43	468.02	2.80	7.97E-2
1090	1.74E-17	11.32	2.64E-16	5.29	5.28E-17	5.94	3.17E-15	1.87	1.10E-13	1.91	95.30	33.00	99.86	464.61	8.50	1.58E-1
1150	9.53E-18	22.84	2.01E-16	11.36	1.55E-17	39.37	1.75E-16	5.13	9.12E-15	5.14	69.30	36.42	99.94	506.60	55.05	2.20E+0
1250	1.19E-16	16.16	3.62E-17	45.58	2.27E-17	24.43	4.31E-17	15.80	3.90E-14	15.82	10.00	91.17	99.96	1072.01	1726.52	1.61E+0
1350	6.20E-16	8.31	6.02E-17	40.37	1.09E-16	11.87	4.28E-17	8.23	1.92E-13	8.23	4.60	209.41	99.98	1898.40	2870.64	2.70E+0
1450	1.63E-16	40.10	1.80E-17	382.91	3.68E-17	40.49	4.55E-17	40.01	4.63E-14	40.01	-3.70	0.00	100.00	0.02	9437.86	7.55E-1
Total	**1.31E-15**		**6.58E-15**		**3.11E-15**		**2.21E-13**		**7.83E-12**			**33.78**		**474.32**	**6.59**	

Lambda K40=5.54E-10, J Factor =8.902E-3, err = 0.968%

CAN #10 ANU, Sample I4 IS10-17, Muscovite

Analysed: 12th June, 2012

Temp (C)	Ar36 (mol)		Ar37 (mol)		Ar38 (mol)		Ar39 (mol)		Ar40 (mol)		Ar40* (%)	Ar40*/ Ar39(K) (%)	Cumala-tive Ar39%	Calculated age (Ma)	Error (1σ)	Ca/K
450	9.47E-18	31.24	2.15E-19	20.38	1.16E-17	70.16	9.10E-16	3.82	2.99E-14	3.84	90.60	29.73	0.56	423.43	20.13	4.49E-4
500	2.06E-17	26.62	2.05E-16	19.09	3.45E-17	19.14	1.92E-15	2.00	6.88E-14	2.04	91.10	32.70	1.72	460.74	13.92	2.03E-1
550	1.31E-17	38.24	2.15E-19	152.48	6.75E-17	3.70	5.22E-15	0.95	1.88E-13	1.00	97.90	35.20	4.91	491.47	5.59	7.84E-5
600	1.23E-17	19.56	5.57E-17	54.20	1.25E-16	4.57	9.21E-15	0.42	3.18E-13	0.53	98.80	34.11	10.53	478.13	2.45	1.15E-2
640	1.65E-17	14.76	2.69E-16	27.09	1.73E-16	2.57	1.26E-14	0.39	4.29E-13	0.47	98.80	33.75	18.18	473.73	2.10	4.07E-2
680	4.67E-17	12.63	1.54E-16	13.53	4.10E-16	4.11	2.98E-14	0.58	1.01E-12	0.72	98.60	33.55	36.34	471.19	3.11	9.81E-3
710	1.70E-17	16.97	7.52E-17	35.35	3.72E-16	1.67	2.96E-14	0.61	9.95E-13	0.74	99.50	33.44	54.39	469.91	3.10	4.83E-3
740	7.20E-18	38.15	4.58E-17	54.95	1.77E-16	4.40	1.44E-14	0.67	4.86E-13	0.84	99.50	33.52	63.20	470.88	3.55	6.03E-3
770	5.45E-18	29.56	4.23E-18	486.84	1.02E-16	6.89	6.92E-15	1.23	2.34E-13	1.27	99.30	33.60	67.42	471.87	5.36	1.16E-3
810	3.77E-17	15.65	7.69E-17	100.91	7.86E-17	4.51	6.41E-15	1.38	2.17E-13	1.41	94.80	32.02	71.33	452.25	6.86	2.28E-2
840	1.78E-17	20.03	2.03E-16	37.50	8.82E-17	5.75	6.56E-15	0.82	2.24E-13	0.91	97.60	33.36	75.33	468.83	4.32	5.87E-2
870	1.69E-17	11.26	1.18E-16	35.31	1.09E-16	5.54	7.46E-15	0.92	2.54E-13	0.98	98.00	33.35	79.88	468.78	4.24	3.01E-2
910	1.34E-17	10.26	1.12E-17	618.73	1.66E-16	2.60	1.27E-14	0.71	4.27E-13	0.76	99.00	33.35	87.62	468.70	3.19	1.67E-3
940	2.13E-17	25.78	1.68E-17	98.67	1.57E-16	7.65	1.22E-14	0.48	4.11E-13	0.54	98.40	33.15	95.06	466.33	2.80	2.62E-3
970	4.91E-18	84.84	2.18E-19	224.18	9.98E-17	12.61	6.62E-15	0.69	2.23E-13	0.75	99.30	33.47	99.10	470.21	3.88	6.25E-5
1000	3.88E-18	243.67	2.18E-19	999.00	2.40E-17	25.34	1.13E-15	0.84	3.94E-14	1.14	97.10	33.79	99.79	474.15	30.85	3.66E-4
1040	3.04E-20	143.13	2.18E-19	100.75	3.03E-20	118.36	1.74E-16	2.58	6.88E-15	2.63	99.80	39.52	99.90	543.50	12.40	2.39E-3
1080	1.32E-18	224.78	2.18E-19	36.25	7.13E-19	417.71	3.99E-17	5.57	3.45E-15	5.71	88.70	76.60	99.92	937.62	214.34	1.04E-2
1150	1.51E-17	18.92	2.19E-19	29.68	3.03E-20	96.39	3.57E-17	11.91	5.62E-15	11.92	20.80	32.77	99.94	461.54	374.18	1.16E-2
1250	4.67E-17	11.57	2.19E-19	77.47	9.04E-18	41.77	3.29E-17	10.56	1.49E-14	10.57	7.40	33.60	99.96	471.86	842.64	1.26E-2
1350	4.81E-17	13.75	2.19E-19	76.05	1.70E-17	18.48	3.57E-17	10.81	1.24E-14	10.82	-14.90	0.00	99.99	0.02	1065.05	1.16E-2
1450	3.52E-17	77.21	8.05E-17	135.02	1.26E-17	80.24	2.31E-17	76.83	1.19E-14	76.84	12.60	67.25	100.00	846.03	5289.68	6.84E+0
Total	**4.11E-16**		**1.32E-15**		**2.23E-15**		**1.64E-13**		**5.61E-12**			**33.49**		**470.47**	**5.14**	

Lambda K40 = 5.54E-10, J factor = 8.897E-3, 0.968%

CAN #10 ANU, Sample I5 IS10-12, Muscovite

Analysed: 15th June, 2012

Temp (C)	Ar36 (mol)	err (%)	Ar37 (mol)	err (%)	Ar38 (mol)	err (%)	Ar39 (mol)	err (%)	Ar40 (mol)	err (%)	Ar40* (%)	Ar40*/ Ar39(K) (%)	Cumula-tive Ar39%	Calculated age (Ma)	Error (1σ)	Ca/K
450	1.59E-17	27.77	2.28E-19	203.60	3.51E-18	102.00	4.45E-16	1.76	1.56E-14	1.80	69.90	24.50	0.14	355.77	39.54	9.74E-4
500	1.59E-17	16.10	4.33E-17	45.44	2.22E-17	16.28	1.08E-15	1.05	3.70E-14	1.18	87.30	30.05	0.47	427.43	10.28	7.65E-2
550	1.96E-17	13.47	2.29E-19	31.00	5.72E-17	11.71	3.92E-15	0.78	1.47E-13	0.88	96.00	35.87	1.70	499.74	4.70	1.11E-4
600	2.28E-17	12.84	8.48E-17	47.99	8.96E-17	4.54	6.73E-15	0.63	2.55E-13	0.84	97.30	36.85	3.79	511.59	4.17	2.39E-2
640	2.11E-17	8.88	1.76E-16	19.67	1.29E-16	3.29	8.66E-15	0.37	3.28E-13	0.51	98.10	37.19	6.49	515.69	2.47	3.86E-2
680	2.09E-17	10.59	1.90E-16	45.20	2.11E-16	3.73	1.46E-14	0.81	5.87E-13	1.05	98.90	39.68	11.05	545.44	5.00	2.46E-2
710	2.31E-17	14.32	1.41E-16	18.08	2.91E-16	4.94	2.02E-14	0.33	8.76E-13	0.62	99.20	42.99	17.35	584.34	3.16	1.32E-2
740	4.09E-17	8.55	8.96E-17	26.79	4.51E-16	1.70	3.40E-14	0.63	1.42E-12	0.86	99.10	41.45	27.92	566.34	4.24	5.01E-3
760	5.17E-18	48.68	3.38E-17	162.95	3.60E-16	1.68	2.80E-14	0.47	1.13E-12	0.81	99.80	40.22	36.66	551.86	3.87	2.29E-3
780	1.87E-17	47.95	5.10E-17	68.79	3.22E-16	2.49	2.30E-14	0.75	9.54E-13	0.88	99.40	41.18	43.83	563.21	4.48	4.21E-3
810	1.75E-17	14.76	2.30E-19	93.07	3.84E-16	5.91	2.98E-14	0.46	1.28E-12	0.62	99.60	42.71	53.12	581.08	3.11	1.47E-5
840	1.43E-17	24.22	5.97E-17	128.49	3.70E-16	2.80	2.87E-14	0.82	1.32E-12	1.15	99.70	45.72	62.06	615.67	6.05	3.95E-3
860	1.72E-17	60.00	1.16E-16	22.34	2.99E-16	2.25	2.29E-14	0.74	1.08E-12	1.07	99.50	46.83	69.20	628.34	5.90	9.63E-3
890	1.60E-17	28.86	4.20E-17	78.79	2.88E-16	3.33	2.24E-14	1.15	1.13E-12	1.26	99.60	49.99	76.19	663.82	7.04	3.55E-3
920	1.32E-17	22.84	1.05E-16	77.13	2.56E-16	4.84	1.89E-14	0.60	1.02E-12	0.77	99.60	53.83	82.07	705.97	4.55	1.05E-2
950	6.51E-18	53.06	2.31E-19	81.64	2.26E-16	2.53	1.70E-14	0.28	9.47E-13	0.76	99.80	55.56	87.37	724.63	4.61	2.58E-5
980	3.17E-20	75.43	2.88E-17	103.11	1.88E-16	2.49	1.50E-14	0.99	8.92E-13	1.36	100.00	59.38	92.05	765.19	8.46	3.64E-3
1010	9.27E-18	94.85	2.28E-16	11.46	1.60E-16	4.56	1.09E-14	0.70	6.18E-13	0.83	99.50	56.33	95.45	732.94	5.61	3.97E-2
1040	2.28E-18	117.54	1.46E-17	115.99	7.39E-17	4.68	5.18E-15	0.40	3.09E-13	0.55	99.80	59.54	97.07	766.90	3.81	5.36E-3
1080	8.88E-18	45.07	1.14E-16	30.27	3.35E-17	9.93	3.19E-15	2.74	1.92E-13	2.76	98.60	59.31	98.06	764.44	17.84	6.79E-2
1150	6.97E-18	130.94	2.33E-19	627.86	4.19E-17	21.61	2.80E-15	6.12	1.81E-13	9.26	98.80	64.10	98.93	814.15	62.17	1.58E-4
1250	4.97E-17	3.69	1.56E-16	37.68	4.93E-17	11.11	3.34E-15	2.49	2.40E-13	2.51	93.90	67.30	99.97	846.54	18.14	8.86E-2
1350	5.10E-17	6.91	2.33E-19	71.97	1.09E-17	76.77	8.43E-17	3.82	1.87E-14	4.38	19.60	43.48	100.00	589.94	182.02	5.25E-3
1450	4.03E-17	296.92	1.39E-16	297.67	1.27E-17	299.43	2.18E-18	296.87	9.94E-15	296.87	-19.70	0.00	100.00	0.02	340658.85	2.86E+02
Total	**4.57E-16**		**1.81E-15**		**4.33E-15**		**3.21E-13**		**1.50E-11**			**46.24**		**621.60**	**6.68**	

LambdaK40 = 5.54E-10, J Factor = 8.897E-3, err = 0.968%

CAN #10 ANU, Sample I6 IS10-28, Muscovite

Analysed: 19th June, 2012

Temp (C)	Ar36 (mol)	err (%)	Ar37 (mol)	err (%)	Ar38 (mol)	err (%)	Ar39 (mol)	err (%)	Ar40 (mol)	err (%)	Ar40* (%)	Ar40*/ Ar39(K) (%)	Cumula-tive Ar39%	Calculated age (Ma)	Error (1σ)	Ca/K
450	5.75E-18	27.46	2.45E-19	43.41	1.73E-19	999.08	3.49E-17	12.99	2.67E-15	13.02	36.20	27.72	0.08	397.31	214.69	1.33E-2
500	9.75E-18	18.53	7.11E-18	365.77	1.63E-17	37.38	9.56E-17	3.76	4.87E-15	3.78	40.80	20.78	0.31	305.66	80.04	1.41E-1
550	4.46E-18	56.26	5.08E-17	61.34	5.93E-18	66.26	2.30E-16	2.39	9.51E-15	2.43	86.20	35.72	0.87	497.38	41.11	4.21E-1
600	1.41E-17	18.78	1.21E-16	11.54	1.01E-17	34.51	5.20E-16	1.63	2.14E-14	1.67	80.60	33.36	2.12	468.32	20.44	4.42E-1
650	2.97E-20	153.56	5.65E-17	51.68	1.72E-17	16.61	1.23E-15	2.04	4.83E-14	2.13	100.00	39.29	5.08	540.30	9.94	8.74E-2
700	9.40E-18	15.50	7.71E-18	226.03	3.47E-17	14.58	3.23E-15	1.42	1.31E-13	1.59	97.90	39.82	12.87	546.53	7.80	4.54E-3
750	2.35E-17	36.33	1.63E-16	35.87	1.52E-16	1.89	1.16E-14	0.39	4.79E-13	1.05	98.50	40.90	40.72	559.31	5.73	2.68E-2
800	3.02E-20	73.65	2.46E-19	64.34	8.73E-17	8.56	6.77E-15	1.29	2.88E-13	1.38	100.00	42.49	57.04	577.85	6.83	6.91E-5
860	1.18E-18	255.58	2.46E-19	179.78	4.38E-17	7.22	3.83E-15	1.17	2.06E-13	1.20	99.80	53.60	66.29	702.77	7.42	1.22E-4
920	1.52E-17	18.37	1.87E-17	612.30	5.83E-17	14.94	4.13E-15	1.17	2.47E-13	2.24	98.20	58.71	76.25	757.44	14.26	8.61E-3
1000	4.27E-18	85.14	1.80E-16	36.62	1.04E-16	11.17	7.79E-15	0.24	4.34E-13	0.73	99.70	55.57	95.02	723.99	4.60	4.40E-2
1080	5.72E-18	118.43	8.94E-17	31.89	2.77E-17	11.02	1.42E-15	0.69	8.03E-14	1.23	97.90	55.33	98.45	721.44	16.87	1.20E-1
1150	4.76E-18	21.32	2.47E-19	61.82	5.93E-18	49.39	3.68E-16	1.95	2.06E-14	2.31	93.10	52.09	99.34	686.30	16.74	1.28E-3
1250	1.32E-17	25.84	1.48E-16	40.30	1.64E-18	236.41	2.42E-16	7.11	1.95E-14	7.26	80.00	64.69	99.92	819.31	73.05	1.17E+0
1350	3.23E-17	22.43	1.67E-16	48.21	3.03E-20	95.87	1.79E-17	18.78	6.02E-15	18.79	-58.30	0.00	99.96	0.02	2173.20	1.94E+1
1450	3.65E-17	25.54	2.30E-17	106.66	3.03E-20	305.91	1.67E-17	18.49	6.76E-15	19.07	-59.30	0.00	100.00	0.02	2914.86	2.64E+0
Total	**1.80E-16**		**1.03E-15**		**5.64E-16**		**4.15E-14**		**2.00E-12**			**47.25**		**632.44**	**10.60**	

LambdaK40 = 5.54E-10, J Factor = 8.886E-3, err = 0.970%

CAN #10 ANU, Sample I7 IS10-31, Muscovite

Analysed: 21st June, 2012

Temp (C)	Ar36 (mol)	err (%)	Ar37 (mol)	err (%)	Ar38 (mol)	err (%)	Ar39 (mol)	err (%)	Ar40 (mol)	err (%)	Ar40* (%)	Ar40*/ Ar39(K) (%)	Cumala-tive Ar39%	Calculated age (Ma)	Error (1σ)	Ca/K
450	1.53E-17	82.32	6.24E-17	118.90	9.00E-18	114.07	1.99E-17	79.69	2.88E-15	79.81	-57.10	0.00	0.29	0.02	3535.60	6.15E+0
500	9.99E-18	88.19	6.12E-18	999.07	6.52E-18	100.18	3.54E-17	11.88	3.06E-15	11.90	3.40	2.92	0.82	46.25	1158.98	3.28E-1
550	1.72E-17	34.62	1.16E-16	33.42	2.61E-17	28.44	4.36E-17	13.73	3.35E-15	13.90	-51.10	0.00	1.46	0.02	667.88	5.20E+0
600	4.72E-18	181.73	1.09E-16	25.62	3.00E-18	86.01	1.31E-16	4.19	5.60E-15	8.06	75.30	32.49	3.40	457.56	244.78	1.60E+0
680	2.71E-20	86.39	1.91E-16	32.19	1.97E-17	25.00	5.03E-16	9.34	1.87E-14	12.28	100.00	37.30	10.92	516.42	54.96	7.23E-1
720	8.77E-18	31.68	9.37E-17	63.02	5.82E-18	67.46	4.49E-16	0.88	1.79E-14	2.24	85.60	34.24	17.64	479.27	25.01	3.97E-1
760	7.39E-19	253.33	1.16E-16	66.74	1.98E-17	13.24	9.95E-16	3.49	3.96E-14	4.19	99.40	39.59	32.54	543.87	20.83	2.22E-1
820	3.02E-20	267.96	1.94E-16	24.32	2.17E-17	12.47	1.75E-15	0.91	7.10E-14	2.07	100.00	40.63	58.71	556.07	9.90	2.11E-1
900	1.33E-18	141.57	1.54E-16	15.66	1.98E-17	16.85	1.14E-15	1.73	5.71E-14	1.99	99.30	49.66	75.82	659.47	12.30	2.56E-1
1000	1.17E-17	72.94	1.77E-16	13.09	1.09E-17	111.75	1.22E-15	2.09	7.06E-14	2.35	95.10	54.94	94.14	717.25	26.57	2.75E-1
1100	2.78E-19	613.14	2.29E-16	50.94	2.92E-18	93.68	2.59E-16	7.82	1.46E-14	7.93	99.50	56.54	97.99	734.37	52.06	1.69E+0
1250	4.83E-18	136.80	1.13E-16	45.87	1.13E-17	52.71	1.08E-16	10.52	4.55E-14	10.53	96.90	412.16	99.60	2777.48	164.84	2.00E+0
1350	2.97E-17	37.69	1.76E-16	46.73	6.98E-18	53.75	1.70E-17	37.31	1.41E-14	37.31	37.80	345.21	99.83	2531.21	1438.39	2.17E+1
1450	2.72E-17	31.26	2.61E-19	203.56	1.23E-17	44.65	1.15E-17	30.14	7.43E-15	30.14	-8.10	0.00	100.00	0.02	4696.97	4.31E-2
Total	**1.32E-16**		**1.74E-15**		**1.76E-16**		**6.69E-15**		**3.71E-13**			**50.43**		**668.03**	**59.91**	

LambdaK40 = 5.54E-10, J Factor = 8.886E-3, err = 0.970%